ISSN 2074-272X

науково-практичний журнал 2026/1

# Електротехніка і Електромеханіка

# Electrical Engineering & Electromechanics

Електричні машини та апарати
Електротехнічні комплекси та системи
Промислова електроніка
Техніка сильних електричних та магнітних полів, інженерна електрофізика
Електроізоляційна та кабельна техніка

Журнал включено до найвищої категорії «А» Переліку фахових видань України

З 2019 р. журнал індексується у Scopus

З 2005 р. журнал індексується у Web of Science Core Collection: Emerging Sources Citation Index

# Electrical Engineering & Electromechanics

Scientific Journal was founded in 2002
**Co-founders:** National Technical University «Kharkiv Polytechnic Institute» (Kharkiv, Ukraine);
Anatolii Pidhornyi Institute of Power Machines and Systems of NAS of Ukraine (Kharkiv, Ukraine)



From no. 1 2019 Journal «Electrical Engineering & Electromechanics» is indexing in **Scopus** and from no. 1 2005 Journal is indexing in **Web of Science Core Collection: Emerging Sources Citation Index (ESCI)**
Also included in DOAJ (Directory of Open Access Journals), in EBSCO's database, in ProQuest's databases – Advanced Technologies & Aerospace Database and Materials Science & Engineering Database, in Gale/Cengage Learning databases.

**Editorial office address**:
National Technical University «Kharkiv Polytechnic Institute», Kyrpychova Str., 2, Kharkiv, 61002, Ukraine
**phone:** +380 67 3594696, **e-mail:** a.m.grechko@gmail.com (**Grechko O.M.)**
**ISSN (print) 2074-272X**
**ISSN (online) 2309-3404**


Approved for printing on 28 December 2025. Format 60 × 90 ⅛. Paper – offset. Laser printing. Edition 50 copies.
Printed by Printing house «Madrid Ltd» (18, Gudanova Str., Kharkiv, 61024, Ukraine)

Electrical Engineering & Electromechanics
Scientific Journal

no. 1, 2026

# Table of Contents

## Electrical Machines and Apparatus



## Electrotechnical Complexes and Systems



## Industrial Electronics



## High Electric and Magnetic Fields Engineering, Engineering Electrophysics



## Electrical Insulation and Cable Engineering

UDC 621.313.33 https://doi.org/10.20998/2074-272X.2026.1.01

V.I. Milykh

# Theory and practice of numerical-field analysis and refinement of electromagnetic and energy parameters in the designs of three-phase induction motors

***Introduction.*** *The paper is devoted to improving the designs of three-phase induction motors (TIMs) based on the application of numerical calculations of their magnetic fields. Considering that the classical system for designing TIMs does not always provide sufficient accuracy of their design parameters, this task is relevant and therefore the developed motors require experimental refinement and additional time and money accordingly.* ***Problem.*** *In classic design of TIMs, magnetic calculations are performed based on magnetic circuit theory. The magnetic circuit of TIMs is divided into conditionally homogeneous sections, on which the magnetic quantities are considered to be distributed evenly, but their real distribution is much more complicated. This approach leads to error in determining the electromagnetic parameters of TIMs and, as a result, inaccuracies in energy, mechanical, thermal, etc. calculations. The* ***goal*** *of the paper is to further develop the existing system for designing TIMs by refining it using numerical-field calculations of electromagnetic and energy parameters.* ***Methodology.*** *The methodology is based on numerical-field verification and refinement of classical design of TIMs. It is strictly deterministic, despite the complexity of linear and nonlinear interrelationships of its structural, electromagnetic, and energy parameters, and therefore it is amenable to adequate algorithmization and programming using iterative calculations. The theoretical foundations of the methodology are reinforced by harmonic analysis of time functions of electromagnetic quantities and a refined determination of the differential leakage resistance of the stator winding. The tool for implementing the methodology is the FEMM program in conjunction with the created Lua scripts.* ***Results.*** *Numerical-field calculations of the electromagnetic and energy parameters of the test TIM developed according to the classical design were performed. This motor has been tested within the synchronous idle and rated load conditions. This demonstrated a sufficiently high efficiency of the provided theoretical and practical foundations of numerical-field calculations and revealed that the TIM project does not meet the declared power and voltage requirement. To reach their nominal values, the method for refining the magnetizing current of the stator winding and the rotor slip is provided.* ***Scientific novelty*** *of this paper is the system of numerical-field calculations of electromagnetic and energy parameters of TIMs, which, in conjunction with the iterative process, ensures its output to the specified nominal stator winding voltage and output power while simultaneously varying the magnetizing current and slip.* ***Practical value.*** *The methodology of numerical-field calculations of TIMs based on the FEMM program and the Lua script is recommended to be integrated into the automated design system for these motors. In addition to verifying and refining the parameters of the designed TIMs, the developed methodology and program can be used to obtain a set of refined operating characteristics in an automated calculation mode.* References 29, tables 5, figures 9.

*Key words:* **three-phase induction motor, automated numerical-field calculations, magnetic field, FEMM, electromagnetic and energy parameters, verification and refinement of design data.**

***Вступ***. *Робота присвячена удосконаленню проєктів трифазних асинхронних двигунів (ТАД) на основі застосування чисельних розрахунків їхніх магнітних полів. Така задача є актуальною, зважаючи не те, що класична система проєктування ТАД не завжди забезпечує достатню точність їхніх проєктних параметрів, тому розроблювані двигуні потребують експериментальної доводки і відповідно додаткових витрат часу та коштів.* ***Проблема.*** *При класичному проєктуванні ТАД магнітний розрахунок виконується на основі теорії магнітних кіл. Магнітопровід ТАД розділяють на умовно однорідні ділянки, на яких магнітні величини вважаються розподіленими рівномірно, проте реальний їхній розподіл є набагато складнішим. Такий підхід призводить до похибки визначення електромагнітних параметрів ТАД, і, як наслідок, неточності енергетичних, механічних, теплових тощо розрахунків.* ***Метою*** *роботи є подальший розвиток системи проєктування ТАД шляхом її уточнення за допомогою чисельно-польових розрахунків електромагнітних та енергетичних параметрів.* ***Методика*** *побудована на чисельно-польовій перевірці та уточненні класичного проєктування ТАД. Вона є суворо детермінованою, незважаючи на складність лінійних та нелінійних взаємозв'язків конструктивних, електромагнітних та енергетичних його параметрів,тому піддається адекватній алгоритмізації і програмуванню із застосуванням ітераційних розрахунків. Теоретичні основи методики підсилені гармонічним аналізом часових функцій електромагнітних величин та уточненим визначенням диференціального опору розсіювання обмотки статора. Інструментом реалізації методики є програма FEMM у сукупності зі створеними скриптами Lua.* ***Результати.*** *Виконано чисельно-польові розрахунки електромагнітних та енергетичних параметрів тестового ТАД, розробленого за класичним проєктом. Цей двигун перевірено у межах режимів синхронного неробочого ходу та номінального навантаження. Це показало достатньо високу ефективність наданих теоретичних і практичних основ чисельно-польових розрахунків і виявило, що проєкт ТАД не відповідає заявленим потужності та напрузі. Для виходу на їхні номінальні значення надано шлях уточнення намагнічувального струму обмотки статора і ковзання ротора.* ***Науковою новизною*** *в роботі є система чисельно-польових розрахунків електромагнітних та енергетичних параметрів ТАД, яка у сукупності з ітераційним процесом забезпечує його вивід на задані номінальні напругу обмотки статора і вихідну потужність при одночасному варіюванні намагнічуівального струму та ковзання.* ***Практична цінність.*** *Методику чисельно-польових розрахунків ТАД на базі програми FEMM і скрипту Lua рекомендовано вбудовувати в автоматизовану систему проєктування цих двигунів. Окрім перевірки і уточнення параметрів проєктованих ТАД, за розробленими методикою і програмою можна отримати в автоматизованому розрахунковому режимі сім'ю уточнених його робочих характеристик.* Бібл. 29, табл. 5, рис. 9.

*Ключові слова:* **трифазний асинхронний двигун, автоматизовані чисельно-польові розрахунки, магнітне поле, FEMM, електромагнітні і енергетичні параметри, перевірка та уточнення проєктних даних.**

**Introduction**. Three-phase induction motors (TIMs) are diverse and widespread in the technosphere around the world. Their improvement is always relevant and occurs due to various factors, including increasing the accuracy and efficiency of the design system.

One of the productive means of improving the design of TIMs is currently the use of numerical field calculations of their magnetic fields (MFs). For this purpose, the publicly available free code FEMM [1],

which is based on the Finite Element Method (FEM), can be used.

The implementation of this code into the TIM design system is facilitated by its convenient interface and the Lua scripting language integrated into it [1, 2]. It provides the creation of program scripts for the automated construction of physical and geometric models of TIMs, reflecting their design, winding currents and magnetic properties of materials. Based on the calculated MFs, the program scripts determine the electromagnetic, power and energy parameters of the designed TIMs.

At present, a combined computational and research system for the design of TIMs has been developed: first, a TIM design is created using classical design methods, such as [3, 4], and then numerical-field studies of TIM are carried out in order to verify, expand the list and improve its design parameters. The author has carried out a number of such various studies, for example, [5–9], etc. And they were subsequently deepened and improved. Naturally, those studies that were carried out at the previous stages were based on larger assumptions and did not yet take into account the achievements of further developments. Therefore, the task now has been to adjust the specified combined computational research system for the design of TIMs, taking into account the achievements obtained and increasing its accuracy by reducing methodological and computational simplifications and assumptions.

**The goal of the work** is to further develop the TIM design system by refining it using numerical field calculations of electromagnetic and energy parameters. The FEMM code in conjunction with the created Lua scripts was adopted as the tools to achieve the goal.

**Analysis of recent research.** It is known that induction motors (IMs) have come a long way in their development, but their intensive research continues, as evidenced by the review of publications provided below, although it is far from exhaustive.

Naturally, there are publications devoted to optimization [10, 11], as well as research on new versions of IMs [12, 13]. For example, in the paper [10], the prediction of IM efficiency is investigated using four optimization algorithms: genetic algorithm (GA), particle swarm optimization (PSO), whale optimization algorithm (WOA) and red fox optimization algorithm (RFO). The algorithms were evaluated based on their convergence behavior, accuracy and experimentally measured efficiency values. In the study [11], the FEM is applied to optimize a single-phase IM. This work focuses on current, torque, efficiency and losses using experimental and simulation methods. In the paper [12], the theoretical basis and tools for further optimization of the design of a shaftless IM with a non-contact suspension are presented. The impact on the starting characteristics of the motor is identified by an analytical method and confirmed by FEM modelling. In the paper [13], a double-squirted rotor cage IM is presented, in which high-temperature superconducting materials and copper rods are embedded in different slots. The paper investigates the influence of the rotor slot structure on the torque, as well as related parameters such as the air gap magnetic flux and torque ripple, etc. The computational models based on FEM are implemented in the Ansys Maxwell software. The study [14] focuses on analyzing the influence of different rotor rod designs and materials on the TIM characteristics also using FEM.

In works [15–17, 8] attention is paid to the improvement and development of the theory of IMs. In [15] it is noted that using FEM it is possible to predict the behavior of electromagnetic fields of TIMs, therefore, numerical modeling based on COMSOL was performed as an early tool for studying the interaction between the distribution of these fields and various parameters. In the article [16] it is noted that 3D and 2D models of the motor were created and a 3D finite element (FE) structure was proposed, and thus a number of motor parameters were obtained. In [17] a new high-precision model of IM modelling based on FEM is proposed. The proposed model allows for fast and accurate modelling of IMs using an inverter circuit model and a control algorithm with high accuracy of reflecting non-ideal characteristics of IMs, such as magnetic saturation, spatial harmonics, asymmetry, etc.

In works [18–20] various parameters and processes in IMs are considered. Thus, in the article [18] a dynamic analysis of a two-phase IM with symmetrical and orthogonal phase windings is provided. Based on the geometric dimensions, a model was created for the FEM analysis using the 2D ANSYS Maxwell software. An analysis of the transient and steady-state processes of the machine currents, electromagnetic torque and speed at idle speed and at full load was carried out. In the article [19] an adaptive neural-fuzzy inference system (ANFIS) is presented as a reliable tool for predicting the reduction of the TIM torque under abnormal conditions. The study identifies the main factors of the reduction, including voltage imbalance, harmonic distortion and temperature increase. In the study [20] a method for calculating electrical and magnetic losses in a single-phase IM with a squirrel-cage rotor and non-uniform stator slots is proposed. The simulation was performed using the FEM and AutoCAD software for modelling of non-symmetrical stator slots. The accuracy of the model results was verified by comparing the rated current, torque and efficiency with the motor data. The aim of the work [8] is to further develop the TIM design system by numerical field calculations of active and reactive resistances of TIM windings in the entire range of slip variation and calculation of its mechanical characteristics. The TIM winding resistances are determined by calculations of MF dissipation using the FEMM code, and in the rotor core – with current displacement.

Considerable attention is paid to the diagnostics of IMs [21–23]. In [21], a method for detecting and diagnosing stator short circuits, rotor core breaks, and eccentricity in large IMs by analyzing the frequency spectrum of the stator current was provided. To study the effects of various fault conditions, a time-stepped FEM simulation was performed on a 2D IM model. This leads to more accurate results than other models, since the design geometry and winding scheme of the machine are reflected. In [22], a FE model was developed to study interturn short circuits of the stator winding. Using the developed FE model, simulations were performed to

understand the behavior of various electrical and magnetic quantities in the time and frequency domains. A prototype machine with short circuits was tested in an experimental setup and the results were compared with simulation and analytical calculations. In [23], it is noted that FEM offers a deep understanding of the fundamental principles and physical operation of the machine. It can model complex topology of magnetic circuits, discrete winding schemes and properties of nonlinear magnetic materials of the machine. It determines various parameters of the machine and can model localized magnetic saturation caused by faults with a high degree of accuracy. This article also provides a literature review on methods for diagnosing faults in IMs using FEM.

There are a number of works, for example [9, 24, 25], which are related to the analysis of active and reactive parameters of the stator winding, the use and improvement of equivalent IM circuits, and their operation. In the article [24], a simplified method for estimating the parameters of the IM T-circuit is described, which is based on their design data and on the interaction of numerical and analytical dimensionless approaches using Thevenin theorem. The work [25] provides an estimate of the electrical and mechanical parameters of AC based on the differential evolution algorithm. A comparative study is carried out using different input signals. Such an algorithm is able to estimate the parameters of the equivalent electrical circuit: stator and rotor resistances and leakage inductances, magnetization inductance, and some mechanical parameters. The purpose of the work [9] is to further develop the TIM design system by numerical-field calculation analysis of the differential leakage reactance of the stator winding, as well as a comparative check of the corresponding empirical formulas inherent in the methods of traditional design calculations.

In the article [26], expressions are given for determining the rotor currents of the circular TIM model using field analysis with the existence of spectral harmonics of the stator magnetomotive force. Expressions are developed for determining the winding data and the feasibility of using the calculation model of the sinusoidal stator winding in order to increase the efficiency of mathematical modeling using the equivalent field model with a fixed rotor and slip frequency using the circular model.

The aim of the work [27] is to develop and verify a method for taking into account, using a weakly coupled circuit-field model, the effect of current displacement in the rotor circuit of an induction motor with a squirrel-cage rotor and an IM with massive ferromagnetic elements of the rotor magnetic circuit. The research method consists in iteratively solving the equations of the loop and field mathematical model by refining the parameters of the IM equivalent circuit based on the results of field analysis and in iteratively adjusting the calculated electromagnetic torque to take into account the effect of current displacement obtained on the basis of equivalent currents in the conductive parts of the rotor. The proposed approach makes it possible to increase the reliability of the results of modeling electromagnetic processes in IMs in starting modes.

It can be summarized that the mentioned scientific publications are devoted to various aspects of the development and research of IMs. And it can be noted that a common research tool is numerical calculations of magnetic fields by FEM using various software products. At the same time, this contributes to the improvement of engineering education: the integration of this method for the study of the efficiency of IMs. This is what the article [28] focuses on the implementation of FEM into the engineering curriculum.

A similar modern approach, that is, the use of FEM for the study and improvement of TIMs, is adopted in this article. But here we consider a relevant aspect that has not yet been sufficiently reflected in the scientific literature. Namely, this concerns the problem of numerical-field analysis and refinement of electromagnetic and energy parameters in TIM projects and their verification in principle.

True, there is a work [5] in which this question is raised. But it did not fully reveal this problem, so here this topic is considered in a more complete volume, taking into account the updated system of knowledge and capabilities. Moreover, the work is structured in such a way as to provide TIM researchers with all the opportunities to use the acquired experience of theoretical and practical skills for independent assimilation and application of the presented material.

**The object for demonstrating** the research performed is the TIM with a short-circuited rotor winding designed in [4], which has a nominal power $P_N$ = 15 kW and a rotation axis height of 160 mm. The main design data of the motor also include the nominal phase voltage $U_{sN}$ = 220 V, the nominal phase current of the stator winding $I_{sN}$ = 28.8 A, the frequency $f_s$ = 50 Hz, the slip $s_N$ = 0.0261 and the power factor $\cos\varphi_{sN}$ = 0.889. The motor has the number of pole pairs $p$ = 2 and the number of phases $m_s$ = 3. The main dimensions include the outer cores diameters of the rotor $d_r$ =184 mm and the stator $d_{se}$ = 272 mm and their length $l_a$ =130 mm, air gap $\delta$ = 0.5 mm. The stator has $Q_s$ = 48 slots, the rotor – $Q_r$ = 38 slots. The stator winding is single-layer, diametrical, distributed. The rotor slots are made closed and without bevel. The core material is steel grade 2013.

For numerical field studies using the FEMM code, a 2D computational model was adopted, which is given in Fig. 1 and reflects its electromagnetic system in cross section.

The computational model of the TIM is automatically converted into a physical-geometric model by the created Lua script, as explained in [7]. The geometric model presents the design of the TIM, the physical model carries the distribution and directions of currents in the windings, as well as the magnetic properties of the cores. In Fig. 1, the phase zones of the stator winding are highlighted, which are indicated by phase current labels.

The FEMM code adopts a rectangular coordinate system $x$, $y$, but additionally uses polar coordinates $r$, $\alpha$. The directions of the rotor rotation frequencies $n$ and of the MF $n_s$ coincide with the direction of the coordinate $\alpha$.

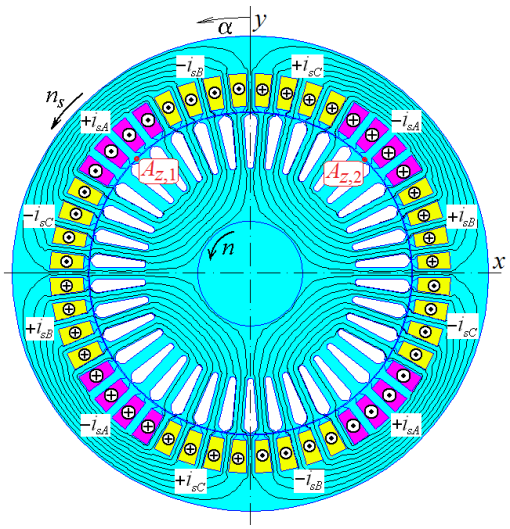


Fig. 1. TIM electromagnetic system with current distribution in the stator winding and the pattern of the lines of force of its magnetic field in the synchronous idle mode

**Preparation of the magnetization curve of the TIM core material.** On the way to calculating the MF of the TIM by the FEMM code, it is important to set the magnetization curves of the electrical steel from which its cores are made. This, at first glance, trivial task should be performed with an understanding of its essence.

In classical design, the magnetic calculation of the TIM is performed on the basis of the theory of magnetic circuits (TMC). That is, the magnetic core is divided into homogeneous sections, and within each, the magnetic quantities are assumed to be the same. To reduce the error, to take into account its heterogeneity, the main magnetization curve (MMC) of the electrical steel is replaced by special curves – different for the teeth and backs of the cores [3, 4].

Changes in the magnetization curves occur very significantly, as shown in Table 1. For MMC of the steel grade 2013, GOST 21427-83 provides the values of magnetic flux density (MFD) $B$ and magnetic field strength (MFS) $H$ at five reference points. At the same values of the magnetic flux density for the teeth and backs of the cores, the values of $H$ of special curves used in the design methods of TIMs are presented [3, 4]. The differences are obvious.

Table 1

Parameters of magnetization curves of steel 2013

| $B$, T | | 1,54 | 1,65 | 1,75 | 1,85 | 2,05 |
|---|---|---|---|---|---|---|
| $H$, A/m | Main | 1000 | 2500 | 5000 | 10000 | 30000 |
| | Teeth | 763 | 990 | 1330 | 1770 | 4400 |
| | Back | 608 | 940 | 1500 | 2811 | 14390 |

Therefore, the question arises – which magnetization curve should be used in numerical field calculations of TIMs? It is logical to use MMC, because in such calculations the distribution of MFD and MFS in the cores is already inhomogeneous.

**Test calculations of the magnetic field by the FEMM code in the synchronous idle mode.** In the classical design system, the magnetic calculation of the TIM, as noted, is performed on the basis of the TMC. According to its terminology, this is a straightforward task: the magnetizing current of the motor $I_\mu$ is calculated based on a given magnetic flux, which is set in the three-phase stator winding. And this is done without the participation of the rotor winding currents, which is called the synchronous idle mode (SIM) [3, 4].

In general, the article is aimed at identifying the shortcomings of the classical design of the TIMs, which arise due to the use of the TMC for electromagnetic calculations. Therefore, the main assumptions on which the classical design is based are retained in the article in order to concentrate on achieving its specific goal and to identify the role of the TMC in the insufficient accuracy of the calculation of electromagnetic quantities. That is, in this article, by analogy, the sinusoidal nature of the rotor and stator currents is assumed, which is common in many publications, although they note that these currents may have a complicated harmonic composition.

Numerical-field calculation using the FEMM code can verify the adequacy of the calculation of the SIM mode, but such a problem, using the same terminology, is the reverse: the magnetizing current $I_\mu$ is set in the stator winding, and the MF is calculated, and on its basis – a number of other electromagnetic parameters of the TIM.

The currents in the phase zones of the stator winding (Fig. 1) are given as for a three-phase symmetrical system:

$$i_{sA} = I_{ms}\cos(\omega_s t);\quad i_{sB} = I_{ms}\cos(\omega_s t - \tfrac{2}{3}\pi);$$
$$i_{sC} = I_{ms}\cos(\omega_s t + \tfrac{2}{3}\pi), \qquad (1)$$

where $I_{ms} = \sqrt{2}\cdot I_s$ is the amplitude of currents; $I_s$ is their effective value; $\omega_s = 2\pi f_s$ is the angular frequency; $t$ is the time.

In the model in Fig. 1, the values of phase currents are given by (1) for the initial time $t = 0$, and then their instantaneous values: $i_{sA} = I_{ms}$, $i_{sB} = i_{sC} = -0.5I_{ms}$. This is the indicated instantaneous directions, which are set according to the indicated conditional positive directions. That is, the signs «+» or «–» before the symbols of the currents are also added to their indicated instantaneous values.

As is known, in all TIM excitation modes, the FEMM code solves a large system of algebraic equations, which are formed on the basis of the FEM and the differential equation describing the MF in the cross section of the TIM electromagnetic system, namely:

$$\mathrm{rot}\left[\frac{1}{\mu(B)}\mathrm{rot}(\vec{k}A_z)\right] = \vec{k}J_z, \qquad (2)$$

where $J_z$, $A_z$ are the axial components of the current density vector and the magnetic vector potential (MVP); $\vec{k}$ is the unit vector of the axial axis $z$; $\mu$ is the magnetic permeability: either the magnetic constant $\mu_0$ for non-magnetic areas, or determined for MFD $B$ from the magnetization curve of the material.

The result of solving equation (2) by the FEMM code is the coordinate distribution of the MVP $A_z(x, y)$.

The calculation of the MF was performed at the design magnetizing current of the stator winding $I_\mu$ = 7.75 A, the value of which is substituted in (1) instead of $I_s$. The calculated picture of the MF in the SIM mode is given in Fig. 1.

To compare the design data and the results of numerical-field calculations, the magnetic flux was first taken, which is defined as

$$\Phi_0 = \left(A_{z,1} - A_{z,2}\right) l_a , \qquad (3)$$

where $A_{z1}$, $A_{z2}$ are the values of the MVP at two points through which the sides of the circuit for which the flux is determined pass.

To determine the magnetic flux at the pole pitch, the points are located in the interval: the first of them is where the MVP has the maximum positive value $A_{z1}$, the second one is where the maximum negative value $A_{z2}$. In the SIM mode, the location of these points is shown in Fig. 1.

In this way, we obtained $A_{z1}$ = 34.859 mWb/m; $A_{z2}$ = –34.857 mWb/m and by (3) $\Phi_0$ = 9.063 mWb. This is close enough, although with a clarification: the magnetic flux in the TIM design has a value of 9.005 mWb.

However, if special separate magnetization curves for the stator teeth and backs were used in the numerical-field calculation (see Table 1), then a less acceptable magnetic flux would be obtained $\Phi_0$ = 9.703 mWb (a difference of 7 % is too large).

In the numerical-field calculations of TIMs, magnetic flux linkage (MFL) plays a significant role.

For the phase winding of the stator, which has $N_s$ consecutive turns, according to Fig. 1, the MFL

$$\Psi_s = N_s \cdot l_a \times$$

$$\times \left( \frac{1}{S_1} \int_{S_1} A_z dS - \frac{1}{S_2} \int_{S_2} A_z dS + \frac{1}{S_3} \int_{S_3} A_z dS - \frac{1}{S_4} \int_{S_4} A_z dS \right), \qquad (4)$$

where integration occurs over the cross-sectional areas $S_1$–$S_4$ of the conductive part of the slots of the phase zones with the currents markings $+i_{sA}$ та $-i_{sA}$ of the phase winding $A$.

This MFL is created by a magnetic field on the active length of the cores, i.e. on the slot part of the TIM stator winding. The determination of areas and integrals for (4) in Lua scripts occurs automatically using special functions. And thus the MFL of the stator phase winding $\Psi_{ms}$ = 0.9843 Wb was obtained.

In the position of the phase winding $A$ considered in Fig. 1, this is the maximum value of the MFL, so it is possible to calculate the effective value of the phase EMF

$$E_s = \sqrt{2}\,\pi\, f_s\, \Psi_{ms} = 218{,}7 \text{ V}, \qquad (5)$$

where the winding distribution is automatically taken into account.

In the TIM design, the similar value is 214.5 V, and the existing EMF error, as a result, gives inaccuracies in further design calculations.

**The refined calculation of the phase EMF of the stator winding.** The considered definition of the MFL and the EMF of the phase winding of the stator can be considered as a first approximation, because the amplitude of the MFL is taken at one position of its phase zones. It is more justified to use a discrete angular function of the MFL on its period.

Specifically, according to the distribution of the MVP in the cross section of the TIM, according to (4), the values of the MFL of the phase winding $A$ are «collected» with a conditional movement of its phase zones in the angular direction. The process of moving of the conditional «mask» of the phase zones in the angular direction along the slot structure of the stator is shown in Fig. 2 (the first three and the last 24th positions are shown).

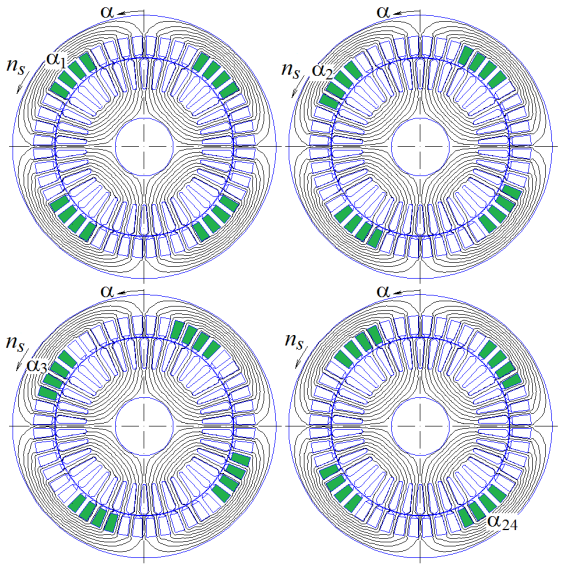


Fig. 2. Movement of the «mask» of the phase zone of the stator winding for collecting the MFL within the period of its angular function against the background of the calculated magnetic field

Thus, the discrete angular numerical function of the MFL appears (Table 2):

$$\Psi_k(\alpha_k); \quad \alpha_k = (k-1)\tau_s; \quad k = 1, 2, 3, \ldots K , \qquad (6)$$

where $k$ is the counter of the positions of the conditionally movable «mask» of the phase zone; $K = Q_s/p$ is the number of such positions within two pole steps $\tau_p$, which is the period of function (6); $\tau_s = 360°/Q_s$ is the tooth-slot step of the stator core.

Table 2

Angular discrete function of the MFL $\Psi_k$ of the phase winding $A$ at 24 angular positions, Wb

| $k$ | 1 | 2 | 3 | 4 | 5 | 6 |
|---|---|---|---|---|---|---|
| $\Psi_k$ | 0,9843 | 0,9430 | 0,8337 | 0,6685 | 0,4617 | 0,2349 |
| $k$ | 7 | 8 | 9 | 10 | 11 | 12 |
| $\Psi_k$ | 0,0001 | –0,2347 | –0,4614 | –0,6683 | –0,8335 | –0,9428 |
| $k$ | 13 | 14 | 15 | 16 | 17 | 18 |
| $\Psi_k$ | –0,9843 | –0,9430 | –0,8337 | –0,6685 | –0,4617 | –0,2349 |
| $k$ | 19 | 20 | 21 | 22 | 23 | 24 |
| $\Psi_k$ | –0,0001 | 0,2347 | 0,4614 | 0,6683 | 0,8335 | 0,9428 |

The angular function (6) is converted into a time function by the relationship $\alpha = \Omega_s t$, where $\Omega_s = \omega_s/p$ is the angular velocity of the TIM rotating magnetic field. The time function obtained in this way preserves the values of the MFL according to Table 2, and it is depicted in Fig. 3 (curve 1).

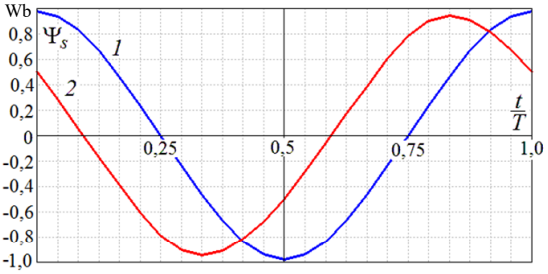


Fig. 3. Time function of the MFL of the stator phase winding within its period $T$: 1 – synchronous idle mode; 2 – nominal load

The function $\Psi_s(t)$ is periodic, therefore it is decomposed into a harmonic Fourier series on its period in two pole steps (Fig. 3), on which the MFL is calculated at $K$ points (in this TIM $K = 24$).

Considering that cosine functions (1) are taken for the stator winding currents, a harmonic series of similar functions is determined for the MFL, i.e. a harmonic time function is obtained, which corresponds to a stationary phase winding $A$:

$$\Psi = \sum_{\nu=1,3,5...}^{N_g} \Psi_{m\nu} \cos(\nu \omega_s t + \gamma_{\psi\nu}), \qquad (7)$$

where the amplitudes of $\Psi_{m\nu}$ and the arguments of $\gamma_{\psi\nu}$ (initial phases) of the harmonics ν are determined by well-known mathematical rules, which was shown in [6, 9] and other works.

It is known that the number of the highest harmonic $N_g$ cannot exceed $K/2$. In (7) the values of $\nu\omega_s t$ and $\gamma_{\psi\nu}$ are measured in electrical radians or degrees.

From the MFL function (7) based on the law of electromagnetic induction by the expression $e = -d\Psi/dt$ we proceed to the harmonic time function of the EMF of the phase winding:

$$e_s = \sum_{\nu=1,3,5...}^{N_g} \nu\omega_s \Psi_{m\nu} \cos\left(\nu \omega_s t + \gamma_{\psi\nu} - \pi/2\right), \qquad (8)$$

where the amplitudes of the $\nu$-th EMF harmonic are separated

$$E_{m\nu} = \nu\omega_s \Psi_{m\nu} \qquad (9)$$

as well as its corresponding initial phase

$$\gamma_{E\nu} = \gamma_{\psi\nu} - \pi/2 . \qquad (10)$$

Also, according to the known relationship for harmonic functions, the effective value of the EMF of the $\nu$ -th harmonic is obtained through the amplitude, namely:

$$E_{s\nu} = \sqrt{2}\pi f_s \nu \Psi_{m\nu} . \qquad (11)$$

Time functions (7) and (8) in Table 2 and Fig. 3, respectively, have a semi-periodic asymmetry:

$$\Psi_{s,k}(\alpha_k) = -\Psi_{s,k}(\alpha_k + \tau_p);\ k = 1, 2, 3, ... K , \qquad (12)$$

therefore, their harmonic series contain only odd harmonics, i.e. for these functions we get $N_g = 11$.

Taking into account the entire harmonic composition, we find the equivalent effective value of the phase EMF of the stator winding

$$E_{seq} = \sqrt{\sum_{\nu=1,3,5...}^{N_g} E_{s\nu}^2} . \qquad (13)$$

The considered method was transformed into a Lua script, which was combined with the calculation of the MF using the FEMM code, and as a result the following results were obtained: amplitude and initial phase of the first harmonic of the MFL $\Psi_{m1} = 0.9630$ Wb; $\gamma_{\psi 1} = 0$, effective value and initial phase of the first harmonic of the phase EMF $E_s = 213.9$ V, $\gamma_{Es} = -\pi/2$; effective value of the total EMF according to (13) $E_{seq} = 214.3$ V.

The harmonic composition of the MFL (7) and EMF (8) in relative units (p.u.) is given in Table 3 (take the values of their first harmonics as the basis), and the effective values of the EMF harmonics $E_{s\nu}$ according to (11) are also given.

Table 3

Harmonic composition of MFL and EMF in the SIM mode

| ν | – | 1 | 3 | 5 | 7 | 9 | 11 |
|---|---|---|---|---|---|---|---|
| $\Psi_{m\nu}$ | p.u. | 1,000 | 0,0203 | 0,0003 | 0,0010 | 0,0009 | 0,0002 |
| $E_{m\nu}$ | p.u. | 1,000 | 0,0610 | 0,0013 | 0,0067 | 0,0078 | 0,0027 |
| $E_{s\nu}$ | V | 213,9 | 13,04 | 0,29 | 1,44 | 1,66 | 0,58 |

Note that here and after that there are harmonics, multiples of three, which supposedly contradicts the classical theory of three-phase electric machines. But this theory is built on the step functions of the distribution of the MMF of the stator winding under the conditions of a toothless rotor and a completely unsaturated magnetic circuit. Under such conditions, the numerical-field calculation and formulas (7), (8) also gave zero third harmonics as well as multiples of it. However, when the magnetic circuit and, first of all, the stator teeth are saturated, these harmonics appeared, and in the load mode, the presence of current in the rotor winding also contributes to such harmonics. The specified features of the harmonic composition are also confirmed in work [29] on the example of a three-phase stator winding of a turbogenerator.

And another significant difference between the classical harmonic analysis methods and the one used in the article is that the first is done according to the conditional stepwise distribution of the MMF and magnetic flux density in a «smooth» interval (in reality, this is nowhere near the case), and the second is done according to the MFL of the winding directly in the slots, taking into account the real geometry of the TIM electromagnetic system and core saturation.

**Refining of the magnetizing current of the stator winding.** To determine the balance of voltages in the electric circuit of the stator winding and further clarify the magnetizing component of its current, the voltage equilibrium equation in vector form is useful:

$$\underline{U}_s = -\underline{E}_s + \underline{U}_{Rs} + \underline{U}_{s\sigma dif} + \underline{U}_{s\sigma fh} , \qquad (14)$$

where the vectors are applied: EMF $\underline{E}_s$; voltage drop across the active resistance of the stator winding $\underline{U}_{Rs}$ and across the inductive resistances of its differential $\underline{U}_{s\sigma dif}$ and frontal $\underline{U}_{s\sigma fh}$ dissipation (the inductive resistance of the slot dissipation is already taken into account in the EMF $\underline{E}_s$ due to the definition of the full MFL of the stator winding (4) within its active part along the length of the TIM cores); the stator winding current vector has a zero initial phase according to (1).

The phase relations of the quantities with (14) are illustrated in Fig. 4 by a vector diagram (VD) of a general form (without observing the scale of the vectors, because it will be used in different calculation modes). We also note that equations (14) and VD in Fig. 4 correspond to the first harmonics of the quantities, because they are also used in TIM designs.

The inverted EMF vector $-\underline{E}_s$ is shifted by an angle $\varphi_{Es} = 180° + \gamma_{Es}$ with respect to the current, and it has the effective values of the active and reactive components: $E_{sa} = E_s\cos\varphi_{Es}$; $E_{sr} = E_s\sin\varphi_{Es}$. The effective values of the voltage drops on the specified resistances are calculated by the formulas $U_{Rs} = R_s I_s$; $U_{s\sigma dif} = X_{s\sigma dif} I_s$; $U_{s\sigma fh} = X_{s\sigma fh} I_s$. These resistances are determined when designing the TIM

and have the values $R_s$= 0.402 Ω, $X_{s\sigma dif}$ = 0.253 Ω; $X_{s\sigma fh}$ = 0.234 Ω.

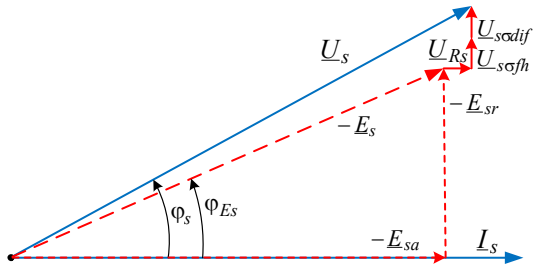


Fig. 4. Vector diagram of voltages in the stator phase winding

Through the components of the vectors according to equation (14) and Fig. 4, the active and reactive components of the phase voltage $\underline{U}_s$ are obtained:

$$U_{sa} = E_{sa} + U_{Rs}\,;\quad U_{sr} = E_{sr} + U_{s\sigma dif} + U_{s\sigma fh}\,,$$

as well as its effective value and phase shift relative to the current $\underline{I}_s$:

$$U_s = \sqrt{U_{sa}^2 + U_{sr}^2}\;;\quad \varphi_s = \text{arctg}(U_{sr}/U_{sa})\,.$$

Considering the SIM mode, it is necessary to substitute the corresponding current $I_\mu$ everywhere instead of $I_s$.

Substitution of all values into the above formulas gives an effective voltage value of 217.7 V, which does not «reach» 220 V, that is, the nominal $U_{sN}$.

Therefore, to reach the nominal voltage of the stator winding, an iterative search for the corresponding magnetizing current was used.

In this way, after three iterations, the refined value of this current $I_\mu$ = 8.09 A was determined, and the values of the remaining quantities mentioned were $\Psi_{m1}$ = 0.9725 Wb; $E_s$ = 216 V, $U_{Rs}$ = 3.3 V; $U_{s\sigma dif}$ = 2 V; $U_{s\sigma fh}$ = 1.9 V; $U_s$ = 220 V.

Additionally, the ratio of the phase voltage to the phase EMF of the stator winding was obtained during synchronous rotation of the rotor and the TIM magnetic field

$$k_{UE} = U_s / E_{ss} = 1{,}028\,, \qquad (15)$$

where $E_{ss} = \sqrt{E_{sa}^2 + (E_{sr} - U_{s\sigma n})^2}$ =214.1 V is the phase EMF without all dissipation components, $U_{s\sigma n}$= $X_{s\sigma n}I_s$ = = 1.9 V is the voltage drop across the slot leakage reactance; $E_{sa}$ = 0; $E_{sr}$ = 216 V is the active and reactive components of EMF $E_s$ (in the SIM mode, according to calculations, $\varphi_{Es}$ = 90° was turned out).

The value of $k_{UE}$ is important for further calculation of the TIM loading mode (in the design from [4] its value is 1.026).

**Calculations of the TIM magnetic field in its loading mode.** For this mode, a strictly deterministic interconnected system of stator and rotor currents is required. The calculation model of the TIM with the system of these currents is given in Fig. 5.

The angular positions of the rotor slots are fixed by the coordinate of the first slot $\alpha_{r1}$, which is closest to the left to the $y$ axis (in Fig. 5 $\alpha_{r1}$ = 0). The remaining slots are numbered by the counter $k$ and they are shifted from each other by the angle of the rotor tooth pitch $\alpha_{rn} = 360°/Q_r$.

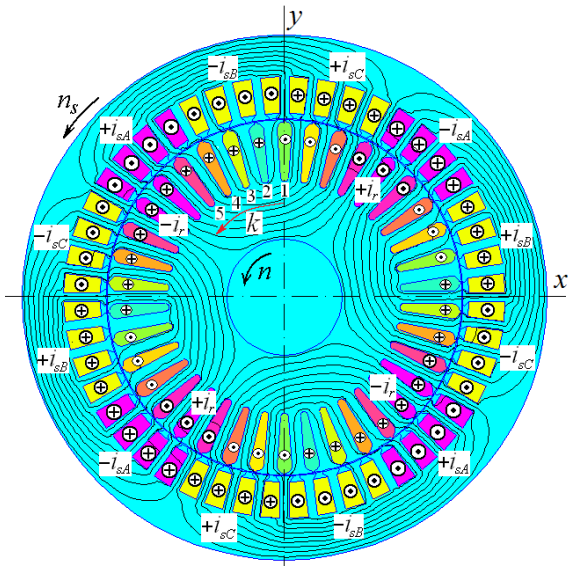


Fig. 5. Distribution of currents in the TIM windings in the rated load mode and the corresponding picture of the power lines of the MF

For calculating the TIM MF in the loading mode, the key is to set the corresponding currents in the windings, taking into account the phase shift between them. For their determination, calculations are used according to the formulas that are given below in the text based on [4].

The basis of such calculations is the slip $s$, for which its design value $s_N$ is initially given, as well as the magnetizing current of the stator winding $I_\mu$, which is determined in the SIM mode. But then their values are refined.

The SIM mode current $I_{sos}$ has a reactive component $I_{srs}$, which is practically equal to $I_\mu$, as well as an active component $I_{sas}$, which is determined under the condition $I_{sas} \ll I_\mu$:

$$I_{sas} = \frac{P_{mags} + m_s R_s I_\mu^2}{m_s U_s}\,, \qquad (16)$$

where $P_{mags}$ are the magnetic losses in the stator core.

The currents in the phase zones of the stator winding in Fig. 5 are determined by the formulas of their symmetrical system (1) and are distributed as in the SIM mode (Fig. 1).

To determine the rotor currents and explain their distribution over the slots, the L-shaped equivalent circuit of the TIM (Fig. 6) [4] and the corresponding VD, which is constructed in Fig. 7, are used. The basic one is the phase current vector $\underline{I}_s$, which, according to (1), has a zero initial phase.

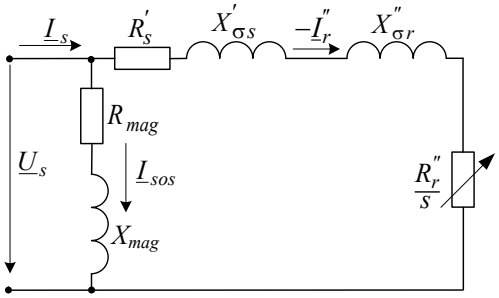


Fig. 6. Converted L-shaped equivalent circuit of the reduced IM

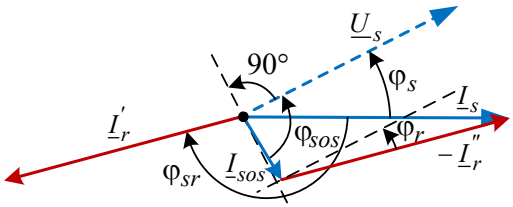


Fig. 7. Vector diagram of phase relations of TIM winding currents

Important for calculating currents and other electromagnetic parameters of the TIM are the active and reactive resistances of its windings. They are reflected in the equivalent circuit, and their values are found during design. To the already given values of the stator winding resistances $R_s$, $X_{s\sigma dif}$; $X_{s\sigma fh}$ we add the total reactance of its dissipation $X_{\sigma s} = 0.725$ Ω.

For a short-circuited rotor winding, the active resistance on its phase part is $R_r = 53.9 \cdot 10^{-6}$ Ω. This active resistance $R'_r = 0.196$ Ω and the leakage reactance $X'_{\sigma r} = 1.02$ Ω reduced to the stator winding are also used.

Reactance of the magnetizing branch of the equivalent circuit:

$$X_{mag} = U_{sN} / I_{\mu} - X_{\sigma s}, \qquad (17)$$

active resistance $R_{mag} << X_{mag}$ due to condition $I_{sas} << I_{\mu}$.

All of the indicated resistances for the equivalent circuit (Fig. 6) have an additional transformation:

$$X'_{\sigma s} = c_1 X_{\sigma s}; R'_s = c_1 R_s; X''_{\sigma r} = c_1^2 X'_{\sigma r}; R''_{\sigma r} = c_1^2 R'_r,$$

where $c_1 = 1 + X_{\sigma s} / X_{mag}$ is the coefficient characterizing the ratio of the voltage vector to the EMF vector of the stator winding during synchronous rotation of the rotor – this is an analogue of the coefficient $k_{UE}$ (15).

Based on the design data of the TIM and in accordance with the equivalent circuit of the combined TIM (Fig. 6) and the VD (Fig. 7), the reactive and active resistances of the load branch:

$$X_{rs} = c_1 (X_{\sigma s} + c_1 X'_{\sigma r}); R_{rs} = c_1 R_s + c_1^2 R'_r / s. \qquad (18)$$

The rotor current of such a motor and its phase shift with respect to the stator winding voltage $U_s$

$$I''_r = \frac{U_s}{\sqrt{R_{rs}^2 + X_{rs}^2}}; \quad \varphi_r = \operatorname{arctg}(X_{rs} / R_{rs}), \qquad (19)$$

and then the effective value of the real (not reduced) rotor winding current

$$I_r = c_1 I''_r K_{Isr}, \qquad (20)$$

where the reduction factor of the rotor winding current to the stator winding current [3]

$$K_{Irs} = \frac{N_s K_{Ws} m_s}{N_r K_{Wr} m_r} \cdot \frac{1}{K_{sq}}, \qquad (21)$$

which includes $N_s = 112$ – the number of consecutive turns in the phase winding of the stator; $K_{Ws} = 0.959$ – its winding coefficient; for a short-circuited rotor winding, the number of phases $m_r = Q_r$, and for each number of turns $N_r = 0.5$, the rotor winding coefficient $K_{Wr} = 1$; the bevel coefficient of its slots $K_{sr} = 1$.

Based on the above, the reactive and active components of the stator phase current are obtained

$$I_{sr} = I_{\mu} + I''_r \sin\varphi_r; \quad I_{sa} = I_{sas} + I''_r \cos\varphi_r, \qquad (22)$$

then its effective value and phase shift angle relative to the phase voltage $U_s$:

$$I_s = \sqrt{I_{sa}^2 + I_{sr}^2}; \quad \varphi_s = \arccos(I_{sa} / I_s). \qquad (23)$$

Thus, according to the VD (Fig. 7), the electrical phase shift angle between the currents $I_s$ and $I_r$ (in degrees) is obtained:

$$\varphi_{sr} = 180° - \varphi_s + \varphi_r, \qquad (24)$$

which in the motor design is converted into a geometric angle

$$\alpha_{sr} = \varphi_{sr} / p. \qquad (25)$$

On the basis provided, a multiphase system of instantaneous current values in the rods of the short-circuited rotor is formed, namely:

$$i_{rk} = I_{mr} \sin\left\{p \cdot \left[\beta + (k-1) \cdot \alpha_{rn} + \alpha_{sr} + \alpha_{r1}\right]\right\}, \qquad (26)$$

where $k = 1, 2, \ldots, Q_r$ is the numbering of the rotor slots adopted in Fig. 5; $I_{mr} = \sqrt{2} \cdot I_r$ is the amplitude of the phase current in the rotor rods; β=0 is the initial phase of stator current.

The calculations yielded the following values: $I_s = 28.8$ A; $\varphi_s = 27.25°$; $\varphi_r = 12.23°$; $\varphi_{sr} = -164.98°$; $K_{Irs} = 16.9$; $I_r = 446$ A; $\alpha_{sr} = -82.49°$.

The distribution of currents along the slots of the stator and rotor at pole pitches $\tau_p$ in dimensionless form is shown in Fig. 8 (the indicated points are meaningful for the currents, the lines are drawn for their visual connection).

In accordance with the presented methodology and the design parameters of the TIM in the nominal load mode, its MF was calculated. The distribution of currents in the TIM slots and the MF picture calculated by the FEMM code are given in Fig. 5.

According to the calculated MF, a number of TIM parameters were determined using the same method as for the SIM mode.

The magnetic flux in the gap per pole pitch according to the formula (3) $\Phi_l = 8.781$ mWb, i.e. it turned out to be 3.1 % less than in the SIM mode.

The time function of the MFL of the stator phase winding in the nominal mode is shown in Fig. 3 (curve 2) in comparison with the similar function in the SIM mode.

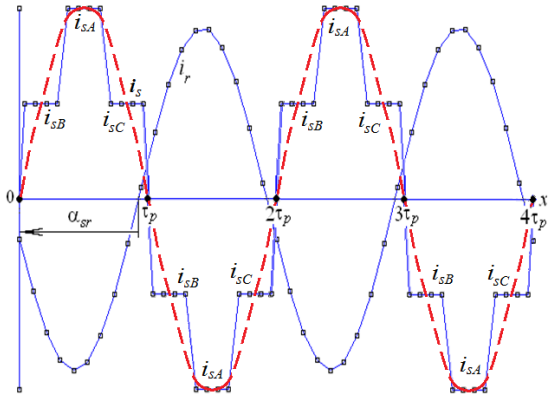


Fig. 8. Angular discrete distributions of winding currents of the rotor $i_r$ and stator $i_s$ of the TIM along its slots on the sweep of the circular line passing through the gap

Table 4 gives the harmonic composition of the time functions of the MFL $\Psi_{mv}$ and the values of the EMF amplitudes $E_{mv}$ (in relative units), as well as the absolute effective values of the EMF $E_{sv}$ of the stator winding, which can be compared with the data in the similar Table 3 for the SIM mode.

Table 4

Harmonic composition of MFL and EMF in the rated loading mode

| ν | – | 1 | 3 | 5 | 7 | 9 | 11 |
|---|---|---|---|---|---|---|---|
| $\Psi_{mv}$ | p.u. | 1,000 | 0,0216 | 0,0069 | 0,0031 | 0,0001 | 0,0011 |
| $E_{mv}$ | p.u. | 1,000 | 0,0648 | 0,0347 | 0,0217 | 0,0011 | 0,0117 |
| $E_{sv}$ | V | 206,9 | 13,41 | 7,18 | 4,49 | 0,23 | 2,42 |

Amplitude and initial phase of the first harmonic of the MFL $\Psi_{m1} = 0.9313$ Wb; $\gamma_{\psi 1} = -56.55^\circ$, effective value and initial phase of the first harmonic of the phase EMF $E_{s1} = 206.9$ V; $\gamma_{E1} = 33.45^\circ$; full EMF by (13) $E_{seq} = 207.5$ V; by (17) phase voltage $U_s = 224.7$ V and the phase shift of the current relative to it $\varphi_s = 34.84^\circ$ (Fig. 7); voltage drops $U_{Rs} = 7$ V; $U_{s\sigma dif} = 7.4$ V; $U_{s\sigma fh} = 6.9$ V.

Using all higher harmonics the effective value of the differential EMF of the stator winding is obtained [9]

$$E_{sdif} = \sqrt{\sum_{\nu=3,5...}^{N_g} E_{s\nu}^2} = 16.05 \text{ V}, \quad (22)$$

as well as the refined differential resistance of the stator winding

$$X_{s\sigma dif} = \frac{E_{sdif}}{I_s} = 0.61 \ \Omega. \quad (23)$$

Note that this resistance is found here in compliance with its mathematical and physical essence, as discussed in [9], and it differs significantly from the design value (see above in the text), which is found using the approximate method. Therefore, further calculations will be performed with the updated value $X_{s\sigma dif}$.

In loading mode, the energy parameters of the TIM are important:

- input electrical power of the TIM:

$$P_{in} = m_s U_s I_s \cos\varphi_s ; \quad (24)$$

- electromagnetic torque, which is determined by a special Lua function through Maxwell magnetic tension tensor

$$M_{em} = \frac{l_a}{\mu_0 (r_s - r_r)} \int_{S_\delta} B_r B_\alpha r \mathrm{d}S , \quad (25)$$

where $B_\alpha$, $B_r$ are the angular and radial components of the magnetic flux density vector; $S_\delta$ is the cross-sectional area of the non-magnetic gap; $r_r$ and $r_s$ are the radii of the circles bounding this plane on the sides of the rotor and stator;

- electromagnetic power transmitted by the rotating magnetic field from the stator to the rotor:

$$P_{em} = M_{em} \Omega_s , \quad (26)$$

where $\Omega_s$ is the angular velocity of this field which has already been mentioned;

- electrical power losses in the stator and rotor windings

$$P_{els} = m_s R_s I_s^2 ; \quad P_{elr} = m_r R_r I_r^2 . \quad (27)$$

The values of the remaining power losses in these calculations do not change and are taken from the TIM design [4]: $P_{mags}$ – magnetic losses in the stator core, $P_{mec}$ – mechanical losses, additional losses $P_{ad}$, $P_{magr}$ – magnetic losses in the rotor core, which consist of surface and pulsation losses.

Taking into account the losses related to the rotor, the output useful power of the TIM is determined:

$$P_{out} = P_{em} - P_{elr} - P_{mag\,r} - P_{mec} - P_{ad} . \quad (28)$$

And finally, the efficiency of the TIM:

$$\eta = P_{out} / P_{in} . \quad (29)$$

The mentioned power losses have the following values: $P_{els}$ = 1046 W; $P_{elr}$ = 407.7 W; $P_{mags}$ = 270 W; $P_{magr}$ = 87.3 W; $P_{mec}$ = 117 W; $P_{ad}$ = 84.3 W.

According to the provided formulas, the integral energy parameters of TIM were obtained: $M_{em} = 97.72$ N·m; $P_{in} = 16.667$ kW; $P_{em} = 15.350$ kW; $P_{out} = 14.741$ kW; $\cos\varphi_s = 0.821$; $\eta = 0.884$.

The phase voltage based on (14) $U_s$ = 224.7 V turned out to be greater than the nominal, but the motor should operate at the nominal voltage of 220 V.

To eliminate the excess $U_s$, it is necessary to reduce the magnetizing current of the stator winding $I_\mu$. Therefore, by iterative method, numerical-field calculations using the provided method found $I_\mu = 7.25$ A, and accordingly, the stator winding current reached $I_s = 29.22$ A. Of course, not only the voltage changed, but also the remaining quantities, which acquired the following values: $\Psi_{m1} = 0.9101$ Wb; $\gamma_{\psi 1} = -57.17^\circ$; $E_{s1} = 202.4$ V; $\gamma_{E1} = 32.83^\circ$; $\alpha_{sr} = 83.10^\circ$; $E_{seq} = 207.5$ V; $U_{Rs} = 7$ V; $U_{s\sigma dif} = 7.4$ V; $U_{s\sigma fh} = 6.8$ V; $U_s = 220$ V; $\varphi_s = 34.28^\circ$; $M_{em} = 95.45$ N·m; $P_{in} = 16.288$ kW; $P_{em} = 14.988$ kW; $P_{out} = 14.379$ kW; $\cos\varphi_s = 0.826$; $\eta = 0.883$.

From all of this, it can be noted that the voltage $U_s$ has become nominal, but the output power $P_{out}$ does not reach the nominal value, which is 15 kW.

It is clear that the task of simultaneously providing nominal voltage and output power is complex, and for its solution, an appropriate method has been developed based on the methodology from [4] and the development of [5].

The complexity of the problem lies in the fact that the input values $s$, $I_\mu$ and the output values $U_s$, $P_{out}$ are interconnected, that is, it is a four-parameter problem, and therefore it is solved by an iterative method. For this purpose, a strictly deterministic method is provided, the essence of which is described further in the text, and then the results of calculations performed by a program on a Lua script, which provides interaction with the FEMM code, are provided.

**Iterative determination of the slip and magnetizing current of the stator winding for simultaneous output to the rated voltage and power of the TIM.** For a visual representation of the technique, a graphical model is used, given in Fig. 9. It is based on a coordinate system with the desired parameters: rotor slip $s$ and magnetizing current of the stator winding $I_\mu$.

This coordinate system is represented in axonometry by the plane $s$, $I_\mu$, in which the point 0 is placed with the coordinates of the slip $s_0$ and the magnetizing current $I_{\mu 0}$, which are given in the current iteration for calculating the voltage $U_s$ and the power $P_{out}$.

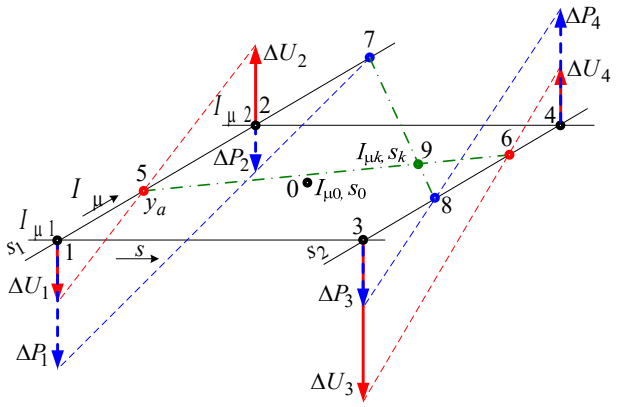


Fig. 9. Diagram of the varying current $I_\mu$ and slip $s$ and the deviation of the desired values $U_s$ and $P_{out}$

In the first iteration, the values of the slip $s_0$ and the current $P_{out}$ are taken directly from the TIM design [4]. In essence, this is the first approximation of the values of the varied quantities of the iterative process to be performed.

Around the coordinate point $s_0$, $I_{\mu 0}$ in the specified plane there is a rectangle with reference points 1, 2, 3 and 4. The corresponding lines 1-2 and 3-4 have the slip coordinates $s_1$ and $s_2$, lines 1-3 and 2-4 have the current coordinates $I_{\mu 1}$ and $I_{\mu 2}$.

Then the sides of the rectangle have dimensions

$$\Delta s = s_2 - s_1;\ \ \Delta I = I_{\mu 2} - I_{\mu 1}. \qquad (30)$$

These dimensions are chosen such that it is possible to allow within their limits a linear dependence of the voltage $U_s$ and the power $P_{out}$ on the slip $s$ and the current $I_\mu$. For example, for the first iteration, it is possible to set $\Delta s = 0.05 s_0$; $\Delta I = 0.05 I_{\mu 0}$ based on experience of calculations, and then for each subsequent iteration these dimensions are halved.

Thus, in Fig. 9 the coordinates of four points 1-4 are given:

$$s_1 = s_0 - \Delta s/2;\ \ s_2 = s_0 + \Delta s/2;\ \ I_{\mu 1} = I_{\mu 0} - \Delta I/2;\ \ I_{\mu 2} = I_{\mu 0} + \Delta I/2. \qquad (31)$$

For each of the given points (31), the MF calculation is performed in the TIM loading mode. According to the results of these calculations, the corresponding values of the phase voltage $U_s$ (14) and the output power $P_{out}$ (28) are determined at these points using the method given above:

$$U_{s,k};\ P_{out,k},\ k = 1, 2, 3, 4, \qquad (32)$$

as well as the mismatches of these quantities relative to their nominal values:

$$\Delta U_k = U_{s,k} - U_{sN};\ \Delta P_k = P_{out,k} - P_N,\ k = 1, 2, 3, 4. \qquad (33)$$

The specific coordinates of the points according to (31) and the values of the mismatch of the phase voltage $U_s$ and the output power $P_{out}$ according to (33) are given in Table 5.

Table 5

Mismatches of values on the first iteration

| Variation | $s_1 = 0.0248$ | $s_2 = 0.0274$ |
|---|---|---|
| $I_{\mu 1} = 6.849$ A | $\Delta U_1 = -2.59$ V<br>$\Delta P_1 = 1311$ W | $\Delta U_3 = -3.17$ V<br>$\Delta P_3 = -218$ W |
| $I_{\mu 2} = 7.571$ A | $\Delta U_2 = 5.19$ V<br>$\Delta P_2 = -787$ W | $\Delta U_4 = 4.83$ V<br>$\Delta P_4 = 377$ W |
| Control point $k$: $s_k = 0.0274$; $I_{\mu k} = 7.135$ A;<br>discrepancy $\Delta U_k = 0.19$ V; $\Delta P_k = 19$ W | | |

Note that Fig. 9 is of a general illustrative nature for the sake of clarity and does not correspond to the data in Table 5, which change with iterations.

The values of the discrepancies (33) are plotted in Fig. 9 at the corresponding points 1–4 as conditional vectors perpendicular to the coordinate plane $s$, $I_\mu$.

As noted, within the coordinate rectangle 1, 2, 3, 4, a linear dependence of $U_s$ and $P_{out}$, $s$ and $I_\mu$ is allowed. Then it is possible to draw straight lines in pairs through the ends of the vectors $\Delta U_1$ and $\Delta U_2$, $\Delta U_3$ and $\Delta U_4$, and similarly through the ends of the vectors $\Delta P_1$ and $\Delta P_2$, $\Delta P_3$ and $\Delta P_4$ (see Fig. 9).

At the intersections of the formed lines with the side lines of the quadrilateral in its plane, the voltage $\Delta U_k$ and power $\Delta P_k$ deviations at points 5, 6 and 7, 8 are equal to 0. Then it is possible to write the linear equations of the formed straight lines, which are shown by a dotted line, and from these equations to determine the coordinates of the intersection points:

$$I_{\mu 5} = I_{\mu 1} - \Delta U_1 \frac{\Delta I}{\Delta U_2 - \Delta U_1};\ I_{\mu 6} = I_{\mu 1} - \Delta U_3 \frac{\Delta I}{\Delta U_4 - \Delta U_3};$$

$$I_{\mu 7} = I_{\mu 1} - \Delta P_1 \frac{\Delta I}{\Delta P_2 - \Delta P_1};\ \ I_{\mu 8} = I_{\mu 1} - \Delta P_3 \frac{\Delta I}{\Delta P_4 - \Delta P_3}.$$

Between points 5 and 6 and similarly between points 7 and 8, straight lines are drawn (in Fig. 9 these are dash-dotted lines), which have analytical expressions:

$$I_\mu = I_{\mu 5} + \frac{I_{\mu 6} - I_{\mu 5}}{\Delta s}(s - s_1); \qquad (34)$$

$$I_\mu = I_{\mu 7} + \frac{I_{\mu 8} - I_{\mu 7}}{\Delta s}(s - s_1). \qquad (35)$$

On line 5-6 $\Delta U_s = 0$, on line 7-8 $\Delta P_{out} = 0$, then at point 9 at their intersection the conditions $\Delta U_s = 0$ and $\Delta P_{out} = 0$ are fulfilled together.

From the system of linear equations (34), (35) we obtain the desired slip and magnetizing current at point $k$:

$$s_k = s_1 + \frac{I_{\mu 5} - I_{\mu 7}}{K_2 - K_1};\ \ I_{\mu k} = I_{\mu 7} + K_2 (s_k - s_1), \qquad (36)$$

where the coefficients $K_1 = \dfrac{I_{\mu 6} - I_{\mu 5}}{\Delta s}$; $K_2 = \dfrac{I_{\mu 8} - I_{\mu 7}}{\Delta s}$.

Substitution of the values of known quantities into these formulas gave $s_k = 0.0274$ and $I_{\mu k} = 7.135$ A, which is in Table 5.

Such values should simultaneously provide the nominal voltage $U_{sN}$ and power $P_{outN}$ of the TIM. To verify this, with the found values of $s_k$ and $I_{\mu k}$, the MF is calculated using a known method and at point $k$, the values of voltage (14) and output power (28) are determined, respectively: $U_s = 220.19$ V and $P_{out} = 15.019$ kW. The corresponding deviations $\Delta U$ and $\Delta P$ according to (33) are only 0.19 V and 19 W, which is reflected in Table 5.

In principle, for practical design, this is already close enough to the specified nominal design parameters of the TIM $U_{sN}$ and $P_{outN}$. The residual differences $\Delta U_s$ and $\Delta P_{out}$ can be explained by the fact that the functions $U_s(s, I_\mu)$ and $P_{out}(s, I_\mu)$ actually differ somewhat from the linear ones adopted in Fig. 9 and in the accompanying formulas.

To demonstrate the theoretical capability of the developed method in terms of reducing the deviations $\Delta U$ and $\Delta P$ and refining the slip $s$ and magnetizing current $I_\mu$, the iterative calculation is repeated.

But in the second iteration, the initial values of slip $s_0$ and current $I_{\mu 0}$ are taken as the values of $s_k$ and $I_{\mu k}$, which are determined in the first iteration. And now the coordinate rectangle 1-2-3-4 is constructed around the new coordinate point $k$, and at the same time its dimensions $\Delta s$ and $\Delta I$ are halved by (30, 31).

After the third iteration, the deviations at the new control point $k$ decreased to $\Delta U_k = 0.01$ V and $\Delta P_k = 4$ W. Therefore, the further iterative process did not make sense, and the calculation results are considered final.

As a result, we obtained $s_N = 0.0274$; $I_\mu = I_{srs} = 7.12$ A; $I_{sN} = 29.9$ A; $I_r = 469.5$ A; $\alpha_{sr} = 83.41^\circ$; $M_{em} = 100$ N·m; $U_s = 220$ V; $P_{in} = 17.1$ kW; $P_{outN} = 15$ kW. That is, the calculation results of the third iteration provided sufficient refinement of the TIM design parameters. If not, it would be possible to continue the iterative calculations.

It should be noted that the presented iterative process is fully automated and its execution, together with the current MF calculations by the FEMM code, is provided by a compiled Lua script.

Thus, the numerical-field verification of the considered TIM design showed the degree of its adequacy, and here it provided its noticeable refinements. At the same time, the refinement of the power factor from 0.889 to 0.898 was revealed; efficiency from 0.875 to 0.878.

In addition, it is important that the application of the presented method to verify not very high-quality designs of other TIMs is able to detect and unacceptable errors and help correct them.

**Conclusions.** A theoretical basis for numerical-field support, verification and refinement of the classical design of three-phase induction motors has been formed. Based on this basis, practical calculations of their electromagnetic and energy parameters have been performed, which became possible thanks to the creation of Lua control scripts using the FEMM code.

The developed theoretical basis is strictly deterministic, despite the complexity of linear and nonlinear relationships between the structural, electromagnetic and energy parameters of the TIMs. Therefore, this basis is amenable to adequate algorithmization and programming using iterative processes.

The general structure of the theoretical basis is reinforced by a harmonic analysis of the angular and time functions of electromagnetic quantities, specifying the definition of the differential leakage resistance of the stator winding.

The developed theoretical and practical bases for checking and refining the design electromagnetic and energy parameters of the TIMs were tested on the example of its published classical design in a full cycle of calculations, which includes both the synchronous idle mode and the rated loading mode.

The results of the test showed a sufficiently high efficiency of the provided theoretical and practical bases of numerical-field calculations, which showed that the TIM design with power of 15 kW is calculated for 225 V instead of 220 V, and the output power reaches only 14.4 kW. It was determined that to reach the nominal values in the design, it is necessary to reduce the magnetizing current of the stator winding from 7.75 A to 7.12 A, and the rotor slip during operation of the TIM will have a value of 0.0274 instead of 0.0261. At the same time, such important motor parameters as torque, efficiency, power factor, stator winding current, etc. are refined.

Given the software implementation of the method of numerical-field calculations of three-phase induction motors based on the FEMM code and the Lua script, it can be built into automated methods for designing such motors.

If the output power of the designed TIM is varied, then according to the developed method and code, a family of its refined operating characteristics can be obtained in an automated calculation mode.

**Conflict of interest.** The author declares no conflict of interest.

REFERENCES


***1.*** *Finite Element Method Magnetics: Download – Stable Distribution (21Apr2019) – 64-bit Executable.* Available at: https://www.femm.info/wiki/Download (Accessed: 05 May 2025).

***2.*** Ierusalimschy R. *Reference Manual of the Programming Language Lua 4.0*. Available at: http://www.lua.org/manual/4.0/ (Accessed: 05 May 2025).

***3.*** Goldberg O.D., Gurin Ya.S., Sviridenko I.S. *Design of electrical machines. 2nd ed., revised and additional*. Moscow, Higher School Publ., 2001. 430 p. (Rus).

***4.*** Kopylov I.P. *Electrical machines designing*. Moscow, Yurait Publ., 2019. 828 p. (Rus).

***5.*** Milykh V.I. Numerically-field analysis of the adequacy of the design data of three-phase induction motors and the method of their refinement on this basis. *Technical Electrodynamics*, 2018, no. 1, pp. 47-55. (Rus). doi: https://doi.org/10.15407/techned2018.01.047.

***6.*** Milykh V.I. Numerical-field analysis of temporal functions and harmonic composition of EMF in windings of a three-phase asynchronous motor. *Technical Electrodynamics*. 2018, no. 3, pp. 56-65. (Rus). doi: https://doi.org/10.15407/techned2018.03.056.

***7.*** Milykh V.I. The system of automated formation of electrical machines computational models for the FEMM software environment. *Technical Electrodynamics*. 2018, no. 4, pp. 74-78. (Ukr). doi: https://doi.org/10.15407/techned2018.04.074.

***8.*** Milykh V.I. Numerical-field analysis of active and reactive winding parameters and mechanical characteristics of a squirrel-cage induction motor. *Electrical Engineering & Electromechanics*, 2023, no. 4, pp. 3-13. doi: https://doi.org/10.20998/2074-272X.2023.4.01.

***9.*** Milykh V.I. Numerical-field analysis of differential leakage reactance of stator winding in three-phase induction motors. *Electrical Engineering & Electromechanics*, 2025, no. 2, pp. 7-18. doi: https://doi.org/10.20998/2074-272X.2025.2.02.

***10.*** Göztaş M., Çunkaş M., Şahman M.A. In-Situ Efficiency Estimation of Induction Motors Using Whale Optimization Algorithm. *Turkish Journal of Electrical Power and Energy Systems*, 2025, vol. 5, no. 2, pp. 114-124. doi: https://doi.org/10.5152/tepes.2025.25001.

***11.*** Michael I.N., Eneh P.I.I. Optimization of a Single-Phase Induction Motor Using Finite Element Method. *International Journal of Research Publication and Reviews*, 2025, vol. 6, no. 2, pp. 4441-4449. doi: https://doi.org/10.55248/gengpi.6.0225.1020.

**12.** Ding Q., Yang Z., Sun X., Zhao Q., Zhu H. Analysis of rotor slot width influence on a bearingless induction motor. *Computers & Electrical Engineering*, 2020, vol. 81, art. no. 106534. doi: https://doi.org/10.1016/j.compeleceng.2019.106534.
**13.** Arish N., Ardestani M., Hekmati A. Optimum Structure of Rotor Slot for a 20 kW HTS Induction Motor. *Physica C: Superconductivity and its Applications*, 2021, vol. 582, art. no. 1353829. doi: https://doi.org/10.1016/j.physc.2021.1353829.
**14.** Ocak C. A FEM-Based Comparative Study of the Effect of Rotor Bar Designs on the Performance of Squirrel Cage Induction Motors. *Energies*, 2023, vol. 16, no. 16, art. no. 6047. doi: https://doi.org/10.3390/en16166047.
**15.** Nascimento D., Smolenski R., Loschi H., Grassi F., Wan L., Hamid A. Electromagnetic Fields on 3-Phase Induction Motor Using Finite Element Analysis. *2021 IEEE International Joint EMC/SI/PI and EMC Europe Symposium*, 2021, pp. 434-439. doi: https://doi.org/10.1109/EMC/SI/PI/EMCEurope52599.2021.9559357.
**16.** Ding Z., Bu W., Cai X., Wu X., Liu S. Finite Element Analysis and Modeling of Three-Phase Induction Motor. *IOP Conference Series: Materials Science and Engineering*, 2019, vol. 677, no. 5, art. no. 052055. doi: https://doi.org/10.1088/1757-899X/677/5/052055.
**17.** Lee J.-H., Kwon Y.-C., Sul S.-K. High-Fidelity Induction Motor Simulation Model Based on Finite Element Analysis. *IEEE Transactions on Industrial Electronics*, 2022, vol. 69, no. 10, pp. 9872-9883. doi: https://doi.org/10.1109/TIE.2022.3163556.
**18.** Ekpo E.G. Dynamic Analysis of Two Phase Induction Motor Using Finite Element Method. *Journal of Emerging Trends in Engineering and Applied Sciences (JETEAS)*, 2020, vol. 11, no. 6, pp. 211-218. Available at: https://www.scholarlinkinstitute.org/jeteas/abstractview.php?id=6.83 (Accessed: 05 May 2025).
**19.** Shaier A.A., Flah A., Kraiem H., Enany M.A., Elymany M.M. Novel technique for precise derating torque of induction motors using ANFIS. *Scientific Reports*, 2025, vol. 15, no. 1, art. no. 8550. doi: https://doi.org/10.1038/s41598-025-92821-z.
**20.** Asaad M., Mejbel A. Losses estimation of a single - phase induction motor based on finite element analysis. *AIP Conference Proceedings*, 2023, vol. 2787, no. 1, art. no. 050019. doi: https://doi.org/10.1063/5.0148207.
**21.** Breivik A. *Fault Detection and Diagnosis of Induction Motor for Ship Propulsion by utilizing Electrical Signature and Finite Element Method.* Master's thesis in Marine Technology. NTNU, Norwegian University of Science and Technology, 2021, 107 p. Available at: https://ntnuopen.ntnu.no/ntnu-xmlui/handle/11250/2781526 (Accessed: 05 May 2025).
**22.** Babu H. *Finite-element analysis of an induction motor with inter-turn short-circuit faults.* Thesis of Master in Electrical Engineering. KTH Royal Institute of Technology, School of Electrical Engineering and Computer Science (EECS), Stockholm, Sweden, 2020, 98 p. Available at: https://urn.kb.se/resolve?urn=urn:nbn:se:kth:diva-290082 (Accessed: 05 May 2025).
**23.** Liang X., Ali M.Z., Zhang H. Induction Motors Fault Diagnosis Using Finite Element Method: A Review. *IEEE Transactions on Industry Applications*, 2020, vol. 56, no. 2, pp. 1205-1217. doi: https://doi.org/10.1109/TIA.2019.2958908.
**24.** Sakhara S., Brahimi M., Nacib L., Layadi T.M. Application of a wavelet neural network approach to detect stator winding short circuits in asynchronous machines. *Electrical Engineering & Electromechanics*, 2023, no. 3, pp. 21-27. doi: https://doi.org/10.20998/2074-272X.2023.3.03.
**25.** Diarra M.N., Li Y., Zhao X. Induction Motors Parameters Identification by Starting Process Using Quantum Particle Swarm Optimization-Trust Region Algorithm (QPSO-TRA). *2023 International Conference on Applied Intelligence and Sustainable Computing (ICAISC)*, 2023, pp. 1-6. doi: https://doi.org/10.1109/ICAISC58445.2023.10200090.
**26.** Popovych O., Golovan I. Currents System for Efficient Mathematical Modeling of an Induction Motor Using the Field Analysis. *2019 IEEE International Conference on Modern Electrical and Energy Systems (MEES)*, 2019, pp. 142-145. doi: https://doi.org/10.1109/MEES.2019.8896624.
**27.** Golovan I.V., Popovych O.M. Consideration of the induced current displacement in the rotor circuit in a weakly coupled circuit-field model of an induction motor. *Technical Electrodynamics*, 2025, no. 3, pp. 22-30. (Ukr). doi: https://doi.org/10.15407/techned2025.03.022.
**28.** Quadrado J.C. Enhancing Engineering Education: Integrating Finite Element Method Analysis for Induction Motors Efficiency Improvement Study. *Proceedings of the 22nd LACCEI International Multi-Conference for Engineering, Education and Technology: Sustainable Engineering for a Diverse, Equitable, and Inclusive Future at the Service of Education, Research, and Industry for a Society 5.0*, 2024, art. no. 2032. doi: https://doi.org/10.18687/LACCEI2024.1.1.2032.
**29.** Milykh V.I., Polyakova N.V. Harmonious analysis of electromagnetic sizes three-phase winding of stators of turbogenerator on basis classic and numeral field methods. *Technical Electrodynamics*, 2013, no. 3, pp. 40-49. (Rus).

*Received 20.08.2025*
*Accepted 08.11.2025*
*Published 02.01.2026*

*V.I. Milykh*[1], *Doctor of Technical Science, Professor,*
[1] National Technical University «Kharkiv Polytechnic Institute», 2, Kyrpychova Str., Kharkiv, 61002, Ukraine,
e-mail: mvikemkpi@gmail.com

*How to cite this article:*
Milykh V.I. Theory and practice of numerical-field analysis and refinement of electromagnetic and energy parameters in the designs of three-phase induction motors. *Electrical Engineering & Electromechanics*, 2026, no. 1, pp. 3-14. doi: https://doi.org/10.20998/2074-272X.2026.1.01

UDC 621.311 https://doi.org/10.20998/2074-272X.2026.1.02

M. Al Soudi, O. Alsayyed, B. Batiha, T. Hamadneh, O.P. Malik, M. Dehghani, Z. Montazeri

# Optimal placement and sizing of distributed generation units in distribution networks using an enhanced particle swarm optimization framework

***Introduction.*** *Optimal planning of distributed generation (DG) units is a critical research topic due to the growing integration of renewable energy and the need to enhance distribution network performance. Classical optimization methods often struggle with the nonlinear, nonconvex, and highly coupled nature of DG allocation problems.* ***Problem.*** *The IEEE 33-bus distribution network experiences significant voltage drops and high active and reactive power losses under normal operating conditions. Determining the optimal placement and sizing of DG units is a complex problem involving multiple interacting variables and operational constraints.* ***Goal.*** *This study aims to improve technical performance by minimizing total active power losses and voltage deviation while ensuring voltage stability and network reliability.* ***Methodology.*** *The particle swarm optimization (PSO) algorithm is enhanced using the Dehghani method (DM) – a population-based modification framework allowing all individuals, including the worst member, to contribute in improving the best solution. The improved PSO-DM algorithm is applied to the IEEE 33 bus system under four cases: the base case without DG and scenarios with 2, 3 and 4 DG units. The objective function includes active power loss minimization and total voltage deviation.* ***Results.*** *The 4-DG configuration significantly improves system performance: active power losses decrease from 210.67 kW to 53.9 kW (74.4 % reduction), reactive losses drop from 142.84 kVAr to 38.42 kVAr (73.1 % reduction), the minimum bus voltage rises from 0.9037 to 0.9741 p.u. and total voltage deviation decreases from 1.8037 p.u. to 0.5129 p.u. (71.6 % improvement). These results demonstrate that PSO-DM effectively balances exploration and exploitation, yielding superior DG allocation solutions.* ***Scientific novelty.*** *Integrating DM into PSO introduces a cooperative solution-refinement mechanism that enhances convergence speed and search accuracy.* ***Practical value.*** *The PSO-DM framework provides a reliable and computationally efficient tool for DG planning in modern smart distribution networks.* References 22, tables 1, figures 3.

*Key words:* **distributed generation, particle swarm optimization, Dehghani method, voltage deviation, power loss minimization, distribution networks.**

***Вступ***. *Оптимальне планування установок розподіленої генерації (DG) є критично важливою темою дослідження через зростаючу інтеграцію відновлюваної енергетики та необхідність підвищення продуктивності розподільчої мережі. Класичні методи оптимізації часто мають проблеми з лінійністю, опуклістю та сильно пов'язаною проблемою розміщення DG.* ***Проблема***. *Розподільна мережа з шинами IEEE 33 зазнає значних падінь напруги та високих втрат активної та реактивної потужності за нормальних умов експлуатації. Визначення оптимального розміщення та розмірів DG є складною проблемою, що включає численні взаємодіючі змінні та експлуатаційні обмеження.* ***Мета***. *Це дослідження спрямоване на покращення технічних характеристик шляхом мінімізації загальних втрат активної потужності та відхилення напруги, забезпечуючи при цьому стабільність напруги та надійність мережі.* ***Методика***. *Алгоритм оптимізації рою частинок (PSO) удосконалено за допомогою методу Dehghani (DM) – популяційної модифікації, що дозволяє всім особам, включаючи найгіршого члена, зробити свій внесок в отримання найкращого рішення. Удосконалений алгоритм PSO-DM застосовується до системи шин IEEE 33 у чотирьох випадках: базовий випадок без DG та сценарії з 2, 3 та 4 DG. Цільова функція включає мінімізацію втрат активної потужності та загальне відхилення напруги.* ***Результати***. *Конфігурація з 4 DG значно покращує продуктивність системи: втрати активної потужності зменшуються з 210,67 кВт до 53,9 кВт (зниження на 74,4 %), реактивної – з 142,84 кВАр до 38,42 кВАр (зниження на 73,1 %), мінімальна напруга на шині зростає з 0,9037 у.о. до 0,9741 у.о., а загальне відхилення напруги зменшується з 1,8037 у.о. до 0,5129 у.о. (покращення на 71,6 %). Ці результати демонструють, що PSO-DM ефективно балансує розвідку та експлуатацію, забезпечуючи кращі рішення для розміщення установок DG.* ***Наукова новизна***. *Інтеграція DM в PSO впроваджує механізм кооперативного уточнення рішень, який підвищує швидкість конвергенції та точність пошуку.* ***Практична значимість***. *Структура PSO-DM забезпечує надійний та обчислювально ефективний інструмент для планування DG у сучасних інтелектуальних розподільчих мережах.* Бібл. 22, табл. 1, рис. 3.

*Ключові слова:* **розподілена генерація, оптимізація рою часток, метод Dehghani, відхилення напруги, мінімізація втрат потужності, розподільні мережі.**

**Introduction.** The increasing penetration of distributed generation (DG) technologies has transformed the operational paradigms of modern distribution systems. Conventionally, radial distribution networks were designed to passively deliver electrical power from centralized power plants to end-users; however, the integration of DG units, such as photovoltaic (PV) systems, wind turbines, fuel cells and microturbines, has introduced new opportunities and challenges in enhancing the efficiency, stability, and sustainability of electrical networks [1]. DG units significantly improve system performance by reducing real power losses, supporting voltage profiles, increasing network reliability, and reinforcing resilience against disturbances [2]. Nevertheless, these benefits are achievable only when DG units are sited and sized optimally. Improper placement or inaccurate sizing may lead to voltage violations, reverse power flow, feeder congestion, or even deterioration of overall network performance. Consequently, the problem of optimal placement and sizing of DG units has become a central research topic in power system planning and operation [3].

DG refers to small-scale, decentralized power generation sources located near the load centers. Their integration offers multiple technical and economic advantages, including reduced transmission losses, deferred network expansion costs, enhanced voltage stability, and improved environmental sustainability [4–6]. As highlighted in recent studies, DG's impact on distribution power networks is highly sensitive to its location and capacity [7]. For instance, the work [8] emphasizes that uncertainty in load demand can significantly influence optimal DG decisions, advocating hybrid metaheuristic frameworks for more reliable solutions. Similarly, an improved salp swarm algorithm is employed to determine DG allocation in radial systems, showing that properly placed DGs minimize power losses and voltage deviations while delivering strong techno-economic gains [9]. In another relevant study, the jellyfish search algorithm is applied to the optimal placement of solar PV-based DGs, using a multi-objective formulation to concurrently reduce real power losses, improve voltage profile, and enhance system stability [10].

Additional literature also confirms the importance of combining analytical indicators with metaheuristic algorithms to improve DG optimization effectiveness. For instance, an integrated approach using an active power loss sensitivity index to identify candidate buses and a modified ant lion optimization algorithm to determine DG sizes is presented in [11]. The incorporation of Lévy flights significantly improves exploration ability and prevents premature convergence. Likewise, hybridized methodologies, such as the modified grey wolf optimization integrated with ETAP software [12], demonstrate the potential of advanced strategies in supporting protection coordination while optimizing DG allocation. Other perspectives in [2, 13–16] explore multi-objective DG-capacitor placement, optimal scheduling with electric vehicles, reconfiguration combined with DG and capacitors, DG placement in microgrids using enhanced differential evolution, and DG-energy storage co-optimization using genetic algorithms. Collectively, these studies reveal a consistent conclusion: metaheuristic algorithms are indispensable tools for addressing the highly nonlinear, multimodal, and constraint-intensive nature of DG allocation problems in modern distribution networks. Numerous metaheuristic algorithms have been introduced and developed to date, and they have found extensive applications in real-world and engineering optimization problems [17–19].

Despite the extensive contribution in the literature, achieving a balanced trade-off between exploration and exploitation remains a key challenge in metaheuristic-based DG optimization. Classical algorithms, such as the particle swarm optimization (PSO), are powerful yet often susceptible to premature convergence, especially when dealing with multimodal search spaces characteristic of DG planning. To address this gap, improved variants of PSO have been proposed to enhance convergence speed, robustness, and accuracy. Motivated by this need, an enhanced PSO algorithm augmented with Dehghani method (DM) is introduced in this study. DMeenhancement introduces adaptive update mechanisms that refine particle movement patterns, strengthen global exploration, and reduce the risk of stagnation. As a result, the DM-enhanced PSO exhibits superior capabilities in escaping local minima and identifying high-quality solutions, making it particularly suitable for DG placement tasks that involve complex operational constraints and nonlinear performance indices.

This **study aims** to improve the technical performance of the distribution network by minimizing total active power losses and voltage deviation while ensuring voltage stability and maintaining reliable system operation. To achieve this objective, the DM-enhanced PSO algorithm is applied to determine the optimal placement and sizing of DG units. The IEEE 33-bus radial distribution system is used as the test platform, and four scenarios are considered – one base case without DG and three cases with 2, 3 and 4 DG units – to comprehensively evaluate the impact of DG penetration on loss reduction, voltage improvement, and overall system performance.

The structure of the paper is organized as follows. Problem formulation, including the mathematical model for DG placement and sizing, objective functions, and system constraints are presented in section «**Problem definition**». The PSO algorithm and details of the enhancements incorporated through the Dehghani method are introduced in section «**Particle swarm optimization and Dehghani method**», and simulation studies and performance evaluation of the proposed method on the IEEE-33 bus system under all test scenarios are provided in section «**Simulation studies and performance analysis**». Finally, section «**Conclusions and future work**» concludes the paper and outlines future research directions, emphasizing the potential extension of DM-enhanced PSO to multi-objective DG planning, integration of storage systems, and real-time optimal operational strategies.

**Problem definition.** The optimal placement and sizing of DG units in radial distribution networks is a nonlinear, constrained optimization problem that aims to simultaneously improve the voltage profile and minimize active power losses. Let the distribution network consist of $N$ buses and $L$ branches. The objective is to determine the optimal locations $\{bk\}$ and corresponding DG sizes $\{P_{DG,k}, Q_{DG,k}\}$ for $k = 1, ..., n_{DG}$, such that network performance is enhanced while satisfying all power flow and operational limits.

**Power flow model and loss formulation.** For each branch $l \in L$ connecting bus $i$ to $j$, the active power loss is calculated as:

$$P_{loss} = \sum_{i=1}^{L} R_l \frac{P_l^2 + Q_l^2}{V_i^2}, \tag{1}$$

where $R_l$ is the line resistance; $P_l$, $Q_l$ are the active and reactive power flows; $V_i$ is the sending-end voltage magnitude.

Nodal active and reactive power balances are:

$$P_i = \sum_{j \in \Omega_i} P_{ij} - P_{D,i} + P_{DG,i}\ ; \tag{2}$$

$$Q_i = \sum_{j \in \Omega_i} Q_{ij} - Q_{D,i} + Q_{DG,i}\ , \tag{3}$$

where $P_{D,i}$, $Q_{D,i}$ denote loads; $P_{DG,i}$, $Q_{DG,i}$ denote DG injections at bus $i$.

Branch power flows in backward-forward sweep include:

$$P_{ij} = \sum_{m \in \Psi(j)} P_{jm} + P_{D,j} - P_{DG,j}\ ; \tag{4}$$

$$Q_{ij} = \sum_{m \in \Psi(j)} Q_{jm} + Q_{D,j} - Q_{DG,j}\ . \tag{5}$$

Bus voltages are updated using:

$$V_j = V_i - \frac{R_{ij} P_{ij} + X_{ij} Q_{ij}}{V_i}.$$

**DG modeling.** A DG unit can operate at unity power factor or supply reactive power depending on the technology. In general:

$$S_{DG,k} = P_{DG,k} + jQ_{DG,k}. \tag{6}$$

DG size constraints are:

$$P_{DG,k}^{\min} \le P_{DG,k} \le P_{DG,k}^{\max}. \tag{7}$$

**Objective function.** To simultaneously minimize active power loss and enhance voltage stability, a weighted multi-objective formulation is adopted:

$$\min F = \omega_1 P_{loss} + \omega_2 \left( \sum_{i=1}^{N} |V_i - 1| \right), \tag{8}$$

subject to: 0.95 p.u. $\le V_i \le$ 1.05 p.u., where: $\omega_1$, $\omega_2$ are the weight coefficients; the second term minimizes total voltage deviation ($VD = \sum_{i=1}^{N} |V_i - 1|$). This formulation

provides a clear and mathematically rigorous representation of the DG placement and sizing problem, enabling the application of metaheuristic algorithms, such as the Dehghani-enhanced PSO, to effectively solve the problem under multiple DG penetration scenarios.

**PSO and Dehghani method.** PSO is a population-based stochastic optimizer [20]. Let a swarm consist of $N_p$ particles, each with position $X_i \in R^D$ and velocity $V_i \in R^D$ at iteration $t$. Each particle retains a personal best $P_{best,i}$ and the swarm maintains a global best $g_{best}$ (also denoted $X_{best}$). The standard PSO update rules are:

$$V_i^{t+1} = \omega V_i^t + C_1 r_1 \left(P_{best,i} - X_i^t\right) + C_2 r_2 \left(g_{best} - X_i^t\right); \quad (9)$$

$$X_i^{t+1} = X_i^t + V_i^{t+1}, \quad (10)$$

where $\omega$ is the inertia weight; $C_1$, $C_2 > 0$ are the cognitive/social coefficients; $r_1$, $r_2 \sim U(0, 1)$ are the uniform random vectors. Objective function $f(x)$ is minimized.

PSO is effective, but can suffer premature convergence and stagnation; the Dehghani method [21] is a population-level improvement operator that uses **component-wise contribution of all individuals** to refine the current best solution.

**Dehghani method – concept and formalization.** DM introduces an auxiliary vector $X_{DM}$ initialized as the current best:

$$X_{DM} \leftarrow X_{best}. \quad (11)$$

For every particle $i = 1, ..., N_p$ and for each dimension $d = 1, ... , D$, DM attempts a component-wise replacement:

$$X_{DM}(d) \leftarrow X_i(d). \quad (12)$$

Compute the objective $f(X_{DM})$. If

$$f(X_{DM}) < f(X_{best}), \quad (13)$$

then accept the improvement:

$$X_{best} \leftarrow X_{DM}, \quad (14)$$

otherwise restore $X_{DM}(d) \leftarrow X_{best}(d)$ and continue. In words: each component of the global best is temporarily replaced by the corresponding component of every population member. If any such replacement yields a better objective, the global best is updated. This process leverages information in all members – including poor solutions – to explore promising coordinate-wise moves.

Algorithmically (pseudo-code):

1. $X_{DM} \leftarrow X_{best}$.
2. For $i = 1$ to $N_p$:
3. ;; For $d = 1$ to $D$:
4. ;;;; $X_{DM}(d) \leftarrow X_i(d)$ and evaluate $f(X_{DM})$.
5. ;;;;;\If $f(X_{DM}) < f(X_{best})$ then $X_{best} \leftarrow X_{DM}$. Else $X_{DM}(d) \leftarrow X_{best}(d)$.
6. ;; End for $d$.
7. End for $i$.

DM is parameter-light (no additional random numbers) and performs $O(N_p \cdot D)$ objective evaluations in the worst case per DM application.

**Integration: DM-enhanced PSO.** In DM-enhanced PSO, the standard PSO loop is preserved. After updating positions and personal/global bests at iteration $t$, apply DM to refine $X_{best}$. That is:

1. Update $V_i^{t+1}$, $X_i^{t+1}$.
2. Update $P_{best,i}$ and $g_{best}$.
3. Apply DM to attempt component-wise improvement of $X_{best}$.
4. Proceed to next iteration.

This hybridization preserves PSO dynamics while enabling coordinate-wise exploitation informed by the entire swarm. Empirically, DM-enhanced PSO increases the probability of escaping local minima and improves final solution quality for high-dimensional, constrained engineering tasks such as DG placement and sizing.

**Simulation studies and performance analysis.** Performance of the DM-enhanced PSO algorithm in solving the optimal placement and sizing of DG units in the IEEE 33-bus radial test system [22] is evaluated in this section. Four study cases are considered:

1) the base case without DG;
2) the optimal integration of 2 DG units;
3) the optimal integration of 3 DG units;
4) the optimal integration of 4 DG units.

The optimization objective simultaneously minimizes power losses and voltage deviation (*VD*). Lower values of *VD* indicate better voltage quality and improved network stability.

Global results obtained by the DM-enhanced PSO-DM are summarized in Table 1.

Table 1

Global results after optimum DG's placement in IEEE 33-bus test system

| Parameters | Base | With 2 DG | With 3 DG | With 4 DG |
|---|---|---|---|---|
| $P_{loss}$, kW | 210.67 | 183.37 | 136.5 | 53.9 |
| $Q_{loss}$, kVAr | 142.84 | 123.3 | 90.87 | 38.42 |
| $V_{\min}$, p.u. | 0.903 | 0.9195 | 0.9344 | 0.9741 |
| *VD* | 1.8037 | 1.6278 | 1.3713 | 0.5129 |
| DG locations (bus) | – | 18,22 | 17,22,33 | 17,18,30,32 |
| $P_{DG}$, kW | – | 129.31<br>306.87 | 240.91<br>297.20<br>200 | 257.88<br>466.97<br>131.15<br>700 |
| $Q_{DG}$, kVAr | – | 62.63<br>148.62 | 116.68<br>143.95<br>96.86 | 124.90<br>226.16<br>63.52<br>339.02 |

The base network exhibits significant losses with an active power loss of 210.67 kW and a reactive power loss of 142.84 kVAr. Furthermore, the voltage deviation is relatively high (*VD* = 1.8037), confirming the weak voltage support typically observed in unreinforced radial systems. The introduction of DG units leads to noticeable performance improvement, and these enhancements intensify as the number of DG units increases.

**Voltage profile analysis.** Voltage profile across all buses for different scenarios is depicted in Fig. 1. In the base case, the minimum voltage drops to approximately 0.903 p.u., revealing the well-known voltage weakness around the mid-feeder section. With 2 DG units, the voltage profile rises uniformly, eliminating the deep dip and improving overall voltage stability. The placement of 3 DG units results in further enhancement, increasing the minimum voltage level and flattening the profile.

The most significant improvement occurs with 4 optimally located DG units. The entire voltage curve shifts upward, with all bus voltages remaining satisfactorily close to 1 p.u. This is also reflected in the voltage deviation value, which sharply decreases to *VD* = 0.5129, representing a 71.6 % improvement compared to the base case. This confirms that PSO-DM efficiently identifies optimal DG sites that contribute maximum voltage support.

**Active power loss reduction.** Active power loss for each bus is shown in Fig. 2. The integration of DG units remarkably reduces feeder losses by supplying power locally and minimizing line currents. Active loss decreases from 210.67 kW in the base case to 183.37 kW with 2 DGs and further to 136.5 kW with 3 DGs. The lowest loss, 53.9 kW, is achieved with 4 DGs, corresponding to a 74.4 % reduction compared with the base network. This significant decline clearly demonstrates the effectiveness of the DM-enhanced PSO optimization in loss minimization.

**Reactive power loss reduction.** Reactive power loss trends (Fig. 3) follow a similar pattern. The losses are reduced from 142.84 kVAr (base case) to 123.3 kVAr (2 DGs), 90.87 kVAr (3 DGs) and finally to 38.42 kVAr (4 DGs). The availability of reactive power support from optimally sized DGs directly enhances the voltage profile and lowers reactive currents, leading to substantial loss mitigation.

**Overall performance discussion.** The combined analysis of Table 1 and Fig. 1–3 clearly demonstrates that the DM-enhanced PSO algorithm delivers highly effective optimization solutions. The addition of DG units systematically improves voltage quality, reduces line loading, and significantly decreases both active and reactive losses. Among the investigated scenarios, the configuration with 4 DG units offers the best overall performance, affirming the strong capability of DM-enhanced PSO in identifying optimal DG allocation patterns.

These results confirm that incorporating DMe into PSO considerably enhances the exploration–exploitation balance, enabling superior DG planning outcomes in radial distribution systems.

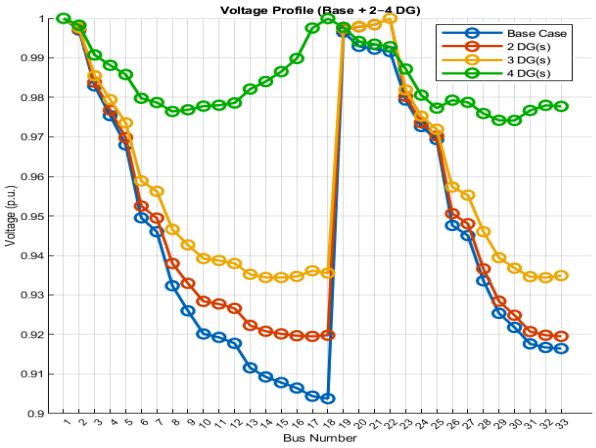


Fig. 1. Voltage profile without and with DGs integration

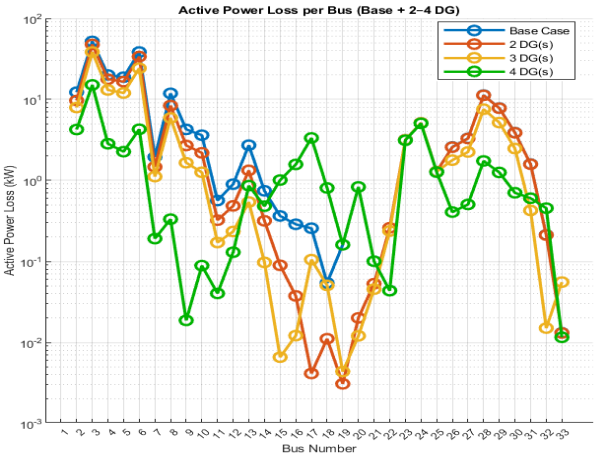


Fig. 2. Active power loss after DG placement

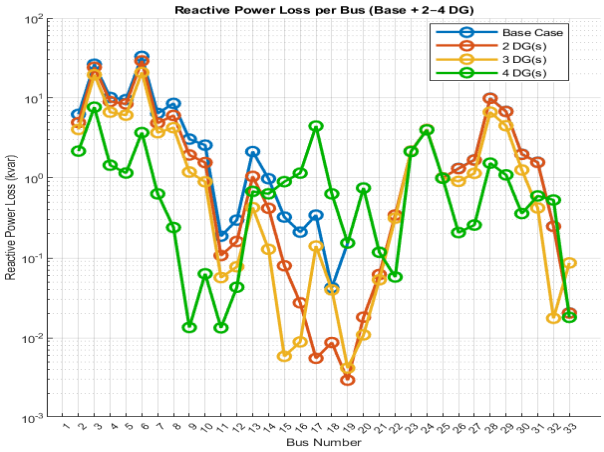


Fig. 3. Reactive power loss after DG placement

**Conclusions and future work.** An enhanced particle swarm optimization framework, augmented with the Dehghani method (DM-enhanced PSO), for determining the optimal placement and sizing of DG units in radial distribution networks is presented in this study. The mathematical formulation simultaneously minimized active power losses and voltage deviation while satisfying operational constraints, including power balance, voltage limits, and branch current ratings. Simulation results on the IEEE 33-bus system demonstrate that the proposed methodology significantly improves network performance across multiple technical criteria.

Simulation results on the IEEE 33-bus system demonstrate that the proposed DM-enhanced PSO methodology significantly improves network performance across multiple technical criteria. In particular, compared with the base case (no DG), the optimal 4-DG configuration reduces total active power loss from 210.67 kW to 53.9 kW, i.e. a reduction of 156.77 kW (≈74.4 %); and reduces total reactive power loss from 142.84 kVAr to 38.42 kVAr, i.e. a reduction of 104.42 kVAr (≈73.1 %). Voltage stability is also improved: the minimum bus voltage increases from 0.903 p.u. to 0.9741 p.u., and total voltage deviation *VD* decreases from 1.8037 to 0.5129 (≈71.6 % improvement). These quantitative results confirm that the DM-enhanced PSO reliably identifies DG placements and sizes that materially reduce both active and reactive losses while improving voltage quality.

Despite the promising results, several avenues remain open for future research. First, incorporating time-varying load models, renewable generation uncertainty, and probabilistic constraints can improve the realism of the optimization framework. Second, extending the model to multi-objective formulations – such as economic cost, emission minimization, and reliability enhancement – would enable more comprehensive planning. Additionally, applying advanced hybrid metaheuristics or reinforcement learning-based strategies may further improve convergence properties. Finally, validating the algorithm on larger and unbalanced distribution networks would provide a more extensive assessment of its scalability and practical applicability.

**Conflict of interest**. The authors declare that they have no conflicts of interest.

REFERENCES

*1.* Cavus M. Advancing Power Systems with Renewable Energy and Intelligent Technologies: A Comprehensive Review on Grid Transformation and Integration. *Electronics*, 2025, vol. 14, no. 6, art. no. 1159. doi: https://doi.org/10.3390/electronics14061159.

*2.* Malika B.K., Pattanaik V., Sahu B.K., Rout P.K., Panda S., Bajaj M. Optimal distributed generation and shunt capacitor bank placement in microgrid distribution planning for enhanced performance. *Neural Computing and Applications*, 2025, vol. 37, no. 22, pp. 17363-17388. doi: https://doi.org/10.1007/s00521-024-10503-9.

*3.* Georgilakis P.S., Hatziargyriou N.D. Optimal Distributed Generation Placement in Power Distribution Networks: Models, Methods, and Future Research. *IEEE Transactions on Power Systems*, 2013, vol. 28, no. 3, pp. 3420-3428. doi: https://doi.org/10.1109/TPWRS.2012.2237043.

*4.* Mazurenko L.I., Dzhura O.V., Shykhnenko M.O. Steady-state analysis of a hybrid power supply system using an induction generator with a shunt AC/DC converter. *Electrical Engineering & Electromechanics*, 2024, no. 2, pp. 67-74. doi: https://doi.org/10.20998/2074-272X.2024.2.10.

*5.* Tami Y., Sebaa K., Lahdeb M., Usta O., Nouri H. Extended mixed integer quadratic programming for simultaneous distributed generation location and network reconfiguration. *Electrical Engineering & Electromechanics*, 2023, no. 2, pp. 93-100. doi: https://doi.org/10.20998/2074-272X.2023.2.14.

*6.* Manohara M., Veera Reddy V.C., Vijaya Kumar M. Exploration and mitigation of power quality problems in radial distribution system by placing distributed generation through voltage stability index. *Electrical Engineering & Electromechanics*, 2023, no. 2, pp. 79-85. doi: https://doi.org/10.20998/2074-272X.2023.2.12.

*7.* Pepermans G., Driesen J., Haeseldonckx D., Belmans R., D'haeseleer W. Distributed generation: definition, benefits and issues. *Energy Policy*, 2005, vol. 33, no. 6, pp. 787-798. doi: https://doi.org/10.1016/j.enpol.2003.10.004.

*8.* Sabry S.S., Al-Yozbaky O.S. Enhanced siting and sizing of distributed generation in radial distribution networks under load demand uncertainty using a hybrid metaheuristic framework. *Electrical Engineering & Electromechanics*, 2025, no. 6, pp. 84-92. doi: https://doi.org/10.20998/2074-272X.2025.6.11.

*9.* Neda O.M. Optimal amalgamation of DG units in radial distribution system for techno-economic study by improved SSA: Practical case study. *Electric Power Systems Research*, 2025, vol. 241, art. no. 111365. doi: https://doi.org/10.1016/j.epsr.2024.111365.

*10.* Rajakumar P., Balasubramaniam P.M., Parimalasundar E., Suresh K., Aravind P. Optimized placement and sizing of solar photovoltaic distributed generation using jellyfish search algorithm for enhanced power system performance. Scientific Reports, 2025, vol. 15, no. 1, art. no. 20755. doi: https://doi.org/10.1038/s41598-025-08227-4.

*11.* Rajakumar P., Balasubramaniam P.M., Aldulaimi M.H., Arunkumar M., Ramesh S., Alam M.M., Al-Mdallal Q.M. An integrated approach using active power loss sensitivity index and modified ant lion optimization algorithm for DG placement in radial power distribution network. *Scientific Reports*, 2025, vol. 15, no. 1, art. no. 10481. doi: https://doi.org/10.1038/s41598-025-87774-2.

*12.* Bouchikhi N., Boussadia F., Bouddou R., Salau A.O., Mekhilef S., Gouder C., Adiche S., Belabbes A. Optimal distributed generation placement and sizing using modified grey wolf optimization and ETAP for power system performance enhancement and protection adaptation. *Scientific Reports*, 2025, vol. 15, no. 1, art. no. 13919. doi: https://doi.org/10.1038/s41598-025-98012-0.

*13.* Prasad K.R.K.V., Kollu R., Ramkumar A., Ramesh A. A multi-objective strategy for optimal DG and capacitors placement to improve technical, economic, and environmental benefits. *International Journal of Electrical Power & Energy Systems*, 2025, vol. 165, art. no. 110491. doi: https://doi.org/10.1016/j.ijepes.2025.110491.

*14.* Alhasnawi B.N., Zanker M., Bureš V. A new smart charging electric vehicle and optimal DG placement in active distribution networks with optimal operation of batteries. *Results in Engineering*, 2025, vol. 25, art. no. 104521. doi: https://doi.org/10.1016/j.rineng.2025.104521.

*15.* Sahay S., Biswal S.R., Shankar G., Jha A.V., Appasani B., Srinivasulu A., Nsengiyumva P. Optimized placement of distributed generators, capacitors, and EV charging stations in reconfigured radial distribution networks using enhanced artificial hummingbird algorithm. *Scientific Reports*, 2025, vol. 15, no. 1, art. no. 11144. doi: https://doi.org/10.1038/s41598-025-89089-8.

*16.* Islam A., Rudra S., Kolhe M.L. Optimizing the placement of distributed energy storage and improving distribution power system reliability via genetic algorithms and strategic load curtailment. *Neural Computing and Applications*, 2025, vol. 37, no. 22, pp. 17589-17608. doi: https://doi.org/10.1007/s00521-025-11037-4.

*17.* Qawaqneh H., Alomari K.M., Alomari S., Bektemyssova G., Smerat A., Montazeri Z., Dehghani M., Malik O.P., Eguchi K. Black-breasted Lapwing Algorithm (BBLA): A Novel Nature-inspired Metaheuristic for Solving Constrained Engineering Optimization. *International Journal of Intelligent Engineering and Systems*, 2025, vol. 18, no. 11, pp. 581-597. doi: https://doi.org/10.22266/ijies2025.1231.36.

*18.* Qawaqneh H., Alomari K.M., Alomari S., Bektemyssova G., Smerat A., Montazeri Z., Dehghani M., Malik O.P., Eguchi K. Kakapo Optimization Algorithm (KOA): A Novel Bio-inspired Metaheuristic for Optimization Applications. *International Journal of Intelligent Engineering and Systems*, 2025, vol. 18, no. 11, pp. 913-929. doi: https://doi.org/10.22266/ijies2025.1231.56.

*19.* Zraiqat A., Batiha B., Al-Refai O., Al-Salih A.A.M.M., Smerat A., Montazeri Z., Dehghani M., Werner F., Ahmed M.A., Ibraheem I.K., Eguchi K. Psychologist Algorithm: A Human-inspired Metaheuristic for Solving Complex Constrained Optimization Problems. *International Journal of Intelligent Engineering and Systems*, 2025, vol. 18, no. 9, pp. 124-137. doi: https://doi.org/10.22266/ijies2025.1031.09.

*20.* Kennedy J., Eberhart R. Particle swarm optimization. *Proceedings of ICNN'95 – International Conference on Neural Networks*, 1995, vol. 4, pp. 1942-1948. doi: https://doi.org/10.1109/ICNN.1995.488968.

*21.* Dehghani M., Montazeri Z., Dehghani A., Samet H., Sotelo C., Sotelo D., Ehsanifar A., Malik O.P., Guerrero J.M., Dhiman G., Ramirez-Mendoza R.A. DM: Dehghani Method for Modifying Optimization Algorithms. *Applied Sciences*, 2020, vol. 10, no. 21, art. no. 7683. doi: https://doi.org/10.3390/app10217683.

*22.* Baran M.E., Wu F.F. Network reconfiguration in distribution systems for loss reduction and load balancing. *IEEE Transactions on Power Delivery*, 1989, vol. 4, no. 2, pp. 1401-1407. doi: https://doi.org/10.1109/61.25627.

*Received 03.08.2025*
*Accepted 19.10.2025*
*Published 02.01.2026*

*M. Al Soudi* [1], *PhD, Assistant Professor,*
*O. Alsayyed* [2], *PhD, Professor,*
*B. Batiha*[3], *PhD, Professor,*
*T. Hamadneh*[4], *PhD, Associate Professor,*
*O.P. Malik*[5], *PhD, Professor,*
*M. Dehghani*[6], *PhD,*
*Z. Montazeri*[6], *PhD Student,*
[1] Department of Basic Scientific Sciences,
Applied Science Private University, Amman 11931, Jordan.
[2] Department of Mathematics, Faculty of Science,
The Hashemite University, P.O. Box 330127, Zarqa 13133, Jordan.
[3] Department of Mathematics, Faculty of Science,
Jadara University, Irbid 21110, Jordan.
[4] Department of Mathematics,
Al Zaytoonah University of Jordan, Amman 11733, Jordan.
[5] Department of Electrical and Software Engineering,
University of Calgary, Canada.
[6] Department of Electrical and Electronics Engineering,
Shiraz University of Technology, Iran,
e-mail: adanbax@gmail.com (Corresponding Author).

*How to cite this article:*
Al Soudi M., Alsayyed O., Batiha B., Hamadneh T., Malik O.P., Dehghani M., Montazeri Z. Optimal placement and sizing of distributed generation units in distribution networks using an enhanced particle swarm optimization framework. *Electrical Engineering & Electromechanics*, 2026, no. 1, pp. 15-19. doi: https://doi.org/10.20998/2074-272X.2026.1.02

UDC 628.4 https://doi.org/10.20998/2074-272X.2026.1.03

Z. Ayache, O. Dahou

# Development of a NARX neural network for a tribo-aero-electrostatic separator with rotating disk electrodes

***Introduction.*** *The exponential growth of waste electrical and electronic equipment (WEEE) requires efficient strategies for plastic waste management. Plastics, a major fraction of WEEE, represent both an environmental challenge due to low biodegradability and a valuable source of secondary raw materials.* ***Problem.*** *Tribo-aero-electrostatic separators with rotating disk electrodes offer a promising solution for fine plastic separation. However, their performance depends on multiple, nonlinear, and time-varying factors such as disk speed, voltage, and particle properties. These complex interactions make analytical modeling and stable process control difficult, limiting industrial implementation. The* ***goal*** *of this work is to develop a reliable dynamic model based on NARX neural networks capable of predicting the real-time evolution of key process variables such as recovered mass and particle charge.* ***Methodology.*** *The proposed NARX neural network learns temporal nonlinear relationships directly from experimental data, avoiding the need for explicit physical equations. Experiments were conducted on a synthetic 50:50 mixture of Acrylonitrile Butadiene Styrene (ABS) and Polystyrene (PS) particles (500-1000 μm) to assess model performance under varying disk speeds, voltages, and air flow rates.* ***Results.*** *The developed model accurately predicts the recovered mass and acquired charge of both ABS and PS over a wide range of operating conditions. The predictions show strong agreement with experimental measurements, maintaining low error levels even at parameter extremes.* ***Scientific novelty.*** *This work represents the first application of NARX neural networks to model the dynamic behavior of a two-rotating-disk tribo-aero-electrostatic separator. The approach captures essential time-dependent interactions that conventional static or analytical models fail to describe.* ***Practical value.*** *The NARX model exhibits high predictive accuracy and robustness across an extended operating domain (4–20 kV, 15–60 rpm, 7–9 $m^3$/h), with errors limited to the $10^{-3}$ g and $10^{-3}$ μC ranges. These characteristics demonstrate its potential for real-time intelligent control and adaptive optimization of electrostatic separation processes in plastic waste recycling.* References 39, tables 3, figures 9.
*Key words:* **electrostatic separation, high voltage, dynamic modeling, NARX neural network, recycling.**

***Вступ***. *Експоненціальне зростання кількості відходів електричного та електронного обладнання (WEEE) вимагає ефективних стратегій управління пластиковими відходами. Пластики, основна частина WEEE, становлять як екологічну проблему через низьку біорозкладність, так і цінне джерело вторинної сировини.* ***Проблема***. *Трибоаероелектростатичні сепаратори з обертовими дисковими електродами пропонують перспективне рішення для тонкого розділення пластику. Однак їхня продуктивність залежить від численних, нелінійних та змінних у часі факторів, таких як швидкість диска, напруга та властивості частинок. Ці складні взаємодії ускладнюють аналітичне моделювання та стабільне керування процесом, обмежуючи промислове впровадження.* ***Метою*** *роботи є розробка надійної динамічної моделі на основі нейронних мереж NARX, здатних прогнозувати еволюцію ключових змінних процесу, таких як відновлена маса та заряд частинок, у реальному часі.* ***Методологія***. *Запропонована нейронна мережа NARX вивчає часові нелінійні залежності безпосередньо з експериментальних даних, уникаючи необхідності явних фізичних рівнянь. Експерименти проводилися на синтетичній суміші частинок акрилонітрилбутадієнстиролу (ABS) та полістиролу (PS) у співвідношенні 50:50 для оцінки продуктивності моделі за різних швидкостей дисків, напруг та швидкостей потоку повітря.* ***Результати***. *Розроблена модель точно прогнозує відновлену масу та набутий заряд як ABS, так і PS у широкому діапазоні робочих умов. Прогнози демонструють високу відповідність з експериментальними вимірюваннями, підтримуючи низький рівень похибки навіть при екстремальних значеннях параметрів.* ***Наукова новизна***. *Ця робота являє собою перше застосування нейронних мереж NARX для моделювання динамічної поведінки трибоаероелектростатичного сепаратора з двома обертовими дисками. Цей підхід враховує важливі залежні від часу взаємодії, які звичайні статичні або аналітичні моделі не можуть описати.* ***Практична значимість***. *Модель NARX демонструє високу прогностичну точність та стійкість у розширеній робочій області (4–20 кВ, 15–60 об/хв, 7–9 $м^3$/год), з похибками, обмеженими діапазонами $10^{-3}$ г та $10^{-3}$ мкКл. Ці характеристики демонструють його потенціал для інтелектуального керування в режимі реального часу та адаптивної оптимізації процесів електростатичного розділення при переробці пластикових відходів.* Бібл. 39, табл. 3, рис. 9.
*Ключові слова:* **електростатична сепарація, висока напруга, динамічне моделювання, нейронна мережа NARX, переробка.**

**Introduction.** The management of plastic waste from electrical and electronic equipment (WEEE) has become a global priority in the face of the exponential growth of such waste and the environmental challenges they pose. Plastics, which account for a significant portion of WEEE streams, represent a major problem due to their low biodegradability and their impact on ecosystems when not properly recycled [1, 2]. The recycling of these plastics offers both economic and environmental opportunities, allowing for a reduction in their impact while meeting the growing demand for secondary raw materials [3].

In this context, several electrostatic separation devices have been developed in research laboratories [4–6]. The tribo-electrostatic separator with two rotating disks, in particular, has shown high efficiency in sorting submillimetric granular mixtures, where charging occurs in a fluidized bed containing the material mix to be separated. In this system, a pair of electrodes in the form of two rotating stainless steel disks, driven by a variable-speed motor and connected to high-voltage power supplies with opposite polarities, is immersed to generate an intense electric field [7, 8].

However, the performance of this process is strongly influenced by a combination of nonlinear, interacting, and time-varying factors, including disk rotational speed, applied voltage, particle charge, and air flow rate [9]. Moreover, environmental factors (such as relative humidity and temperature of ambient air) influence the separation process [10–12]. These dependencies make process behavior highly dynamic and sensitive to perturbations, resulting in difficulties in maintaining stable and optimal separation conditions. This complexity limits the industrial application of separators due to the difficulty in maintaining optimal performance in a stable manner [13].

Consequently, it becomes essential to develop dynamic models capable of accurately describing the transient behavior of tribo-aero-electrostatic separators

and predicting their performance under varying operational conditions. The design of advanced control systems for such devices relies on the availability of internal models able to capture their nonlinear and time-dependent dynamics. Traditional analytical and phenomenological modeling approaches, while useful for simplified cases, fail to adequately describe these complex dynamics, particularly when multiple coupled parameters evolve simultaneously in time [14].

In this context, artificial intelligence (AI) offers a powerful and innovative alternative. Artificial neural networks (ANNs), in particular, have emerged as tools of choice for modeling and identifying complex processes [15–19]. Unlike traditional approaches, neural networks do not require explicit knowledge of the underlying physical relationships. They are capable of learning directly from experimental data by identifying complex nonlinear relationships between input and output variables. This learning ability makes them particularly well-suited for multifactorial processes where interactions are difficult to model analytically.

ANNs have been effectively used to model and optimize electrostatic separation processes. For instance, in roll-type electrostatic separation, ANNs combined with genetic algorithms have been employed to maximize insulation product yield by optimizing control variables such as high voltage and roll electrode speed [20]. In the context of industrial electrostatic separators with rotating electrodes, ANNs facilitate multicriterion optimization, addressing the complexity of adjusting control variables in dynamic industrial environments [21, 22]. ANNs also play a crucial role in predicting the performance of electrostatic separation in food waste recovery, demonstrating high accuracy in aligning experimental and predicted results [23].

Nevertheless, most ANN-based models reported in the literature remain static or empirical, which limits their ability to represent the temporal evolution and dynamic interactions inherent to electrostatic separation systems. This limitation is particularly critical for tribo-aero-electrostatic separators with rotating electrodes, where the charging, transport, and separation of particles evolve over short and long time scales [24]. To overcome these limitations, this study focuses on the development and validation of a Nonlinear Autoregressive with Exogenous Inputs (NARX) neural network model designed to capture the dynamic behavior of a tribo-aero-electrostatic separator equipped with two rotating disk electrodes operating under high-voltage conditions**.** The NARX structure, known for its ability to represent systems with memory and feedback, has demonstrated strong performance in modeling nonlinear time-series processes [25–28], making it particularly suitable for this application.

The **goal** of this work is to develop a reliable dynamic model based on NARX neural networks capable of predicting the real-time evolution of key process variables such as recovered mass and particle charge. Experiments are carried out on a synthetic 50:50 mixture of acrylonitrile butadiene styrene (ABS) and polystyrene (PS), two representative thermoplastic polymers of WEEE streams, with particle sizes ranging from 500 to 1000 μm. The dataset is acquired through a LabVIEW based data acquisition system, allowing accurate and real-time monitoring of operational parameters such as disk rotational speed, applied voltage, and air flow rate.

**Materials and methods**. A tribo-aero-electrostatic separator equipped with two rotating disk electrodes (Fig. 1) was used for this study. In this device, the separation of fine granular materials is achieved under the combined influence of electrostatic and aerodynamic forces. Granular materials are first introduced into a fluidized bed inside the separation chamber, where repeated particle–particle and particle–wall collisions induce tribo-electric charging**.** Simultaneously, a controlled air flow maintains the particles in suspension, ensuring homogeneous mixing and frequent collisions. Inside the chamber, two stainless-steel disk electrodes rotate at adjustable seeds and are polarized by high-voltage supplies of opposite polarity.


Fig. 1. Tribo-aero-electrostatic separator with two rotating disks: 1 – control panel; 2 – variable speed DC motors; 3 –vibrating feeder; 4 – cylindrical feeder; 5 – separation chamber with two rotating disk electrodes; 6 – Faraday cages; 7 – balances; 8 – blower; 9 – electrometers (Keithley 6514); 10 – portable colorimeter NH310; 11 – computer [7]

The charged particles are driven toward the electrode of opposite sign and adhere to its surface under the combined effect of electrostatic and aerodynamic forces (Fig. 2). Brushes or scrapers then detach the particles from the disks and direct them to separate collectors. Less-charged or neutral particles remain suspended until they acquire sufficient charge to be collected [29].

Fig. 2. Collection of insulating particles in the two-rotating-disk tribo-aero-electrostatic separator

Previous investigations on this separator configuration have demonstrated its capability to selectively sort fine polymer mixtures and confirmed the strong influence of parameters such as electrode voltage, disk speed, and air flow rate on separation efficiency [24,

30–33]. Building upon these findings, the present work extends the analysis toward continuous operation and dynamic modeling to support the development of a data-driven predictive model based on NARX neural networks. The material mixture used consists of two polymer types: brown ABS and white PS (∅0.5–1 mm), supplied by APR2 (France), a company specializing in WEEE recycling (Fig. 3). The studied mixture is balanced (50 % ABS / 50% PS) and continuously fed by a vibratory mechanism. According to their positions in the tribo-electric series, ABS becomes positively charged while PS becomes negatively charged, and they are collected respectively by the negative and positive electrodes [30].

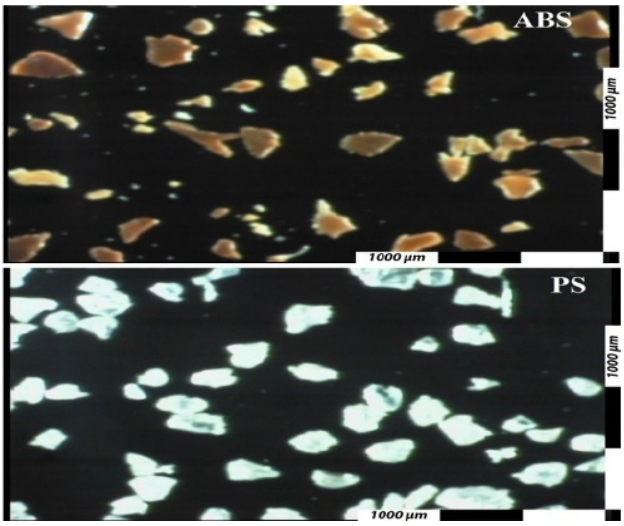

Fig. 3. Micrographs of ABS and PS particles composing the studied materials

The separator is equipped with a monitoring and control panel that enables real-time acquisition of key operating data: high-voltage levels, disk rotation speed, fan speed, and air flow rate. Separated materials are gathered in Faraday-type tanks connected to Keithley 6514 electrometers and placed on electronic balances (0.1 g resolution, 2 kg capacity). Measurements of electric charge and mass are recorded through a LabVIEW based data acquisition system. All experiments are conducted under controlled ambient conditions (relative humidity 40–50 %, temperature 17–21 °C).

The data collected in this study come from multiple experimental series as described in [31]. The effect of high voltage was evaluated in experiments conducted at a fixed disk rotational speed of 30 rpm and a constant air flow rate of 8 $m^3$/h, for voltages of ±4 kV, ±8 kV, ±12 kV, ±16 kV, and ±20 kV. In the second series of experiments, the disk rotational speed was successively adjusted to 15 rpm, 30 rpm, 40 rpm, 50 rpm, and 60 rpm, while maintaining a constant voltage of ±12 kV and an air flow rate of 8 $m^3$/h. Finally, a separation experiment was carried out with the fluidization air flow rate varied by adjusting the blower speed to 7 $m^3$/h, 7.5 $m^3$/h, 8 $m^3$/h, 8.5 $m^3$/h, and 9 $m^3$/h, at a constant rotational speed of 30 rpm and voltage of ± 12 kV.

The resulting dataset, composed of synchronized time-series measurements of mass and charge, served as the basis for training and validating the proposed NARX neural network model.

**Architecture and implementation of the NARX neural network.** There are currently several types of ANNs used in various applications [32]. In this work, we focus specifically on the NARX neural network model, which is a type of recurrent neural network well suited for modeling nonlinear systems, particularly time series [33]. Figure 4 illustrates the topology of the NARX network defined in study. The equation defining the NARX model is as follows:

$$y(t+1)=f[y(t),\dots y(t-d_y+1);u(t),\dots,u(t-d_u+1)], \quad (1)$$

where $u(t)$, $y(t)$ are the input and output of the network at time $t$; $d_u$, $d_y$ are the input and output orders; $f$ is the nonlinear function.

Equation (1) can be expressed in vector form as:

$$\boldsymbol{y}(t+1)=f[\boldsymbol{y}(t);\boldsymbol{u}(t)]. \quad (2)$$

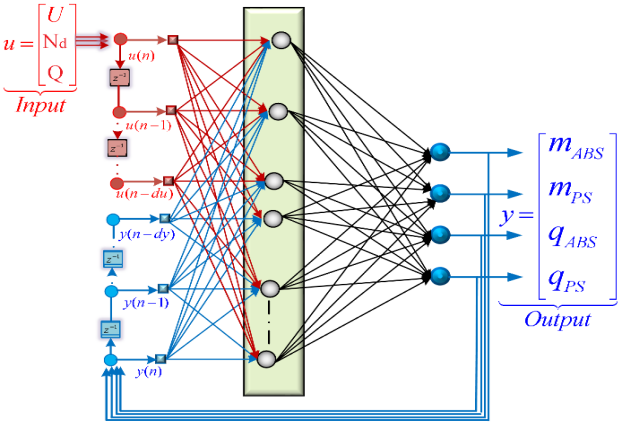

Fig. 4. NARX neural network with delayed input

The input vector $\boldsymbol{u}=[U,\ N_d,\ Q]^T$ consists of 3 elements: the high voltage applied to the electrodes ($U$), the rotational speed of the electrodes ($N_d$) and the air flow rate of the blower ($Q$); $T$ is the transpose of the vector. In contrast, the output vector $\boldsymbol{y}$ = $[m_{ABS},\ m_{PS},\ q_{ABS},\ q_{PS}]^T$ consists of 4 elements: the collected mass of ABS and BS ($m_{ABS}$, $m_{PS}$) and the electrical charge of the collected mass of ABS and PS ($q_{ABS}$, $q_{PS}$). This network also employs tapped delay lines to store previous values of the input sequence $\boldsymbol{u}(t)$ and output sequence $\boldsymbol{y}(t)$. Moreover, the NARX network output, $\boldsymbol{y}(t)$, is fed back to the network input (through delays), since $\boldsymbol{u}(t)$ depends on $y(t–1)$, $y(t–2),\dots,y(t–d_y)$. However, for efficient training, this feedback loop can be opened.

To optimize the training conditions of the network, data preprocessing is highly recommended. Therefore, all data used for training and testing are normalized within the range [–1, +1]. This normalization helps reduce training time while improving the network's performance [34]. The dataset is typically divided into training, validation, and, if available, test sets, with common splits of 70/30 or 70/15/15 [35]. For temporally correlated data, block-wise segmentation is required to preserve the dynamics, with each subset including at least one complete cycle.

In this study, the entire dataset of mass and mass charge measurements collected in the previous section was used to train the NARX network in order to determine the optimal number of neurons in the hidden layer. These dynamic data consist of a total of 6950 measurement points, of which 70 % (4864 points) were

used for training and 30 % (2086 points) for testing, to validate the performance of the NARX neural network. The model characteristics are summarized in Table 1, and the implementation was carried out in MATLAB using the Neural Network Toolbox.

Table 1

Structure of the studied neural network

| Neural network type | NARX |
|---|---|
| Training algorithm | Levenberg-Marquardt |
| Initialization algorithm | Nguyen-Widrow |
| Hidden neurons activation function | Hyperbolic tangent |
| Output neurons activation function | Identity |

There is no universal rule to determine the optimal neural network structure (number of layers, number of neurons, types of connections) or its parameters (activation functions, input delays, feedback delays). An iterative process, inspired by previous work [36–39], was implemented to optimize the NARX network structure. This process determines the number of neurons in the hidden layer as well as the delays on the inputs and feedback outputs by testing various configurations and selecting the best one based on a performance criterion.

Based on the above, the search for the optimal structure was conducted using the parameters listed in Table 2.

Table 2

NARX network parameters

| | |
|---|---|
| Search range of number of neurons (NN) in the hidden layer | [5, 30] |
| Search range for the number of input delays | [1, 3] |
| Search range for the number of output delays | [1, 6] |
| Number of reinitializations per configuration | 10 |
| Total number of final reinitializations | 50 |

The selection of the optimal model is based on the mean squared error (MSE) given by (3) and the maximum coefficient of determination ($R$-squared), which defines the goodness of fit of the experimental data (4), mean error (ME) (5) and mean absolute error (MAE) (6):

$$MSE = \sum_{i}^{N} (\boldsymbol{M}_i - \boldsymbol{Y}_i)^2 \Big/ N ; \tag{3}$$

$$R^2 = 1 - \sum_{i}^{N} (\boldsymbol{M}_i - \boldsymbol{Y}_i)^2 \Big/ \sum_{i}^{N} (\boldsymbol{M}_i - \overline{\boldsymbol{Y}}_i)^2 ; \tag{4}$$

$$ME = \sum_{i}^{N} (\boldsymbol{M}_i - \boldsymbol{Y}_i) \Big/ N_e ; \tag{5}$$

$$MAE = \sum_{i}^{N} |\boldsymbol{M}_i - \boldsymbol{Y}_i| \Big/ N , \tag{6}$$

where $N$ is the number of samples used for training; $N_e$ is the number of experiments performed for each variation parameter; $\boldsymbol{M}_i$ is the measured value; $\bar{\boldsymbol{Y}}_i$ is the average output; $\boldsymbol{Y}_i$ is the output provided by the network.

The total number of configurations tested is 540 (30×3×6). Each configuration is tested 10 times, and the best one is tested again 50 times, resulting in a total of 5,450 training runs (540×10+50) (Fig. 5). The search for the optimal structure was performed on a machine equipped with an Intel® Core™ i7-11800X 2.3 GHz processor. The optimization results are shown in Table 3. Using 24 hidden neurons, an input delay of 1 step, and an output delay of 2 steps achieves the best performance.

Table 3

Results of the optimal structure search

| | |
|---|---|
| Number of neurons (NN) in the hidden neurons | 24 |
| Input delays | 1 |
| Output delays | 3 |
| Number of elements | 169 |
| MSE | $21.2 \cdot 10^{-6}$ |
| $R^2$ | >0.9999 |

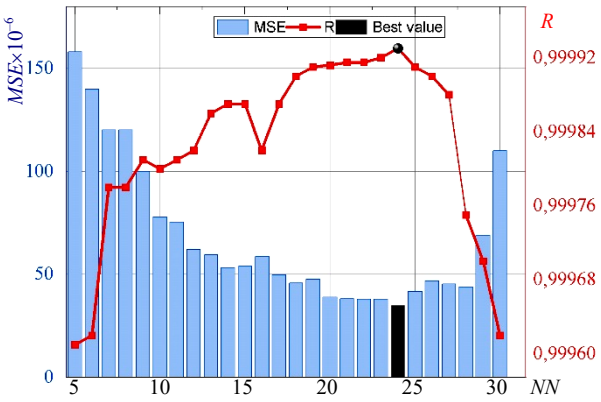


Fig. 5. Performance of the NARX network as a function of the number of neurons in the hidden layer

In Fig. 6 the graphs *a*, *b*, *e* and *f* show the model prediction results at different voltages (4–20 kV). The train and test training data, represented by a circle symbol and blue and black discontinuous line, are compared to the data predicted by the NARX network, represented by a cross symbol and red and orange solid line.

Visual inspection reveals exceptional agreement between experimental measurements and model predictions across all voltage levels. Both recovered mass (Fig. 6,*a*,*b*) and acquired charge (Fig. 6,*e*,*f*) show a strong positive correlation with applied voltage, following expected physical principles of electrostatic separation. The nearly perfect overlap between prediction curves and experimental data demonstrates the model's capability to capture the underlying system dynamics without explicit physical modeling.

Quantitative analysis confirms this observational assessment. The average prediction errors remain below 0,035 for mass recovery (Fig. 6,*c*,*d*) and 0,05 for charge acquisition (Fig. 6,*g*,*h*) across the entire voltage range. Notably, the model maintains its predictive accuracy for both training and testing data sets, indicating excellent generalization capabilities without over fitting. The slight error increase at voltage extremes (particularly at 4 kV) can be attributed to signal-to-noise ratio challenges in low-intensity separation conditions.

The investigation of disk rotational speed influence (Fig. 7) shows that, unlike the applied voltage, this parameter does not exert a significant effect on particle recovery. Across the full range of tested speeds (15–60 rpm), the collected masses remain nearly constant, with variations within ±2 g for ABS and ±3 g for PS, indicating that rotational speed is not a critical factor in the overall separation performance.

The NARX model accurately reproduces this insensitivity. In the test dataset, the mean error (ME) is around 5.5 mg for ABS and 7 mg for PS, while for the charges it remains limited to $\pm 9 \cdot 10^{-3}$ μC.

A temporal analysis, however, reveals transient fluctuations up to $8 \cdot 10^{-3}$ at the beginning of the sequences, reflecting the short-term instability induced by particle motion initiation and air flow turbulence in the fluidized bed. These fluctuations quickly decay, and the prediction errors converge back to zero in the steady-state regime.

The comparison between training and validation datasets highlights a remarkable consistency, as the errors remain of the same order of magnitude in both cases. This robustness confirms that the NARX model not only captures the overall stability of the process but also its transient regimes, while reinforcing the finding that disk rotational speed does not significantly influence the recovery outcome.

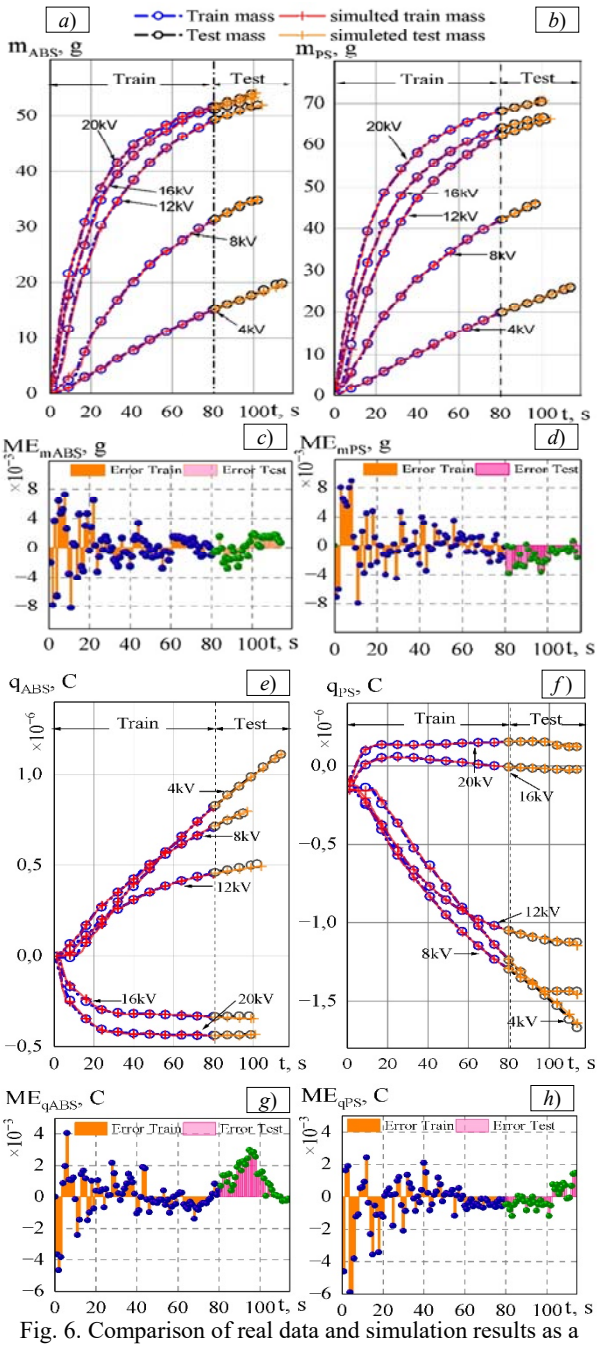


Fig. 6. Comparison of real data and simulation results as a function of high voltage variation: recovered ABS (*a*) and PS (*b*) mass; average error at each measured point for ABS (*c*) and PS (*d*) mass; recovered ABS (*e*) and PS (*f*) charge; average error at each measured point for ABS (*g*) and PS (*h*) charge

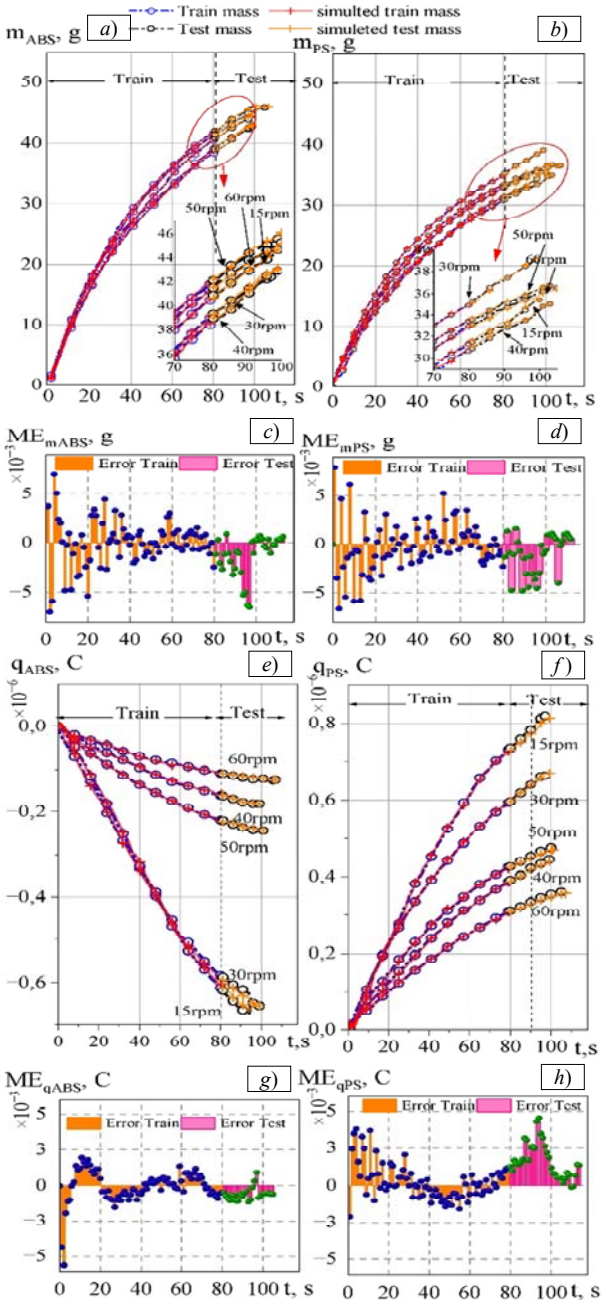


Fig. 7. Comparison of real data and simulation results as a function of variation of disk rotational speed: recovered ABS (*a*) and PS (*b*) mass; average error at each measured point for ABS (*c*) and PS (*d*) mass; recovered ABS (*e*) and PS (*f*) charge; average error at each measured point for ABS (*g*) and PS (*h*) charge

The investigation of air flow rate influence (Fig. 8) shows that this parameter has a noticeable effect on the recovery of both ABS and PS particles. As the air flow increases from 7 to 9 $m^3$/h, the collected masses exhibit measurable variations, reflecting the direct role of fluidization intensity on particle suspension and residence time. The NARX model accurately captures these dynamics. In the test dataset, ME remains within 4.2 mg for ABS and 6.8 mg for PS, while charge prediction errors are confined to $\pm 9 \cdot 10^{-3}$ μC. A temporal analysis highlights transient fluctuations of about $7.8 \cdot 10^{-3}$ at the beginning of the sequences, attributed to turbulence effects and rapid redistribution of particles when air flow is modified. These deviations quickly stabilize, and the

errors converge toward values close to zero once steady-state conditions are reached.

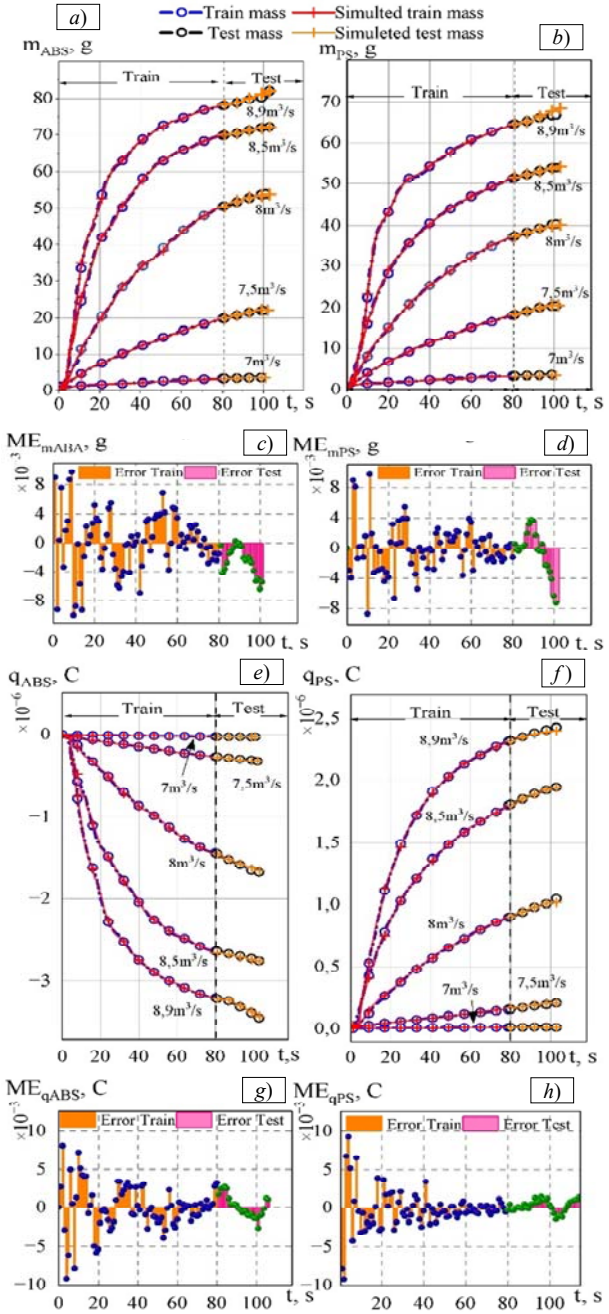


Fig. 8. Comparison of real data and simulation results as a function of air flow rate: recovered ABS (*a*) and PS (*b*) mass; average error at each measured point for ABS (*c*) and PS (*d*) mass; recovered ABS (*e*) and PS (*f*) charge; average error at each measured point for ABS (*g*) and PS (*h*) charge

Figure 9 shows MAE for the prediction of recovered mass and acquired charge of ABS and PS materials, as a function of voltage, disk rotational speed, and air flow rate, with a distinction between training and testing data.

The results show that the NARX model provides good accuracy during the training phase, with low MAE values for all variables. In the tests, slight increases in error appear at the extreme values of the parameters, reflecting sensitivity to extrapolation. For ABS, the errors are more pronounced for electrical charge prediction, especially at high air flow rates, where they reach values of 7.75 mC and 8.88 mC for air flow values of 8.5 $m^3$/h and 8.9 $m^3$/h, respectively. This is probably due to unmodeled complex electrostatic phenomena. PS shows better stability, especially for mass prediction (it does not exceed 9.6 mg, see Fig. 9,*b*), although errors also slightly increase under reaches 9.5 mg for test data (see Fig. 9,*c*).

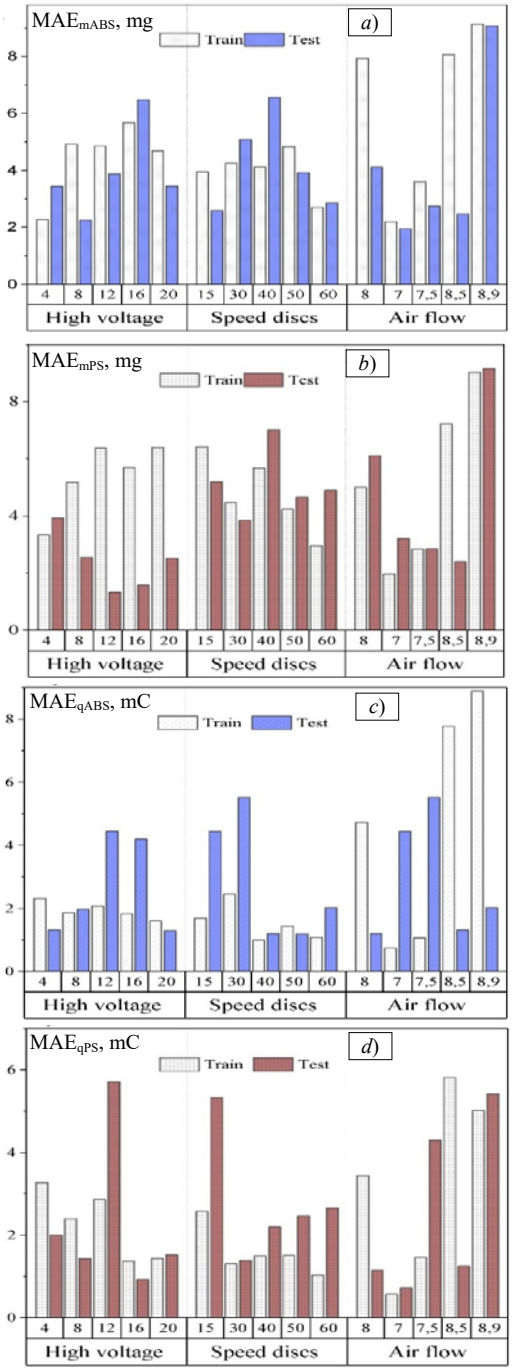


Fig. 9. MAE of predicted mass and charge for ABS and PS as functions of voltage, disk speed, and air flow rate (training vs. testing data): MAE of the predicted ABS (*a*) and PS (*b*) mass; MAE of the predicted ABS (*c*) and PS (*d*) charge

The main contribution of Fig. 9 lies in its ability to precisely identify the model's weak spots, without undermining its overall robustness. Indeed, MAE values remain largely within acceptable limits, even during testing, confirming that the NARX model provides a reliable approximation of the system's behavior over a wide range of operating conditions.

**Conclusions.** In this work, a NARX neural network has been developed and applied to model the dynamic behavior of a two-rotating-disk tribo-aero-electrostatic separator operating under high-voltage electric fields**.** The proposed model considers key process variables, including applied voltage, disk rotational speed, and air flow rate, as inputs, while the predicted outputs are the recovered mass and the acquired electrical charge of the separated particles.

The main objective of the study was to develop a dynamic model capable of accurately reproducing the nonlinear and time-dependent behavior of the separation process, thereby overcoming the limitations of traditional static or empirical approaches. The dynamic and recurrent structure of the NARX network enables it to capture complex temporal interactions between electrical, aerodynamic, and tribo-electric phenomena. The model was trained and tested using time-series data collected under multiple experimental conditions, allowing a thorough evaluation of its generalization capability.

Quantitative validation results confirm the high predictive accuracy and robustness of the proposed approach. Across the full operating range (4–20 kV, 15–60 rpm, 7–9 $m^3/h$), the ME for mass prediction remains below 5.5 mg for ABS and 7 mg for PS, while the MAE for charge prediction is limited to $\pm 9 \cdot 10^{-3}$ μC. Even at extreme conditions (e.g., ±4 kV or high air flow rates), the model maintains acceptable accuracy, with maximum deviations not exceeding 9.6 mg for mass and 8.9 μC for charge, confirming its robustness to parameter variations.

From a scientific standpoint, this work represents the first application of a NARX neural network to the dynamic modeling of a tribo-aero-electrostatic separator equipped with two rotating disk electrodes**.** The model successfully bridges the gap between analytical modeling and real-time predictive intelligence, providing a reliable foundation for further system optimization.

From a practical perspective, the robustness of the model across a wide range of operating conditions (4–20 kV, 15–60 rpm, 7–9 $m^3/h$) confirms its suitability for integration into intelligent control architectures for industrial electrostatic separation processes.

Future research will focus on developing a closed-loop control strategy that leverages the NARX model to optimize separation efficiency in real time**.** Such an intelligent control system will enable adaptive process regulation and enhanced operational stability in industrial plastic recycling applications.

**Conflict of interest**. The authors declare that they have no conflicts of interest.

REFERENCES


***1.*** Geyer R., Jambeck J.R., Law K.L. Production, use, and fate of all plastics ever made. *Science Advances*, 2017, vol. 3, no. 7, art. no. e1700782. doi: https://doi.org/10.1126/sciadv.1700782.

***2.*** Menad N., Guignot S., van Houwelingen J.A. New characterisation method of electrical and electronic equipment wastes (WEEE). *Waste Management*, 2013, vol. 33, no. 3, pp. 706-713. doi: https://doi.org/10.1016/j.wasman.2012.04.007.

***3.*** Gundupalli S.P., Hait S., Thakur A. A review on automated sorting of source-separated municipal solid waste for recycling. *Waste Management*, 2017, vol. 60, pp. 56-74. doi: https://doi.org/10.1016/j.wasman.2016.09.015.

***4.*** Daiku H., Inoue T., Tsukahara M., Maehata H., Kakeda K. Electrostatic separation technology for waste plastics-development of a high-purity type separator for plastics. *Proceedings Second International Symposium on Environmentally Conscious Design and Inverse Manufacturing*, 2001, pp. 562-565. doi: https://doi.org/10.1109/ECODIM.2001.992424.

***5.*** Zenkiewicz M., Zuk T. Physical basis of tribocharging and electrostatic separation of plastics. *Polimery*, 2014, vol. 59, no. 04, pp. 314-323. doi: https://doi.org/10.14314/polimery.2014.314.

***6.*** Mach F., Adam L., Kacerovský J., Karban P., Doležel I. Evolutionary algorithm-based multi-criteria optimization of triboelectrostatic separator. *Journal of Computational and Applied Mathematics*, 2014, vol. 270, pp. 134-142. doi: https://doi.org/10.1016/j.cam.2014.02.009.

***7.*** Mekhalef Benhafssa A., Medles K., Boukhoulda M.F., Tilmatine A., Messal S., Dascalescu L. Study of a Tribo-Aero-Electrostatic Separator for Mixtures of Micronized Insulating Materials. *IEEE Transactions on Industry Applications*, 2015, vol. 51, no. 5, pp. 4166-4172. doi: https://doi.org/10.1109/TIA.2015.2434794.

***8.*** Tilmatine A., Benabboun A., Brahmi Y., Bendaoud A., Miloudi M., Dascalescu L. Experimental Investigation of a New Triboelectrostatic Separation Process for Mixed Fine Granular Plastics. *IEEE Transactions on Industry Applications*, 2014, vol. 50, no. 6, pp. 4245-4250. doi: https://doi.org/10.1109/TIA.2014.2319584.

***9.*** Achouri I.-E., Boukhoulda M.-F., Medles K., Richard G., Zeghloul T., Dascalescu L. Electrostatic Separation of Tribocharged Granular Mixtures of Two or More Plastics Originating From WEEE. *IEEE Transactions on Industry Applications*, 2022, vol. 58, no. 6, pp. 7701-7708. doi: https://doi.org/10.1109/TIA.2022.3197544.

***10.*** Achouri I.-E., Dani C., Zeghloul T., Lungu M., Dascalescu L. Effect of ambient humidity on the tribo-electrostatic separation of granular plastic wastes. *Particulate Science and Technology*, 2024, vol. 42, no. 6, pp. 908-914. doi: https://doi.org/10.1080/02726351.2023.2295399.

***11.*** Benabderrahmane A., Dani C., Medles K., Zeghloul T., Tomasella F., Lungu M., Dascalescu L., Parenty A. Effect of storage at different levels of relative humidity of ambient air on the tribo-electrostatic separation of granular plastics containing brominated flame retardants. *IEEE Transactions on Industry Applications*, 2023, pp. 1-6. doi: https://doi.org/10.1109/TIA.2023.3272872.

***12.*** Dani C., Achouri I.-E., Zeghloul T., Aouimeur D., Lungu M., Dascalescu L. Triboelectric Charging and Electrostatic Separation of Granular Plastic Wastes Exposed to Long-Term Action of High Levels of Ambient Humidity. *IEEE Transactions on Industry Applications*, 2025, vol. 61, no. 1, pp. 1194-1201. doi: https://doi.org/10.1109/TIA.2024.3462902.

***13.*** Achouri I.E., Zeghloul T., Richard G., Medles K., Nouri H., Dscalescu L. Premises for industrial application of a two-rotating-disks-type tribo-aero-electrostatic separator for micronized WEEE. *2017 IEEE Industry Applications Society Annual Meeting*, 2017, pp. 1-4. doi: https://doi.org/10.1109/IAS.2017.8101697.

***14.*** Carlson R. Design of Experiments, Principles and Applications, L. Eriksson, E. Johansson, N. Kettaneh- Wold, C. Wikström and S. Wold, Umetrics AB, Umeå Learnways AB, Stockholm, 2000, ISBN 91-973730-0-1, xii + 329 pp. *Journal of Chemometrics*, 2001, vol. 15, no. 5, pp. 495-496. doi: https://doi.org/10.1002/cem.686.

***15.*** Nelles O. *Nonlinear System Identification. From Classical Approaches to Neural Networks, Fuzzy Models, and Gaussian Processes*. Springer, 2020. 1225 p. doi: https://doi.org/10.1007/978-3-030-47439-3.

***16.*** Haykin S. *Neural Networks and Learning Machines. 3rd Ed.* Pearson Publ., 2008. 936 p.

***17.*** Bengharbi A.A., Laribi S., Allaoui T., Mimouni A. Photovoltaic system faults diagnosis using discrete wavelet transform based artificial neural networks. *Electrical Engineering & Electromechanics*, 2022, no. 6, pp. 42-47. doi: https://doi.org/10.20998/2074-272X.2022.6.07.
***18.*** Vasilevskij V.V., Poliakov M.O. Reproducing of the humidity curve of power transformers oil using adaptive neuro-fuzzy systems. *Electrical Engineering & Electromechanics*, 2021, no. 1, pp. 10-14. doi: https://doi.org/10.20998/2074-272X.2021.1.02.
***19.*** Rouaibia R., Djeghader Y., Moussaoui L. Artificial neural network and discrete wavelet transform for inter-turn short circuit and broken rotor bars faults diagnosis under various operating conditions. *Electrical Engineering & Electromechanics*, 2024, no. 3, pp. 31-37. doi: https://doi.org/10.20998/2074-272X.2024.3.04.
***20.*** Touhami S., Medles K., Dahou O., Tilmatine A., Bendaoud A., Dascalescu L. Modeling and Optimization of a Roll-Type Electrostatic Separation Process Using Artificial Neural Networks. *IEEE Transactions on Industry Applications*, 2013, vol. 49, no. 4, pp. 1773-1780. doi: https://doi.org/10.1109/TIA.2013.2256451.
***21.*** Dahou O., Medles K., Touhami S., Boukhoulda M.F., Tilmatine A., Dascalescu L. Application of Genetic Algorithms to the Optimization of a Roll-Type Electrostatic Separation Process. *IEEE Transactions on Industry Applications*, 2011, vol. 47, no. 5, pp. 2218-2223. doi: https://doi.org/10.1109/TIA.2011.2161851.
***22.*** Dahou O., Touhami S., Ayache Z. Optimal control of an industrial electrostatic rotating electrode separator using artificial intelligence technics. *Przegląd Elektrotechniczny*, 2019, vol. 95, no. 11, pp. 170-175. doi: https://doi.org/10.15199/48.2019.11.44.
***23.*** Lai K., Lim S., Teh P., Yeap K. An Artificial Neural Network Approach to Predicting Electrostatic Separation Performance for Food Waste Recovery. *Polish Journal of Environmental Studies*, 2017, vol. 26, no. 4, pp. 1921-1926. doi: https://doi.org/10.15244/pjoes/68963.
***24.*** Achouri I.E., Zeghloul T., Medles K., Richard G., Nouri H., Dascalescu L. Tribo-aero-electrostatic separation of micronized waste plastics. *ESA '17 - Annual Meeting of the Electrostatics Society of America*, 2017, pp. 1-8. Available at: https://hal.science/hal-04427166 (Accessed 02 May 2025).
***25.*** Ardakani A.H., Abdollahian S.A., Abdollahi F. NARX Transformer: A Dynamic Model for Leveraging Multicycle Data in Long-Term Battery State of Health Estimation. *IEEE Transactions on Instrumentation and Measurement*, 2024, vol. 73, pp. 1-8. doi: https://doi.org/10.1109/TIM.2024.3460947.
***26.*** Ezzeldin R., Hatata A. Application of NARX neural network model for discharge prediction through lateral orifices. *Alexandria Engineering Journal*, 2018, vol. 57, no. 4, pp. 2991-2998. doi: https://doi.org/10.1016/j.aej.2018.04.001.
***27.*** Chen C., Chen H., Shi J., Yue D., Shi G., Lyu D. Estimating Lithium-Ion Battery Health Status: A Temporal Deep Learning Approach With Uncertainty Representation. *IEEE Sensors Journal*, 2025, vol. 25, no. 14, pp. 26931-26943. doi: https://doi.org/10.1109/JSEN.2025.3572291.
***28.*** Kalaycioglu S., de Ruiter A. Vibration Control of Satellite Antennas via NMPC and NARX Neural Networks. *IEEE Transactions on Aerospace and Electronic Systems*, 2025, vol. 61, no. 4, pp. 9406-9433. doi: https://doi.org/10.1109/TAES.2025.3551276.
***29.*** Bouhamri N., Zelmat M.E., Tilmatine A. Micronized plastic waste recycling using two-disc tribo-electrostatic separation process. *Advanced Powder Technology*, 2019, vol. 30, no. 3, pp. 625-631. doi: https://doi.org/10.1016/j.apt.2018.12.012.
***30.*** Messal S., Zeghloul T., Mekhalef-Benhafssa A., Medles K., Dascalescu L. Experimental study of a tribo-aero-electrostatic separator for finely-grinded matter. *Journal of Electrostatics*, 2017, vol. 89, pp. 59-68. doi: https://doi.org/10.1016/j.elstat.2017.08.004.
***31.*** Zeghloul T., Mekhalef Benhafssa A., Richard G., Medles K., Dascalescu L. Effect of particle size on the tribo-aero-electrostatic separation of plastics. *Journal of Electrostatics*, 2017, vol. 88, pp. 24-28. doi: https://doi.org/10.1016/j.elstat.2016.12.003.
***32.*** Achouri I.E., Zeghloul T., Richard G., Medles K., Nouri H., Dascalescu L. Factors that Influence the Performance of a Two-Rotating Disks-Type Tribo-Aero-Electrostatic Separator for Micronized WEEE. *IEEE Transactions on Industry Applications*, 2019, vol. 55, no. 1, pp. 802-811. doi: https://doi.org/10.1109/TIA.2018.2866546.
***33.*** Mekhalef Benhafssa A., Zeghloul T., Aksa W., Medles K., Dascalescu L. Continuous operation of a fluidized-bed disk-type electrostatic separator for micronized plastic waste. *Waste Management*, 2018, vol. 79, pp. 763-769. doi: https://doi.org/10.1016/j.wasman.2018.08.044.
***34.*** Sjoberg J. Neural networks for modelling and control of dynamic systems, M. Nørgaard, O. Ravn, N. K. Poulsen and L. K. Hansen, Springer, London, 2000, xiv+246pp. *International Journal of Robust and Nonlinear Control*, 2001, vol. 11, no. 9, pp. 881-882. doi: https://doi.org/10.1002/rnc.585.
***35.*** Tsungnan Lin, Horne B.G., Tino P., Giles C.L. Learning long-term dependencies in NARX recurrent neural networks. *IEEE Transactions on Neural Networks*, 1996, vol. 7, no. 6, pp. 1329-1338. doi: https://doi.org/10.1109/72.548162.
***36.*** Sola J., Sevilla J. Importance of input data normalization for the application of neural networks to complex industrial problems. *IEEE Transactions on Nuclear Science*, 1997, vol. 44, no. 3, pp. 1464-1468. doi: https://doi.org/10.1109/23.589532.
***37.*** Salinas D., Flunkert V., Gasthaus J., Januschowski T. DeepAR: Probabilistic forecasting with autoregressive recurrent networks. *International Journal of Forecasting*, 2020, vol. 36, no. 3, pp. 1181-1191. doi: https://doi.org/10.1016/j.ijforecast.2019.07.001.
***38.*** Qi M., Zhang G.P. An investigation of model selection criteria for neural network time series forecasting. *European Journal of Operational Research*, 2001, vol. 132, no. 3, pp. 666-680. doi: https://doi.org/10.1016/S0377-2217(00)00171-5.
***39.*** Shrestha A., Mahmood A. Review of Deep Learning Algorithms and Architectures. *IEEE Access*, 2019, vol. 7, pp. 53040-53065. doi: https://doi.org/10.1109/ACCESS.2019.2912200.

*Received 18.08.2025*
*Accepted 20.10.2025*
*Published 02.01.2026*

*Z. Ayache*[1], *Assistant Lecturer,*
*O. Dahou*[2], *PhD, Associate Professor,*
[1] IRECOM Laboratory,
Djillali Liabes University of Sidi Bel-Abbes, Algeria,
e-mail: zouaoui.ayache@univ-sba.dz
[2] Electrical Engineering Department,
Mustapha Stambouli University of Mascara, Algeria,
e-mail: o.dahou@univ-mascara.dz (Corresponding Author)

*How to cite this article:*
Ayache Z., Dahou O. Development of a NARX neural network for a tribo-aero-electrostatic separator with rotating disk electrodes. *Electrical Engineering & Electromechanics*, 2026, no. 1, pp. 20-27. doi: https://doi.org/10.20998/2074-272X.2026.1.03

UDC 621.317 https://doi.org/10.20998/2074-272X.2026.1.04

A. Bounab, A. Chaiba, S. Belkacem, A. Chariete

# Performance improvement of parallel dual-star permanent magnet synchronous machines via type-2 fuzzy direct torque control with a single six-phase inverter

***Introduction.*** *The growing need for efficient and high-performance electric drive systems has led to increased research in advanced control strategies for multi-machine configurations. Among them, dual-star permanent magnet synchronous machines (DSPMSMs) connected in parallel to a single inverter offer a promising solution for applications requiring high reliability and precise control.* ***Problem.*** *Conventional direct torque control (DTC) strategies, typically relying on PI controllers, suffer from significant torque and flux ripples, which negatively impact system efficiency and dynamic response. Moreover, these traditional controllers face challenges in handling parameter variations and external disturbances, limiting their applicability in demanding environments.* ***Goal.*** *This study aims to enhance the performance of DSPMSM drive systems by improving speed regulation, minimizing torque and flux fluctuations, and increasing robustness against disturbances, thereby ensuring greater efficiency and stability.* ***Methodology.*** *To address these challenges, we propose a novel DTC strategy that replaces the conventional PI controller with a type-2 fuzzy logic controller (T2-FLC). This intelligent control approach leverages the adaptability of fuzzy logic to improve response accuracy and dynamic performance. The proposed methodology is validated through extensive simulations using MATLAB/Simulink, analyzing various operating conditions and comparing the performance with conventional DTC techniques.* ***Results.*** *Simulation results confirm that the T2-FLC-based DTC significantly reduces torque and flux ripples while ensuring precise speed regulation. The proposed approach also demonstrates improved robustness against disturbances and parameter variations, outperforming traditional PI-based DTC in terms of efficiency and control accuracy.* ***Scientific novelty****. This research introduces an innovative application of T2-FLC in DTC for parallel-connected DSPMSMs, offering a novel control strategy that effectively mitigates the drawbacks of conventional methods. The integration of T2-FLC into the DTC framework provides enhanced adaptability and superior performance, distinguishing this study from existing works.* ***Practical value.*** *The proposed control strategy enhances the reliability, efficiency, and stability of DSPMSM-based drive systems, making it well-suited for high-performance applications such as railway traction, electric vehicles, and industrial automation. By improving control precision and robustness, this approach contributes to the advancement of intelligent drive technologies in modern electric propulsion systems.* References 39, tables 4, figures 16.

*Key words:* **permanent magnet synchronous machine, type-2 fuzzy logic controller, direct torque control, six-phase inverter, multi-machines system.**

***Вступ****. Зростаюча потреба в ефективних та високопродуктивних системах електроприводу призвела до посилення досліджень удосконалених стратегій керування для багатомашинних конфігурацій. Серед них, синхронні машини з постійними магнітами та обмоткою статора за схемою з'єднання «зірка» із спільним регулюванням струмів обмоток статора (DSPMSM), що підключені паралельно до одного інвертора, пропонують перспективне рішення для застосувань, які вимагають високої надійності та точного керування.* ***Проблема****. Традиційні стратегії прямого керування крутним моментом (DTC), які базуються на PI-контролерах, мають значні пульсації крутного моменту та потоку, що негативно впливає на ефективність системи та динамічну характеристику. Крім того, ці традиційні контролери стикаються з проблемами обробки коливань параметрів та зовнішніх збурень, що обмежує їхню застосовність у складних умовах.* ***Мета****. Це дослідження спрямоване на підвищення продуктивності систем приводу DSPMSM шляхом покращення регулювання швидкості, мінімізації коливань крутного моменту та потоку, а також підвищення стійкості до збурень, тим самим забезпечуючи більшу ефективність та стабільність.* ***Методологія****. Для вирішення цих проблем запропоновано нову стратегію DTC, яка замінює традиційний PI-контролер контролером з нечіткою логікою 2-го типу (T2-FLC). Цей інтелектуальний підхід до керування використовує адаптивність нечіткої логіки для покращення точності відгуку та динамічних характеристик. Запропонована методологія перевірена за допомогою масштабної симуляції з використанням MATLAB/Simulink, аналізуючи різні робочі умови та порівнюючи продуктивність з традиційними DTC методам.* ***Результати*** *моделювання підтверджують, що DTC на основі T2-FLC значно зменшує пульсації крутного моменту та потоку, забезпечуючи при цьому точне регулювання швидкості. Запропонований підхід демонструє покращену стійкість до збурень та коливань параметрів, перевершуючи традиційний DTC на основі PI з точки зору ефективності та точності керування.* ***Наукова новизна****. Це дослідження представляє інноваційне застосування T2-FLC у DTC для паралельно з'єднаних DSPMSM, пропонуючи нову стратегію керування, яка ефективно усуває недоліки звичайних методів. Інтеграція T2-FLC у структуру DTC забезпечує покращену адаптивність та високу продуктивність, що відрізняє це дослідження від існуючих робіт.* ***Практична значимість****. Запропонована стратегія керування підвищує надійність, ефективність та стабільність систем приводу на основі DSPMSM, що робить її добре придатною для високопродуктивних застосувань, таких як залізниця, електромобілі та промислова автоматизація. Завдяки покращенню точності та надійності керування, цей підхід сприяє розвитку інтелектуальних технологій приводу в сучасних електричних рушійних системах.* Бібл. 39, табл. 4, рис. 16.

*Ключові слова:* **синхронна машина з постійними магнітами, контролер з нечіткою логікою 2 типу, пряме управління крутним моментом, шестифазний інвертор, багатомашинна система.**

**Introduction.** In today's rapidly evolving industrial landscape, there is an increasing focus on optimizing system performance while reducing weight, volume, and operating costs. To achieve this ambitious goal, the concept of using a multi-machine drive system powered by a single inverter has emerged as an innovative solution. Such systems find applications in various industries, including paper and rolling mills, transportation, electric traction, marine propulsion, and electric vehicles.

In the domain of multi-motor drives, the design and control strategy of the drive system must be carefully tailored to meet the specific requirements of the application. These include factors such as output power, speed control, and accuracy [1–8]. The implementation of drive techniques involving the parallel connection of two dual-star permanent magnet synchronous machines (DSPMSMs), both powered by a six-phase pulse width modulation (PWM) inverter, has been adopted in various

industrial applications [1, 2, 9]. However, when it comes to controlling the speed of multi-phase drives, traditional control mechanisms face persistent challenges due to parameter variations, flux and torque ripples, and the effects of power disturbances on the load [9–11].

To address these issues, this paper proposes an innovative approach [12] by integrating a type-2 fuzzy logic controller (T2-FLC) with direct torque control (DTC) to regulate the speed of two DSPMSMs operating in parallel [13–15]. This method not only improves system performance but also mitigates torque and flux ripples that could otherwise affect operational efficiency. The motivation behind this work lies in overcoming the limitations of traditional DTC methods [9–11], which are known for their sensitivity to rotor parameter variations and challenges in managing variable switching frequencies due to the use of hysteresis controllers [12].

In response, this work explores a state-of-the-art methodology by integrating a T2-FLC, aiming to overcome these limitations and provide a more suitable approach for systems affected by uncertainty.

Extensive research on the application of type-2 fuzzy logic in engineering is ongoing, highlighting several advantages over type-1 fuzzy logic controller (T1-FLC) in systems affected by uncertainty [15–19]. Recent studies confirm that the T2-FLC offers better performance than T1-FLC in managing uncertain or imprecise system parameters [20–22].

Before presenting the proposed methodology, it is important to review the current state of the art. DSPMSMs, featuring two star-connected three-phase stator windings shifted by 30°, offer several advantages over conventional three-phase PMSMs. These include lower torque ripple, reduced current harmonics, higher reliability, and greater power capability [23]. Moreover, DTC has proven effective in achieving high dynamic performance in AC motor drives [24]. Traditional DTC methods estimate torque and flux to select appropriate voltage vectors, keeping errors within hysteresis bands. While this enables fast torque response, it results in variable switching frequencies [25].

Fuzzy logic controller (FLC) provides an alternative control strategy that relies on linguistic rules and membership functions (MFs) rather than complex mathematical models [26]. FLC is recognized for its robustness against uncertainties and is particularly well-suited for complex, nonlinear systems. T2-FLCs are distinguished by their ability to handle higher degrees of uncertainty compared to T1-FLCs [27].

Recent studies have investigated the integration of intelligent control techniques to enhance the performance of DTC. Notable developments include fuzzy-based DTC strategies for induction motors, which have demonstrated improved speed regulation and reduced maintenance costs [1]. Fuzzy logic controllers have also been incorporated into DTC systems to improve the efficiency, reliability, and dynamic behavior of variable-speed drives in a wide range of applications. For example, fuzzy-2 DTC combined with space vector pulse width modulation has shown faster dynamic responses, lower total harmonic distortion (THD) in current and voltage, and reduced capacitor voltage spikes in induction motor drives, outperforming conventional PI-DTC schemes [24].

Furthermore, FLCs have been applied to DTC schemes to improve the overall performance of variable-speed drive systems. In [25], a fractional-order FLC was introduced to enhance the dynamic performance of DTC in induction motors, leading to significant gains in efficiency and reliability. In [27], FLC was employed to optimize electromagnetic torque and speed regulation in induction machines, effectively replacing conventional hysteresis comparators and PI speed controllers.

Additionally, DTC has been integrated with adaptive fuzzy control in the case of DSPMSMs, significantly reducing harmonic currents and improving efficiency in high-power traction applications [28]. Fuzzy logic-based control has also been applied to grid-connected photovoltaic inverters, stabilizing output voltage and current, minimizing THD, and enabling power injection into the grid when generation exceeds local demand [29].

In PMSMs, fuzzy logic-based DTC techniques have enabled the reduction of torque and flux ripples without modifying the inverter's switching frequency [30]. Moreover, fuzzy logic has been used for the control of DSPMSMs connected in parallel and supplied by a single six-phase inverter, achieving superior speed tracking performance, particularly under load disturbances [15].

In the context of five-phase interior PMSMs, a fuzzy logic-based DTC space vector modulation approach was proposed, offering fast and simple speed control while outperforming classical DTC methods [18].

In this paper, we propose an innovative speed control approach for DSPMSMs operating in parallel and supplied by a single six-phase PWM inverter. Our contribution lies in the integration of a T2-FLC with DTC to address the complex challenges of multi-motor control. The use of a six-phase PWM inverter, as emphasized in this work, enhances both system reliability and overall performance compared to traditional configurations.

The integration of T2-FLC plays a crucial role in addressing elevated levels of uncertainty, which are often encountered in real-world applications. Combined with DTC, well known for its high dynamic performance in AC motor drives, the proposed approach yields an intelligent and adaptive control strategy that significantly improves system behavior under varying operating conditions. This research highlights the advantages of T2-FLC over its T1-FLC counterpart, particularly in scenarios where uncertainty is a dominant factor, thus demonstrating the practical relevance of T2-FLC implementation in industrial contexts. In summary, the proposed method constitutes a significant advancement in motor drive control, with the potential to enhance the reliability, efficiency, and overall performance of electric drive systems across a wide range of applications.

**The goal of the work** is to enhance the performance of DSPMSM drive systems by improving speed regulation, minimizing torque and flux fluctuations, and increasing robustness against disturbances, thereby ensuring greater efficiency and stability. Unlike conventional DTC approaches that rely on PI controllers and suffer from significant torque and flux ripples, the proposed method introduces an adaptive and intelligent control scheme that improves dynamic response, minimizes electromagnetic ripples, and ensures stable operation under parameter uncertainties and external disturbances.

**System configuration.** Figure 1 shows the configuration of the proposed DTC system applied to two DSPMSMs operating in parallel and driven by a single six-phase inverter. This topology effectively mitigates the risk of over-magnetization in the machines, preserving performance and system integrity.

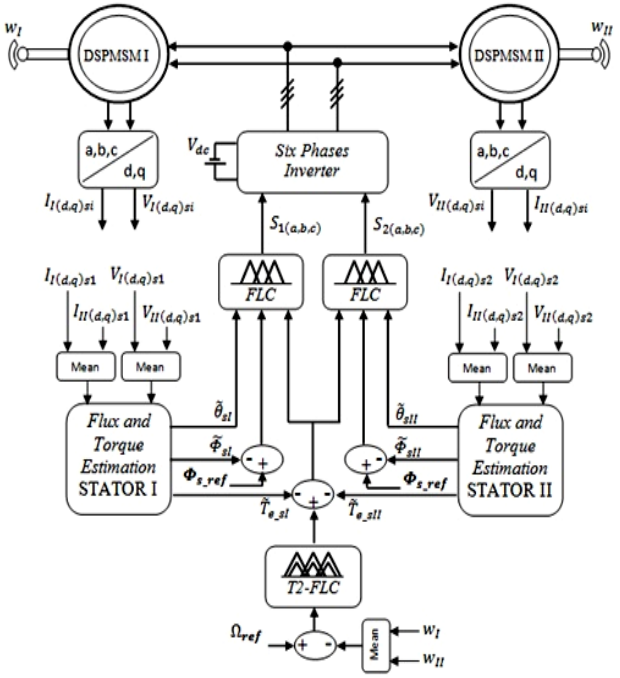


Fig. 1. Block diagram of the type-2 fuzzy logic-based DTC for two DSPMSMs

The core principle of DTC lies in determining the appropriate switching states of the voltage source inverter to directly control the stator voltage vectors. The selection of these vectors is based on a predefined switching table that considers torque and flux errors, along with the position of the stator flux vector. This process is critical to achieving accurate control and optimizing the overall performance of the drive system.

The rotational speed of both machines is measured using high-precision sensors, enabling fine speed regulation. To achieve this level of control accuracy, the T2-FLC is embedded within the outer speed regulation loop of the DSPMSM drive, as shown in Fig. 1.

Additionally, the system's capability to handle a wide range of disturbances is thoroughly evaluated. These disturbances include internal factors such as parameter variations, as well as external influences such as load changes and speed fluctuations. This comprehensive analysis demonstrates the system's ability to maintain stable and reliable performance, even under dynamic and uncertain operating conditions. This aspect reflects the scientific rigor and practical relevance of the proposed approach.

**DSPMSM model.** A comprehensive mathematical model is developed to represent the dynamic behavior of the DSPMSM. The state variables include stator currents, stator flux components, and rotor speed, while the control inputs are the stator voltages ($V_{ds}$, $V_{qs}$). The model is formulated in the ($d$–$q$) reference frame, which rotates synchronously with the rotor magnetic field. The dynamic behavior is expressed through a set of differential equations (1–4) [31, 32]:

$$\begin{cases} V_{ds1,i}=R_{s1,i}\cdot I_{ds1,i}+\dfrac{\mathrm{d}\Phi_{ds1,i}}{\mathrm{d}t}-w_{si}\cdot\Phi_{qs1,i};\\ V_{qs1,i}=R_{s1,i}\cdot I_{qs1,i}+\dfrac{\mathrm{d}\Phi_{qs1,i}}{\mathrm{d}t}-w_{si}\cdot\Phi_{ds1,i};\\ V_{ds2,i}=R_{s2,i}\cdot I_{ds2,i}+\dfrac{\mathrm{d}\Phi_{ds2,i}}{\mathrm{d}t}-w_{si}\cdot\Phi_{qs2,i};\\ V_{qs2,i}=R_{s2,i}\cdot I_{qs2,i}+\dfrac{\mathrm{d}\Phi_{qs2,i}}{\mathrm{d}t}-w_{si}\cdot\Phi_{ds2,i}, \end{cases} \quad (1)$$

where the expressions of stators fluxes are:

$$\begin{cases} \Phi_{ds1,i}=L_{ds1,i}\cdot I_{ds1,i}+M_{ds2,i}\cdot I_{ds2,i}+\Phi_{PM,i};\\ \Phi_{qs1,i}=L_{qs1,i}\cdot I_{qs1,i}+M_{qs2,i}\cdot I_{qs2,i};\\ \Phi_{ds2,i}=L_{ds2,i}\cdot I_{ds2,i}+M_{ds1,i}\cdot I_{ds1,i}+\Phi_{PM,i};\\ \Phi_{qs2,i}=L_{qs2,i}\cdot I_{qs2,i}+M_{qs1,i}\cdot I_{qs1,i}. \end{cases} \quad (2)$$

In these equations, the subscripts ($s_1$, $s_2$) designate the 1st and 2nd stator of both DSPMSMs, while subscripts ($i$ = 1, 2) denote variables and parameters about DSPSM1 and DSPSM2, respectively. The variables and parameters include: [($V_{ds1,i}$, $V_{qs1,i}$,), ($V_{ds2,i}$, $V_{qs2,i}$)]; [($I_{ds1,i}$, $I_{qs1,i}$,), ($I_{ds2,i}$, $I_{qs2,i}$)]; [($\Phi_{ds1,i}$, $\Phi_{qs1,i}$,), ($\Phi_{ds2,i}$, $\Phi_{qs2,i}$)]; [($L_{ds1,i}$, $L_{qs1,i}$,), ($L_{ds2,i}$, $L_{qs2,i}$)]; [($M_{ds1,i}$, $M_{qs1,i}$,), ($M_{ds2,i}$, $M_{qs2,i}$)] and $\Phi_{PM,i}$, representing voltage, currents, stator flux linkage, stator inductance, mutual inductance in the ($d$–$q$) axis, and the permanent magnet flux, respectively.

The mechanical equation of the machine is:

$$J_i\frac{\mathrm{d}\Omega_i}{\mathrm{d}t}+fr_i\cdot\Omega_i=T_{e_i}-T_{r_i}, \quad (3)$$

where $J$ is the moment of inertia; $fr$ is the friction coefficient; $T_e$ is the electromagnetic torque; $T_r$ is the load torque; $\Omega$ is the rotor's mechanical speed [13].

The structural representation of the DSPMSM in the electrical domain is depicted in Fig. 2.

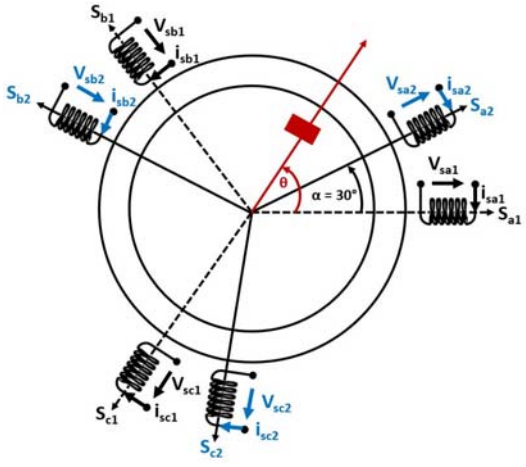


Fig. 2. Schematic of the DSPMSM stator windings

The electromagnetic torque equation is articulated in terms of stator currents and stator flux as:

$$T_{e_i}=p\cdot\begin{pmatrix}\Phi_{ds1,i}\cdot I_{qs1,i}-\Phi_{qs1,i}\cdot I_{ds1,i}+\\ +\Phi_{ds2,i}\cdot I_{qs2,i}-\Phi_{qs2,i}\cdot I_{ds2,i}\end{pmatrix}, \quad (4)$$

where $p$ is the number of pole pairs.

**Six-phase inverter model.** The stator windings of the DSPMSMs are supplied by a six-phase voltage source inverter, as shown in Fig. 3 [33]. In this configuration, the

notation $K_{a1}$, $K_{b1}$, $K_{c1}$ represent the switches of the upper half-bridge, while $K_{a2}$, $K_{b2}$, $K_{c2}$ correspond to the switches of the lower half-bridge. Additionally, $n_1$ and $n_2$ denote the neutral points associated with stator 1 and stator 2, respectively.

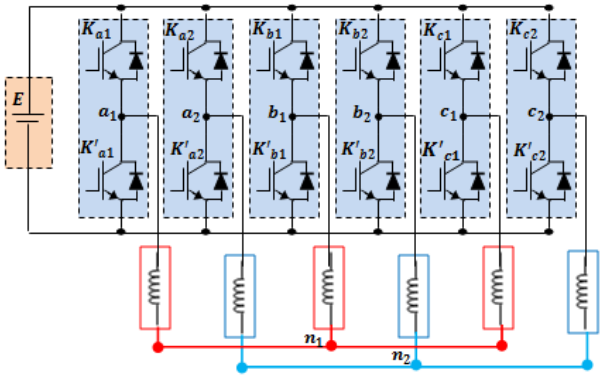


Fig. 3. Schematic diagram of the six-phase inverter

It is important to note that, since the windings of stator 1 and stator 2 are assumed to be ideally balanced and their neutral points are not connected, the phase voltages do not contain any zero-sequence components. As a result, equation (5) remains valid under these conditions:

$$\begin{aligned} V_{sa1}+V_{sb1}+V_{sc1}&=0;\\ V_{sa2}+V_{sb2}+V_{sc2}&=0. \end{aligned} \tag{5}$$

Furthermore, equation (6) accurately represents the voltage vector generated by the six-phase inverter:

$$\begin{bmatrix} V_{sa1}\\ V_{sb1}\\ V_{sc1}\\ V_{sa2}\\ V_{sb2}\\ V_{sc2} \end{bmatrix} = \begin{bmatrix} 2 & -1 & -1 & 0 & 0 & 0\\ -1 & 2 & -1 & 0 & 0 & 0\\ -1 & -1 & 2 & 0 & 0 & 0\\ 0 & 0 & 0 & 2 & -1 & -1\\ 0 & 0 & 0 & -1 & 2 & -1\\ 0 & 0 & 0 & -1 & -1 & 2 \end{bmatrix} \begin{bmatrix} V_{a10}\\ V_{b10}\\ V_{c10}\\ V_{a20}\\ V_{b20}\\ V_{c20} \end{bmatrix}. \tag{6}$$

When multiple motors are connected in parallel and supplied by a single inverter, the inverter directly controls the current to ensure proper system operation. However, discrepancies in speed or parameter variations between the two motors can lead to an imbalance in the currents flowing through each stator winding. The stator currents $I_{s1,i}$ and $I_{s2,i}$ are flowing in each machine, can be represented by $I_{s,i}$ which flows equally in both stators windings and $\Delta I_{s,i}$ which circulates between each stator winding (Fig. 4) and described as [16]:

$$I_{si}=I_{s1,i}+I_{s2,i}; \tag{7}$$

$$\Delta I_{s,i}=\frac{I_{s2,i}-I_{s1,i}}{2}. \tag{8}$$

The mean control strategy is based on averaging the input variables of both motors to form a virtual mean motor model. The measured variables for both machines include the stator currents $I_{s1,i}$ and $I_{s2,i}$ and rotor speeds ($\omega_1$, $\omega_2$). The corresponding average quantities are computed as:

$$I_{si}=\frac{I_{s1,i}+I_{s2,i}}{2}; \tag{9}$$

$$\omega_i=\frac{\omega_1+\omega_2}{2}. \tag{10}$$

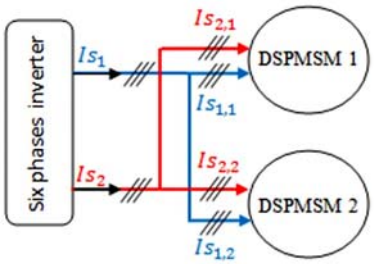


Fig. 4. Current decomposition in the parallel-connected dual motor system

**DTC based on fuzzy logic.** DTC operates on a fundamental principle that involves selecting appropriate switching commands for the voltage inverter to control the stator voltage vectors. These vectors are carefully chosen from a predefined lookup table based on the estimated torque and flux errors, as well as the angular position of the stator flux vector. Two comparators continuously monitor the key control variables: stator flux and electromagnetic torque.

A hysteresis controller is integrated into the DTC scheme to maintain the error between each control variable and its reference within a defined hysteresis band. In the case of a two-level controller, the voltage vector selection depends solely on the polarity of the error rather than its magnitude. To avoid unnecessary switching when the flux error becomes negligible, a hysteresis band centered around zero is introduced [15].

Fundamentally, DTC relies on the orientation and regulation of the stator flux. The mathematical expression of the stator flux in the Park reference frame is given as:

$$\begin{aligned} \Phi_{ds(1,2)}&=\frac{1}{2}\int_0^t\left(V_{1ds(1,2)}+V_{2ds(1,2)}\right)dt-\\ &-\frac{1}{2}\int_0^t R_s\cdot\left(I_{1ds(1,2)}+I_{2ds(1,2)}\right)dt; \end{aligned} \tag{11}$$

$$\begin{aligned} \Phi_{qs(1,2)}&=\frac{1}{2}\int_0^t\left(V_{1qs(1,2)}+V_{2qs(1,2)}\right)dt-\\ &-\frac{1}{2}\int_0^t R_s\cdot\left(I_{1qs(1,2)}+I_{2qs(1,2)}\right)dt; \end{aligned} \tag{12}$$

Consequently, the stator flux module is:

$$\Phi_{s1}=\sqrt{\Phi_{ds1}^2+\Phi_{qs1}^2}; \tag{13}$$

$$\Phi_{s2}=\sqrt{\Phi_{ds2}^2+\Phi_{qs2}^2}. \tag{14}$$

The electromagnetic torque can be estimated from the estimated magnitudes of the flux, and the measured magnitudes of the line currents:

$$\begin{aligned} T_e=\frac{p}{2}\big[&\Phi_{ds1}\cdot\left(I_{1qs1}+I_{2qs1}\right)-\Phi_{qs1}\cdot\left(I_{1ds1}+I_{2ds1}\right)+\\ &+\Phi_{ds2}\cdot\left(I_{1qs2}+I_{2qs2}\right)-\Phi_{qs2}\cdot\left(I_{2ds2}+I_{2ds2}\right). \end{aligned} \tag{15}$$

To enhance the performance of conventional DTC, particularly by reducing torque and flux ripples and improve the THD of the stator current, the hysteresis controllers and switching table are replaced with fuzzy logic-based decision blocks. These blocks take as inputs the stator flux angle, torque error, and flux error, resulting in a fuzzy logic-based DTC scheme [14, 19, 31].

The universe of discourse for the stator flux angle is divided into 6 fuzzy sets ($t_1$–$t_6$) (Fig. 5,*a*). Triangular MFs are used for all angular sectors ($t_i$). The universe of discourse for the electromagnetic torque error is divided into 3 fuzzy sets (Fig. 5,*b*): Negative torque error (*N*), Zero torque error (*Z*) and Positive torque error (*P*). Triangular MFs are assigned to the central fuzzy set (*Z*), while trapezoidal MFs are used for the boundary sets (*P*) and (*N*).

Similarly, the universe of discourse for the stator flux error is divided into 2 fuzzy sets (Fig. 5,*c*): Negative flux error (*N*), Positive flux error (*P*). For both sets, trapezoidal MFs are selected to better accommodate uncertainties at the boundaries of the domain.

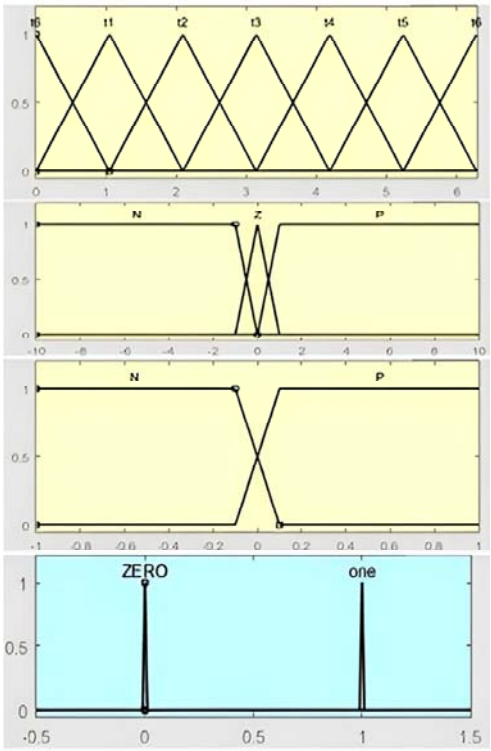


Fig. 5. MFs of the input and output variables used in the fuzzy DTC

The output variable, illustrated in Fig. 5,*d*, is decomposed into 3 sub-outputs, corresponding to the 3 switching signals $S_a$, $S_b$, $S_c$ used to control the inverter switches in a two-level configuration. The universe of discourse for each sub-output is divided into 2 fuzzy sets: Zero and One. Trapezoidal MFs are selected for both sets to ensure robust switching decisions under uncertainty.

T2-FLC, which relies on type-2 fuzzy sets (T2-FS), is a powerful approach for managing complex and nonlinear systems [34]. To address higher levels of uncertainty in modelling and control, T2-FS are introduced as an extension of the conventional type-1 fuzzy sets (T1-FS) to better handle uncertainty and imprecision in complex systems [16, 34–36]. Numerous studies have demonstrated that T2-FLC offers superior performance compared to T1-FLC, particularly in environments characterized by high levels of uncertainty and nonlinearity. The fuzzy rule base forms the core of the T2-FLC system. It encapsulates expert knowledge through a set of fuzzy rules that describe the expected behavior of the system under different operating conditions. In this work, the rule base consists of 36 fuzzy rules (Table 1).

Table 1

Set of fuzzy rules

| Flux error $\Delta\Phi$ | Torque error $\Delta T_e$ | Stator flux angle $\theta$ | | | | | |
|---|---|---|---|---|---|---|---|
| | | $t_1$ | $t_2$ | $t_3$ | $t_4$ | $t_5$ | $t_6$ |
| *P* | *P* | *V*3 | *V*4 | *V*5 | *V*6 | *V*1 | *V*2 |
| | *Z* | *V*0 | *V*7 | *V*0 | *V*7 | *V*0 | *V*7 |
| | *N* | *V*1 | *V*2 | *V*3 | *V*4 | *V*5 | *V*6 |
| *N* | *P* | *V*4 | *V*5 | *V*6 | *V*1 | *V*2 | *V*3 |
| | *Z* | *V*7 | *V*0 | *V*7 | *V*0 | *V*7 | *V*0 |
| | *N* | *V*6 | *V*1 | *V*2 | *V*3 | *V*4 | *V*5 |

where:

*V*0= [0 0 0]; *V*1= [1 0 0]; *V*2= [1 1 0]; *V*3= [0 1 0];
*V*4= [0 1 1]; *V*5= [0 0 1]; *V*6= [1 0 1]; *V*7= [1 1 1].

**T-2FLC of DSPMSM**. This section describes the implementation of T2-FLC, which effectively replaced the PI controller in order to achieve faster response times while maintaining system stability and eliminating static error. T2-FLC is well-suited to handling complex non-linear systems that exhibit a degree of uncertainty [16]. It does not require an exact model of the system or precise parameter values [17].

T2-FLC contains 4 elements [16, 18]:

- **Fuzzification**. This initial step involves the transformation of classical data into MFs such as negative grand (NG), equal zero (EZ) and so on.
- **Fuzzy inference engine**. This component leverages a lookup table that consolidates control derivatives obtained from the interplay of control rules and MFs .
- **Type reducer**. This essential component of the T2-FLC is responsible for transforming the output of T1-FS and subsequently transferring it to the defuzzification process.
- **Defuzzification**. The output from the type reducer is further processed through the defuzzification process, which converts MFs into crisp data.

In this specific application (Fig. 6) the T2-FLC uses 2 input variables: the speed error ($e_s$) and the variation in speed error ($\Delta e_s$). The output variable $U_f$ is generated through the fuzzy inference and defuzzification process, and corresponds to the electromagnetic torque reference $T_e$.

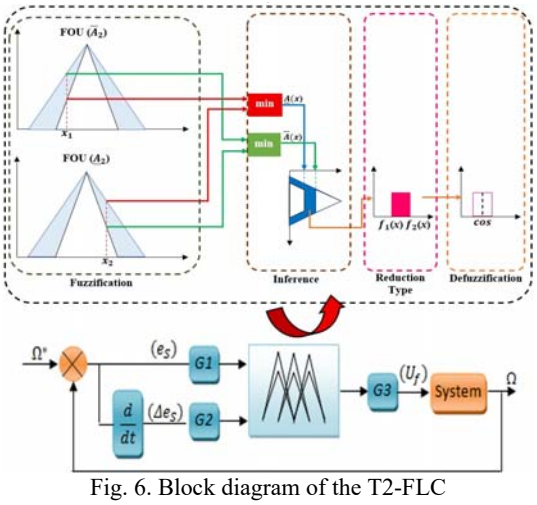


Fig. 6. Block diagram of the T2-FLC

MFs associated with the input variables are depicted in Fig. 7. T2-FLC follows the conventional IF–THEN rule-based structure; however, it differs from classical fuzzy controllers by employing T2-FS for both the antecedents and the consequents [37–39]. T2-FLC represents an innovative and robust control strategy that

offers enhanced flexibility in managing uncertainties and handling complex nonlinear dynamics. By incorporating a footprint of uncertainty (FOU) in its MFs, the T2-FLC has the potential to significantly improve the performance and reliability of control systems operating under imprecise or variable conditions.

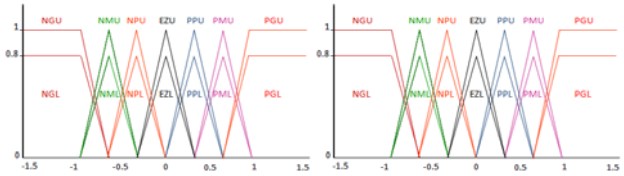

Fig. 7. MFs of the input variables

To illustrate the operation of the proposed T2-FLC for speed control, a few representative fuzzy rules are presented below:

Rule 1: if $e_s$ is NG, and $\Delta e_s$ is NG then $U_f$ is NG.
Rule 2: if $e_s$ is NG, and $\Delta e_s$ is NM then $U_f$ is NG.
Rule 3: if $e_s$ is NG, and $\Delta e_s$ is NP then $U_f$ is NG.
……
Rule 36: if $e_s$ is PG, and $\Delta e_s$ is PG then $U_f$ is PG.

**Simulation results and discussion.** The described mathematical model was used to develop the simulation environment in MATLAB/Simulink. The parameters of the DSPMSM were adopted from [14] and are listed in Table 2.

Table 2
Simulation parameters of the DSPMSM

| Parameter | Value |
|---|---|
| Nominal stator voltage $U$, V | 220 |
| Stator resistances $R_{s1} = R_{s2}$, Ω | 0.12 |
| Stator inductance $L_s$, mH | 0.8 |
| Mutual inductance $L_m$, mH | 0.3 |
| Flux linkage $\Phi_{PM}$, Wb | 0.394 |
| Pole pairs $p$ | 4 |
| Moment of inertia $J$, kg·m$^2$ | $5 \cdot 10^{-5}$ |
| Viscous friction coefficient $fr$, N·m·s/rad | 0 |
| PI controller gain (integral) $K_i$ | 3 |
| PI controller gain (proportional) $K_p$ | 900 |
| T2-FLC gains $G_1$, $G_2$, $G_3$ | 0.021 |
| | 0.012 |
| | 100 |

The simulation model was developed to enable the performance evaluation of various DTC strategies. To that end, 3 distinct test scenarios were defined for comparative analysis:

**Test 1. Speed reversal with load torque steps.** This scenario evaluates tracking performance and disturbance rejection capabilities. A trapezoidal reference speed profile alternating between +150 rad/s, –150 rad/s and +50 rad/s was applied. Simultaneously, a load torque of 20 N·m was imposed on both machines.

**Test 2. Load torque variation.** Designed to assess the dynamic response to external load disturbances, this test involved stepping the load torque from 0 to 20 N·m, then to 40 N·m, and finally back to 20 N·m, while maintaining a constant reference speed of 150 rad/s.

**Test 3. Parameter uncertainty**. This test focuses on evaluating robustness against internal variations by modelling +100 % increase in the stator resistance $R_s$.

The proposed T2-FLC was compared via conventional PI-DTC scheme. Performance metrics such as speed tracking accuracy, electromagnetic torque ripple, and robustness to disturbances were recorded for a comprehensive quantitative comparison.

The simulation results clearly indicate that the T2-FLC significantly enhances the control performance of the DSPMSM under all test conditions, particularly in terms of disturbance rejection and reduced torque ripple, outperforming the classical PI-DTC strategy.

**Test 1.** In the 1st scenario, both motors were subjected to a trapezoidal reference speed profile comprising positive and negative transitions. A load torque of 20 N·m was applied at different time intervals: motor 1 at $t \in [0.1, 0.2]$ and motor 2 at $t \in [0.14, 0.2]$. The simulation results (Fig. 8, 9) provide a detailed view of the system's dynamic behavior, highlighting the effectiveness of the proposed T2-FLC in tracking and disturbance rejection.

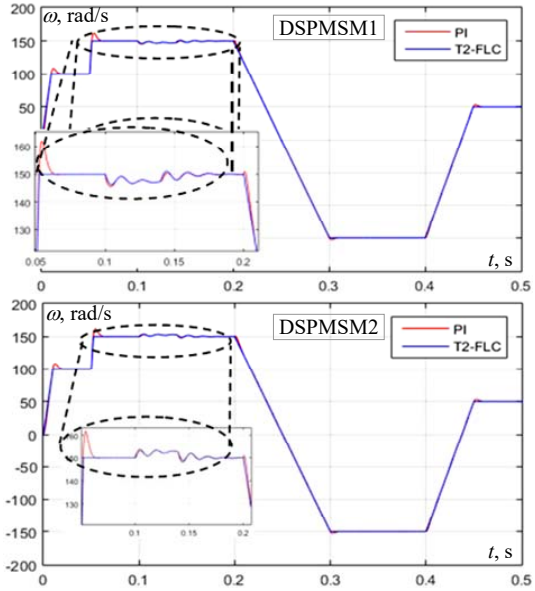

Fig. 8. Speed response of the two DSPMSMs in Test 1

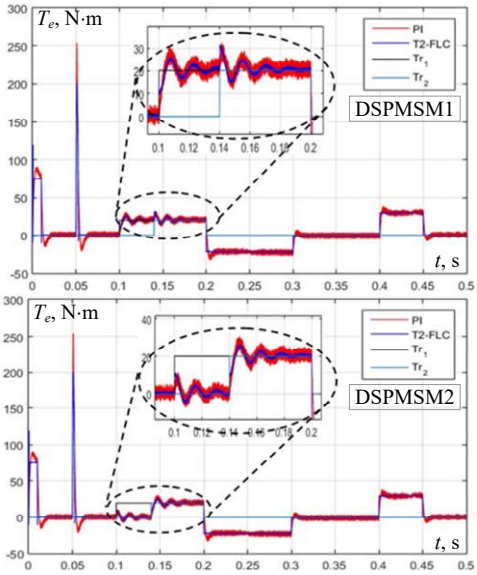

Fig. 9. Torque waveforms of the two DSPMSMs in Test 1

It is evident from the simulation results that the T2-FLC exhibits superior performance in accurately tracking the reference speed trajectory. To facilitate a quantitative comparison between the proposed T2-FLC and the conventional PI-based DTC, several performance indices

have been calculated, including the Integral Squared Error (ISE), Integral Absolute Error (IAE), and Integral Time Squared Error (ITSE) (see Table 3).

T2-FLC successfully tracks a wide speed range, achieving a transition from +150 rad/s to –150 rad/s at $t$=0.2 s, and reaching 50 rad/s at $t$=0.4 s. Moreover, the controller demonstrates significantly reduced oscillation amplitudes and enhanced disturbance rejection, confirming its superior dynamic response and robustness compared to the classical PI controller

**Test 2.** In this scenario, the system's ability to handle external load disturbances was thoroughly evaluated. The load torque applied to the motors was varied in three steps: from 0 N·m to 20 N·m at $t$=0.12 s, then increased to 40 N·m at $t$=0.2 s, and finally reduced back to 20 N·m at $t$=0.28 s. The corresponding simulation results motor speed, electromagnetic torque, and stator currents are illustrated in Fig. 10–12.

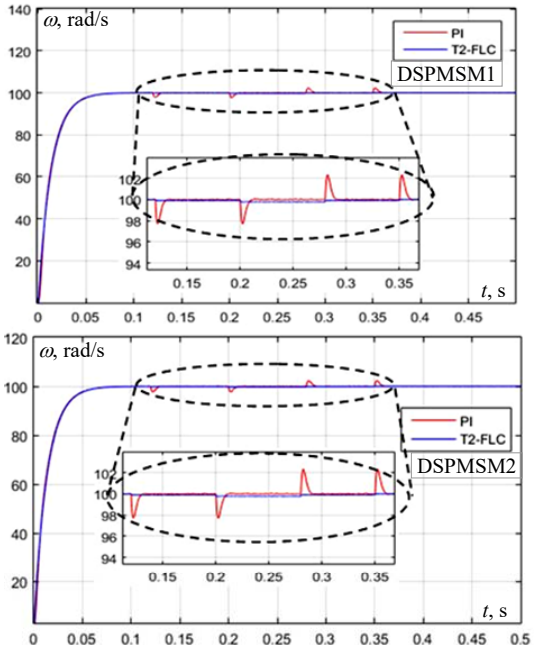


Fig. 10. Speed response of the two DSPMSMs under load torque variation

As shown in Fig. 10, T2-FLC maintained accurate speed regulation across all disturbance intervals, with deviations confined within a narrow margin of ±0.5 rad/s from the reference speed of 150 rad/s. This result underscores the controller's strong capability for disturbance rejection, consistent with findings reported in [9]. In contrast, the PI-based DTC exhibited notable speed deviations, reaching over ±2 rad/s, revealing its limitations in coping with rapid load variations.

The torque waveforms (Fig. 11) further highlight the contrast between the two control strategies. T2-FLC achieved a peak-to-peak torque ripple of only ±3 N·m, demonstrating smoother torque behavior and better dynamic stability. In comparison, the PI controller showed substantial oscillations, with ripple amplitudes reaching ±10 N·m, indicating poorer disturbance rejection and less stable operation. It is important to note that minimizing torque pulsations is critical for precise and efficient operation of PMSMs, particularly in applications requiring high dynamic performance [7].

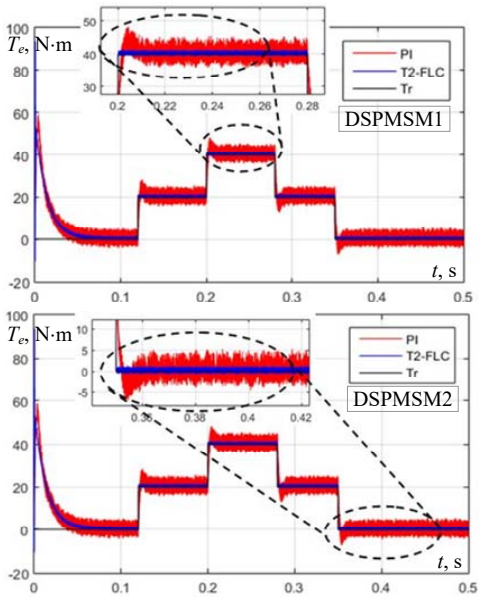


Fig. 11. Comparison of torque ripple under T2-FLC and PI controllers in Test 2

The stator current (Fig. 12) offers additional insight into the performance distinction between the T2-FLC and the PI controller.

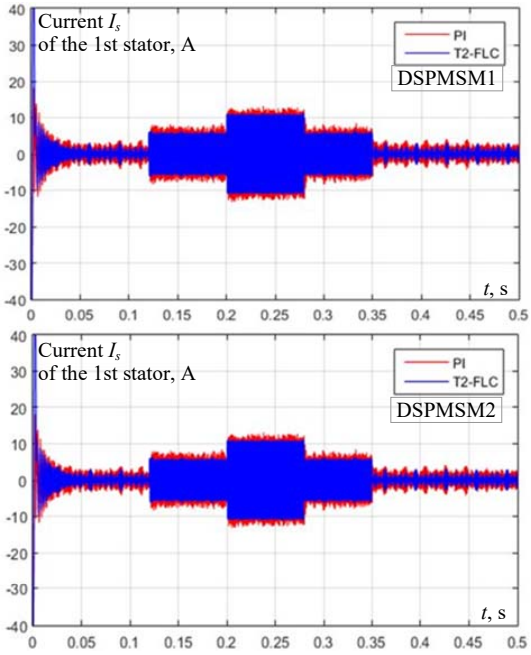


Fig. 12. Stator current response of the two DSPMSMs under load torque variation (Test 2)

Under load variations, the T2-FLC maintains a smooth and nearly circular current trajectory, indicating stable operation and consistent current regulation. In contrast, the PI controller displays noticeable distortions and irregularities in the current locus, along with a slower settling time following torque disturbances, as also noted in [11]. These results confirm the robustness and dynamic stability of the T2-FLC, even under fluctuating load conditions. In summary, the load torque variation test demonstrates that the T2-FLC offers superior disturbance rejection, smoother current dynamics, and faster recovery than the conventional PI-based DTC approach.

**Test 3.** While the previous tests focused on the response to external disturbances such as speed reversals

and load torque variations, this experiment evaluates the robustness of the control strategy under an internal disturbance. Specifically, a 100 % increase in stator resistance was introduced to simulate parameter uncertainty, which is common in real-world operating conditions due to temperature variation or aging effects. Figure 13 illustrates the speed responses of both DSPMSMs under this condition. The results reveal a clear distinction in performance between the two control approaches. T2-FLC shows strong robustness, maintaining precise speed tracking despite the abrupt internal change. The speed error remains within a narrow tolerance band, indicating effective compensation for the parameter deviation. Figures 13–16 illustrate the impact of these parameter variations on speed, torque, stator current, and stator flux.

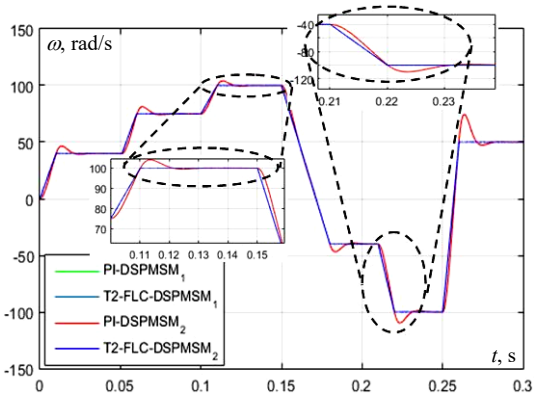

Fig. 13. Speed response of the two DSPMSMs under internal parameter variation (Test 3)

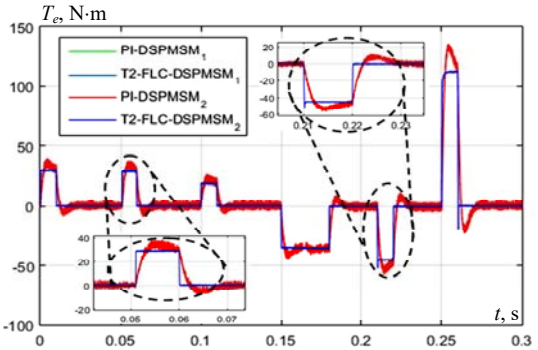

Fig. 14. Torque ripple performance of DSPMSMs under stator resistance variation

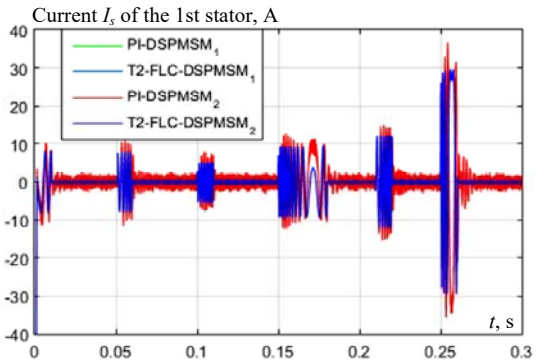

Fig. 15. Stator current response of the two DSPMSMs under internal parameter variation (Test 3)

In contrast, the PI-based DTC exhibits degraded performance, with noticeable speed deviations and slower convergence to the reference trajectory. This confirms the sensitivity of conventional PI control to internal parameter variations, and highlights the adaptive nature of the T2-FLC in uncertain environments.

Overall, this test reinforces the T2-FLC's superior adaptability and resilience in the presence of internal uncertainties, further validating its effectiveness for real-time motor drive applications.

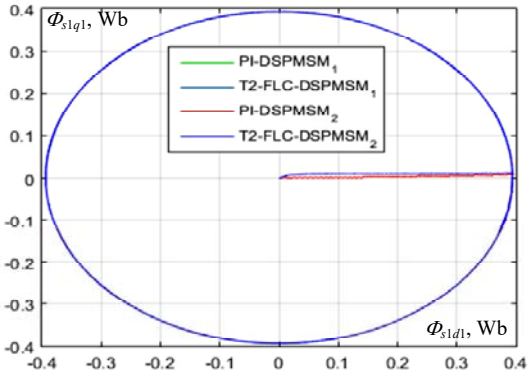

Fig. 16. Comparison of stator flux behavior under internal disturbances (Test 3)

**Discussion.** The simulation results offer valuable insights into the performance of the T2-FLC for the DSPMSM when compared to the conventional PI controller. This section provides a detailed interpretation of those results, supported by quantitative metrics. Table 3 shows a summary of performance indices ISE, IAE and ITSE across 3 test scenarios. The recorded values clearly validate the simulation outcomes and confirm the effectiveness of the proposed T2-FLC strategy.

Table 3

Comparison of ISE, IAE and ITSE for PI and T2-FLC under different test conditions

| | Controller | ISE | IAE | ITSE |
|---|---|---|---|---|
| Test 1 | PI | 3.425 | 0.2889 | 0.204 |
| | T2-FLC | 2.355 | 0.0982 | 0.1197 |
| Test 2 | PI | 0.1892 | 0.0912 | 0.01832 |
| | T2-FLC | 0.0066 | 0.0388 | 0.00139 |
| Test 3 | PI | 1.738 | 0.3162 | 0.387 |
| | T2-FLC | 0.0769 | 0.0401 | 0.0194 |

In addition to the error-based indices, dynamic performance was also assessed. As shown in Table 4, the T2-FLC controller outperformed the PI controller across all measured criteria. The settling time was reduced from 0.52 s to 0.28 s, and the overshoot was lowered from 12 % to 7 %. The steady-state error decreased significantly from 0.04 to less than 0.01. Furthermore, under a load disturbance applied at $t$ = 1.5 s, the T2-FLC restored the system stability within 0.12 s, while the PI controller required 0.26 s.

Table 4

Dynamic performance comparison between PI and T2-FLC

| Performance metrics | PI | T2-FLC |
|---|---|---|
| Settling time, s | 0.52 | 0.28 |
| Overshoot, % | 12 % | 7 % |
| Steady-state error | 0.04 | <0.01 |
| Recovery time after disturbance, s | 0.26 | 0.12 |

The results consistently demonstrate the superiority, robustness, and adaptability of the proposed control approach. T2-FLC provides improved tracking accuracy, reduced torque ripple, and better disturbance rejection under both external and internal perturbations. These findings confirm that T2-FLC is a reliable and promising

control solution for DSPMSMs, especially in demanding industrial and traction applications.

In the first test, both motors were subjected to a trapezoidal speed profile with a 20 N·m load torque applied. The results in Fig. 8, 9 highlight the superior performance of T2-FLC controller. T2-FLC shown exceptional speed tracking capabilities, efficiently transitioning between positive and negative speed values. Notably, transient speed oscillations were significantly reduced, emphasizing its improved dynamic response compared to the standard PI controller.

The second test assessed the system's response to varying load torque. As seen in Fig. 10, T2-FLC controller consistently maintained precise speed regulation even under fluctuating load conditions, showcasing its robust disturbance rejection capabilities. In contrast, PI controller exhibited greater speed deviations, indicating its inferior ability to reject disturbances. Analysis of torque waveforms (Fig. 11) demonstrated that T2-FLC effectively minimized torque pulsations, a critical factor for the precise control of PMSM. Additionally, the stator current locus plot (Fig. 12) showed that T2-FLC maintained a cleaner and more consistent response, even in the presence of load variations.

The final test evaluated the performance of both controllers under parametric uncertainties, specifically a 100 % increase in stator resistance. PI controller exhibited sensitivity to these disturbances, with noticeable deviations in the system's responses. In contrast, T2-FLC controller displayed resilience and maintained stable performance, highlighting its robustness against internal parameter mismatches.

Overall, the results from these tests suggest that the proposed T2-FLC controller offers significant advantages over the conventional PI controller, particularly in terms of dynamic response, disturbance rejection, and robustness. T2-FLC controller demonstrated precise speed control, reduced torque pulsations, and consistent performance under varying load conditions and internal disturbances. This highlights the potential of T2-FLC to enhance the efficiency and robustness of DSPMSMs in practical applications. While T2-FLC controller shows considerable promise, it is important to acknowledge certain limitations, such as the increased computational complexity. Future work could focus on optimizing the controller for real-time applications, with a particular emphasis on reducing computational overhead and ensuring real-time performance. Additionally, experimental validation in practical settings is essential to confirm the simulation results and further refine the controller for industrial applications.

**Conclusions.** In this study, an intelligent DTC strategy based on T2-FLC was proposed for the speed regulation of two parallel-connected DSPMSMs powered by a single six-phase inverter. By replacing the conventional PI controller with T2-FLC, the proposed control approach aims to enhance dynamic performance, robustness, and precision in multi-machine drive systems.

Simulation results confirmed that T2-FLC significantly improves tracking accuracy, reduces torque and flux ripples, and enhances the system's ability to reject external disturbances and withstand internal parameter variations. Compared to the conventional PI-based DTC, the proposed method consistently delivered superior dynamic response, better stability, and greater resilience to uncertainties.

These findings demonstrate the potential of T2-FLC-based DTC as a robust and efficient control solution for complex multi-machine architectures, particularly in high-performance applications such as electric traction, marine propulsion, and industrial automation.

Future work will focus on the real-time implementation of the proposed controller and its experimental validation on a physical test bench to further assess its practical applicability and performance in real-world environments. This step is essential to confirm the simulation outcomes and to verify the robustness of T2-FLC under actual operating conditions.

**Conflict of interest**. The authors declare that they have no conflicts of interest.

REFERENCES


***1.*** Barrero F., Duran M.J. Recent Advances in the Design, Modeling, and Control of Multiphase Machines—Part I. *IEEE Transactions on Industrial Electronics*, 2016, vol. 63, no. 1, pp. 449-458. doi: https://doi.org/10.1109/TIE.2015.2447733.

***2.*** Jones M., Vukosavic S.N., Levi E. Parallel-Connected Multiphase Multidrive Systems With Single Inverter Supply. *IEEE Transactions on Industrial Electronics*, 2009, vol. 56, no. 6, pp. 2047-2057. doi: https://doi.org/10.1109/TIE.2009.2017219.

***3.*** Parsa L. On advantages of multi-phase machines. *31st Annual Conference of IEEE Industrial Electronics Society, 2005. IECON 2005*, 6 p. doi: https://doi.org/10.1109/IECON.2005.1569139.

***4.*** Demir Y., Aydin M. A Novel Dual Three-Phase Permanent Magnet Synchronous Motor With Asymmetric Stator Winding. *IEEE Transactions on Magnetics*, 2016, vol. 52, no. 7, pp. 1-5. doi: https://doi.org/10.1109/TMAG.2016.2524027.

***5.*** Kozovsky M., Blaha P. Double three-phase PMSM structures for fail operational control. *IFAC-PapersOnLine*, 2019, vol. 52, no. 27, pp. 1-6. doi: https://doi.org/10.1016/j.ifacol.2019.12.733.

***6.*** Vu D.T., Nguyen N.K., Semail E., Nguyen T.T.N. Current Harmonic Eliminations for Seven-Phase Non-sinusoidal PMSM Drives applying Artificial Neurons. *Lecture Notes in Networks and Systems*, 2021, vol. 178, pp. 270–279. doi: https://doi.org/10.1007/978-3-030-64719-3_31.

***7.*** Nguyen N.L., Fadel M., Llor A. A new approach to Predictive Torque Control with Dual Parallel PMSM system. *2013 IEEE International Conference on Industrial Technology (ICIT)*, 2013, pp. 1806-1811. doi: https://doi.org/10.1109/ICIT.2013.6505950.

***8.*** Wang X., Yan H., Sala G., Buticchi G., Gu C., Zhao W., Xu L., Zhang H. Selective Torque Harmonic Elimination for Dual Three-Phase PMSMs Based on PWM Carrier Phase Shift. *IEEE Transactions on Power Electronics*, 2020, vol. 35, no. 12, pp. 13255-13269. doi: https://doi.org/10.1109/TPEL.2020.2991264.

***9.*** Anka Rao M., Vijayakumar M., Kumar N.P. Speed control of parallel connected DSIM fed by six phase inverter with IFOC strategy using ANFIS. *International Journal of Research and Engineering*, 2017, vol. 4, no. 9, pp. 244-249.

***10.*** Lee Y., Ha J.-I. Control Method for Mono Inverter Dual Parallel Surface-Mounted Permanent-Magnet Synchronous Machine Drive System. *IEEE Transactions on Industrial Electronics*, 2015, vol. 62, no. 10, pp. 6096-6107. doi: https://doi.org/10.1109/TIE.2015.2420634.

***11.*** Ramachandran G., Veerana S., Padmanaban S. Vector control of a three-phase parallel connected two motor single inverter speed sensorless drive. *Turkish Journal of Electrical Engineering & Computer Sciences*, 2016, vol. 24, pp. 4027-4041. doi: https://doi.org/10.3906/elk-1410-48.

***12.*** Wang Z., Wang X., Cao J., Cheng M., Hu Y. Direct Torque Control of T-NPC Inverters-Fed Double-Stator-Winding PMSM Drives With SVM. *IEEE Transactions on Power Electronics*, 2018, vol. 33, no. 2, pp. 1541-1553. doi: https://doi.org/10.1109/TPEL.2017.2689008.

***13.*** Kamel T., Abdelkader D., Said B., Padmanaban S., Iqbal A. Extended Kalman Filter Based Sliding Mode Control of Parallel-Connected Two Five-Phase PMSM Drive System. *Electronics*, 2018, vol. 7, no. 2, art. no. 14. doi: https://doi.org/10.3390/electronics7020014.

***14.*** Laggoun L., Kiyyour B., Boukhalfa G., Belkacem S., Benaggoune S. Direct Torque Control Using Fuzzy Second Order Sliding Mode Speed Regulator of Double Star Permanent Magnet Synchronous Machine. *Lecture Notes in Electrical Engineering*, 2021, vol. 682, pp. 139-153. doi: https://doi.org/10.1007/978-981-15-6403-1_10.
***15.*** Tir Z., Malik O.P., Eltamaly A.M. Fuzzy logic based speed control of indirect field oriented controlled double star induction motors connected in parallel to a single six-phase inverter supply. *Electric Power Systems Research*, 2016, vol. 134, pp. 126-133. doi: https://doi.org/10.1016/j.epsr.2016.01.013.
***16.*** Bounab A., Chaiba A., Belkacem S. Evaluation of the High Performance Indirect Field Oriented Controlled Dual Induction Motor Drive Fed by a Single Inverter using Type-2 Fuzzy Logic Control. *Engineering, Technology & Applied Science Research*, 2020, vol. 10, no. 5, pp. 6301-6308. doi: https://doi.org/10.48084/etasr.3799.
***17.*** Liang Q., Mendel J.M. Interval type-2 fuzzy logic systems: theory and design. *IEEE Transactions on Fuzzy Systems*, 2000, vol. 8, no. 5, pp. 535-550. doi: https://doi.org/10.1109/91.873577.
***18.*** Mehedi F., Yahdou A., Djilali A., Benbouhenni H. Direct Torque Fuzzy Controlled Drive for Multi-phase IPMSM Based on SVM Technique. *Journal Europeen des Systemes Automatises*, 2020, vol. 53, no. 2, pp. 259-266. doi: https://doi.org/10.18280/jesa.530213.
***19.*** Mehedi F., Nezli L., Mahmoudi M.O.H., Taleb R., Boudana D. Fuzzy logic based vector control of multi-phase permanent magnet synchronous motors. *Journal of Renewable Energies*, 2023, vol. 22, no. 1, pp. 161-170. doi: https://doi.org/10.54966/jreen.v22i1.734.
***20.*** Bai Y., Wang D. On the Comparison of Type 1 and Interval Type 2 Fuzzy Logic Controllers Used in a Laser Tracking System. *IFAC-PapersOnLine*, 2018, vol. 51, no. 11, pp. 1548-1553. doi: https://doi.org/10.1016/j.ifacol.2018.08.276.
***21.*** Karnik N.N., Mendel J.M. Operations on type-2 fuzzy sets. *Fuzzy Sets and Systems*, 2001, vol. 122, no. 2, pp. 327-348. doi: https://doi.org/10.1016/S0165-0114(00)00079-8.
***22.*** Sedaghati A., Pariz N., Siahi M., Barzamini R. A new fractional-order developed type-2 fuzzy control for a class of nonlinear systems. *International Journal of Systems Science*, 2023, vol. 54, no. 15, pp. 2840-2858. doi: https://doi.org/10.1080/00207721.2020.1867927.
***23.*** Fouad B., Ali C., Samir Z., Salah S. Direct Torque Control of Induction Motor Fed by Three-level Inverter Using Fuzzy Logic. *Advances in Modelling and Analysis C*, 2017, vol. 72, no. 4, pp. 248-265. doi: https://doi.org/10.18280/ama_c.720404.
***24.*** Venkataramana Naik N., Panda A., Singh S.P. A Three-Level Fuzzy-2 DTC of Induction Motor Drive Using SVPWM. *IEEE Transactions on Industrial Electronics*, 2016, vol. 63, no. 3, pp. 1467-1479. doi: https://doi.org/10.1109/TIE.2015.2504551.
***25.*** Kamalapur G., Aspalli M.S. Direct torque control and dynamic performance of induction motor using fractional order fuzzy logic controller. *International Journal of Electrical and Computer Engineering*, 2023, vol. 13, no. 4, pp. 3805-3816. doi: https://doi.org/10.11591/ijece.v13i4.pp3805-3816.
***26.*** Moussaoui L. Performance enhancement of direct torque control induction motor drive using space vector modulation strategy. *Electrical Engineering & Electromechanics*, 2022, no. 1, pp. 29-37. doi: https://doi.org/10.20998/2074-272X.2022.1.04.
***27.*** Lokriti A., Zidani Y., Doubabi S. Fuzzy logic control contribution to the direct torque and flux control of an induction machine. *2011 International Conference on Multimedia Computing and Systems*, 2011, pp. 1-6. doi: https://doi.org/10.1109/ICMCS.2011.5945645.
***28.*** Boudana D., Nezli L., Tlemçani A., Mahmoudi M., Tadjine M. Robust DTC Based on Adaptive Fuzzy Control of Double Star Synchronous Machine Drive with Fixed Switching Frequency. *Journal of Electrical Engineering*, 2012, vol. 63, no. 3, pp. 133-143. doi: https://doi.org/10.2478/v10187-012-0021-y.
***29.*** Hannan M.A., Ghani Z.A., Mohamed A., Uddin M.N. Real-time testing of a fuzzy logic controller based grid-connected photovoltaic inverter system. *2014 IEEE Industry Application Society Annual Meeting*, 2014, pp. 1-8. doi: https://doi.org/10.1109/IAS.2014.6978394.
***30.*** Kakouche K., Guendouz W., Rekioua T., Mezani S., Lubin T. Application of Fuzzy Controller to Minimize Torque and Flux Ripples of PMSM. *2019 International Conference on Advanced Electrical Engineering (ICAEE)*, 2019, pp. 1-6. doi: https://doi.org/10.1109/ICAEE47123.2019.9015066.
***31.*** Naas B., Nezli L., Naas B., Mahmoudi M.O., Elbar M. Direct Torque Control Based Three Level Inverter-fed Double Star Permanent Magnet Synchronous Machine. *Energy Procedia*, 2012, vol. 18, pp. 521-530. doi: https://doi.org/10.1016/j.egypro.2012.05.063.
***32.*** Guezi A., Bendaikha A., Dendouga A. Direct torque control based on second order sliding mode controller for three-level inverter-fed permanent magnet synchronous motor: comparative study. *Electrical Engineering & Electromechanics*, 2022, no. 5, pp. 10-13. doi: https://doi.org/10.20998/2074-272X.2022.5.02.
***33.*** Lallouani H., Saad B., Letfi B. DTC-SVM based on Interval Type-2 Fuzzy Logic Controller of Double Stator Induction Machine fed by Six-Phase Inverter. *International Journal of Image, Graphics and Signal Processing*, 2019, vol. 11, no. 7, pp. 48-57. doi: https://doi.org/10.5815/ijigsp.2019.07.04.
***34.*** Srinivas G., Durga Sukumar G., Subbarao M. Total harmonic distortion analysis of inverter fed induction motor drive using neuro fuzzy type-1 and neuro fuzzy type-2 controllers. *Electrical Engineering & Electromechanics*, 2024, no. 1, pp. 10-16. doi: https://doi.org/10.20998/2074-272X.2024.1.02.
***35.*** Khemis A., Boutabba T., Drid S. Model reference adaptive system speed estimator based on type-1 and type-2 fuzzy logic sensorless control of electrical vehicle with electrical differential. *Electrical Engineering & Electromechanics*, 2023, no. 4, pp. 19-25. doi: https://doi.org/10.20998/2074-272X.2023.4.03.
***36.*** Rahali H., Zeghlache S., Cherif B.D.E., Benyettou L., Djerioui A. Robust adaptive fuzzy type-2 fast terminal sliding mode control of robot manipulators in attendance of actuator faults and payload variation. *Electrical Engineering & Electromechanics*, 2025, no. 1, pp. 31-38. doi: https://doi.org/10.20998/2074-272X.2025.1.05.
***37.*** Kaddache M., Drid S., Khemis A., Rahem D., Chrifi-Alaoui L. Maximum power point tracking improvement using type-2 fuzzy controller for wind system based on the double fed induction generator. *Electrical Engineering & Electromechanics*, 2024, no. 2, pp. 61-66. doi: https://doi.org/10.20998/2074-272X.2024.2.09.
***38.*** Loukal K., Benalia L. Type-2 Fuzzy Logic Controller of a Doubly Fed Induction Machine. *Advances in Fuzzy Systems*, 2016, vol. 2016, art. no. 8273019. doi: https://doi.org/10.1155/2016/8273019.
***39.*** Rahali H., Zeghlache S., Benalia L. Adaptive Field-Oriented Control Using Supervisory Type-2 Fuzzy Control for Dual Star Induction Machine. *International Journal of Intelligent Engineering and Systems*, 2017, vol. 10, no. 4, pp. 28-40. doi: https://doi.org/10.22266/ijies2017.0831.04.

*Received 18.06.2025*
*Accepted 20.09.2025*
*Published 02.01.2026*

*A. Bounab*[1]*, PhD Student,*
*A. Chaiba*[1]*, Professor,*
*S. Belkacem*[1]*, Professor,*
*A. Chariete*[2]*, Doctor of Technical Science,*
[1] Department of Electrical Engineering,
University of Batna2, Algeria,
e-mail: bounab_alaeddine@yahoo.fr (Corresponding Author).
[2] Energy and Information Technology Hub,
University of Technology of Belfort-Montbéliard, France.

*How to cite this article:*
Bounab A., Chaiba A., Belkacem S., Chariete A. Performance improvement of parallel dual-star permanent magnet synchronous machines via type-2 fuzzy direct torque control with a single six-phase inverter. *Electrical Engineering & Electromechanics*, 2026, no. 1, pp. 28-37. doi: https://doi.org/10.20998/2074-272X.2026.1.04

UDC 681.516 https://doi.org/10.20998/2074-272X.2026.1.05

H. Mostefaoui, S. Tahraoui, M. Souaihia, R. Taleb, M. Mostefaoui

# Advanced control of twin rotor multi-input multi-output systems using seagull optimization for linear quadratic regulator tuning

***Introduction.*** *During the past decade, advanced control of complex multi-input multi-output (MIMO) systems has been a sustained focus owing to their growing use in aerospace and robotic platforms. The twin rotor MIMO system (TRMS) serves as a helicopter-like benchmark system for testing advanced control techniques. Its nonlinear behavior and significant cross-coupling render it difficult to control using traditional methods.* ***Problem.*** *The TRMS features strong nonlinear dynamics and cross-coupling effects that challenge conventional control methods. Manual tuning of control parameters often results in suboptimal performance and reduced robustness. The* ***goal*** *of this study is to optimize the linear quadratic regulator (LQR) weighting matrices Q and R for the TRMS using the seagull optimization algorithm (SOA) to improve transient performance, minimize overshoot, and accelerate stabilization in both pitch and yaw compared to classical LQR tuning.* ***Methodology****. The new approach integrates the SOA with LQR control theory. The SOA determines the best values of Q and R matrices by minimizing a cost function defined by system performance metrics. SOA-optimized LQR is evaluated through simulations and contrasted with the classical LQR under identical conditions. Population size is 50 agents with a maximum of 100 iterations to achieve convergence.* ***Results.*** *Simulation results show that the SOA-optimized LQR has a remarkable improvement in the system's time response. In comparison to the classical LQR, these results provide a shorter settling time from 7.35 s to 5.34 s (≈28 %), decreases overshoot (≈3 % vs. 30 % open loop), increases damping, and reduces oscillations. The pitch and yaw angle responses across several control schemes clearly demonstrate the superior performance of the proposed optimization technique.* ***Scientific novelty****. This work demonstrates, for the first time, the use of SOA for optimal tuning of LQR in a TRMS benchmark. It opens new avenues to enhance the performance of high-order nonlinear systems, pointing toward more accurate and stable control techniques in industrial and aerospace engineering fields.* ***Practical value****. The technique provides an efficient method to enhance the functionality of complex nonlinear systems without requiring manual tuning, and it has potential applications in the industrial and aerospace areas.* References 38, tables 3, figures 4.

*Key words:* **seagull optimization algorithm, linear quadratic regulator, twin rotor multi-input multi-output system, parameter tuning, control performance.**

***Вступ****. Протягом останнього десятиліття розширене управління складними багатовходовими та багатовихідними (MIMO) системами знаходилося в центрі уваги у зв'язку з їх зростаючим використанням в аерокосмічній техніці та робототехніці. Двороторна MIMO система (TRMS) служить еталонною системою, подібною до вертольоту, для тестування передових методів управління. Її нелінійна поведінка та значний перехресний зв'язок ускладнюють управління традиційними методами.* ***Проблема****. TRMS характеризується сильною нелінійною динамікою та ефектами перехресного зв'язку, що кидають виклик традиційним методам управління. Ручне налаштування параметрів керування часто призводить до неоптимальних характеристик та зниження надійності.* ***Метою*** *роботи є оптимізація вагових матриць Q і R лінійно-квадратичного регулятора (LQR) для TRMS з використанням алгоритму оптимізації «чайка» (SOA) для покращення перехідних характеристик, мінімізації перерегулювання та прискорення стабілізації як за висотою, так і за напрямком в порівнянні з класичним LQR налаштуванням.* ***Методика****. Новий підхід інтегрує SOA з теорією управління LQR. SOA визначає найкращі значення матриць Q і R шляхом мінімізації функції вартості, яка визначається метриками продуктивності системи. Оптимізований за допомогою SOA LQR оцінюється за допомогою моделювання та порівнюється з класичним LQR за ідентичних умов. Кількість становить 50 агентів з максимумом 100 ітерацій для досягнення збіжності.* ***Результати****. Результати моделювання показують, що оптимізований SOA LQR забезпечує значне покращення часу відгуку системи. У порівнянні з класичним LQR, ці результати забезпечують більш короткий час встановлення з 7,35 с до 5,34 с (≈28 %), зменшують перерегулювання (≈3 % порівняно з 30 % у розімкнутому контурі), збільшують демпфування і зменшують коливання. Реакції кутів за висотою та напрямком для кількох схем управління наочно демонструють високу продуктивність запропонованого методу оптимізації.* ***Наукова новизна****. У цій роботі вперше демонструється використання SOA для оптимального налаштування LQR у TRMS. Це відкриває нові можливості для підвищення продуктивності нелінійних систем високого порядку, вказуючи шлях до більш точних та стабільних методів управління в промисловій та аерокосмічній техніці.* ***Практична значимість****. Метод забезпечує ефективне підвищення функціональності складних нелінійних систем без необхідності ручного налаштування та має потенційні галузі застосування у промисловій та аерокосмічній техніці.* Бібл. 38, табл. 3, рис. 4.

*Ключові слова:* **алгоритм оптимізації «чайка», лінійний квадратичний регулятор, двороторна багатовхідна багатовихідна система, налаштування параметрів, характеристики керування.**

**Introduction.** The twin rotor multi-input multi-output (MIMO) system (TRMS) remains one of the most highly regarded benchmark platforms within the fields of control research and educational applications, as it effectively represents the challenges of real-world multivariable systems. Constructed to mirror the dynamic properties of a helicopter with two distinct rotors, the TRMS demonstrates notable inter-axis coupling, nonlinear behavior, and open-loop instability, making its control particularly challenging [1–3]. These features make the TRMS an ideal platform for designing and refining advanced control strategies, such as those applied to MIMO systems, where the complex interaction between control variables is critically important [3–5].

Traditionally, robust control methodologies have been employed to address the significant nonlinear cross-coupling inherent in the TRMS. Among these methodologies, the linear quadratic regulator (LQR) is particularly appealing due to its capacity to stabilize the system by minimizing a quadratic performance index that penalizes deviations in state variables and control efforts. Recent studies on TRMS control have confirmed the effectiveness of LQR-based strategies. Adaptive LQR approaches have exhibited superior performance relative to classical LQR and PID controllers, whereas SimMechanics-based LQR designs incorporating steady-state compensation and optimal state-feedback formulations have yielded favorable outcomes for pitch and yaw regulation [6–12].

Traditional PID control is characterized by its simplicity and robustness, rendering it appropriate for systems exhibiting relatively low levels of complexity [13, 14]. However, in the case of nonlinear and tightly coupled MIMO systems like the TRMS, intelligent methodologies are more advantageous. Neural networks [5] and fuzzy logic controllers [15, 16] are capable of addressing uncertainties and complex dynamics without the need for precise models.

Although numerous conventional control methodologies have been employed in the context of TRMS, they frequently do not adequately address its nonlinear dynamics and pronounced pitch–yaw coupling [3, 5, 17]. To enhance regulatory capabilities and robustness, contemporary research endeavors have concentrated on intelligent control methodologies. For example, a butterfly-inspired particle swarm optimization algorithm has been implemented to optimize the parameters of controllers within TRMS [18, 19], while a multi-objective genetic algorithm has contributed to the improvement of stability and tuning precision [20]. Moreover, the integration of inverse modeling with AI-driven controllers has been suggested to effectively manage intricate dynamic interactions [21]. These approaches have succeeded in advancing tracking and damping performance; however, they often fall short in the direct optimization of transient characteristics. To the best of our knowledge, this is among the first studies applying seagull optimization algorithm (SOA) to dynamically tune LQR weighting matrices for TRMS, specifically targeting multi-objective transient improvements.

To address this limitation, the current study introduces a seagull-optimized LQR controller, which is designed to enhance settling time, overshoot, and the overall stability of the system within cross-coupled nonlinear environments.

The **goal** of this study is to optimize the linear quadratic regulator (LQR) weighting matrices $Q$ and $R$ for the TRMS using the seagull optimization algorithm (SOA) to improve transient performance, minimize overshoot, and accelerate stabilization in both pitch and yaw compared to classical LQR tuning.

This paper applies the seagull optimization algorithm to automatically adjust the $Q$ and $R$ matrices of the LQR for the TRMS, with the goal of enhancing the balance between response speed and system stability. In contrast to traditional LQR or PID designs, which often necessitate significant manual tuning due to nonlinearities and intense cross-couplings, the SOA offers a self-optimizing feature that decreases the amount of tuning required. By adaptively probing the $Q$-$R$ space, the proposed technique results in superior transient performance, including faster rise time, reduced overshoot, and quicker settling when compared to both classical manual tuning methods and less adaptive optimization strategies.

**The TRMS model.** The TRMS is a laboratory platform that is widely used for teaching and research in multivariable control (Fig. 1). The mechanical design features a beam attached to a pivot that rotates about two orthogonal axes, allowing for coupled pitch and yaw movements similar to the interaction between the main and tail rotors of helicopters [3, 22]. Two DC motor-driven rotors supply the actuation: the «main» rotor primarily influences vertical (pitch) dynamics, whereas the «tail» rotor generates lateral torque for yaw control; the interaction between these channels results in significant cross-coupling, rendering the system a valuable benchmark for study [22–28]. An arm connected to the beam provides stability by balancing angular momentum. The TRMS contains multiple sensors, including incremental encoders and tachogenerators, that monitor 4 essential state variables: pitch angle, yaw angle, pitch angular velocity and yaw angular velocity [28]. Aerodynamic forces and torques are produced by adjusting the rotor speeds, which are controlled via the supply voltage to the DC motors. The system operates in three control modes [3]:

- single degree of freedom (rotors controlled independently);
- two degrees of freedom (both rotors simultaneously);
- decoupled control (cross-couplings modeled and compensated).

In every control mode, the aim is to direct the beam along a defined path, reducing transient errors in the resulting angles. The TRMS system, developed by feedback instruments limited, is an example of a high-level nonlinear system and provides a valuable platform for control studies.

Fig. 1. The general view of the TRMS [23]

Figure 2 presents a simplified diagram of the TRMS. To control TRMS two inputs are used: $u_1$ (applied to the main rotor) and $u_2$ (applied to the tail rotor). Dynamic couplings between two motors are the most important feature of the TRMS system. The position beams are measured by incremental encoders, which deliver a relative position signal [28] Therefore, whenever real-time TRMS simulation is executed, it should not be forgotten that setting the proper initial conditions is a critical issue.

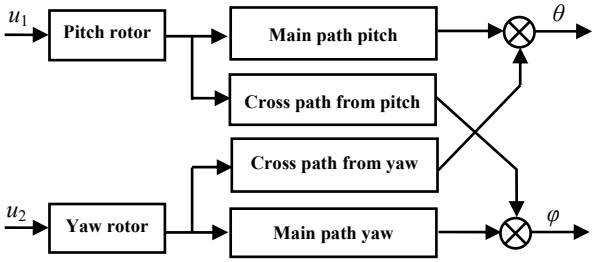


Fig. 2. Diagram of TRMS functions

**Modeling and analysis**. The modeling requires four linear models: two describing the main dynamic paths from $u_1$ to $\varphi$ (pitch) and from $u_2$ to $\theta$ (yaw) and two additional models for the cross-coupling dynamics, from $u_1$ to $\theta$ and from $u_2$ to $\varphi$.

The main rotor (pitch angle) equation is defined by:

$$I_1\ddot{\varphi} = M_1 - M_{FF} - M_{B\varphi} - M_g, \qquad (1)$$

where $I_1$ is the moment of inertia of vertical plane; $M_1$ is the gross momentum of the main rotor; $M_{FF}$ is the gravitational momentum; $M_{B\varphi}$ is the momentum due to frictional force; $M_g$ is the gyroscopic momentum.

The momentum is defined as follows:

$$M_1 = a_1\tau_1^2 + b_1\tau_1; \qquad (2) \qquad M_{FF} = M_g \sin\varphi; \qquad (3)$$

$$M_{B\varphi} = B_{1\varphi}\dot{\varphi} + B_{2\varphi}\sin(2\varphi)\dot{\varphi}^2; (4) \quad M_g = K_{gy}M_1\dot{\theta}\cos\varphi, (5)$$

where $a_1$, $b_1$ are the static characteristic of parameter; $B_{\varphi 1}$, $B_{\varphi 2}$ are the friction momentum function.

The torque $\tau_1$ generated by the main rotor is linked to the input voltage $u_1$ and is can be represented by the following transfer function:

$$\tau_1 = \frac{K_1}{T_{11}s + T_{10}}u_1, \qquad (6)$$

where $K_1$ is the gain of the main rotor; $T_{11}$, $T_{10}$ are the main rotor time constants.

In the same way, we develop the equations of the tail rotor (yaw angle), with the moment produced by the latter described by:

$$I_2\ddot{\theta} = M_2 - M_{B\theta} - M_R, \tag{7}$$

where $I_2$ is the horizontal rotor moment of inertia; $M_2$ is the tail rotor's gross momentum; $M_{B\theta}$ is the friction momentum; $M_R$ is the cross-reaction momentum:

$$M_2 = a_2\tau_2^2 + b_2\tau_2; \tag{8}$$

$$M_{B\theta} = B_{1\theta}\dot{\varphi} + B_{2\theta}\operatorname{sign}\dot{\theta}; \tag{9}$$

$$M_R = \frac{K_c(T_0 s + 1)}{T_p s + 1} M_1, \tag{10}$$

where $a_2$, $b_2$ are the static characteristic of parameters; $K_c$ is the cross-reaction momentum gain; $T_p$ is the cross-reaction parameter; $T_0$ is the cross-reaction momentum of the parameter.

The dynamic behavior of «Motor 2» is modeled in a manner analogous to that of «Motor 1» with the torque $\tau_2$ produced by the tail rotor being related to the input voltage $u_2$ and represented by the following transfer function:

$$\tau_2 = \frac{K_2}{T_{21}s + T_{20}} u_2, \tag{11}$$

where $T_{20}$, $T_{21}$ are the tail rotor time constants; $K_2$ is the tail rotor gain.

The main physical parameters of TRMS described in Table 1 play a paramount role concerning the determination of the system dynamic behavior. Besides, these parameters are very important and useful in the development of different control strategies for achieving the wanted performance of the system.

Table 1

TRMS parameters [27]

| Parameters and description | Value |
|---|---|
| $I_1$ – moment of inertia of vertical plane (pitch axis) | 0.068 kg·m$^2$ |
| $I_2$ – moment of inertia of horizontal plane (yaw axis) | 0.02 kg·m$^2$ |
| $a_1$ – static characteristic of parameter | 0.00135 |
| $b_1$ – static characteristic of parameter | 0.0924 |
| $a_2$ – static characteristic of parameter | 0.02 |
| $b_2$ – static characteristic of parameter | 0.09 |
| $M_g$ – gravity momentum | 0.32 N·m |
| $B_{\theta 1}$ – parameter of friction momentum | 0.006 N·m·s/rad |
| $B_{\theta 2}$ – parameter of friction momentum | 0.001 N·m·s$^2$/rad |
| $B_{\varphi 1}$ – parameter of friction momentum | 0.1 N·m·s/rad |
| $B_{\varphi 2}$ – parameter of friction momentum | 0.01 N·m·s$^2$/rad |
| $K_{gv}$ – parameter of gyroscopic moment | 0.05 s/rad |
| $K_1$ – motor 1 (pitch) gain | 1.1 |
| $K_2$ – motor 2 (tail) gain | 0.8 |
| $T_{11}$ – motor 1 denominator parameter | 1.1 |
| $T_{10}$ – motor 1 denominator parameter | 1 |
| $T_{21}$ – motor 2 denominator parameter | 1 |
| $T_{20}$ – motor 2 denominator parameter | 1 |
| $T_p$ – cross-reaction momentum parameter | 2 |
| $T_0$ – cross reaction momentum parameter | 3.5 |
| $K_c$ – cross-reaction momentum gain | −0.2 |

**State space representation.** The state-space representation of the TRMS describes the system behavior as a set of matrices (***A***, ***B***, ***C***, ***D***), defining how the system state varies with time in response to control inputs:

$$\begin{cases} \dot{\boldsymbol{x}}(t) = \boldsymbol{A}\cdot\boldsymbol{x}(t) + \boldsymbol{B}\cdot\boldsymbol{u}(t); \\ \boldsymbol{y}(t) = \boldsymbol{C}\cdot\boldsymbol{x}(t) + \boldsymbol{D}\cdot\boldsymbol{u}(t), \end{cases} \tag{12}$$

where $\boldsymbol{x}(t)$ is the state vector; $\boldsymbol{u}(t)$ is the control input. The matrices ***A***, ***B***, ***C***, ***D*** define the dynamics of the system. The state variables include the pitch and yaw angles together with their corresponding angular velocities. The control vector $\boldsymbol{u}(t)$ consists of the voltages applied to the main rotor (affecting pitch) and the tail rotor (affecting yaw). The output vector $\boldsymbol{y}(t)$ corresponds to the measured pitch and yaw angles [12].

The system is linearized around the equilibrium points where $\varphi$=0 and $\theta$=0, so the nonlinear components become simpler and thus the system simpler to analyze. The state vector $\boldsymbol{x}(t)$ and control input $\boldsymbol{u}(t)$ for the TRMS are delivered by:

$$\boldsymbol{x} = \begin{bmatrix} \varphi \\ \theta \\ \tau_1 \\ \tau_2 \\ M_R \\ \dot{\varphi} \\ \dot{\theta} \end{bmatrix}; \tag{13}$$

$$\boldsymbol{u} = \begin{bmatrix} u_1 \\ u_2 \end{bmatrix}. \tag{14}$$

From (5), we can describe our system as

$$\boldsymbol{A} = \begin{bmatrix} 0 & 0 & 0 & 0 & 0 & 1 & 0 \\ 0 & 0 & 0 & 0 & 0 & 0 & 1 \\ 0 & 0 & -0{,}909 & 0 & 0 & 0 & 0 \\ 0 & 0 & 0 & -1 & 0 & 0 & 0 \\ 0 & 0 & 0{,}218181 & 0 & -0{,}5 & 0 & 0 \\ -4{,}70588 & 0 & 1{,}358823 & 0 & 0 & -0{,}088235 & 0 \\ 0 & 0 & 0 & 4{,}5 & -50 & -5 & 0 \end{bmatrix};$$

$$\boldsymbol{B} = \begin{bmatrix} 0 & 0 \\ 0 & 0 \\ 1 & 0 \\ 0 & 0{,}8 \\ -0{,}35 & 0 \\ 0 & 0 \\ 0 & 0 \end{bmatrix}; \quad \boldsymbol{C} = \begin{bmatrix} 1 & 0 & 0 & 0 & 0 & 0 & 0 \\ 0 & 1 & 0 & 0 & 0 & 0 & 0 \end{bmatrix}; \quad \boldsymbol{D} = \begin{bmatrix} 0 & 0 \\ 0 & 0 \end{bmatrix}.$$

**LQR formulation.** LQR is designed to optimize a quadratic cost function, effectively balancing state regulation with control effort. This makes it particularly well-suited for intricate systems like the TRMS [9, 29]. For the TRMS, the severe cross-coupling and nonlinear dynamics require an energy efficient control approach. In the LQR problem, the cost function is usually given by:

$$J = \int_0^\infty (x^T Q x + u^T R u)\mathrm{d}t, \tag{15}$$

where ***x*** is the state vector, encompassing the pitch and yaw angles as well as their corresponding angular velocities; the vector ***u*** indicates the control inputs that are applied to the rotors; ***Q*** is the state-weighting matrix that is positive semi-definite which penalizes variations in the pitch and yaw states, in contrast ***R*** is the positive definite weighting matrix that prioritizes the reduction of control effort [11, 25, 26].

The purpose of the LQR controller is to determine an optimal state feedback gain matrix ***K***, such that the control law:

$$u(t) = -\boldsymbol{K} \cdot x(t)\,. \quad (16)$$

The matrix $\boldsymbol{K}$ results from solving the algebraic Riccati equation, which balances state regulation (minimizing deviations) and control effort (minimizing energy use). The resulting $\boldsymbol{K}$ provides optimal feedback gains that stabilize the system with high efficiency [25, 29–31].

This work applies SOA to tune the $\boldsymbol{Q}$ and $\boldsymbol{R}$ matrices of the LQR, improving stability and energy efficiency in the nonlinear TRMS. The new method assures improved control performance.

**Seagull optimization algorithm** (SOA) is a population-based metaheuristic proposed by Dhiman and Kumar in 2019 and is inspired by the migratory and predatory behaviors of seagulls [32]. Migration here refers to periodic motion of gulls while searching for rich food sources to keep their energy levels. During migration, all seagulls avoid any collision with others while updating positions in accordance with information about the best-performing individual in the population [32, 33]. This behavior motivates the seagulls to attack a target in a spiral path through the air. In SOA, migration performs global exploration, and attack performs local exploitation [33]. By integrating both behaviors, the SOA continuously updates the positions of the seagulls to identify the optimal solution. The SOA algorithm is comprised of two main phases: the migration (exploration) phase and the attack (exploitation) phase [33].

**Migration phase**. The migration behavior of the seagulls involves 3 steps:

1. Collision avoidance.
2. Moving towards the best agent.
3. Convergence towards best agent.

**Collision avoidance**. To prevent the collision with the neighboring seagulls, a variable $A$ is used to update the position of every seagull:

$$C_s = A \cdot P_s(t), \quad (17)$$

where $C_S$ is the position where the seagull will not collide with another one; $P_s(t)$ is the current position of seagull; $t$ is the iterations number; $A$ is utilized to find the new position of seagulls.

It is updated as [32, 34].

$$A = f_c - t \cdot \left(f_c / T_{\max}\right), \quad (18)$$

where $T_{\max}$ is the maximum number of iterations; $f_c$ (set to 2) is the frequency to control the variable $A$ which is linearly decreases from $f_c$ to 0.

**Movement towards the best seagull.** After avoiding collisions, the seagulls move toward the best seagull [34–38]. This behavior can be mathematically modeled as follows:

$$M_s = B - (P_{best}(t) - P_s(t)) \quad (19)$$

$$B = 2 \cdot A^2 \cdot rd, \quad (20)$$

where $M_s$ is the direction leading to the optimal location; $P_{best}(t)$ refers to the current position of the most effective search agent; $B$ is the movement behavior of the search agent, which is essential for balancing exploitation and exploration; $rd$ is the randomly generated value that falls between 0 and 1 [36].

**Convergence towards best agent.** After determining the convergence direction, the seagull move toward the best search agent [33, 38]:

$$D_s = \left| C_s + M_s \right|, \quad (21)$$

where $D_S$ is the distance between seagulls and the best search agent.

**Attacking phase**. In the second phase, after reaching a new location, seagulls execute a spiral attack on prey. This predatory behavior can be mathematically modeled as follows:

$$P(t) = D_s \, x \cdot y \cdot z + P_{best}(t), \quad (22)$$

where $P(t)$ retains the best solution; $x$, $y$, $z$ are the spiral components:

$$x = r \cdot \cos\theta\,; \quad (23) \qquad y = r \cdot \sin\theta\,; \quad (24)$$

$$z = r \cdot \theta\,; \quad (25) \qquad r = \mu \cdot e^{\theta v}, \quad (26)$$

where $r$ is the spiral radius during the seagull's motion, while $\mu$ and $v$ are the correlation constants that define the spiral shape; $\theta$ is the angle, which is a random value within the range of $[0, 2\pi]$ [35].

In the standard SOA, both $\mu$ and $v$ are set to 1. The updated position of the seagull is determined using equations (23)–(26), as illustrated:

$$P_s(t+1) = D_s \, x \cdot y \cdot z + P_{best}(t), \quad (27)$$

where $P_s(t+1)$ is the new position of the search agent.

**Results and discussions.** In this study, SOA was utilized for the TRMS. The population size was set to 50 agents, which is a balance between exploration capability and computational cost. The optimization process was allowed to perform at a maximum of 100 iterations $T_{\max}$=100, therefore providing sufficient time for convergence.

The frequency control parameter $f_c$ was set as 2, and the movement behavior parameter $A$ started at 2 and linearly decreased to 0 over iterations to reduce collisions and enhance convergence. The best position $P_{best}(t)$ was updated incrementally, improving the global best solution at each iteration $A$ random variable $rd$ uniformly generated in the range of 0 to 1 was included to maintain a balance between exploration and exploitation by introducing stochastic variability. In addition, collision avoiding mechanisms and distance calculation based on the current position of the agents and their iteration steps were implemented to ensure an optimally balanced and effective search process. As shown in Table 2, in open loop the system is rapid (rise time 0.896 s), but unstable with lengthy overshoot of 30.34 % and settling time of 65.88 s, indicating an under damped system.

Table 2

Temporal characteristics for pitch response

| Characteristic of pitch | Open loop | Classical LQR | SOA-optimized LQR |
|---|---|---|---|
| Rise time, s | 0.896 | 4.0069 | 1.2379 |
| Settling time, s | 65.88 | 7.3462 | 5.3055 |
| Overshoot, % | 30.34 | 1.3589 | 3.0618 |

With the classical LQR controller, the TRMS becomes stable with a slower rise time of 4.0069 s, settling time of 7.3462 s and smaller overshoot of 1.3589 %, showing improved damping. The performance of SOA-optimized is accomplished with the rise time of 1.2379 s, settling time of 5.3055 s and controlled overshoot of 3.0618 %, achieving a balance between speed and stability.

The TRMS in open-loop yaw (Table 3) response is very slow with a rise time of 316.18 s and a settling time of 455.89 s, indicating severe instability. The classical LQR controller enhances the performance significantly, by minimizing the rise time to 0.75 s and settling time to 6.28 s, and an overshoot of 10.72 %, which shows a minor oscillatory response. The SOA-optimized LQR further reduces these values, the rise time coming to 0.48 s and settling time coming to 2.67 s, which shows accelerated convergence. The overshoot is reduced to 9.71 %, indicating a damped response.

Table 3

Temporal characteristics for yaw response

| Characteristic of yaw | Open loop | Classical LQR | SOA-optimized LQR |
|---|---|---|---|
| Rise time, s | 316.18 | 0.75 | 0.48 |
| Settling time, s | 455.89 | 6.28 | 2.67 |
| Overshoot, % | 0 | 10.72 | 9.71 |

For pitch response, the SOA-optimized LQR decreases settling time to 5.3055 s (7.3462 s for classical LQR) with a 28 % decrease but keeps the overshoot in control at 3.0618 %. For yaw response also, the settling time decreases from 6.28 s to 2.67 s, a significant 57 % decrease, with an eased overshoot of 9.71 %.

Figures 3, 4 illustrate the pitch and yaw angle response of the system under 3 control modes: open-loop, classical LQR, and SOA-optimized LQR.

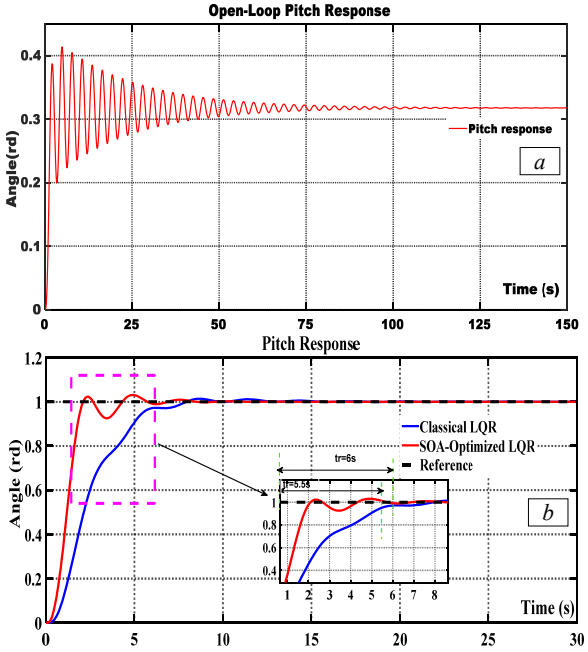


Fig. 3. Temporal characteristics of pitch responses under open loop (*a*); with LQR and SOA controller (*b*)

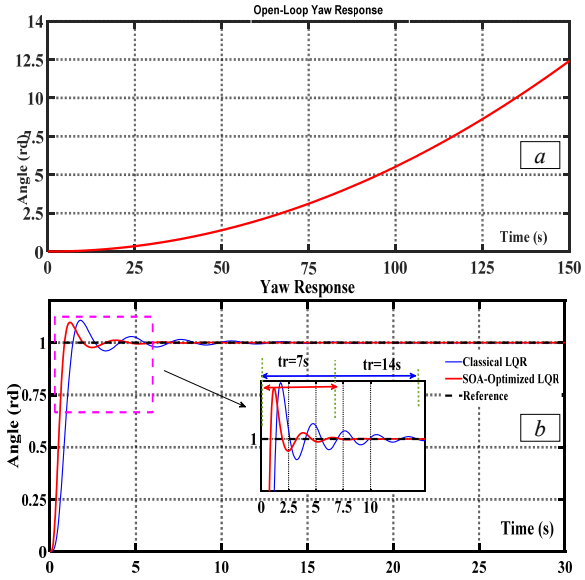


Fig. 4. Temporal characteristics of yaw responses under open loop (*a*); with LQR and SOA controller (*b*)

The SOA-optimized LQR shows significant improvement in settling time and stability compared to open-loop and standard LQR control. Although the rise time is slightly increased, the settling time and overshoot have been significantly reduced, realizing a balance speed between stability. These results validate the performance of SOA in regulating control parameters of deeply coupled complex MIMO systems as well as in dealing with nonlinearities.

**Conclusions.** Twin rotor MIMO system was effectively controlled with an SOA-optimized LQR algorithm, demonstrating improved dynamic response (pitch settling ≈28 % faster; yaw ≈57 % faster vs classical LQR) and enhanced stability compared to open-loop (overshoot ≈3 % vs 30 % open-loop pitch) and standard LQR control strategies.

This research proposed a new contribution by combining the seagull optimization algorithm with systematic parameter space exploration, adding a new reference for adaptive control of dynamic systems. The limited trade-offs observed in this study indicate potential for future progress.

Future research might focus on real-time implementation, addressing computational complexity and robustness against external disturbances, in order to enable reliable experimental applications.

**Conflict of interest.** The authors of the article declare that there is no conflict of interest.

REFERENCES


***1.*** Milovanovic M.B., Antic D.S., Milojkovic M.T., Spasic M.D. Adaptive Control of Nonlinear MIMO System With Orthogonal Endocrine Intelligent Controller. *IEEE Transactions on Cybernetics*, 2022, vol. 52, no. 2, pp. 1221-1232. doi: https://doi.org/10.1109/TCYB.2020.2998505.

***2.*** Cao C., Huang X., Cao W., Wang H., Yang Y., Xu J. MIMO Control of a Twin Rotor Aerodynamical System (TRAS). *2025 9th International Conference on Robotics, Control and Automation (ICRCA)*, 2025, pp. 265-269. doi: https://doi.org/10.1109/ICRCA64997.2025.11011049.

***3.*** Ebirim K.U., Horri N.M., Prempain E. A 2DoF Twin Rotor MIMO System for Teaching and Research. *IFAC-PapersOnLine*, 2024, vol. 58, no. 16, pp. 6-11. doi: https://doi.org/10.1016/j.ifacol.2024.08.453.

***4.*** Danh H.D., Van C.N., Van Q.V. Tracking Iterative Learning Control of TRMS using Feedback Linearization Model with Input Disturbance. *Journal of Robotics and Control (JRC)*, 2025, vol. 6, no. 1, pp. 446-455. doi: https://doi.org/10.18196/jrc.v6i1.25579.

***5.*** Han S.-Y., Zhang C.-Y. ASMAC: An Adaptive Slot Access MAC Protocol in Distributed VANET. *Electronics*, 2022, vol. 11, no. 7, art. no. 1145. doi: https://doi.org/10.3390/electronics11071145.

***6.*** Dutta L., Das D.K. Nonlinear Disturbance Observer Based Adaptive Explicit Nonlinear Model Predictive Control Design for a Class of Nonlinear MIMO System. *IEEE Transactions on Aerospace and Electronic Systems*, 2022, vol. 59, no. 2, pp. 1965-1979. doi: https://doi.org/10.1109/TAES.2022.3211252.

***7.*** Shah A.Q., Awais M., Zafar M., Ahmed A., Mudassar M., Muneer M., Saif M., Razzaq A., Jang S.-H., Kim S., Park Y. A comparative study of linear control strategies on the aerodynamics twin rotor system. *Journal of Mechanical Science and Technology*, 2023, vol. 37, no. 8, pp. 4301-4310. doi: https://doi.org/10.1007/s12206-023-0746-5.

***8.*** Bilal H., Yin B., Aslam M.S., Anjum Z., Rohra A., Wang Y. A practical study of active disturbance rejection control for rotary flexible joint robot manipulator. *Soft Computing*, 2023, vol. 27, no. 8, pp. 4987-5001. doi: https://doi.org/10.1007/s00500-023-08026-x.

***9.*** Faisal R.F., Abdulwahhab O.W. Design of an Adaptive Linear Quadratic Regulator for a Twin Rotor Aerodynamic System. *Journal of Control, Automation and Electrical Systems*, 2021, vol. 32, no. 2, pp. 404-415. doi: https://doi.org/10.1007/s40313-020-00682-w.

***10.*** Fahmizal, Nugroho H.A., Cahyadi A.I., Ardiyanto I. Twin Rotor MIMO System Control using Linear Quadratic Regulator with Simechanics. *2021 7th International Conference on Electrical, Electronics and Information Engineering (ICEEIE)*, 2021, pp. 301-306. doi: https://doi.org/10.1109/ICEEIE52663.2021.9616893.

***11.*** Ranjan K.V., Laxmi V. Design of an Optimal Controller for a Twin Rotor Mimo System (TRMS). *2022 International Conference on*

*Sustainable Computing and Data Communication Systems (ICSCDS)*, 2022, pp. 950-959. doi: https://doi.org/10.1109/ICSCDS53736.2022.9760778.
**12.** Darsouni Z., Rezgui S.E., Benalla H., Rebahi F., Boumendjel M.A.M. Ensuring service continuity in electric vehicles with vector control and linear quadratic regulator for dual star induction motors. *Electrical Engineering & Electromechanics*, 2025, no. 2, pp. 24-30. doi: https://doi.org/10.20998/2074-272X.2025.2.04.
**13.** Latreche K., Taleb R., Bentaallah A., Toubal Maamar A.E., Helaimi M., Chabni F. Design and experimental implementation of voltage control scheme using the coefficient diagram method based PID controller for two-level boost converter with photovoltaic system. *Electrical Engineering & Electromechanics*, 2024, no. 1, pp. 3-9. doi: https://doi.org/10.20998/2074-272X.2024.1.01.
**14.** Alnaib I.I., Alsammak A.N. Optimization of fractional PI controller parameters for enhanced induction motor speed control via indirect field-oriented control. *Electrical Engineering & Electromechanics*, 2025, no. 1, pp. 3-7. doi: https://doi.org/10.20998/2074-272X.2025.1.01.
**15.** Boudia A., Messalti S., Zeghlache S., Harrag A. Type-2 fuzzy logic controller-based maximum power point tracking for photovoltaic system. *Electrical Engineering & Electromechanics*, 2025, no. 1, pp. 16-22. doi: https://doi.org/10.20998/2074-272X.2025.1.03.
**16.** Khemis A., Boutabba T., Drid S. Model reference adaptive system speed estimator based on type-1 and type-2 fuzzy logic sensorless control of electrical vehicle with electrical differential. *Electrical Engineering & Electromechanics*, 2023, no. 4, pp. 19-25. doi: https://doi.org/10.20998/2074-272X.2023.4.03.
**17.** Kadri K., Boudjema F., Bouzid Y., Ouahab B., Draris H.I. A linear Active Disturbance Rejection Control based PSO to control Twin Rotor MIMO System with experimental validation. *2023 International Conference on Electrical Engineering and Advanced Technology (ICEEAT)*, 2023, pp. 1-7. doi: https://doi.org/10.1109/ICEEAT60471.2023.10425852.
**18.** Sivadasan J., Shiney J.R.J. Modified nondominated sorting genetic algorithm-based multiobjective optimization of a cross-coupled nonlinear PID controller for a Twin Rotor System. *Journal of Engineering and Applied Science*, 2023, vol. 70, no. 1, art. no. 133. doi: https://doi.org/10.1186/s44147-023-00305-6.
**19.** Cabuker A.C., Almali M.N., Parlar I. Evaluation of controller parameters on the twin rotor multiple input multiple output system using butterfly-based particle swarm optimization. *Journal of Scientific Reports-A*, 2023, no. 052, pp. 174-189. doi: https://doi.org/10.59313/jsr-a.1198441.
**20.** Çelebi B., Bilgiç B. Optimizing TRMS stability: a multi-objective genetic algorithm approach to PID controller design. *Engineering Computations*, 2025, vol. 42, no. 2, pp. 710-721. doi: https://doi.org/10.1108/EC-06-2024-0476.
**21.** Al-Talabi A., Fahad T.O., Mohammed A.A., Mary A.H. Inverse modeling, analysis and control of twin rotor aerodynamic systems with optimized artificial intelligent controllers. *PLOS One*, 2025, vol. 20, no. 5, art. no. e0322999. doi: https://doi.org/10.1371/journal.pone.0322999.
**22.** Gopmandal F., Ghosh A. LQR-based MIMO PID control of a 2-DOF helicopter system with uncertain cross-coupled gain. *IFAC-PapersOnLine*, 2022, vol. 55, no. 22, pp. 183-188. doi: https://doi.org/10.1016/j.ifacol.2023.03.031.
**23.** Aidoud M., Feliu-Batlle V., Sebbagh A., Sedraoui M. Small signal model designing and robust decentralized tilt integral derivative TID controller synthesizing for twin rotor MIMO system. *International Journal of Dynamics and Control*, 2022, vol. 10, no. 5, pp. 1657-1673. doi: https://doi.org/10.1007/s40435-022-00916-6.
**24.** Sajjad Moosapour S., Mehdipour H., Keramatzadeh M. Sliding Mode Disturbance Observer-Based Control of a Laboratory Twin Rotor Multi Input-Multi Output System. *IEEE Access*, 2025, vol. 13, pp. 394-406. doi: https://doi.org/10.1109/ACCESS.2024.3523850.
**25.** Tran A.-M.D., Vu T.V. Robust MIMO LQR Control with Integral Action for Differential Drive Robots: A Lyapunov-Cost Function Approach. *Engineering, Technology & Applied Science Research*, 2025, vol. 15, no. 4, pp. 24775-24781. doi: https://doi.org/10.48084/etasr.11583.
**26.** Dehnavi V.S., Shafiee M. LQR for Generalized Systems Using Metaheuristic Algorithms Based on Disturbance Observer. *2020 28th Iranian Conference on Electrical Engineering (ICEE)*, 2020, pp. 1-5. doi: https://doi.org/10.1109/ICEE50131.2020.9260723.
**27.** Zeghlache S., Benyettou L., Djerioui A., Ghellab M.Z. Twin Rotor MIMO System Experimental Validation of Robust Adaptive Fuzzy Control Against Wind Effects. *IEEE Systems Journal*, 2022, vol. 16, no. 1, pp. 409-419. doi: https://doi.org/10.1109/JSYST.2020.3034993.
**28.** Ezekiel D.M., Samikannu R., Matsebe O. Pitch and Yaw Angular Motions (Rotations) Control of the 1-DOF and 2-DOF TRMS: A Survey. *Archives of Computational Methods in Engineering*, 2021, vol. 28, no. 3, pp. 1449-1458. doi: https://doi.org/10.1007/s11831-020-09423-3.
**29.** Senoussaoui A., Chenafa M., Sahraoui A., Kacimi A., Houcine R. LQGi/LTR controller with integrators and feedforward controller applied to a Twin Rotor MIMO System. *Przeglad Elektrotechniczny*, 2021, vol. 97, no. 4, pp. 48-53. doi: https://doi.org/10.15199/48.2021.04.08.
**30.** Faisal R.F., Abdulwahhab O.W. Design of an Adaptive Linear Quadratic Regulator for a Twin Rotor Aerodynamic System. *Journal of Control, Automation and Electrical Systems*, 2021, vol. 32, no. 2, pp. 404-415. doi: https://doi.org/10.1007/s40313-020-00682-w.
**31.** Nekrouf S., Chekroun S. Optimal controller design for a birotor helicopter. *Przegląd Elektrotechniczny*, 2021, vol. 97, no. 11, pp. 93-96. doi: https://doi.org/10.15199/48.2021.11.16.
**32.** Kumar V., Kumar D., Kaur M., Singh D., Idris S.A., Alshazly H. A Novel Binary Seagull Optimizer and its Application to Feature Selection Problem. *IEEE Access*, 2021, vol. 9, pp. 103481-103496. doi: https://doi.org/10.1109/ACCESS.2021.3098642.
**33.** Jiang H., Yang Y., Ping W., Dong Y. A Novel Hybrid Classification Method Based on the Opposition-Based Seagull Optimization Algorithm. *IEEE Access*, 2020, vol. 8, pp. 100778-100790. doi: https://doi.org/10.1109/ACCESS.2020.2997791.
**34.** Hanif M., Mohammad N., Biswas K., Harun B. Seagull Optimization Algorithm for Solving Economic Load Dispatch Problem. *2023 International Conference on Electrical, Computer and Communication Engineering (ECCE)*, 2023, pp. 1-6. doi: https://doi.org/10.1109/ECCE57851.2023.10101516.
**35.** Hou P., Liu J., Ni F., Zhang L. Hybrid Strategies Based Seagull Optimization Algorithm for Solving Engineering Design Problems. *International Journal of Computational Intelligence Systems*, 2024, vol. 17, no. 1, art. no. 62. doi: https://doi.org/10.1007/s44196-024-00439-2.
**36.** Ragab M., Alshehri S., Alhakamy N.A., Alsaggaf W., Alhadrami H.A., Alyami J. Machine Learning with Quantum Seagull Optimization Model for COVID-19 Chest X-Ray Image Classification. *Journal of Healthcare Engineering*, 2022, vol. 2022, art. no. 6074538. doi: https://doi.org/10.1155/2022/6074538.
**37.** Wang J., Li Y., Hu G. Hybrid seagull optimization algorithm and its engineering application integrating Yin–Yang Pair idea. *Engineering with Computers*, 2022, vol. 38, no. 3, pp. 2821-2857. doi: https://doi.org/10.1007/s00366-021-01508-2.
**38.** Aribowo W., Muslim S., Achmad F., Hermawan A.C. Improving Neural Network Based on Seagull Optimization Algorithm for Controlling DC Motor. *Jurnal Elektronika Dan Telekomunikasi*, 2021, vol. 21, no. 1, pp. 48-54. doi: https://doi.org/10.14203/jet.v21.48-54.

*Received 16.07.2025*
*Accepted 07.09.2025*
*Published 02.01.2026*

*H. Mostefaoui*[1], *Doctor of Electrical Engineering,*
*S. Tahraoui*[1], *Doctor of Electrical Engineering, Associate Professor,*
*M. Souaihia*[2], *Doctor of Electrical Engineering,*
*R. Taleb*[2], *Full Professor,*
*M. Mostefaoui*[2], *Doctor, Associate Professor,*
[1] Electrical Engineering Department, 2SAIL Laboratory,
Hassiba Benbouali University, Algeria,
e-mail: h.mostefaoui@univ-chlef.dz (Corresponding Author);
s.tahraoui@univ-chlef.dz
[2] Electrical Engineering Department,
Laboratoire Génie Electrique et Energies Renouvelables (LGEER),
Hassiba Benbouali University, Algeria,
e-mail: m.souaihia@univ-chlef.dz; r.taleb@univ-chlef.dz;
m.mostefaoui@univ-chlef.dz

*How to cite this article:*
Mostefaoui H., Tahraoui S., Souaihia M., Taleb R., Mostefaoui M. Advanced control of twin rotor multi-input multi-output systems using seagull optimization for linear quadratic regulator tuning. *Electrical Engineering & Electromechanics*, 2026, no. 1, pp. 38-43. doi: https://doi.org/10.20998/2074-272X.2026.1.05

UDC 681.516 https://doi.org/10.20998/2074-272X.2026.1.06

Q.B. Nguyen, X.C. Nguyen

# Finite-time robust position tracking control for DC motors under uncertain dynamics

***Introduction.*** *This study proposes a finite-time robust control law for position tracking of a DC motor under conditions of model uncertainty and external disturbances. The motor operates through a pulse-width modulation (PWM) unit and an H-bridge power circuit, aiming to achieve finite-time position tracking while minimizing the effects of model uncertainties and external disturbances.* ***Problem.*** *The main challenge lies in achieving accurate and rapid position and speed regulation for the DC motor while maintaining high performance, despite model inaccuracies and external disturbances. The* ***goal*** *of this paper is to design a robust finite-time position tracking control law for a DC motor based on the differential geometric approach, ensuring high tracking accuracy and control efficiency in the presence of disturbances and parameter uncertainties.* ***Scientific novelty.*** *The integration of finite-time control based on a virtual system, diffeomorphism transformation, and disturbance compensation introduces an innovative solution for DC motor position tracking under incomplete modeling and external perturbations.* ***Methodology.*** *The study employs the differential geometric method to construct a virtual system with finite-time characteristics and uses Lyapunov theory to prove global stability in the presence of uncertainties and disturbances. A finite-time virtual system is proposed after analyzing the incomplete dynamic model of the DC motor.* ***Results.*** *To validate the proposed approach, MATLAB simulations were conducted and compared with a conventional sliding mode controller. The results demonstrate improved settling time and robustness of the proposed method in DC motor position tracking. The findings confirm that the proposed controller provides intuitive and precise control, accurate position tracking, and enhanced performance regulation. It also exhibits strong robustness against model uncertainties and external disturbances. The* ***practical value*** *of the proposed method is considerable, as it offers a reliable and efficient position control scheme for DC motors using PWM. The method ensures precise position control and robust performance under varying conditions and external interferences, making it well-suited for real-world DC motor control applications.* References 23, tables 1, figures 12.

*Key words:* **DC motor, finite-time control, sliding mode control, diffeomorphism transformation, differential geometric method.**

***Вступ***. *У дослідженні пропонується робастний закон керування зі скінченним часом для відстеження положення двигуна постійного струму в умовах невизначеності моделі та зовнішніх збурень. Двигун працює через блок широтно-імпульсної модуляції (PWM) та схему живлення Н-подібного моста, метою чого є досягнення відстеження положення зі скінченним часом, мінімізуючи вплив невизначеностей моделі та зовнішніх збурень.* ***Проблема***. *Основна проблема полягає в досягненні точного та швидкого регулювання положення та швидкості двигуна постійного струму, зберігаючи при цьому високу продуктивність, незважаючи на неточності моделі та зовнішні збурення.* ***Метою*** *роботи є розробка робастного закону керування відстеженням положення двигуна постійного струму зі скінченним часом на основі диференціально-геометричного підходу, що забезпечує високу точність відстеження та ефективність керування за наявності збурень та невизначеностей параметрів.* ***Наукова новизна***. *Інтеграція керування зі скінченним часом на основі віртуальної системи, перетворення дифеоморфізму та компенсації збурень пропонує інноваційне рішення для відстеження положення двигуна постійного струму за неповного моделювання та зовнішніх збурень.* ***Методологія***. *У дослідженні використовується диференціально-геометричний метод для побудови віртуальної системи з характеристиками зі скінченним часом та теорія Ляпунова для доведення глобальної стійкості за наявності невизначеностей та збурень. Після аналізу неповної динамічної моделі двигуна постійного струму запропоновано віртуальну систему зі скінченним часом.* ***Результати***. *Для перевірки запропонованого підходу було проведено моделювання в MATLAB та порівняно зі звичайним контролером ковзного режиму. Результати демонструють покращений час встановлення та стійкість запропонованого методу відстеження положення двигуна постійного струму. Отримані дані підтверджують, що запропонований контролер забезпечує інтуїтивно зрозуміле та точне керування, точне відстеження положення та покращене регулювання продуктивності. Він також демонструє високу стійкість до невизначеностей моделі та зовнішніх збурень.* ***Практична значимість*** *запропонованого методу є значною, оскільки він пропонує надійну та ефективну схему керування положенням для двигунів постійного струму з використанням PWM. Метод забезпечує точне керування положенням та стійку роботу за різних умов та зовнішніх перешкод, що робить його добре придатним для реальних застосувань керування двигунами постійного струму.* Бібл. 23, табл. 1, рис. 12.

*Ключові слова:* **двигун постійного струму, кінцеве керування, ковзний режим керування, дифеоморфне перетворення, диференціально-геометричний метод.**

**Introduction.** A DC motor has been widely applied in various fields such as robotics, servo systems, biomedical devices, and embedded systems due to its simple structure, ease of control, and low cost [1, 2]. However, achieving precise control of DC motors remains a significant challenge because of their strong nonlinear characteristics, parameter uncertainties (such as friction, inductance, and back electromotive force), and external disturbances including load variations or dead zones [3]. In particular, for small-scale DC motors driven by pulse-width modulation (PWM), direct measurement of the armature current is often difficult, which highlights the need for developing control strategies based on incomplete or uncertain models [4].

Over the past decades, numerous control approaches have been proposed to improve the trajectory-tracking performance of DC motors. However, the conventional PID control method cannot accurately capture the dynamic variations of motor excitation [4, 5]. Consequently, with the growing interest in nonlinear systems, a wide range of control theories and techniques related to nonlinear dynamics have been employed to address DC motor drive control problems, such as backstepping control [3], sliding mode control (SMC) [6, 7], adaptive control [8, 9], fuzzy control [2, 10], neural network-based control [11], and robust control [12]. In studies [13–15], several optimization-based methods were proposed for tuning controller parameters using nature-inspired optimization algorithms, aiming to minimize steady-state error and shorten the transient response. However, these studies did not consider the finite-time response of the system and were limited to ensuring only asymptotic stability.

The finite-time control technique [16–19] offers significant advantages, including rapid response,

predefined convergence time, and strong robustness against disturbances. The application of finite-time control in tracking problems has yielded remarkable results. In many practical cases, DC motors require real-time control, and the system must achieve stability within a short period. Therefore, employing finite-time control techniques for DC motors under disturbances and model uncertainties has attracted considerable attention from researchers seeking to enhance control performance. In [16], a controller was developed to ensure that the transient motion process is almost completed within a predetermined finite time, after which the desired trajectory is tracked with a specified precision. In [17], a novel finite-time disturbance observer was proposed for trajectory tracking of DC motors with model uncertainties and exogenous disturbances. The application of finite-time control has also produced impressive results in electromechanical systems with DC motor actuators, as reported in [18, 19]. Furthermore, studies [20–23] have introduced an approach to control law design based on the diffeomorphic control method. This method utilizes geometric transformations to map the actual system into a simplified virtual system, enabling the design of a control law that ensures the real system states are embedded into a desired invariant manifold [20]. The main advantage of diffeomorphic control lies in its flexible design framework, which can be readily extended to various nonlinear systems, allowing the designer to specify desired manifold properties directly.

**Purpose and objectives of the article**. This paper proposes a synthesis technique for a finite-time robust control law based on geometric control theory. The approach involves constructing a virtual system with both asymptotic and finite-time stability properties and establishing a diffeomorphic transformation between the real and virtual systems to derive the control law. The proposed control law ensures the equivalence of dynamic properties between the real and virtual systems, meaning that the real system also achieves finite-time stability. To guarantee the robustness of the control system under model uncertainties and external disturbances, a disturbance compensation component is incorporated. A Lyapunov-based stability analysis is then carried out to rigorously prove the global finite-time robust stability of the overall system.

**1. System description and modeling.**

**1.1. Experimental setup and operating principle.** The study of the motor control algorithm was conducted on an experimental system. Figure 1 illustrates the connection diagram of the motor control model based on a microcontroller platform. The experimental setup for DC motor position control was developed in the Control Systems Laboratory at Le Quy Don Technical University and serves as the research object.

The nominal parameters of the motor were approximately determined through measurements and the manufacturer's datasheet. The YFROBOT Metal Gearmotor GA25 operates at a 12 V DC supply and is equipped with a 34:1 gearbox, which increases torque while reducing rotational speed. Additionally, a Hall-effect encoder is directly mounted on the motor shaft to provide position feedback.

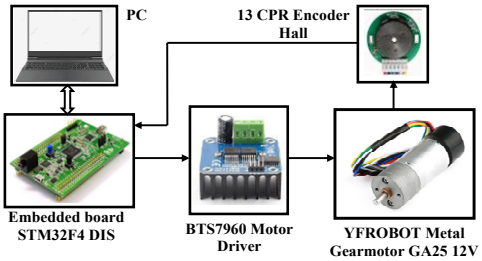

Fig. 1. Block diagram of the experimental DC motor control setup

The embedded controller is implemented on an STM32F411 microcontroller. The microcontroller acquires the motor shaft's angular position through a 13-CPR Hall-effect encoder, whose signals are read via the built-in external interrupt interface. The rotational speed of the motor shaft and the control algorithm are executed within the embedded software. The control signal is generated in the form of PWM using the microcontroller's internal timer and transmitted via GPIO to the BTS7960 motor driver module, enabling the motor to rotate precisely to the desired position.

**1.2. Nonlinear mathematical model of the DC motor.** The schematic diagram of the DC motor is shown in Fig. 2, where $R$ is the armature resistance, $L$ is the armature inductance, $v$ is the applied voltage, $i$ is the armature current, $e$ is the back electromotive force (back EMF), $J_M = J + \Delta J$ is the load moment of inertia, $J$ is the nominal inertia, $\Delta J$ represents its bounded variation, $B$ is the viscous friction coefficient, $\tau$ is the electromagnetic torque generated by the motor, $\theta$ is the angular position, and $\omega$ the angular velocity of the motor shaft.

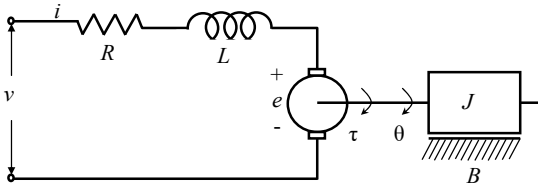

Fig. 2. Model of the permanent magnet DC motor system

The dynamic equations of the DC motor, according to [4], are expressed as

$$\begin{cases} \dfrac{\mathrm{d}\theta(t)}{\mathrm{d}t} = \omega(t); \\ L\dfrac{\mathrm{d}i(t)}{\mathrm{d}t} = v(t) - Ri(t) - k_w\omega(t); \\ J\dfrac{\mathrm{d}\omega(t)}{\mathrm{d}t} = k_i i(t) - B\omega(t) - C\,\mathrm{sgn}(\omega) + d_1(t), \end{cases} \quad (1)$$

where $k_w$ is the back EMF constant; $k_i$ is the motor torque constant, $C$ is the static friction of the motor. The disturbance term $d_1(t)$ accounts for external disturbance torques and model uncertainties (for example, inertia variations $\Delta J$).

For small-scale DC motors, the control method typically employs PWM signals applied to an H-bridge circuit, which makes accurate and efficient current measurement highly complex. The electrical time constant ($L/R$) is typically much smaller than the mechanical time constant ($J/B$). Therefore, the current dynamics reach steady state much faster than the mechanical dynamics. This allows the armature current $i$ to be considered nearly steady, meaning that $i \approx v/R$.

Nevertheless, when operating in high-frequency or large-angle regimes, the inductance $L$ can influence the transient response, and this approximation may require further validation through experimental comparison. Let the state variables be defined as $\theta=x_1$, $\omega=x_2$ and $v=u$. The dynamic model of the DC motor can be rewritten in the following form [5, 8, 10]:

$$\begin{cases} \dot{x}_1 = x_2; \\ \dot{x}_2 = -\dfrac{B}{J}x_2 - \dfrac{C}{J}\operatorname{sgn}(x_2) + \dfrac{k_i}{JR}u + d(t), \end{cases} \quad (2)$$

where $d(t)$ represents both the electrical model uncertainties and the disturbance term $d_1(t)$.

**Assumption 1**. The disturbance term $d(t)$ is bounded within the interval $(-D, D)$, where $D$ is a positive constant.

In this study, the DC motor is coupled to the load through a gearbox with minimal backlash. The stiffness of the coupling and the gearbox is assumed to be sufficiently high, allowing the elastic effects to be neglected. Therefore, the system can be reasonably modeled as a single-mass electromechanical system rather than a two-mass one. The control objective is to design a finite-time robust position-tracking controller for the DC motor to follow a given reference trajectory $x_{sp}(t)$, based on the incomplete mathematical model (2) in the presence of the disturbance $d(t)$.

**2. Synthesis of a finite-time robust position-tracking control law (RFTC) for the DC motor.**

**2.1. Fundamentals of finite-time control theory.**

Consider a nonlinear system that can be described as follows:

$$\dot{\boldsymbol{x}}(t) = f(\boldsymbol{x}(t), \boldsymbol{u}),\ \boldsymbol{x}(0) = \boldsymbol{x}_0\,, \quad (3)$$

where $x \in R_n$ is the state vector of the system; $f(0)=0$. The function $f(\boldsymbol{x})$ is the continuous nonlinear function defined in an open neighborhood around the origin.

**Definition 1** [23]. Given an initial time $t_0$, a positive constant $T$, and two state sets $\boldsymbol{X}_0$ and $\boldsymbol{X}_t$, system (3) is said to be finite-time stable with respect to ($t_0$, $T$, $\boldsymbol{X}_0$, $\boldsymbol{X}_t$) if

$$\boldsymbol{x}_0 \in \boldsymbol{X}_0 \Rightarrow \boldsymbol{x}(t) = \boldsymbol{X}_t, \quad t \in [t_0, t_0 + T], \quad (4)$$

where $\boldsymbol{x}(t)$ denotes the solution of (3) starting from the initial state $\boldsymbol{x}_0$ at time $t_0$.

**Lemma 1** [20]. Assume there exists a continuously differentiable function $V(\boldsymbol{x}) \in C^1$, defined in a neighborhood $U \subset R^n$ of the origin, and real constants $c>0$ and $0<\alpha<1$ such that:

1) $V(\boldsymbol{x})$ is positive definite on $U$;

2) $\dot{V}(\boldsymbol{x}) + cV^{\alpha}(\boldsymbol{x}) \le 0, \quad \forall \boldsymbol{x} \in U$ .

Then, the origin of the system is finite-time stable. The settling time depends on the initial state $\boldsymbol{x}_0$ and satisfies

$$T_x(\boldsymbol{x}_0) \le \frac{V^{1-\alpha}(\boldsymbol{x}_0)}{k(1-\alpha)} \quad (5)$$

for all $\boldsymbol{x}_0$ within some open neighborhood of the origin. If $U=R^n$ and $V(\boldsymbol{x})$ is radially unbounded (i.e., $V(\boldsymbol{x}) \to +\infty$ as $\boldsymbol{x} \to +\infty$), then system (4) is globally finite-time stable at the origin of the coordinate system.

**Lemma 2.** Consider the strict-feedback system given by

$$\begin{cases} \dot{z}_1 = z_2; \\ \dot{z}_2 = -\lambda \operatorname{sgn}(c_1 z_1 + z_2)\left|c_1 z_1 + z_2\right|^{2\beta-1} + c_1 v_1 \dfrac{z_1}{\sqrt{z_1^2 + \varepsilon^2}} - c_1 z_2, \end{cases} \quad (6)$$

where $v_1>0$, $\varepsilon>0$, $\lambda>0$, $\beta \in (0.5, 1)$, $c_1>0$. Then, system (6) is globally finite-time stable.

**Proof.** Consider the Lyapunov function

$$V_f = 0.5 s^2 = 0.5(c_1 z_1 + z_2)^2\,. \quad (7)$$

Taking the time derivative yields

$$\dot{V}_f = (c_1 z_1 + z_2)(c_1 \dot{z}_1 + \dot{z}_2) =$$

$$= (c_1 z_1 + z_2)\left( -\lambda \operatorname{sgn}(c_1 z_1 + z_2)\left|c_1 z_1 + z_2\right|^{2\beta-1} \right) = -\lambda |s|^{2\beta}.$$

From this, we obtain:

$$\dot{V}_f + 2^{\beta} \lambda V_f{}^{\beta} \le 0\,. \quad (8)$$

From **Lemma 1**, it follows that the virtual system (6) is globally finite-time stable, which guarantees that system (6) evolves on the manifold $s=0$. Next, it is necessary to show that the motion on the manifold $s=0$ drives the system (6) states to the origin $z_1=0$.

With $s=0$, we have

$$z_2 = -c_1 z_1\,. \quad (9)$$

Substituting this into (6) gives

$$\dot{z}_1 = -v_1 \frac{z_1}{\sqrt{z_1^2 + \varepsilon^2}} - c_1 z_1\,. \quad (10)$$

Now, consider estimating the settling time of (10) with the initial condition $z_1(0)=z_{1,0}$ and define $t_p$ as the minimum time after which $|z|$ does not exceed a prescribed value $\Delta$.

To analyze convergence, consider the Lyapunov function

$$V = z_1{}^2\,, \quad (11)$$

whose time derivative is

$$\dot{V} = 2 z_1 \dot{z}_1 = -2\left( v_1 \frac{z_1}{\sqrt{z_1^2 + \varepsilon^2}} + c_1 \right) z_1{}^2 \le 0\,. \quad (12)$$

From (13), it is evident that the solution of (10) converges to the origin. Moreover, from (12) we obtain

$$\dot{V} \le -2\left( v_1 \frac{z_1}{\sqrt{z_1^2 + \varepsilon^2}} + c_1 \right) z_1{}^2; \quad (13)$$

$$\frac{\mathrm{d}V}{V} \le -2\left( v_1 \frac{z_1}{\sqrt{z_1^2 + \varepsilon^2}} + c_1 \right) \mathrm{d}t\,. \quad (14)$$

Integrating this inequality for $V$ evolving from $V_0$, corresponding to the time interval from 0 to $t_p$, yields

$$t_p \le \frac{\sqrt{z_{1,0}^2 + \varepsilon^2}}{v_1 + c_1 \sqrt{z_{1,0}^2 + \varepsilon^2}} \ln\left( \frac{z_{1,0}}{\Delta} \right). \quad (15)$$

In classical linear control theory, the settling time $t_p$ is defined as the time after which the deviation between the instantaneous response and the steady-state value does not exceed a specified threshold $\Delta$. The results above demonstrate that system (6) is finite-time stable with respect to the manifold $s=0$ and that the state variable $z_1$

converges to within the prescribed bound $\Delta$ in the finite time $t_p$, determined by the initial conditions and the chosen value of $\Delta$.

Therefore, according to **Definition 1**, it can be concluded that system (6) is globally finite-time stable.

**2.2. Synthesis of a robust finite-time control (RFTC) law based on the differential geometric method.** To design the finite-time control law $u$ for system (2), it is assumed that the system operates without disturbances, i.e., $d(t)=0$. Based on the differential geometric method, a diffeomorphic transformation is established between the nonlinear system (2) and the virtual system (6) with respect to $x_i$. Consider the transformation $z_1=x_1-x_{sp}$, where $x_{sp}$ is the desired angular position of the motor shaft. Under this construction, the diffeomorphic transformation is expressed as follows

$$\begin{cases} z_1 = x_1 - x_{sp}; \\ z_2 = x_2 - \dot{x}_{sp} + v_1 \dfrac{z_1}{\sqrt{z_1^2 + \varepsilon^2}}. \end{cases} \tag{16}$$

This means that $z_i$ depends only on $x_i$. Therefore, by substituting $z_2$ from the last equation of transformation (16) into the last equation of system (2), and combining it with system (6), the following control law is obtained:

$$u = \frac{JR}{k_i}\begin{pmatrix} \dfrac{B}{J}x_2 + \dfrac{C}{J}\operatorname{sgn}(x_2) + \ddot{x}_{sp} - \varepsilon^2 v_1 \dfrac{x_2 - \dot{x}_{sp}}{\left(z_1^2 + \varepsilon^2\right)^{1.5}} \\ -\lambda \operatorname{sgn}(c_1 z_1 + z_2)\left|c_1 z_1 + z_2\right|^{2\beta-1} \\ + c_1 v_1 \dfrac{z_1}{\left(z_1^2 + \varepsilon^2\right)^{0.5}} - c_1 z_2 \end{pmatrix}. \tag{17}$$

The control law is acceptable only if a diffeomorphic mapping exists between system (3), when $d(t)=0$, and system (6), meaning that the Jacobian matrix of the mapping between the two systems must be non-singular, which implies that:

$$\det\begin{bmatrix} \dfrac{\partial z_1}{\partial x_1} & \dfrac{\partial z_1}{\partial x_2} \\ \dfrac{\partial z_2}{\partial x_1} & \dfrac{\partial z_2}{\partial x_2} \end{bmatrix} = \begin{vmatrix} 1 & 0 \\ \dfrac{\varepsilon_2 v_1}{\left(z_1^2 + \varepsilon^2\right)^{1.5}} & 1 \end{vmatrix} \neq 0. \tag{18}$$

According to **Lemma 2**, the control law (17) guarantees that system (2), in the absence of disturbances, achieves finite-time stability, where the settling time is determined by the sum of the time required for the state to reach the manifold $s=0$ (5) and the time $t_p$ (15).

To mitigate the effect of the disturbance term $d(t)$ on the stability and control performance of the DC motor under control law (17), a disturbance compensation component is further incorporated into the control law as follows:

$$u_r = u - \frac{JR}{k_i}\delta \operatorname{sgn}(c_1 z_1 + z_2). \tag{19}$$

**Theorem 1.** Under the conditions of parameters $v_1>0$, $\varepsilon>0$, $\lambda>0$, $\beta\in(0.5, 1)$, $c_1>0$, $\delta>\Delta$ and **Assumption 1**, the control law (19) ensures that system (2) is globally asymptotically stable.

**Proof.** Consider the Lyapunov function defined in (7). Taking its time derivative and substituting from (2), (6), and (9), we obtain:

$$\dot{V}_f = (c_1 z_1 + z_2)\begin{pmatrix} -\lambda \operatorname{sgn}(c_1 z_1 + z_2)\left|c_1 z_1 + z_2\right|^{2\beta-1} \\ -\delta \operatorname{sgn}(c_1 z_1 + z_2) + d(t) \end{pmatrix} = \tag{20}$$

$$= 2^{\beta}\lambda V_f{}^{\beta} - \left|c_1 z_1 + z_2\right|\left(\delta - \operatorname{sgn}(c_1 z_1 + z_2)\mathrm{d}(t)\right).$$

According to **Assumption 1**, if $\delta\geq D$ is chosen, it always follows that $\dot{V}_f \leq 0$. Consequently, system (3) is globally asymptotically stable. The structural block diagram of the DC motor control system employing control law (19) is shown in Fig. 3. It is noteworthy that the saturation blocks in the figure constrain the controller's voltage, considering the electromechanical limits of both the power circuitry and the motor. This ensures that the motor accurately and feasibly tracks the reference trajectory.

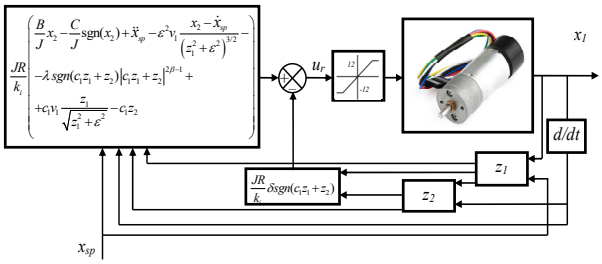

Fig. 3. Block diagram of the DC motor control system

**2.3. Design of the SMC law.** From system (2), the control signal must be determined so that the control objective $x_1=x_{sp}$ is achieved. The output tracking error of the system is defined as:

$$e_1 = x_1 - x_{sp}. \tag{21}$$

The sliding surface of the controller is chosen as:

$$s = \dot{e}_1 + \gamma e_1. \tag{22}$$

where $\gamma>0$ is the parameter ensuring the asymptotic stability of the sliding surface. Applying SMC theory, we obtain:

$$\left(\dot{x}_2 - \ddot{x}_{sp}\right) + \gamma\left(\dot{x}_1 - \dot{x}_{sp}\right) = -K \operatorname{sgn}(s), \tag{23}$$

where $K$ is the positive constant.

Hence, the SMC law is expressed as:

$$u = \frac{JR}{k_i}\begin{pmatrix} \dfrac{B}{J}x_2 + \dfrac{C}{J}\operatorname{sgn}(x_2) + \ddot{x}_{sp} \\ -\gamma\left(x_2 - \dot{x}_{sp}\right) - K \operatorname{sgn}(s) \end{pmatrix}. \tag{24}$$

**3. Simulation and experimental results.**

**3.1. Simulation results.** To validate the effectiveness of the proposed finite-time control law for the DC motor, numerical simulations were carried out in the MATLAB environment. The parameters of the motor and its load in the mathematical model were determined from the datasheet and through direct measurements on the physical system, given as: $J$ = 0.225 kg·m$^2$; $R$=9.1 Ω; $L$=6 mH; $C$=0.001 N·m; $B$ = 6.25 $10^{-5}$ N·m·s/rad; $k_i$=6.8 N·m/A, $k_w$ = 0.015 N·m/A. The parameters of the proposed control law, $c_1$, $v_1$, $\lambda$, $\beta$, and $\varepsilon$, were selected to satisfy the global stability conditions derived in the previous section. In this study, these parameters were chosen as: $c_1$=15, $v_1$=2, $\lambda$=20, $\beta$=0.9, $\varepsilon$=0.001 and $\delta$=7. For comparison, the parameters of the SMC were set as $K$=380, $\gamma$=100. To alleviate the chattering phenomenon in the control law (24), the sign function sgn($s$) was replaced by a linear saturation function bounded within [–1, 1]. The simulations were performed on the dynamic model of the

DC motor (1) over a period of 10 s, under a disturbance $d_1(t)$ = 5+sin(0.05$t$), an additional pulse-like external torque was applied to the load, resulting in a total disturbance of $d_1(t)$ +9. The initial conditions of the motor shaft were set to the origin, i.e., $x_1$=0, $x_2$=0.

In the first simulation scenario, the reference signal varied over time as follows: from 0 s to 2 s, the desired position was set to $x_{sp}$ = 1 rad; from 2 s to 8 s, $x_{sp}$ = –1 rad; and from 8 s to 10 s, $x_{sp}$ = 0 rad. The simulation results presented in Fig. 4–6 demonstrate that both control laws, SMC and RFTC, enable the DC motor shaft to accurately track the reference signal with negligible steady-state error. As shown in Fig. 4, the position responses during the transient phase reveal that the SMC controller exhibits noticeable oscillations, a longer settling time, and a higher overshoot compared to the RFTC controller (as summarized in Table 1). Figure 5 shows the position tracking errors over time, showing that both controllers quickly eliminate the steady-state error; however, their transient behaviors differ: SMC presents small local oscillations around transition points, while RFTC achieves a smoother response. The most remarkable comparison appears in Fig. 6, where the SMC controller generates high-amplitude control pulses at step transitions, whereas the RFTC provides a smoother and more continuous control signal. During the disturbance period between 3.5 s and 4 s, the angular response, tracking error, and control voltage of the RFTC controller clearly outperform those of SMC. Specifically, the RFTC achieves a faster settling time – approximately 1.25 s shorter – with less oscillation in the control input $u$ and lower overall energy consumption. These findings indicate that when fast response, vibration attenuation, and enhanced robustness and accuracy are required, the RFTC controller proves to be more effective and reliable than the SMC law.

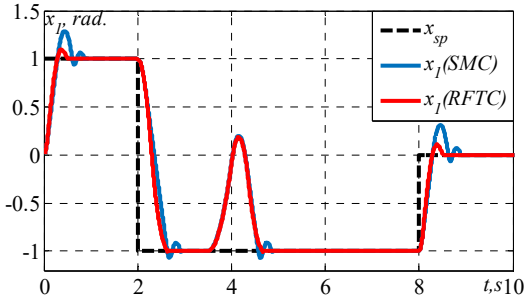

Fig. 4. Position tracking response of the DC motor using RFTC and SMC controllers (1st scenario)

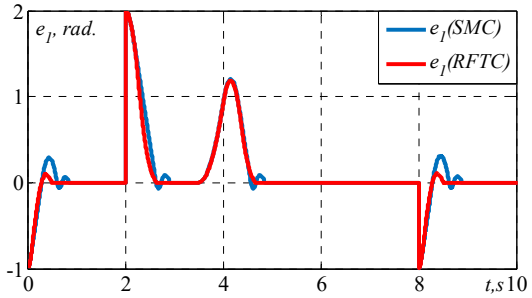

Fig. 5. Position tracking error of the DC motor using RFTC and SMC controllers (1st scenario)

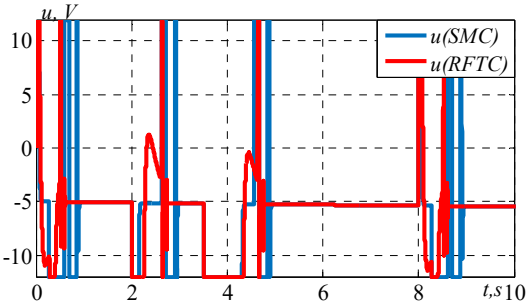

Fig. 6. Control voltage applied to the DC motor using RFTC and SMC controllers (1st scenario)

Table 1

Position response performance indices in the first scenario

| Variable | $t$ = (0–2) s | | $t$ = (2–8) s | | $t$ = (8–10) s | |
|---|---|---|---|---|---|---|
| | RFTC | SMC | RFTC | SMC | RFTC | SMC |
| Settling time, s | 0.5 | 0.863 | 0.6 | 0.94 | 0.52 | 0.88 |
| Overshoot, % | 10 | 29.1 | 0.2 | 3.6 | 11 | 31 |
| Steady-state error, rad | $2.5\cdot10^{-4}$ | $4\cdot10^{-4}$ | $2.5\cdot10^{-4}$ | $4\cdot10^{-4}$ | $2.8\cdot10^{-4}$ | $4.9\cdot10^{-4}$ |

In the second simulation scenario, the reference signal was defined as $x_{sp}$=cos($t$)+0.3sin(0.5$t$). The simulation results presented in Fig. 7–9 demonstrate that both SMC and RFTC control laws achieve effective trajectory tracking performance for the DC motor. As shown in Fig. 7, the position responses obtained using both controllers closely follow the reference trajectory $x_{sp}$. However, during the transient period, the RFTC controller exhibits a noticeably faster response and avoids the oscillations observed in the SMC controller. In particular, under external disturbances, the RFTC controller provides superior tracking capability and converges more rapidly to the desired trajectory. Figure 8 illustrates the position tracking error, where both controllers achieve very small errors that quickly converge to zero after the initial transient phase. Nevertheless, the proposed RFTC controller yields smaller transient errors. Remarkably, RFTC achieves faster error stabilization with nearly no oscillations, whereas the SMC controller still exhibits local high-frequency oscillations during the early response stage. The control input signals shown in Fig. 9 clearly highlight the distinction between the two methods. The SMC controller generates large-amplitude, abrupt control pulses at the beginning of the response and exhibits chattering under sudden disturbances. In contrast, the RFTC controller produces a smoother and more continuous control signal. This observation suggests that RFTC can effectively reduce vibration and mechanical wear compared to SMC.

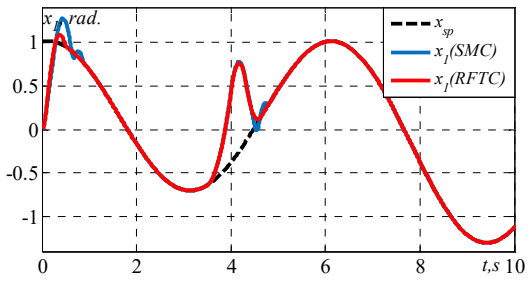

Fig. 7. Position tracking response of the DC motor using RFTC and SMC controllers (2nd scenario)

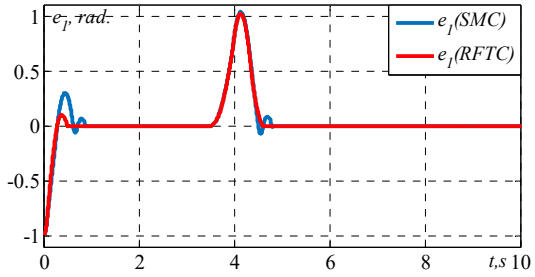

Fig. 8. Position tracking error of the DC motor using RFTC and SMC controllers (2nd scenario)

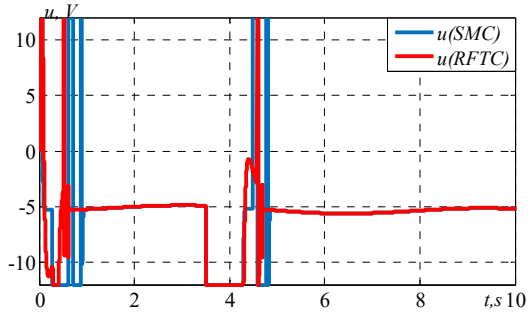

Fig. 9. Control voltage applied to the DC motor using RFTC and SMC controllers (2nd scenario)

**3.2. Experimental results.** In this section, the objective is to validate the proposed controller on a real-time hardware setup in the laboratory, using the same reference signals as in the previous simulations. The experimental drive system is illustrated in Fig. 10. The motor shaft is coupled with a flywheel-type load to introduce additional inertia. The complete control algorithm was implemented on an embedded STM32 board programmed using STM32CubeIDE, while data acquisition was performed through the STMStudio software.

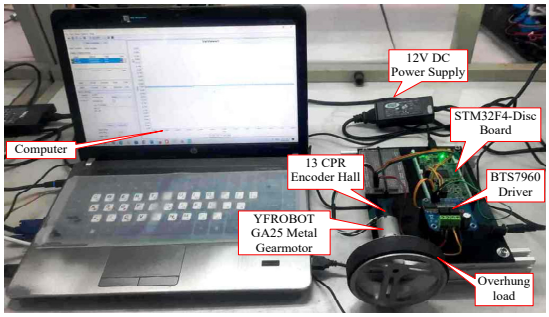

Fig. 10. The experimental drive system

Figures 11, 12 present the angular position responses of the real DC motor system under the SMC and RFTC control laws for two types of reference signals: step and sinusoidal. The results indicate that both controllers ensure satisfactory tracking performance; however, there are noticeable differences in the quality of the responses. For the step reference, both controllers enable the motor shaft to follow the desired trajectory with negligible steady-state error. Nevertheless, the RFTC controller achieves significantly faster response times compared to SMC, with settling times of approximately 0.2 s, 0.5 s, and 0.19 s for each transition, respectively. It should be noted, however, that the proposed controller exhibits a slightly larger overshoot than the SMC controller. When tracking the sinusoidal reference, the RFTC demonstrates superior continuous tracking capability and faster recovery under external disturbances. In contrast, the SMC controller responds more slowly, although it still maintains acceptable tracking accuracy. Furthermore, variations in the SMC controller parameters can lead to oscillations around the reference trajectory. Overall, the experimental results confirm that the RFTC controller provides accurate and well-damped responses in the real system, particularly excelling in fast and smooth tracking of continuous trajectories, while the SMC controller retains its advantage in robustness against disturbances.

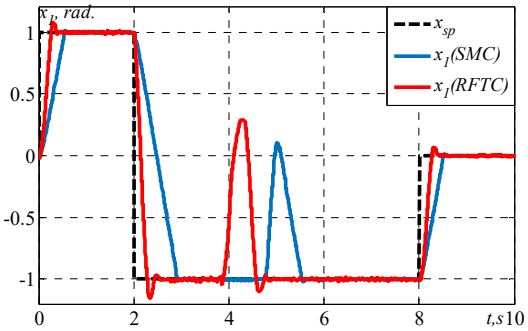

Fig. 11. Position response of the DC motor in the real system under the 1st scenario

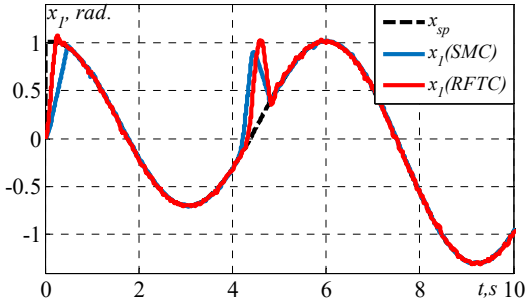

Fig. 12. Position response of the DC motor in the real system under the 2nd scenario

**Conclusions.** This paper presents a synthesis method for a robust finite-time control law based on differential geometry, applied to position control of a DC motor under external disturbances. The proposed control law guarantees finite-time stability of the system in the presence of model uncertainties and external perturbations. By constructing a virtual system with a nonlinear feedback structure and applying a diffeomorphic transformation, the control law is designed such that the system state trajectories converge to a neighborhood of the equilibrium point within a finite time. The finite-time stability and disturbance rejection capability are rigorously proven using Lyapunov theory. Both simulation and experimental results, compared with the conventional SMC under two reference signal scenarios, demonstrate the superiority of the proposed method. In future work, the authors plan to incorporate observers, neural networks, and fuzzy logic to further improve the performance and overcome the remaining limitations of the proposed control strategy.

**Acknowledgements**. This work was supported by a university-level research project at Le Quy Don Technical University under Grant No. 25.01.65.

**Conflict of interest**. The authors declare that they have no conflicts of interest.

REFERENCES


***1.*** Weng C. DC servo motor angle control based on PID control system. *IET Conference Proceedings*, 2024, vol. 2024, no. 19, pp. 1-9. doi: https://doi.org/10.1049/icp.2024.3955.

***2.*** Srinivas G., Durga Sukumar G., Subbarao M. Total harmonic distortion analysis of inverter fed induction motor drive using neuro fuzzy type-1 and neuro fuzzy type-2 controllers. *Electrical Engineering & Electromechanics*, 2024, no. 1, pp. 10-16. doi: https://doi.org/10.20998/2074-272X.2024.1.02.

***3.*** Wang X., Wang S. Adaptive Back-stepping Control of Servo Systems With Asymmetric Dead Zone. *International Journal of Control, Automation and Systems*, 2024, vol. 22, no. 9, pp. 2711-2722. doi: https://doi.org/10.1007/s12555-024-0202-z.

***4.*** Alejandro-Sanjines U., Maisincho-Jivaja A., Asanza V., Lorente-Leyva L.L., Peluffo-Ordóñez D.H. Adaptive PI Controller Based on a Reinforcement Learning Algorithm for Speed Control of a DC Motor. *Biomimetics*, 2023, vol. 8, no. 5, art. no. 434. doi: https://doi.org/10.3390/biomimetics8050434.

***5.*** Garcia-Chica A., Torres-Moreno J.L., Gimenez A. PID Control of DC Actuators. Consideration to Energy Robotic Design. *IFAC-PapersOnLine*, 2024, vol. 58, no. 7, pp. 258-262. doi: https://doi.org/10.1016/j.ifacol.2024.08.071.

***6.*** Dawane M.K., Malwatkar G.M., Deshmukh S.P. Performance improvement of DC servo motor using sliding mode controller. *Journal of Autonomous Intelligence*, 2023, vol. 7, no. 3, art. no. 1162. doi: https://doi.org/10.32629/jai.v7i3.1162.

***7.*** Alnaib I.I., Alsammak A.N., Mohammed K.K. Brushless DC motor drive with optimal fractional-order sliding-mode control based on a genetic algorithm. *Electrical Engineering & Electromechanics*, 2025, no. 2, pp. 19-23. doi: https://doi.org/10.20998/2074-272X.2025.2.03.

***8.*** Du H., Tao L., Deng X., Xu, B. Adaptive Parameter Identification Based Tracking Control of Servo Systems with Unknown Actuator Backlash Compensation. *Actuators*, 2025, vol. 14, no. 6, art. no. 288. doi: https://doi.org/10.3390/act14060288.

***9.*** Wang J., Xu W., Fang S., Chen Y., Wang Y., Wang W. Adaptive control schemes based on characteristic model for servo motor drives. *IET Power Electronics*, 2023, vol. 16, no. 13, pp. 2238-2248. doi: https://doi.org/10.1049/pel2.12544.

***10.*** Song C., Liu J., Yu J., Ma Y., Zhang X., Lv Z. Adaptive Fuzzy Finite-time Tracking Control for A Class of DC Motor with State Constraints. *2020 7th International Conference on Information, Cybernetics, and Computational Social Systems (ICCSS)*, 2020, pp. 682-686. doi: https://doi.org/10.1109/ICCSS52145.2020.9336834.

***11.*** Xu C., Hu J. Adaptive robust control of a class of motor servo system with dead zone based on neural network and extended state observer. *Proceedings of the Institution of Mechanical Engineers, Part I: Journal of Systems and Control Engineering*, 2022, vol. 236, no. 9, pp. 1724-1737. doi: https://doi.org/10.1177/09596518221099783.

***12.*** Sai Lakshmi S., Jeyasenthil R., Babu U.B. Robust controller design based on IMC scheme for motion control of DC servo systems. In: Kumar S., Tripathy M., Jena P. (eds) Control Applications in Modern Power Systems (EPREC 2023). doi: https://doi.org/10.1007/978-981-99-9054-2_16.

***13.*** Yıldırım Ş., Bingol M.S., Savas S. Tuning PID controller parameters of the DC motor with PSO algorithm. *International Review of Applied Sciences and Engineering*, 2024, vol. 15, no. 3, pp. 281-286. doi: https://doi.org/10.1556/1848.2023.00698.

***14.*** Dong Z., Chen S., Sun Z., Tang B., Wang W. A Servo Control Algorithm Based on an Explicit Model Predictive Control and Extended State Observer with a Differential Compensator. *Actuators*, 2025, vol. 14, no. 6, art. no. 281. doi: https://doi.org/10.3390/act14060281.

***15.*** Cui P., Zheng Z., Fu J., Zhang Q., An L. A Fault-Tolerant Control Method for a PMSM Servo Drive System with a Four-Leg Inverter. *Electronics*, 2023, vol. 12, no. 18, art. no. 3857. doi: https://doi.org/10.3390/electronics12183857.

***16.*** Amieur T., Taibi D., Kahla S., Bechouat M., Sedraoui M. Tilt-fractional order proportional integral derivative control for DC motor using particle swarm optimization. *Electrical Engineering & Electromechanics*, 2023, no. 2, pp. 14-19. doi: https://doi.org/10.20998/2074-272X.2023.2.03.

***17.*** Jastrzębski M., Kabziński J., Mosiołek P. Finite-Time, Robust, and Adaptive Motion Control with State Constraints: Controller Derivation and Real Plant Experiments. *Energies*, 2022, vol. 15, no. 3, art. no. 934. doi: https://doi.org/10.3390/en15030934.

***18.*** Nguyen M.H., Ahn K.K. A Finite-Time Disturbance Observer for Tracking Control of Nonlinear Systems Subject to Model Uncertainties and Disturbances. *Mathematics*, 2024, vol. 12, no. 22, art. no. 3512. doi: https://doi.org/10.3390/math12223512.

***19.*** Nguyen X.C., Le D.T. Adaptive finite-time synergetic control for flexible-joint robot manipulator with disturbance inputs. *Electrical Engineering & Electromechanics*, 2025, no. 3, pp. 45-52. doi: https://doi.org/10.20998/2074-272X.2025.3.07.

***20.*** Khatir A., Bouchama Z., Benaggoune S., Zerroug N. Indirect adaptive fuzzy finite time synergetic control for power systems. *Electrical Engineering & Electromechanics*, 2023, no. 1, pp. 57-62. doi: https://doi.org/10.20998/2074-272X.2023.1.08.

***21.*** Chiem N.X., Thuy P.X. A Finite-time Controller Design Based on Strick-feedback System for Flexible Joint Manipulator. *International Journal of Control, Automation and Systems*, 2025, vol. 23, no. 6, pp. 1829-1838. doi: https://doi.org/10.1007/s12555-024-0939-4.

***22.*** Vesović M., Jovanović R., Trišović N. Control of a DC motor using feedback linearization and gray wolf optimization algorithm. *Advances in Mechanical Engineering*, 2022, vol. 14, no. 3. doi: https://doi.org/10.1177/16878132221085324.

***23.*** Ambrosino, R., Ariola, M., Garone, E., Amato, F., & Tartaglione, G. New conditions for finite-time stability of impulsive dynamical systems via piecewise quadratic functions. *IET Control Theory & Applications*, 2022, vol. 16, no. 13, pp. 1341-1351. doi: https://doi.org/10.1049/cth2.12308.



*Received 20.08.2025*
*Accepted 30.10.2025*
*Published 02.01.2026*



*Q.B. Nguyen*[1], *MSc of Automatic Control,*
*X.C. Nguyen*[2], *Doctor of Automatic Control,*
[1] Control, Automation in Production and Improvement of Technology Institute (CAPITI), Hanoi, Vietnam,
e-mail: qbinhk37@gmail.com
[2] Department of Automation and Computing Techniques, Le Quy Don Technical University, Hanoi, Vietnam,
e-mail: chiemnx@mta.edu.vn (Corresponding Author)



*How to cite this article:*
Nguyen Q.B., Nguyen X.C. Finite-time robust position tracking control for DC motors under uncertain dynamics. *Electrical Engineering & Electromechanics*, 2026, no. 1, pp. 44-50. doi: https://doi.org/10.20998/2074-272X.2026.1.06

UDC 621.316 https://doi.org/10.20998/2074-272X.2026.1.07

B.M. Anwer, A.N. Alsammak

# An integrated series active power filter combined with a PV-battery system based on a fuzzy logic controller to enhance power quality for various linear and non-linear loads

***Introduction.*** *Rapid capacity development and the incorporation of new loads are adding complexity to the distribution power system. As a result, the distribution system faces additional power quality issues, particularly with increasingly sensitive equipment and distributed generation.* ***Problem.*** *Modern power systems face escalating power quality degradation due to non-linear loads. Voltage disturbances (sags, swells) and harmonic distortions directly affect the sensitive equipment, causing significant economic losses. The* ***goal*** *of this work is to design, model, and evaluate series active power filters (SAPFs) integrated with energy management for an independent solar storage system, using a multi-stage DC-DC converter. The objective focuses on mitigating voltage harmonics and grid disturbances resulting from diverse loads (linear, non-linear, and combined) and integrating renewable energy (PV). Control is achieved through an intelligent fuzzy logic controller (FLC) and a PI controller to ensure a stable DC voltage and reduce the total harmonic distortion (THD) of the voltage to less than 5 %.* ***Methodology.*** *This study models and analyzes a unique SAPF configuration integrated with a PV-battery storage system utilizing MATLAB/Simulink. Outcomes of the proposed control, wherever the FLC regulates the DC-link voltage reference signals utilize the instantaneous reactive power theory. The suggested methodology entails simulation studies across four scenarios: an analysis of performance to keep voltage components and a comparison of the proposed SAPF performance with existing research on linear, non-linear, and combined loads.* ***Results.*** *Simulation results show the effectiveness of the control approach in mitigating the voltage THD level to less than 5 % under various operating conditions that included the main supply voltage and loads, which satisfies the international PQ standards (IEEE Std. 519). The* ***scientific novelty*** *lies in the combination of a new 3-phase SAPF with a PV-battery system by FLC and a cascaded DC/DC converter. This allows effective voltage disturbance and harmonic compensation in various load situations without conventional transformers.* ***Practical value.*** *This research offers a robust solution for power quality problems in modern grids, reducing losses by ensuring stable, no-distortion power for sensitive industrial loads across varied operating conditions.* References 46, tables 3, figures 19.

*Key words*: **power quality, series active power filter, PV-battery system, fuzzy logic control, voltage disturbances, harmonic mitigation, linear and nonlinear loads.**

***Вступ***. *Швидке розширення потужностей та включення нових навантажень ускладнюють систему розподілу електроенергії. В результаті система розподілу стикається з додатковими проблемами якості електроенергії, особливо через дедалі чутливе обладнання та розподілену генерацію.* ***Проблема***. *Сучасні енергосистеми стикаються зі зростаючим погіршенням якості електроенергії через нелінійні навантаження. Коливання напруги (провали, збільшення) та гармонічні спотворення безпосередньо впливають на чутливе обладнання, спричиняючи значні економічні втрати.* ***Метою*** *роботи є проєктування, моделювання та оцінка послідовних активних фільтрів потужності (SAPF), інтегрованих з управлінням енергією, для незалежної системи сонячного накопичення енергії, з використанням багатоступеневого перетворювача постійного струму. Мета зосереджена на зменшенні гармонік напруги та коливань у мережі, що виникають внаслідок різних навантажень (лінійних, нелінійних та комбінованих) та інтеграції відновлюваної енергії (PV). Керування досягається за допомогою інтелектуального контролера з нечіткою логікою (FLC) та PI-контролера для забезпечення стабільної напруги постійного струму та зменшення загального коефіцієнта гармонійних спотворень (THD) напруги до менш ніж 5 %.* ***Методологія***. *Це дослідження моделює та аналізує унікальну конфігурацію SAPF, інтегровану з системою зберігання PV батарей, використовуючи MATLAB/Simulink. Результати запропонованого керування, де FLC регулює сигнали опорної напруги ланки постійного струму, використовують теорію миттєвої реактивної потужності. Запропонована методологія включає дослідження моделювання за чотирма сценаріями: аналіз продуктивності для підтримки складових напруги та порівняння запропонованої продуктивності SAPF з існуючими дослідженнями лінійних, нелінійних та комбінованих навантажень.* ***Результати*** *моделювання показують ефективність підходу до керування у зменшенні рівня THD напруги до менш ніж 5 % за різних робочих умов, включаючи основну напругу живлення та навантаження, що відповідає міжнародним стандартам PQ (IEEE Std. 519).* ***Наукова новизна*** *полягає в поєднанні нового трифазного SAPF з системою PV батарей за допомогою FLC та каскадного перетворювача постійного струму. Це дозволяє ефективно компенсувати коливання напруги та гармоніки в різних ситуаціях навантаження без використання звичайних трансформаторів.* ***Практична значимість***. *Це дослідження пропонує надійне рішення для проблем якості електроенергії в сучасних мережах, зменшуючи втрати, забезпечуючи стабільну потужність без спотворень для чутливих промислових навантажень за різних умов експлуатації.* Бібл. 46, табл. 3, рис. 19.

*Ключові слова:* **якість електроенергії, послідовний активний фільтр потужності, система фотоелектричних батарей, нечітка логіка керування, збурення напруги, зменшення гармонік, лінійні та нелінійні навантаження.**

**Introduction.** Reliability is a crucial concept for utility companies and their customers in general. It holds particular significance for businesses operating in highly competitive environments because it directly affects profitability, a key driver in the industry. Although electrical transmission and distribution systems have attained a very high degree of dependability, disruptions cannot be completely eliminated. Any distortion in the voltage waveform can lead to operational issues with electrical and electronic devices [1]. To ensure uninterrupted production, users require a consistent sine wave shape, constant frequency, symmetrical and standard voltage value [2, 3].

The focus on improving efficiency and minimizing variations in industrial operations has resulted in more use of the complex equipment that is highly sensitive to voltage disturbances, such as voltage sags, voltage swells, interruptions, and harmonics [4]. Voltage sags are considered the most critical, as sensitive loads are particularly sensitive to temporary voltage changes [5]. In some cases, these issues might result in the total stoppage of an entire production line, especially in high-tech industries like semiconductor manufacturing, causing significant economic losses for affected changes [2, 6].

Traditionally, solutions to address power quality issues relied on conventional passive filters [7]. However, their limitations, such as fixed compensation, resonance with source impedance, and challenges in tuning time-dependent filter parameters, have created a demand for active and hybrid filters [8]. Active filters offer better compensation compared to passive filters, and when combined with passive elements, they form hybrid filters that provide cost-effective and optimal solutions [2, 9].

As a result, the advancement of active filter technology has progressed to mitigate voltage-related power quality issues, especially in systems that include diode bridge converters with substantial DC-link capacitive filters [10]. Series active power filter (SAPF) is preferred in such applications. Although series filters efficiently remove voltage and current harmonics, they are not optimal for ensuring zero voltage regulation at the point of common coupling (PCC). Additionally, a series filter to handle voltage-related concerns is more efficacious than employing a shunt filter for better utilization of system ratings [2, 11]. Most addressing escalating challenges of power quality degradation in modern electrical systems have been solved by using FACTS devices, such as a 3-phase SAPF for power distribution systems [7]. The impact on power supply and quality of energy with the growing number of power electronic devices, which are not linear in nature and can comprise voltage deviation and harmonic distortions, is a serious issue, and thus, the reliability and performance of electrical distribution systems are affected [2, 12].

To mitigate the detrimental effects experienced by the systems, the proposed architecture in this study possesses unique characteristics and capabilities for energy management of stand-alone photovoltaic (PV)-battery energy storage systems integrated with the SAPF. The objective of this cooperative control is to effectively counteract both sag and swell voltage, as well as harmonic distortions in load voltage, thereby ensuring superior power quality and overall stability of the power system.

**Review of the literature.** The following section reviews the most significant research works in the literature on SAPFs and hybrid SAPF configurations for improving PQ. As outlined in [13], the methodology analyzed fuzzy logic-based phase-locked loops (PLLs) and linear controllers (RST and PID) for SAPF suppression of non-linear load voltage dips, with the most attention being given to fuzzy hysteresis band control, where a performance comparison with traditional techniques using higher complexity was carried out. The work [14] proposes a SAPF based on an adaptive fuzzy logic controller. It aims at improving the power quality in stand-alone wind/solar power systems by eliminating the voltage problems such as modulation, surges, distortion, and imbalance, resulting from non-common loads. The power sources are used to prop up the AC side to minimize voltage distortion and to satisfy the standard of IEEE 519-1992 as well as to improve the use of renewable energy sources. A key contribution of [15] is a new control strategy, fuzzy slide mode pulse width modulation (FSMPWM), compared with PI control, for a series hybrid active power filter to enhance power factor. FSMPWM can reduce the total harmonic distortion (THD) and perform better than a hysteresis controller. Another advantage of the FSMPWM is that it can suppress noise, standardize switching frequency, and cope with voltage dips/spikes. This is confirmed via MATLAB simulation based on IEEE-519 laws. The study [16] highlighted how hybrid active power filters with sliding mode control were capable of managing harmonic pollution due to non-linear loads under smart grid environment development, and support was given to active versus passive alternatives. The work [17] confirms the superiority of the ANFIS-based control of the SAPFs for harmonics and voltage disturbances mitigation. By extensive simulations and experimental tests, it is shown that the ANFIS controller has proven superior to the backstepping sliding mode control by minimizing the THD, thereby increasing the power quality at the grid level. Its robustness and flexibility make it a good candidate. Building upon previous work, [18] developed a new control algorithm for SAPFs in the low-voltage distribution grid serving a voltage source non-linear load in order to use the feeder impedance factor practically calculated via simulation and experiment. The authors of [19] presented an improved second-order generalized integrator controlled series hybrid active power filter for harmonic current suppression in 3-phase interfaces, involving PV systems showing substantial THD drop. The results from [20] investigated hybrid SAPFs, using an adaptive neuro-fuzzy inference system for better power quality control in power grid-connected systems with non-linear loads. Further analysis by [21] studied the influence of power electronics-generated harmonics and also confirmed in simulation as well as measurement that shunt and SAPF can suppress these distortions. Specifically, [22] focused on presenting the improved quality of power by connecting SAPFs to the proton exchange membrane fuel cell through advanced AI-based control in both conventional and PV-integrated distribution systems. The work [23] concentrated on SAPFs to alleviate source-produced voltage, and the matrix pencil method was reported as a superior method compared to traditional methods in terms of THD reduction. In general, these investigations constitute an important part of the work on the advancements of SAPFs and their hybrid forms for power quality conditioning in different electrical systems. The proposed PV-battery system without an MV transformer employs a multi-stage DC-DC converter and an integrated energy management control concept [24]. A PI controller optimizes PV DC voltage [25, 26] under various loads.

By directly addressing the adverse impacts of non-linear power electronics, this integrated SAPF and PV-battery system offers a robust, efficient solution to the growing challenges of maintaining power quality in contemporary electrical systems.

The **goal** of this work is to design, model, and evaluate series active power filters (SAPFs) integrated with energy management for an independent solar storage system, using a multi-stage DC-DC converter. The objective focuses on mitigating voltage harmonics and grid disturbances resulting from diverse loads (linear, non-linear, and combined) and integrating renewable energy (PV). Control is achieved through an intelligent fuzzy logic controller (FLC) and a PI controller to ensure a stable DC voltage and reduce the THD of the voltage to less than 5 %.

**Active power filter (APF).** The core operating principle of active filtering is based on the extraction and subsequent injection of reference signals that include prominent harmonics at the PCC. This complex process is executed using specialized modulation methods, including pulse width modulation (PWM). In shunt APF applications, source current harmonics are predominant, whereas voltage harmonics are rather small and are not substantially influenced by non-linear loads [27]. Consequently, numerous researchers inadvertently employ classic SAPFs with sinusoidal voltage sources and non-linear loads (Fig. 1), configurations typically intended for shunt APF applications [28, 29].

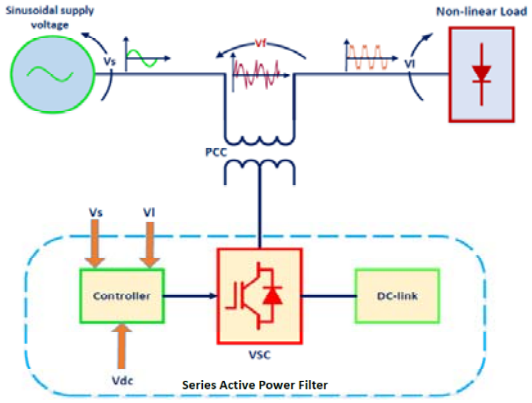

Fig. 1. Classic SAPF

Conversely, in the context of SAPFs, when appropriately configured under linear load conditions with a voltage source exhibiting significant harmonic distortion, the resultant current waveform inherently mirrors the source voltage's harmonic profile. This phenomenon may compromise the efficacy of reference-signal extraction techniques, particularly in linear load scenarios [29]. To address this challenge, a comprehensive investigation into the applicability and robustness of extraction methodologies within SAPF frameworks is imperative, with emphasis on linear load configurations (Fig. 2).

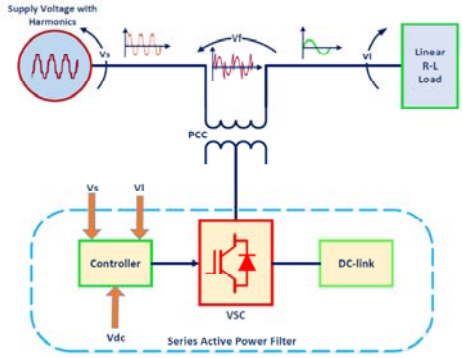

Fig. 2. Modern SAPF

The present study undertakes a rigorous analysis of linear, non-linear, and hybrid (combined linear and non-linear) loads conditions, while also accounting for source voltage anomalies such as sags, swells, and significant harmonic distortion (Fig. 3). The characteristics of SAPF types can be clarified through the flowchart (Fig. 4).

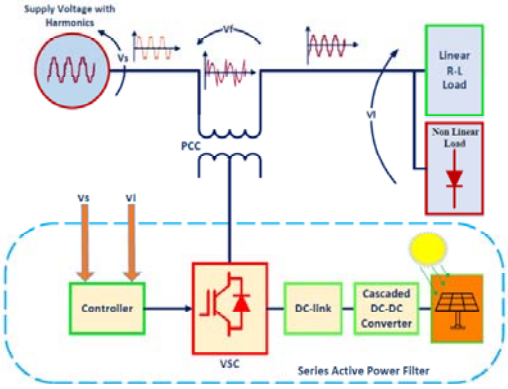

Fig. 3. Developed SAPF

When checking the flowchart, notice that the advanced SAPF excels at enhancing power quality, making it well-suited for environments with distorted source voltage and distorted current loads. Its flexible and precise operation effectively mitigates voltage distortion originating from both the source voltage and the flow of distorted current through the system's impedance, capably handling linear, non-linear, and combined load types. The modern SAPF employs contemporary technology to improve power quality and is also effective in situations with distorted source voltage.

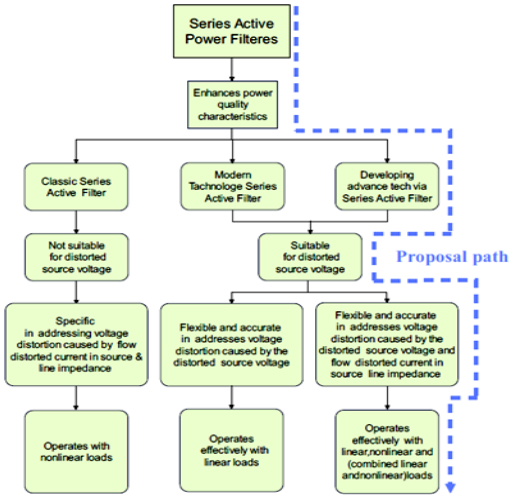

Fig. 4. Flowchart characteristics of SAPFs with proposal path

It offers flexible and accurate correction of voltage distortion caused by the distorted source voltage and functions efficiently with linear loads. In contrast, the Classic SAPF improves power quality but is not ideal for distorted source voltage conditions. It specifically targets voltage distortion resulting from distorted current flow within.

**Medium-voltage grid integration of PV systems through advanced DC-DC conversion topologies.** The escalating concerns surrounding environmental degradation and the limitations of conventional energy sources have propelled PV technology to the forefront of renewable energy research and deployment. Over the past decade, significant advancements in solar cell efficiency and manufacturing processes have established PV power generation as a compelling alternative and complementary energy resource, particularly within hybrid energy systems [25, 30]. This rapid expansion of PV adoption is further fueled by the increasing demand for distributed generation, highlighting the crucial role of solar energy in meeting renewable electricity targets [31].

However, the growing integration of distributed solar PV generation into low- and medium-voltage distribution networks introduces a range of technical challenges. These include alterations in voltage profiles (such as voltage rise and imbalances), potential overloading of feeder components, increased activity of voltage regulation devices, voltage fluctuations, power quality degradation, elevated energy losses, and a reduction in overall network reliability [23, 26]. Concurrently, ongoing innovations in PV technology have led to significant cost reductions, with PV module prices experiencing a substantial decline (80–85 % between 2009 and 2016) [32], further accelerating their adoption in these years until now.

A critical component in optimizing the performance of PV systems, particularly under varying solar irradiance and temperature conditions, is the maximum power point tracking (MPPT) system. Given the inherent low efficiency of PV modules in suboptimal conditions and their non-

linear voltage-current characteristics, an MPPT system is indispensable for extracting maximum power output. Usually adopting algorithms of perturb and observe for its simple operation, the MPPT system also requires a joint utilization DC-DC converter to behave as a control interface [33, 34]. This converter adapts its duty cycle according to the variations of the environmental conditions in order to operate continuously at the MPPT [35]. There are many different types of DC-DC converter topologies, such as buck, boost, buck-boost, Cuk, Sepic, etc., which individually have their own special characteristics and limitations for the dedicated application [36, 37].

In order to efficiently control the output voltage of PV modules and to achieve the maximum power point tracking, it is necessary to have a DC-DC converter. This research focuses specifically on the boost converter topology, known for its ability to step up the input voltage level. Boost converters find widespread application in battery-powered systems where higher operating voltages are required for electronic devices. The fundamental principle of power transfer in this converter relies on the interaction of a power switch, an inductor, a capacitor, and a diode, with power flow managed through the switching action of the power switch. Output voltage regulation is achieved by controlling the duty cycle of the switch using PWM at a fixed switching frequency [36, 38].

The increasing penetration of PV generation has profoundly impacted power system operation. While distributed generation offers numerous benefits, the intermittent nature of solar resources presents challenges for distribution system operators concerning power quality, efficiency, and grid stability. This evolving scenario necessitates a shift from solely focusing on active power generation from PV systems to exploring their reactive power capabilities for enhanced grid support and voltage regulation. Recent research has explored generalized optimization frameworks applicable to various distribution networks, integrating dynamic PV control strategies [39]. The growing awareness of energy security and climate change has further spurred the proliferation of distributed energy resources, with PV systems gaining prominence in low-voltage distribution networks due to their decreasing costs and lack of moving parts [40, 41].

In the context of medium-voltage distribution networks, DC-DC converters play a crucial role in harnessing energy from PV panels. The standard DC voltage for residential system between 400–600 V, while the commercial PV modules typically have voltage limitations below 1 kV, in addition, the utility-scale PV may go up to 1.5 kV and DC bus voltages are often significantly higher; high step-up ratio DC-DC converters are required.

One effective approach to achieve the required high voltage gains is through the utilization of multiple cascaded submodules from low voltage DC (LVDC) to medium voltage DC (MVDC). Three primary cascaded DC-DC converter configurations exist: the input-independent output-series (IIOS) type, the low-voltage bus-based (LVBB) type, and the two-stage conversion (TSC) type, as shown in Fig. 5–7 [24, 42].

The more efficient proposed multiport cascaded converter, which includes capacitors and battery storage groups (Fig. 8). The capacitors handle the high-frequency ripple and the transient response. This method gives a more efficient and reliable MVDC supply.

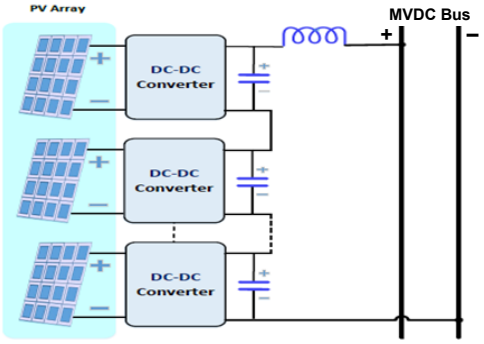

Fig. 5. Multiport cascaded converter type IIOS for MVDC

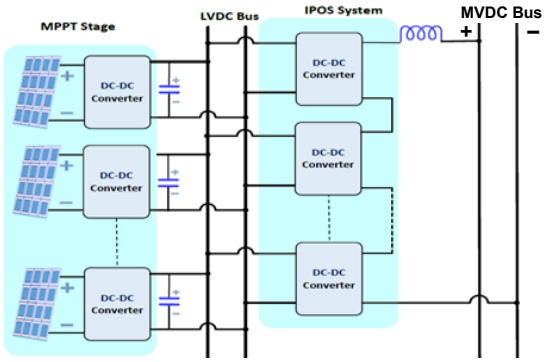

Fig. 6. Multiport cascaded converter type LVBB for MVDC

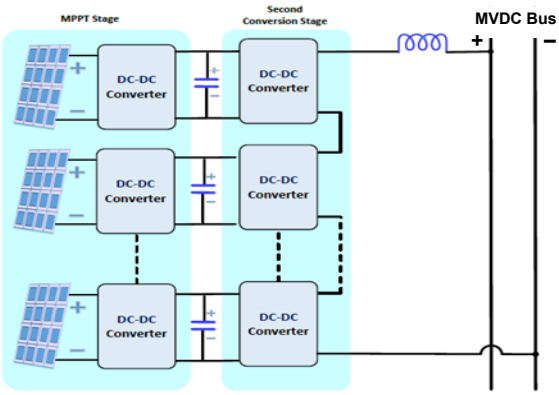

Fig. 7. Multiport cascaded converter type TSC for MVDC

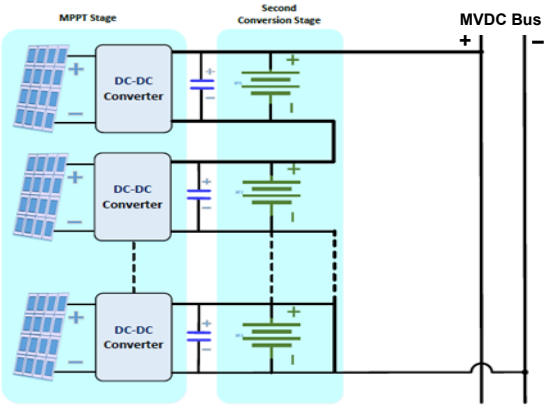

Fig. 8. Proposed multiport cascaded converter for MVDC

The proposed type of power system architecture utilizes a PV array to charge a battery bank through a boost DC-DC converter. This specific converter topology is employed to step up the voltage from the PV array to the required charging voltage of the battery. The suggestion used batteries have a capacity of 16.5 MW over 10 min. It can be increased if more support time is needed. A PI controller meticulously regulates the duty cycle of the boost converter's switching elements. This

closed-loop control ensures a stable and consistent DC voltage is maintained across the battery terminals, compensating for variations in solar irradiance and battery state-of-charge. To construct a cascaded system, multiple identical units, each encompassing the PV array, a boost DC-DC converter with PI control, and a battery bank, are connected in series. This serial connection allows for a scalable increase in the overall system voltage output, offering enhanced flexibility for higher voltage applications and facilitating modular design and maintenance. The following section will detail how the cascaded system's output voltage is accurately controlled and explain the principles for determining the necessary number of stages to achieve target voltage levels.

**Control system.** The control system has been split into two stages: first, control of the DC link and reference signal extraction using a conventional PI controller, and second, control of the DC link stages using an intelligent FLC. In DC link systems, voltage regulation is a critical aspect, achievable through either external or internal DC sources. When an internal source is utilized, a supplementary control circuit becomes essential to maintain the DC link voltage at a predefined reference, necessitating the feedback of the V-DC value to the controller. However, for the scope of this investigation, an external DC source is considered. Conventional control methodologies often face limitations in non-linear systems due to their reliance on precise mathematical models. In contrast, FLC offers a significant advantage by its inherent capacity to process data characterized by uncertainty, imprecision, and even apparent contradictions [14, 15]. FLCs emulate human-like control reasoning, diverging from traditional controllers by obviating the need for a rigorous mathematical model to address the inherent vagueness and uncertainty frequently encountered in linguistic problem formulations. Fuzzy logic demonstrates proficiency in representing uncertain and imprecise system knowledge, while fuzzy control enables decision-making even with uncertain inputs or outputs, based on a set of imprecise rules [43, 44].

The ANFIS, a hybrid intelligent control architecture, synergistically integrates the interpretability of fuzzy logic with the adaptive learning capabilities of neural networks. This integration facilitates the realization of robust, self-optimizing control frameworks. Grounded in a Takagi-Sugeno-type fuzzy inference model, ANFIS eliminates reliance on manual rule formulation and expert-driven parameter tuning, thereby significantly enhancing adaptability and operational efficiency in complex, non-linear environments [45].

In the current work, an ANFIS creates an FLC that has been specifically designed for seven-stage DC-link voltage regulation. The input-output data set for training ANFIS contains two inputs and one output. Four Gaussen membership functions characterize both input variables. The training error is about $3.9 \cdot 10^{-3}$ with 50 epochs. The designed structure of the fuzzy logic controller is depicted in Fig. 9. This system employs two critical input variables load current (ranging from 1.4–11.5 kA) and THD (0–22.8 %) to generate a single control output. This output undergoes saturation and iterative error minimization, converging to approximately zero.

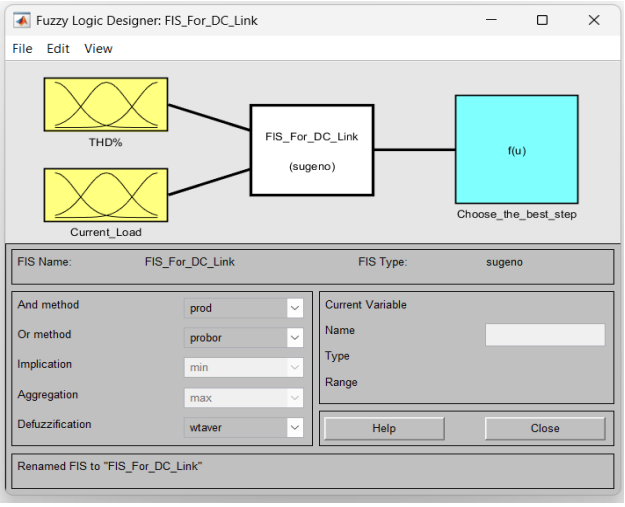


Fig. 9 The designed structure of the fuzzy logic controller

The computed control signal dynamically determines the minimum DC voltage amplitude, ensuring compliance with active power demands under varying operating conditions. This is achieved via a demultiplexer (Demux) driven activation mechanism that selectively engages a predefined number of cascaded power-stage modules. The power circuit (Fig. 10) comprises seven series-connected stages. By dynamically adjusting the number of active stages, the system achieves precise output voltage regulation while compensating for losses and maintaining stability during voltage sags, swells, or harmonic distortions.

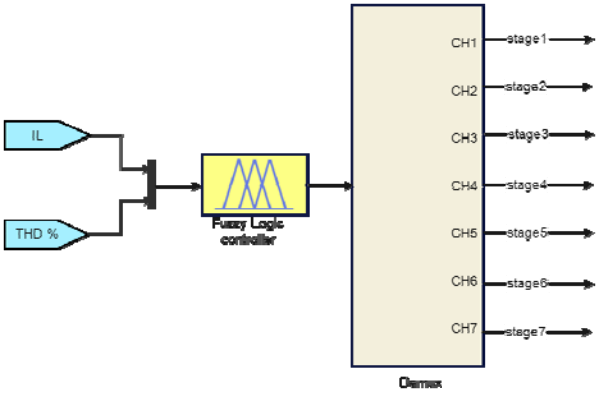


Fig. 10 The designed fuzzy logic controller with Demux

**Control of voltage extraction**. The SAPF is connected in series with the power circuit via a transformer with a 1:1 turn ratio. The primary elements of the SAPF are the voltage source inverter (VSI), the DC-link, and the control algorithm. IGBT transistors are the predominant switching devices used in the VSI module. For this investigation, PWM was used as the modulation method. Under conditions where standard power equations become invalid, Akagi theorized that instantaneous reactive power theory (IRPT) transforms into a theoretical framework used in a series filter, operating as a dual *d–q* theory for regulation. This theoretical framework entails the incorporation of a current source, either at the source or load, to ensure sinusoidal current waveforms inside the circuit, thereby isolating harmonic content exclusively within the voltage signal [23].

The MATLAB/Simulink for the proposed model that included the sample power system with the proposed SAPF, controlled by a fuzzy logic controller is shown in Fig. 11.

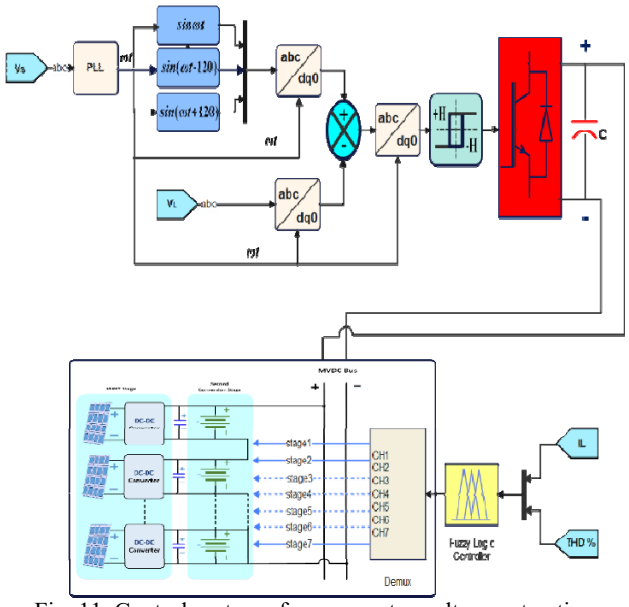


Fig. 11. Control system of compensator voltage extraction

The control circuit depicted in Fig. 11 derives the reference signal from the source voltage, which is fed into a PLL to extract the instantaneous phase angle ($\omega t$). This phase angle serves as the synchronization basis for generating independent voltage sources within the system. Subsequently, the voltages of both the independent sources and the load are transformed from the 3-phase (ABC) reference frame to the synchronous dq0 (direct-quadrature-zero) reference frame using the extracted $\omega_t$ [46]. A subtraction operation is then performed between the dq0 components of the load voltage and those of the independent sources. The resulting difference, representing the required compensation signal, is transformed back from the dq0 frame to the 3-phase (ABC) domain.

This compensation signal addresses harmonic distortions, mitigates voltage sag by injecting supplementary voltage, or suppresses voltage swell by subtracting excess components. These disturbances originate from the primary power source. The compensation process is implemented via a SAPF, which utilizes a voltage source converter (VSC) operating under a hysteresis PWM control strategy. The VSC is powered by an external PV-DC link, and its switching is triggered by the reference signal generated through the aforementioned control steps. Compensation is injected into the power line via a series-connected converter, ensuring that the voltage delivered to the load remains sinusoidal, free of distortions, and compliant with high power quality standards.

**Proposed simulation.** This section presents a computational analysis of the proposed SAPF topology using MATLAB/Simulink. The simulation framework, depicted in Fig. 12, incorporates the parameters detailed in Table 1. The voltage source is configured to emulate a distorted grid supply; the series filter block incorporates a 3-phase 1:1 isolating transformer. The controller unit incorporates the extraction algorithm based on IRPT, PWM generation, and a seven-stage cascaded DC-DC converter topology. This converter, regulated by a PV system, achieves medium-voltage levels through operational control enabled by a demultiplexing unit for signal routing and an FLC system, which enhances dynamic stability and transient response.

Table 1

Simulation parameters for the proposed design

| Parameters | Range |
|---|---|
| Source voltage and frequency | 6600 V, 50 Hz |
| Source impedance | 0.01 mH, 0.05 Ω |
| Coupling reactance | 1 mH |
| Coupling capacitance with resistance | 2000 μF, 1 Ω |
| DC link voltage | (5000–13000) V |
| One-stage linear load | 5 mH, 1 Ω |
| One-stage non-linear load | 3 mH, 6 Ω |
| Transformers | 6600Y / 6600Y |

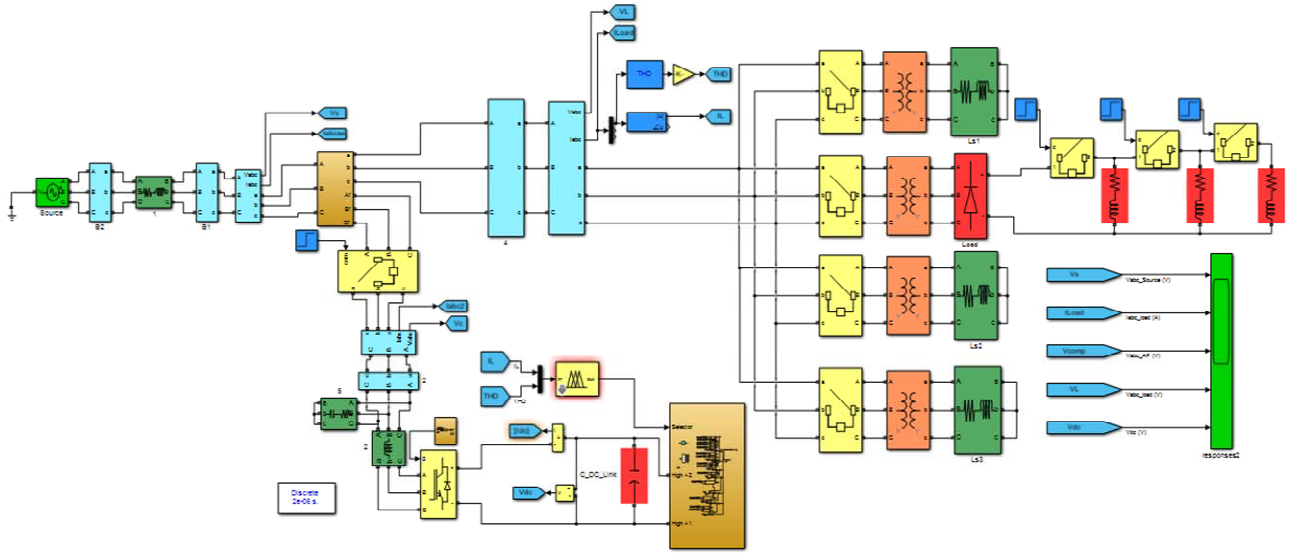

Fig. 12. Proposed SAPF in MATLAB/Simulink

To validate the efficacy of the proposed SAPF-based extraction technique **comprehensive simulations** were conducted across four operational scenarios involving diverse load conditions.

1) First scenario.

This study evaluates the SAPF effectiveness in mitigating harmonic distortions and transient anomalies within a harmonically distorted grid. The system, with consistent voltage source properties (Table 2), is subjected to a 3-step non-linear load (NL1, NL2, NL3) (Fig. 13). Using fast Fourier transform (FFT), the SAPF's ability to suppress voltage harmonics from both load and source, compensate for harmonic source issues (Fig. 14), address voltage sags/swells, and counteract voltage droop due to source impedance is rigorously analyzed. Crucially, an FLC dynamically manages DC-link stages, ensuring stable power delivery to sensitive equipment despite varying load conditions.

Table 2

The dynamic characteristics of the source voltage over time for all scenarios

| Voltage source | Time, s |
|---|---|
| Normal voltage without SAPF | 0–0.1 |
| Normal voltage with SAPF | 0.1–0.2 |
| Decrease 25 % voltage (sag) | 0.2–0.4 |
| Normal voltage with SAPF | 0.4–0.6 |
| Increase 25 % voltage (swell) | 0.6–0.8 |
| Normal voltage with SAPF | 0.8–1 |
| Normal voltage with SAPF | 1–1.2 |
| Normal voltage with SAPF | 1.2–1.4 |
| Harmonic source | 1.4–1.6 |

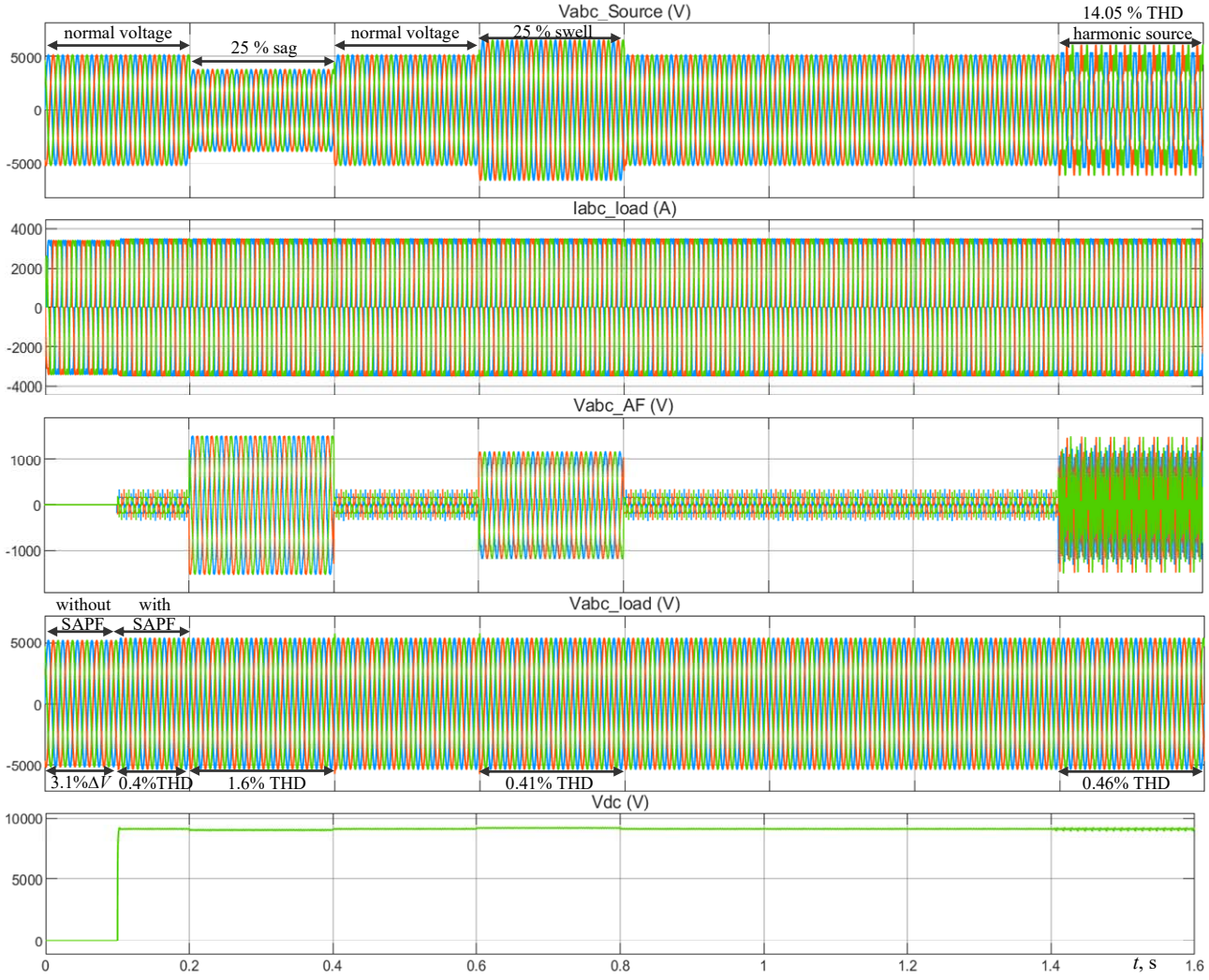


Fig. 13. Voltage waveforms and load current scenario 1

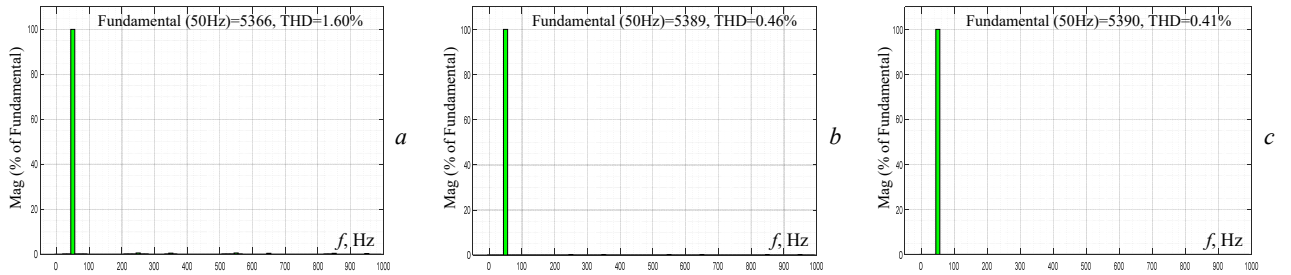


Fig. 14. Vabc_load FFT analysis scenario 1: *a* – during sag source; *b* – during swell source; *c* – during harmonic source

2) Second scenario.

This assessment evaluates the SAPF effectiveness under high linear loads and grid harmonic distortion.

The system, using consistent voltage source properties (Table 2), undergoes a 3-step linear load (L1, L2, L3) (Fig. 15). The focus is on mitigating source harmonics, compensating for transient disturbances, and suppressing voltage drops from source impedance.

FFT analysis details the results as shown in Fig. 16. FLC optimizes DC-link stage selection to maintain voltage quality for linear loads.

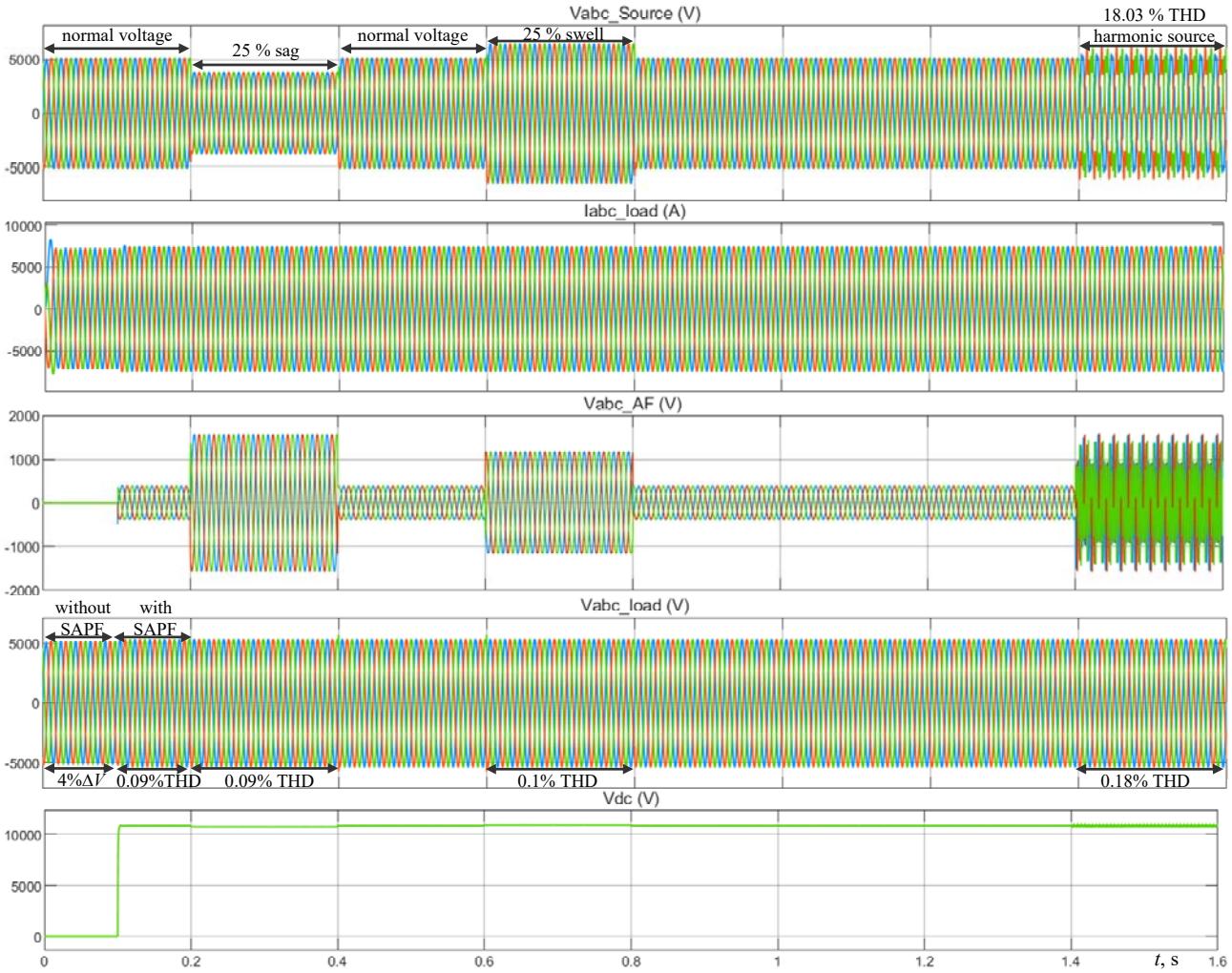


Fig. 15. Voltage waveforms and load current scenario 2

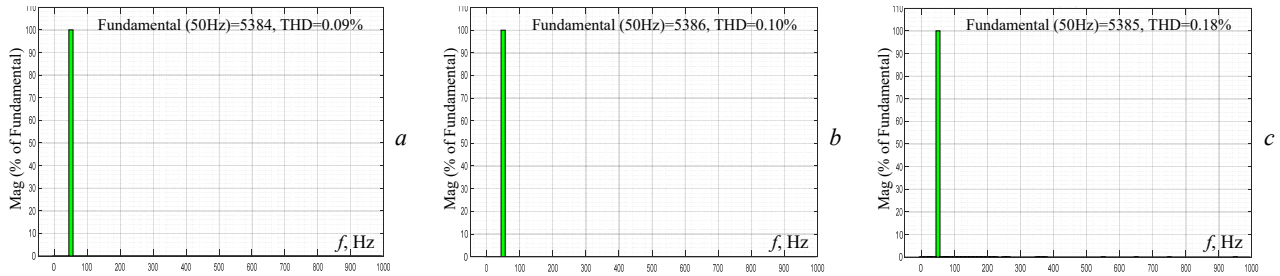


Fig. 16. Vabc_load FFT analysis scenario 2: *a* – during sag source; *b* – during swell source; *c* – during harmonic source

3) Third scenario.

This investigation assesses the SAPF's robustness under combined linear (L1, L2, L3) and non-linear (NL1, NL2, NL3) loads, with consistent voltage source properties (Table 2) (Fig. 17).

It evaluates the system's capacity to attenuate harmonics, address transient disturbances, and mitigate voltage droop in highly complex conditions.

A fuzzy-controlled DC-link adaptation ensures consistent performance under extreme load demands. The primary focus remains on mitigating source harmonics, compensating for transient disturbances, and suppressing voltage drops caused by source impedance.

FFT analysis provides detailed results (Fig. 18).

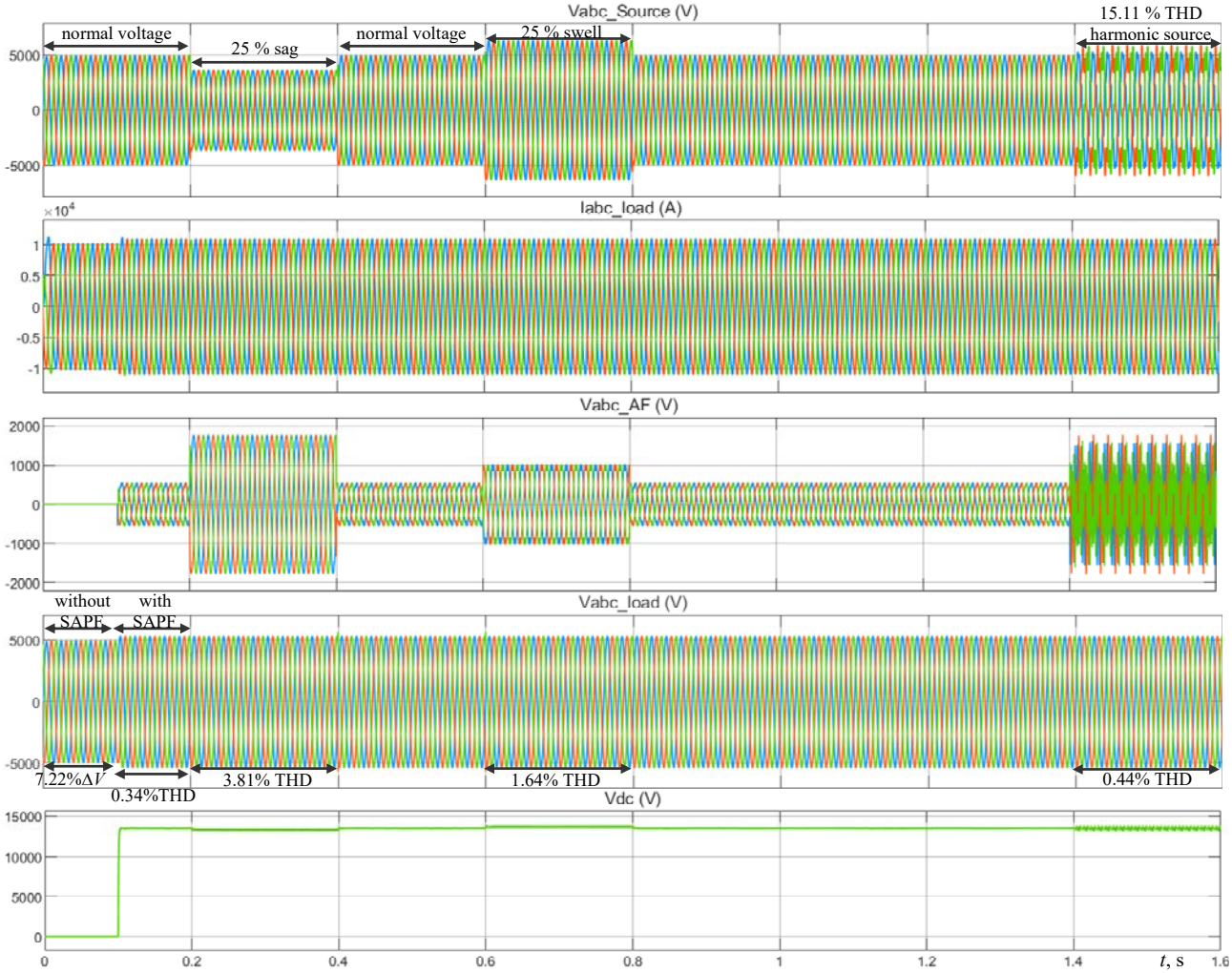


Fig. 17. Voltage waveforms and load current scenario 3

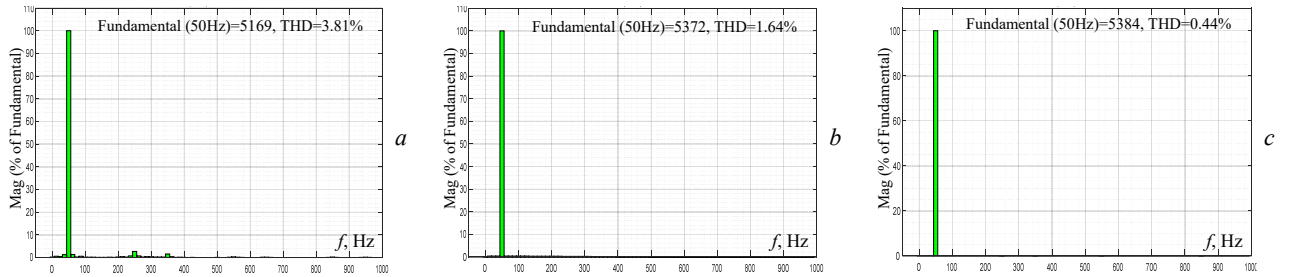


Fig. 18. Vabc_load FFT analysis scenario 3: *a* – during sag source; *b* – during swell source; *c* – during harmonic source

4) Fourth scenario. This section synthesizes the preceding analyses to demonstrate the precision of the SAPF and the accuracy of its DC-link voltage regulation (Fig. 19). The fuzzy logic control system dynamically selects the optimal DC-link stage by assessing load characteristics (magnitude and type) (Table 3), and the load voltage THD. This adaptive selection ensures efficient and precise compensation. Collectively, the simulations validate the SAPF's capability to enhance voltage quality across diverse load and grid conditions. FLC plays a pivotal role in optimizing DC-link dynamics, thereby ensuring both system stability and effective harmonic suppression.

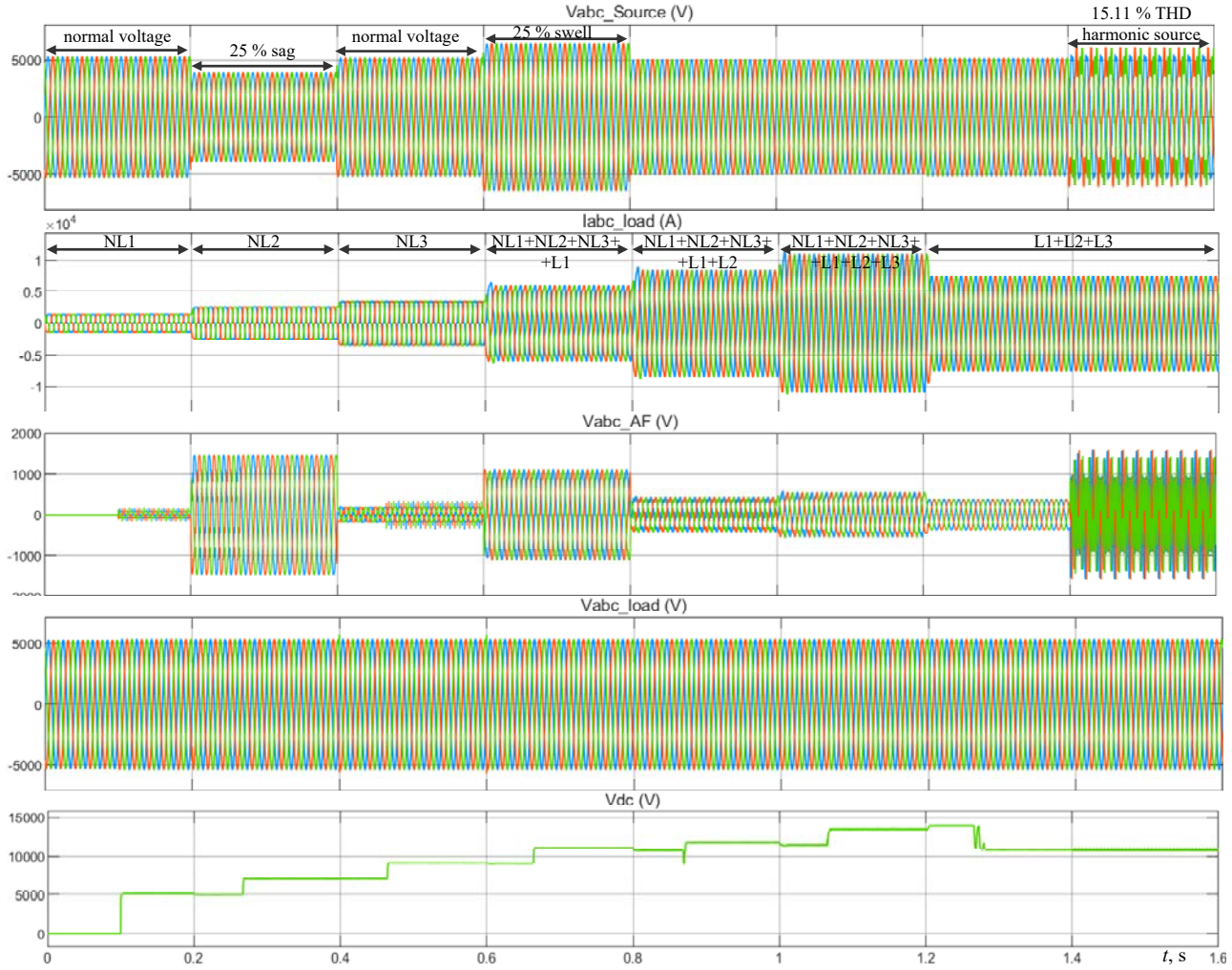


Fig. 19. Voltage waveforms and load current for the fourth scenario

Table 3

Load variations within the fourth scenario

| Time, s | Loads type |
|---|---|
| 0–0.1 | NL1 without SAPF |
| 0.1–0.2 | NL1 with SAPF |
| 0.2–0.4 | NL2 |
| 0.4–0.6 | NL3 |
| 0.6–0.8 | NL1+ NL2+ NL3+ L1 |
| 0.8–1 | NL1+ NL2+ NL3+ L1+ L2 |
| 1–1.2 | NL1+ NL2+ NL3+ L1+ L2+ L3 |
| 1.2–1.4 | L1+ L2+ L3 |
| 1.4–1.6 | L1+ L2+ L3 |

**Results discussion.** This study aims to evaluate the performance of a SAPF in mitigating power quality disturbances, including voltage sags, swells, and harmonic voltage sources. The voltage source values over time will be set according to the parameters listed in Table 2.

In the first scenario, the experimental results of this scenario demonstrate a significant improvement in the voltage waveform under non-linear load conditions following the introduction of the successive effective filter. The voltage stabilizing to the source value, indicating successful compensation for voltage drops, evidences this improvement (e.g., up to 3.1 % $\Delta V$) at the source without the use of SAPF (Fig. 13). Furthermore, FFT analysis, as Fig. 14,*a*,*b*,*c* confirms the system's efficiency in managing the load voltage, with observed THD values of 1.6 % during voltage sag, 0.41 % during voltage swell, and 0.46 % in the presence of a harmonic source exhibiting a 14.05 % THD

In the second scenario, the results of this scenario demonstrate a significant improvement in the voltage waveform with a high linear load after the introduction of the successive effective candidate. This improvement is evidenced by the voltage's stabilization to the source value, indicating successful compensation for voltage drops, which evidences this improvement (e.g., up to 4 % $\Delta V$) at the source without the use of SAPF (Fig. 15). Moreover, the FFT analyzer verifies that the system efficiently handles the load voltage, according to the following detected THD: 0.09 % for voltage sag, 0.1 % during voltage swell, and 0.07 % with a load-source that injects 18.03 % THD. These THD values are shown in Fig. 16,*a*,*b*,*c*.

In the third scenario, the results of this scenario demonstrate a significant improvement in the voltage waveform under combined 3-stage linear and 3-stage non-linear loads, with consistent voltage source properties (Table 2) after the introduction of the successive effective candidate. This improvement is evidenced by the voltage's stabilization to the source value, indicating successful compensation for voltage drops, which evidences this improvement (e.g., up to 7.22 % $\Delta V$) at the source without the use of SAPF (Fig. 17). Furthermore, the FFT analyzer confirms the system's efficiency in managing the load voltage, with the observed THD measured 3.81 % during voltage sag, 1.64 % during voltage swell, and 0.44 % in the presence of a harmonic source exhibiting a 15.11 % THD. These specific THD values are visually represented in Fig. 18,*a*,*b*,*c*.

In the fourth scenario, this section synthesizes prior analyses to demonstrate the efficacy of the SAPF and the precision of its DC-link voltage regulation. This is observed across diverse load conditions, as comprehensively presented in Table 3 and visually depicted in Fig. 19. The FLC dynamically determines the optimal harmonic compensation phase, and the quality of compensation is directly affected by the THD value. This type of adaptive control allows an effective, highly accurate compensation that is to be held stable below 5 % THD, in line with industry levels. Besides, the installation of SAPF helps to reduce the voltage drop developed across the source impedance, which in turn enhances the overall performance of the system.

**Conclusions**. This paper presents a novel 3-phase SAPF topology to address the increasing challenges of power quality deterioration in modern electrical systems, including electric power distribution networks. The proposed SAPF, the sole SAPF integrated with PV-battery energy storage, significantly enhances power quality. The outcome is highly effective in mitigating voltage abnormalities such as sags and swells, as well as filtering harmonic distortions in load voltage across various load circumstances (linear, non-linear, and mixed).

The THD values were measured well below the 5 % over the whole frequency range, 5 % (e.g., 1.6 % during sag, 0.41 % during swell, and 0.46 % with a harmonic source for non-linear loads), validating its efficiency. A key innovation is using an FLC system for dynamic DC-link voltage regulation and optimal harmonic compensation, which eliminates the need for medium-voltage transformers. The results confirm the SAPF's capability to ensure enhanced power quality, overall system stability, and proficient voltage management even during significant voltage drops (up to 7.22 % $\Delta V$) at the source without relying on conventional SAPFs. This robust and efficient solution offers a promising direction for maintaining optimal power quality in contemporary electrical grids. This work provides a future recommendation to enhance the efficiency and sustainability of the proposed system by adding a battery management system (BMS), which aims to precisely coordinate charging and discharging operations among the energy storage units (batteries). Implementing a BMS ensures a balanced distribution of the stored energy consumption, thereby avoiding uneven stress on individual units. Practically speaking, this extends the operational lifespan of the batteries (number of cycles) and improves the overall performance and reliability of the energy storage system.

**Acknowledgment.** The authors would like to express their sincere gratitude to the University of Mosul, College of Engineering, Department of Electrical Engineering, for their invaluable assistance with this effort.

**Conflict of interest.** The authors declare that they have no conflicts of interest.

REFERENCES

***1.*** Salleh Z.M.T., Alsammak A.N.B., Mohammed H.A. Enhancing Power System Transient Stability Using Static Var Compensator Based on a Fuzzy Logic Controller. *Journal Européen Des Systèmes Automatisés*, 2024, vol. 57, no. 6, pp. 1565-1572. doi: https://doi.org/10.18280/jesa.570603.

***2.*** Chaudhari M.A., Chandraprakash. Three-phase Series Active Power Filter as Power Quality Conditioner. *2012 IEEE International Conference on Power Electronics, Drives and Energy Systems (PEDES)*, 2012, pp. 1-6. doi: https://doi.org/10.1109/PEDES.2012.6484387.

***3.*** Zorig A., Babes B., Hamouda N., Mouassa S. Improving the efficiency of a non-ideal grid coupled to a photovoltaic system with a shunt active power filter using a self-tuning filter and a predictive current controller. *Electrical Engineering & Electromechanics*, 2024, no. 6, pp. 33-43. doi: https://doi.org/10.20998/2074-272X.2024.6.05.

***4.*** Qasim A.Y., Tahir F.R., Alsammak A.N.B. Improving Power Quality in Distribution Systems Using UPQC: An Overview. *Journal Européen Des Systèmes Automatisés*, 2024, vol. 57, no. 2, pp. 311-322. doi: https://doi.org/10.18280/jesa.570201.

***5.*** Manohara M., Muthukaruppasamy S., Dharmaprakash R., Sendilkumar S., Dattatreya Bharadwaj D., Parimalasundar E. Power quality enhancement of grid-integrated solar photovoltaic system with unified power quality conditioner. *Electrical Engineering & Electromechanics*, 2024, no. 6, pp. 44-48. doi: https://doi.org/10.20998/2074-272X.2024.6.06.

***6.*** Qasim A.Y., Tahir F.R., Alsammak A.N.B. Utilizing UPQC-Based PAC-SRF Techniques to Mitigate Power Quality Issues under Non-Linear and Unbalanced Loads. *Journal Européen Des Systèmes Automatisés*, 2023, vol. 56, no. 5, pp. 823-831. doi: https://doi.org/10.18280/jesa.560513.

***7.*** Kalyan K., Rao M.S., Gawre S. Improvement of Power Quality Using Series Active Power Filter (SAPF). *2020 IEEE International Students' Conference on Electrical, Electronics and Computer Science (SCEECS)*, 2020, pp. 1-5. doi: https://doi.org/10.1109/SCEECS48394.2020.151.

***8.*** Kim Y.S., Kim J.S., Ko S.H. Three-phase three-wire series active power filter, which compensates for harmonics and reactive power. *IEE Proceedings - Electric Power Applications*, 2004, vol. 151, no. 3, pp. 276-282. doi: https://doi.org/10.1049/ip-epa:20040208.

***9.*** Muthukaruppasamy S., Dharmaprakash R., Sendilkumar S., Parimalasundar E. Enhancing off-grid wind energy systems with controlled inverter integration for improved power quality. *Electrical Engineering & Electromechanics*, 2024, no. 5, pp. 41-47. https://doi.org/10.20998/2074-272X.2024.5.06.

***10.*** Benazza B., Ouadi H. Backstepping Control of Three-Phase Multilevel Series Active Power Filter. *2020 International Conference on Electrical and Information Technologies (ICEIT)*, 2020, pp. 1-6. doi: https://doi.org/10.1109/ICEIT48248.2020.9113178.

***11.*** Bousnoubra C., Djeghader Y., Belila H. Contribution of using a photovoltaic unified power quality conditioner in power quality improvement. *Electrical Engineering & Electromechanics*, 2024, no. 4, pp. 42-47. doi: https://doi.org/10.20998/2074-272X.2024.4.05.

***12.*** Venkatraman K., Selvan M.P., Moorthi S. Performance of Series Active Filter in low voltage distribution system with non linear loads. *2011 Annual IEEE India Conference*, 2011, pp. 1-6. doi: https://doi.org/10.1109/INDCON.2011.6139548.

***13.*** Mekri F., Machmoum M., Aït-Ahmed N., Mazari B. A comparative study of voltage controllers for series active power filter. *Electric Power Systems Research*, 2010, vol. 80, no. 6, pp. 615-626. doi: https://doi.org/10.1016/j.epsr.2009.10.025.

***14.*** Pazhanimuthu C., Ramesh S. Grid integration of renewable energy sources (RES) for power quality improvement using adaptive fuzzy logic controller based series hybrid active power filter (SHAPF). *Journal of Intelligent & Fuzzy Systems*, 2018, vol. 35, no. 1, pp. 749-766. doi: https://doi.org/10.3233/JIFS-171236.

***15.*** Das S.R., Ray P.K., Mohanty A. Fuzzy Sliding Mode Based Series Hybrid Active Power Filter for Power Quality Enhancement. *Advances in Fuzzy Systems*, 2018, pp. 1-8. doi: https://doi.org/10.1155/2018/1309518.

***16.*** Nakade V., Patil S. Implementation of Power Quality Enhancement using Hybrid Series Active Filter. *2019 International Conference on Communication and Electronics Systems (ICCES)*, pp. 238-241. doi: https://doi.org/10.1109/ICCES45898.2019.9002378.

***17.*** Toumi T., Allali A., Meftouhi A., Abdelkhalek O., Benabdelkader A., Denai M. Robust control of series active power filters for power quality enhancement in distribution grids: Simulation and experimental

validation. *ISA Transactions*, 2020, vol. 107, pp. 350-359. doi: https://doi.org/10.1016/j.isatra.2020.07.024.
**18.** Mishra K.K., Gupta R. Impedance Factor based Control Strategy for Series Active Power Filter in Distribution System. *IECON 2020 The 46th Annual Conference of the IEEE Industrial Electronics Society*, pp. 2987-2992. doi: https://doi.org/10.1109/IECON43393.2020.9255093.
**19.** Pazhanimuthu C., Baranilingesan I., Karthick A. An improved control algorithm for Series Hybrid Active Power Filter based on SOGI-PLL under dynamic load conditions. *Solid State Communications*, 2021, vol. 333, art. no. 114357. doi: https://doi.org/10.1016/j.ssc.2021.114357.
**20.** Cholamuthu P., Irusappan B., Paramasivam S.K., Ramu S.K., Muthusamy S., Panchal H., Nuvvula R.S.S., Kumar P.P., Khan B. A Grid-Connected Solar PV/Wind Turbine Based Hybrid Energy System Using ANFIS Controller for Hybrid Series Active Power Filter to Improve the Power Quality. *International Transactions on Electrical Energy Systems*, 2022, pp. 1-14. doi: https://doi.org/10.1155/2022/9374638.
**21.** Rustemli S., Satici M.A., Şahin G., Van Sark W. Investigation of harmonics analysis power system due to non-linear loads on the electrical energy quality results. *Energy Reports*, 2023, vol. 10, pp. 4704-4732. doi: https://doi.org/10.1016/j.egyr.2023.11.034.
**22.** Sathish Babu P., Balasundar C., Sundarabalan C.K. ANFIS controlled fuel cell powered series active filter for voltage waveform augmentation in the distribution grid. *E-Prime - Advances in Electrical Engineering, Electronics and Energy*, 2024, vol. 7, art. no. 100425. doi: https://doi.org/10.1016/j.prime.2024.100425.
**23.** Rafiq Nazer M.N., Noorwali A., Tajuddin M.F.N., Khan M.Z., Ahmad Tazally M.A.I., Ahmed J., Babu T.S., Ghazali N.H., Chakraborty C., Manoj Kumar N. Scenario-Based Investigation on the Effect of Partial Shading Condition Patterns for Different Static Solar Photovoltaic Array Configurations. *IEEE Access*, 2021, vol. 9, pp. 116050-116072. doi: https://doi.org/10.1109/ACCESS.2021.3105045.
**24.** Zhuang Y., Liu F., Huang Y., Zhang X., Zha X. A Voltage-Balancer-Based Cascaded DC–DC Converter With a Novel Power Feedforward Control for the Medium-Voltage DC Grid Interface of Photovoltaic Systems. *IEEE Access*, 2019, vol. 7, pp. 178094-178107. doi: https://doi.org/10.1109/ACCESS.2019.2959040.
**25.** Aravind S., Vinatha U., Jayasankar V.N. Wind-solar grid connected renewable energy system with series active self tuning filter. *2016 International Conference on Electrical, Electronics, and Optimization Techniques (ICEEOT)*, pp. 1944-1948. doi: https://doi.org/10.1109/ICEEOT.2016.7755028.
**26.** Meftouhi A., Abdelkhalek O., Allali A., Abdelkader A.B., Toumi T. PV integrated series active filter for sag voltage and harmonic compensation. *International Journal of Power Electronics and Drive Systems*, 2019, vol. 10, no. 3, pp. 1255-1262. doi: https://doi.org/10.11591/ijpeds.v10.i3.pp1255-1262.
**27.** Guergah M., Nebti K., Rezgui S.E., Benalla H., Ould-Abdeslam D. Power quality enhancement using active power filter five-level cascade H-bridge under unbalanced and distorted grid. *Electrical Engineering & Electromechanics*, 2023, no. 1, pp. 20-24. doi: https://doi.org/10.20998/2074-272X.2023.1.03.
**28.** Salmerón Revuelta P., Pérez Litrán S., Prieto Thomas J. Combined Shunt and Series Active Power Filters. *Active Power Line Conditioners*, 2016, pp. 231-284. doi: https://doi.org/10.1016/B978-0-12-803216-9.00007-9.
**29.** El Ghaly A., Tarnini M., Al Barakeh Z., Chahine K. Compensating voltage waveform distortions using a practical topology of series active power filters. *Results in Engineering*, 2024, vol. 22, art. no. 102032. doi: https://doi.org/10.1016/j.rineng.2024.102032.
**30.** Nguyen D., Lehman B. An Adaptive Solar Photovoltaic Array Using Model-Based Reconfiguration Algorithm. *IEEE Transactions on Industrial Electronics*, 2008, vol. 55, no. 7, pp. 2644-2654. doi: https://doi.org/10.1109/TIE.2008.924169.
**31.** Mimouni A., Laribi S., Sebaa M., Allaoui T., Bengharbi A.A. Fault diagnosis of power converters in a grid connected photovoltaic system using artificial neural networks. *Electrical Engineering & Electromechanics*, 2023, no. 1, pp. 25-30. doi: https://doi.org/10.20998/2074-272X.2023.1.04.
**32.** Mishra S., Ziar H., Isabella O., Zeman M. Selection Map for PV Module Installation Based on Shading Tolerability and Temperature Coefficient. *IEEE Journal of Photovoltaics*, 2019, vol. 9, no. 3, pp. 872-880. doi: https://doi.org/10.1109/JPHOTOV.2019.2900695.
**33.** Chaib H., Hassaine S., Mihoub Y., Moreau S. Intelligent power control strategy based on self-tuning fuzzy MPPT for grid-connected hybrid system. *Electrical Engineering & Electromechanics*, 2025, no. 3, pp. 23-30. doi: https://doi.org/10.20998/2074-272X.2025.3.04.
**34.** Hessad M.A., Bouchama Z., Benaggoune S., Behih K. Cascade sliding mode maximum power point tracking controller for photovoltaic systems. *Electrical Engineering & Electromechanics*, 2023, no. 1, pp. 51-56. doi: https://doi.org/10.20998/2074-272X.2023.1.07.
**35.** Shahir F.M., Aberoumandazar M., Babaei E. High Gain DC-DC Boost Converter Applied in Hybrid System of Photovoltaic and Battery. *2021 International Symposium on Devices, Circuits and Systems (ISDCS)*, 2021, pp. 1-4. doi: https://doi.org/10.1109/ISDCS52006.2021.9397922.
**36.** Surya P.P., Irawan D., Zuhri M. Review and comparison Of DC-DC converters for maximum power point tracking system in standalone photovoltaic (PV) module. *2017 International Conference on Advanced Mechatronics, Intelligent Manufacture, and Industrial Automation (ICAMIMIA)*, 2017, pp. 242-247. doi: https://doi.org/10.1109/ICAMIMIA.2017.8387595.
**37.** Latreche K., Taleb R., Bentaallah A., Toubal Maamar A.E., Helaimi M., Chabni F. Design and experimental implementation of voltage control scheme using the coefficient diagram method based PID controller for two-level boost converter with photovoltaic system. *Electrical Engineering & Electromechanics*, 2024, no. 1, pp. 3-9. doi: https://doi.org/10.20998/2074-272X.2024.1.01.
**38.** Farswan R.S., Datta A., Kamble G., Fernandes B.G. A low leakage transformer-less 3-level DC-DC boost converter for transformer-less PV inverters. *2015 17th European Conference on Power Electronics and Applications (EPE'15 ECCE-Europe)*, 2015, pp. 1-10. doi: https://doi.org/10.1109/EPE.2015.7309321.
**39.** Bonfiglio A., Brignone M., Delfino F., Procopio R. Optimal Control and Operation of Grid-Connected Photovoltaic Production Units for Voltage Support in Medium-Voltage Networks. *IEEE Transactions on Sustainable Energy*, 2014, vol. 5, no. 1, pp. 254-263. doi: https://doi.org/10.1109/TSTE.2013.2280811.
**40.** Yang T., Mok K.-T., Ho S.-S., Tan S.-C., Lee C.-K., Hui R.S.Y. Use of Integrated Photovoltaic-Electric Spring System as a Power Balancer in Power Distribution Networks. *IEEE Transactions on Power Electronics*, 2019, vol. 34, no. 6, pp. 5312-5324. doi: https://doi.org/10.1109/TPEL.2018.2867573.
**41.** Parimalasundar E., Kumar N.M.G., Geetha P., Suresh K. Performance investigation of modular multilevel inverter topologies for photovoltaic applications with minimal switches. *Electrical Engineering & Electromechanics*, 2022, no. 6, pp. 28-34. doi: https://doi.org/10.20998/2074-272X.2022.6.05.
**42.** Huang X., Wang H., Guo L., Ju C., Liu R., Meng S., Wang Y., Xu H. Large-scale photovoltaic generation system connected to HVDC grid with centralized high voltage and high power DC/DC converter. *2017 20th International Conference on Electrical Machines and Systems (ICEMS)*, 2017, pp. 1-6. doi: https://doi.org/10.1109/ICEMS.2017.8056289.
**43.** Ayat Y., Badoud A.E., Mekhilef S., Gassab S. Energy management based on a fuzzy controller of a photovoltaic/fuel cell/Li-ion battery/supercapacitor for unpredictable, fluctuating, high-dynamic three-phase AC load. *Electrical Engineering & Electromechanics*, 2023, no. 3, pp. 66-75. doi: https://doi.org/10.20998/2074-272X.2023.3.10.
**44.** Adiche S., Larbi M., Toumi D. Optimizing voltage control in AC microgrid systems with fuzzy logic strategies and performance assessment. *Electrical Engineering & Electromechanics*, 2025, no. 3, pp. 11-17. doi: https://doi.org/10.20998/2074-272X.2025.3.02.
**45.** Mohammed H.A., Alsammak A.N.B. An Intelligent Hybrid Control System using ANFIS-Optimization for Scalar Control of an Induction Motor. *Journal Européen Des Systèmes Automatisés*, 2023, vol. 56, no. 5, pp. 857-862. doi: https://doi.org/10.18280/jesa.560516.
**46.** Zerzouri N., Ben Si Ali N., Benalia N. A maximum power point tracking of a photovoltaic system connected to a three-phase grid using a variable step size perturb and observe algorithm. *Electrical Engineering & Electromechanics*, 2023, no. 5, pp. 37-46. doi: https://doi.org/10.20998/2074-272X.2023.5.06.

*Received 29.07.2025*
*Accepted 25.09.2025*
*Published 02.01.2026*

*B.M. Anwer*[1]*, MSc, Assistant Lecturer, PhD Student,*
*A.N. Alsammak*[1]*, PhD, Professor,*
[1] Electrical Engineering Department,
College of Engineering, University of Mosul, Iraq,
e-mail: ahmed_alsammak@uomosul.edu.iq (Corresponding Author)

*How to cite this article:*
Anwer B.M., Alsammak A.N. An integrated series active power filter combined with a PV-battery system based on a fuzzy logic controller to enhance power quality for various linear and non-linear loads. *Electrical Engineering & Electromechanics*, 2026, no. 1, pp. 51-62. doi: https://doi.org/10.20998/2074-272X.2026.1.07

UDC 621.314 https://doi.org/10.20998/2074-272X.2026.1.08

A. Nayli, S. Guizani, F. Ben Ammar

# Association smooth-pole dual open-end windings permanent magnet synchronous machine with cascaded 2-level inverters for improved performances

***Introduction.*** *Power segmentation is an increasingly important priority in high-power industrial drive applications that utilize AC machines.* ***Problem****. To improve the dynamic performance, reliability and power segmentation of drive systems in high-power applications (above the megawatt range), it's advantageous to replace a single high-power converter with several low-power converters. This principle is applied to the combination of AC machines and inverter structures.* ***Goal.*** *The authors propose a novel dual open-end windings permanent magnet synchronous machine. This machine reduces the required size of the power supply inverters while also improving dynamic performances and lifespan. Its power supply using 2-levels cascading inverters, further enhances these performances.* ***Methodology.*** *For this study, the mathematical model of the system in the Park reference frame is introduced and validated using the MATLAB/Simulink environment. First, simulation results are presented for the proposed machine supplied by four conventional two-level inverters based on the pulse width modulation technique. Next, the new machine is fed by four multilevel converters, with each converter consisting of two two-level inverters. To further demonstrate the benefits of this converter structure, the authors then use a configuration with three cascaded two-level inverters. The* ***results*** *demonstrate that the use of the new machine with conventional two-level inverters ensures power segmentation and improves the quality of the voltage, stator current, and torque. Furthermore, associating this same machine with cascaded multilevel inverter structures significantly enhances dynamic performance and reliability. The* ***scientific novelty*** *lies in the synergy achieved by integrating the novel synchronous machine with the cascaded two-level inverters, enabling the system to simultaneously surpass conventional limitations in both performance and reliability.* ***Practical value.*** *A simulation model of the novel dual open-end winding permanent magnet synchronous machine was implemented to validate the superior performance achieved with cascaded multilevel inverter structures for voltage supply compared to conventional two-level inverters.* References 19, table 2, figures 17.

*Key words:* **smooth-pole dual open end permanent magnet synchronous machine, cascaded 2-levels inverters, power segmentation, reliability.**

***Вступ****. Сегментація потужності стає все більш важливим завданням у потужних промислових приводних системах, що використовують машини змінного струму.* ***Проблема****. Для покращення динамічних характеристик, надійності та сегментації потужності приводних систем у потужних установках (вище мегаватного діапазону) доцільно замінити один потужний перетворювач кількома малопотужними перетворювачами. Цей принцип застосовується для комбінації машин змінного струму та інверторних структур.* ***Мета****. Автори пропонують нову синхронну машину з двома відкритими обмотками та постійними магнітами. Ця машина зменшує необхідні розміри інверторів живлення, одночасно покращуючи динамічні характеристики та термін служби. Її живлення із використанням дворівневих каскадних інверторів додатково підвищує ці характеристики.* ***Методика****. Для цього дослідження розроблена математична модель системи у системі координат Парка, яка перевірена у MATLAB/Simulink. Спочатку представлені результати моделювання для пропонованої машини, що живиться чотирма звичайними дворівневими інверторами на основі методу широтно-імпульсної модуляції. Потім нова машина заживлювалась від чотирьох багаторівневих перетворювачів, кожен із яких складається з двох дворівневих інверторів. Для подальшої демонстрації переваг даної структури перетворювача автори використовують конфігурацію з трьома каскадно з'єднаними дворівневими інверторами.* ***Результати*** *показують, що використання нової машини із звичайними дворівневими інверторами забезпечує сегментацію потужності та покращує якість напруги, струму статора та крутного моменту. Крім того, поєднання цієї машини з каскадно з'єднаними багаторівневими інверторними структурами значно підвищує динамічні характеристики і надійність.* ***Наукова новизна*** *полягає в синергії, яка досягається за рахунок інтеграції нової синхронної машини з каскадно з'єднаними дворівневими інверторами, що дозволяє системі одночасно долати традиційні обмеження як за продуктивністю, так і за надійністю.* ***Практична значимість****. Реалізована імітаційна модель нової синхронної машини з двома відкритими обмотками та постійними магнітами для підтвердження високих характеристик, що досягаються за допомогою каскадно з'єднаних багаторівневих інверторних структур для живлення напруги порівняно із звичайними дворівневими інверторами.* Бібл. 19, табл. 2, рис. 17.

*Ключові слова:* **гладкополюсна синхронна машина з постійними магнітами та двостороннім відкритим виводом, каскадні дворівневі інвертори, сегментація потужності, надійність.**

**Introduction.** The machine-converter associations are widely used in application industrial drives [1–3]. But this association machine with conventional converter is not without disadvantage especially in high power. To ensure the power segmentation, the improvement the reliability and consequently the availability of this association inverter-machine, several researches have also been developed. The research at the level of inverter structures includes cascaded H-bridge multilevel inverters, diode clamped multilevel inverters, flying-capacitor multilevel inverters, cascaded two-level inverters and other structures [4–8] and in synchronous or asynchronous machines structures, in particular the permanent magnet synchronous machine (PMSM) includes multiphase machines [9, 10], the multi-star machines [11, 12], the open-end stator winding machine [13, 14] and the multiphase open-end stator windings machine [15]. Recently, some researchers have developed the new machine structure; it is the dual three-phase open-end stator windings AC machines supplied by four voltage source inverters [16–18]. Furthermore, this machine offers good solution for the power segmentation and best dynamic performance compared with classic machine, double star machine and open-end stator winding machine. Also, this machine increases the liberty degrees of system drive in degraded mode.

The **goal** of this work is to present a novel dual open-end windings permanent magnet synchronous machine (DOEWPMSM). This machine is designed to improve dynamic performance and lifetime, while reducing the size of the required power inverters. The use of cascaded two-level inverters improves these performances. In the first part, the mathematical modeling of novel machine is presented in the Park reference frame and implemented in MATLAB/Simulink environment. In the second part, the

proposed machine is fed by four voltage source inverters using a pulse width modulation (PWM) technique. The results obtained for the total harmonic distortion (THD) of the phase-to-phase voltage, the THD of the stator current, and the torque ripple are shown. To improve the performance of the new machine, a combination of cascaded inverter structures is used. In the first configuration, two cascaded 2-level inverters are used, while the second configuration consists of three cascaded 2-level inverters [19]. The simulation results obtained from the cascaded configurations show significant advantages in terms of voltage, current and torque quality.

**Modeling of the smooth-pole DOEWPMSM.** The windings of this machine shifted by 0° in the (*d*, *q*) Park reference ($\omega_{(d,\,q)} = \omega_r$) are represented in Fig. 1.

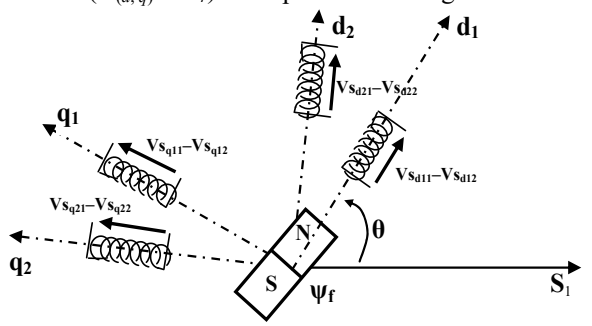


Fig. 1. Windings representation in the (*d*, *q*) reference frame

The relation that links the flux and the currents is:

$$\begin{bmatrix}\psi_{sd1}\\ \psi_{sd2}\\ \psi_{sq1}\\ \psi_{sq2}\end{bmatrix}=\begin{bmatrix}L_d & M_d & 0 & 0\\ M_d & L_d & 0 & 0\\ 0 & 0 & L_q & M_q\\ 0 & 0 & M_q & L_q\end{bmatrix}\begin{bmatrix}i_{sd1}\\ i_{sd2}\\ i_{sq1}\\ i_{sq2}\end{bmatrix}+\begin{bmatrix}\psi_f\\ \psi_f\\ 0\\ 0\end{bmatrix}. \quad (1)$$

The voltage is related by the following matrix:

$$\begin{bmatrix}V_{sd11}-V_{sd12}\\ V_{sd21}-V_{sd22}\\ V_{sq11}-V_{sq12}\\ V_{sq21}-V_{sq22}\end{bmatrix}=\begin{bmatrix}R_s & 0 & 0 & 0\\ 0 & R_s & 0 & 0\\ 0 & 0 & R_s & 0\\ 0 & 0 & 0 & R_s\end{bmatrix}\begin{bmatrix}i_{sd1}\\ i_{sd2}\\ i_{sq1}\\ i_{sq2}\end{bmatrix}+\frac{d}{dt}\begin{bmatrix}\psi_{sd1}\\ \psi_{sd2}\\ \psi_{sq1}\\ \psi_{sq2}\end{bmatrix}+ \quad (2)$$

$$+\begin{bmatrix}0 & 0 & -\omega_{dq} & 0\\ 0 & 0 & 0 & -\omega_{dq}\\ \omega_{dq} & 0 & 0 & 0\\ 0 & \omega_{dq} & 0 & 0\end{bmatrix}\begin{bmatrix}\psi_{sd1}\\ \psi_{sd2}\\ \psi_{sq1}\\ \psi_{sq2}\end{bmatrix},$$

where $R_s$ is the stator resistance; $L_d = L_q = L$ is the stator inductance in *d*, *q* axis for the smooth-pole synchronous machine; $M_d$ is the mutual inductance of the stator in $d_1$, $d_2$ axis; $M_q$ is the mutual inductance of stator in $q_1$, $q_2$ axis; $\psi_f$ is the flux of the permanent magnet by pole.

If the smooth-pole DOEWPMSM is supplied by voltage sources, the mathematical current model is written in (*d*, *q*) reference frame, and described as:

$$\frac{d}{dt}[I]=[A]\cdot[I]+[B]\cdot[V], \quad (3)$$

where: $[\boldsymbol{I}]=\begin{bmatrix}i_{sd1} & i_{sd2} & i_{sq1} & i_{sq2}\end{bmatrix}^T$ is the state vector;

$[\boldsymbol{V}]=\begin{bmatrix}V_{sd11}-V_{sd12}\\ V_{sd21}-V_{sd22}\\ V_{sq11}-V_{sq12}\\ V_{sq21}-V_{sq22}\\ \psi_f\end{bmatrix}^T$ is the control vector.

The state matrix [***A***] is:

$$[A]=-\begin{bmatrix}\frac{R_sL}{L^2-M_d^2} & \frac{-R_sL}{L^2-M_d^2} & -\omega_{dq} & 0\\ \frac{-R_sL}{L^2-M_d^2} & \frac{R_sL}{L^2-M_d^2} & 0 & -\omega_{dq}\\ \omega_{dq} & 0 & \frac{R_sL}{L^2-M_q^2} & \frac{-R_sM_q}{L^2-M_q^2}\\ 0 & \omega_{dq} & \frac{-R_sM_q}{L^2-M_q^2} & \frac{R_sL}{L^2-M_q^2}\end{bmatrix}. \quad (4)$$

The matrix [***B***] is:

$$[B]=\begin{bmatrix}\frac{L}{L^2-M_d^2} & \frac{-M_d}{L^2-M_q^2} & 0 & 0 & 0\\ \frac{-M_d}{L^2-M_q^2} & \frac{L}{L^2-M_d^2} & 0 & 0 & 0\\ 0 & 0 & \frac{L}{L^2-M_d^2} & \frac{-M_q}{L^2-M_q^2} & \frac{-\omega_{dq}}{L-M_q}\\ 0 & 0 & \frac{-M_q}{L^2-M_q^2} & \frac{L}{L^2-M_d^2} & \frac{-\omega_{dq}}{L-M_q}\end{bmatrix}. \quad (5)$$

The electromagnetic torque of the DOEWPMSM is:

$$T_{em}=\frac{3}{2}p((M_d-M_q)(i_{sd2}i_{sq1}+i_{sd1}i_{sq2})+\psi_f(i_{sq1}+i_{sq2})). \quad (6)$$

The drive mechanical equation is:

$$T_{em}-T_r=J\frac{d\omega}{dt}+f\cdot\omega. \quad (7)$$

**Case 1. Supply of the DOEWPMSM by 2-levels inverters.** The DOEWPMSM is fed by four three-phase 2-level inverters based on PWM technique (Fig. 2) with:
$Vs_{A11}$, $Vs_{A12}$, $Vs_{A13}$ are the simple voltage of inverter $A_1$;
$Vs_{A21}$, $Vs_{A22}$, $Vs_{A23}$ are the simple voltage of inverter $A_2$;
$Vs_{B11}$, $Vs_{B12}$, $Vs_{B13}$ are the simple voltage of inverter $B_1$;
$Vs_{B21}$, $Vs_{B22}$, $Vs_{B23}$ are the simple voltage of inverter $B_2$;
($Vs_{A11}$–$Vs_{A12}$) is the pole voltage of inverter $A_1$;
($Vs_{A21}$–$Vs_{A22}$) is the pole voltage of inverter $A_2$;
($Vs_{B11}$–$Vs_{B12}$) is the pole voltage of inverter $B_1$;
($Vs_{B21}$–$Vs_{B22}$) is the pole voltage of inverter $B_2$;
$U_A$ = ($Vs_{A11}$–$Vs_{A12}$)–($Vs_{A21}$–$Vs_{A22}$) is the phase-to-phase voltage of machine stator winding A;
$U_B$ = ($Vs_{B11}$–$Vs_{B12}$)–($Vs_{B21}$–$Vs_{B22}$) is the phase-to-phase voltage of machine stator winding B.

The voltages ($Vs_{A11}$–$Vs_{A12}$), ($Vs_{A21}$–$Vs_{A22}$), $U_A$ (winding A) and same simulation results for winding B are shown in Fig. 3.

Figure 4 shows the harmonic content of the phase-to-phase machine voltage.

Figure 5 shows the simulation results of the speed and the torque. At time $t$ = 1 s the impact of torque $T_r$ = 180 N·m is applied.

In order to analyse the torque quality, the definition of the torque undulations $\Delta T_{em}$ by the expression is:

$$\Delta T_{em}=\frac{T_{max}-T_{em}}{T_{em}}\cdot 100\%. \quad (8)$$

The enlarging effect of the torque for a load torque $T_r = T_n$ is indicated in Fig. 6.

Then, the torque undulation is:

$$\Delta T_{em}=\frac{211.5-180}{180}\cdot 100\%=17.5\%.$$

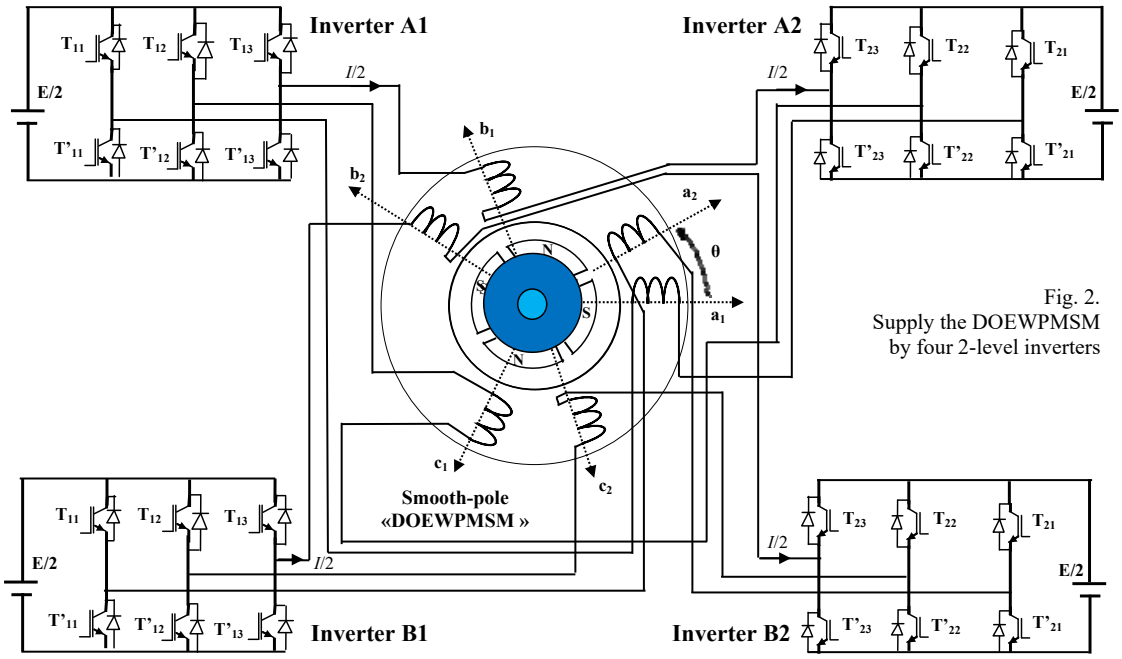


Fig. 2.
Supply the DOEWPMSM
by four 2-level inverters

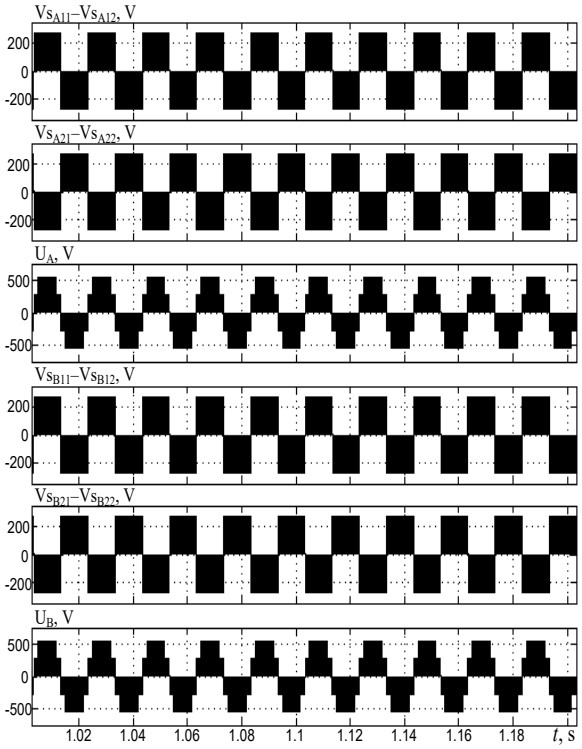


Fig. 3. Pole voltages of inverters and phase-to-phase voltages of machine stator windings A and B

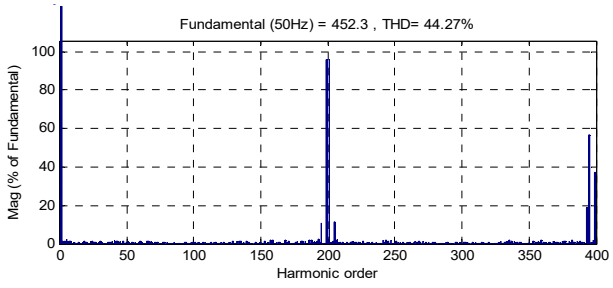


Fig. 4. Harmonic content of machine voltage

The simulation results of the stator currents $I_{s11}$ of the winding A and $I_{s21}$ of the winding B are shown in Fig. 7.

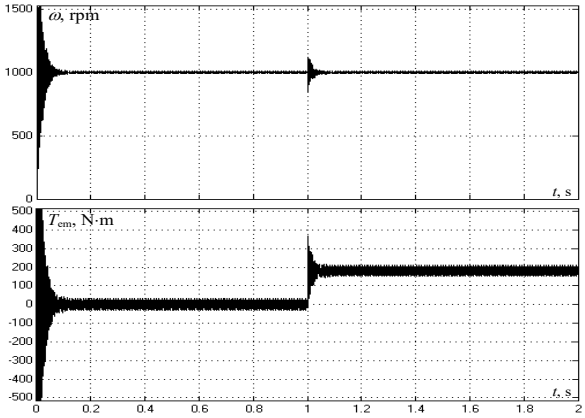


Fig. 5. The simulation results of the speed and the torque

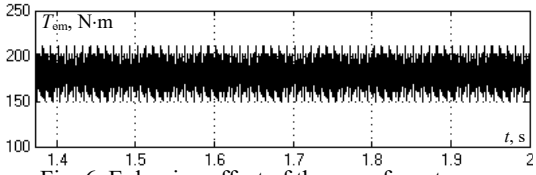


Fig. 6. Enlarging effect of the waveform torque

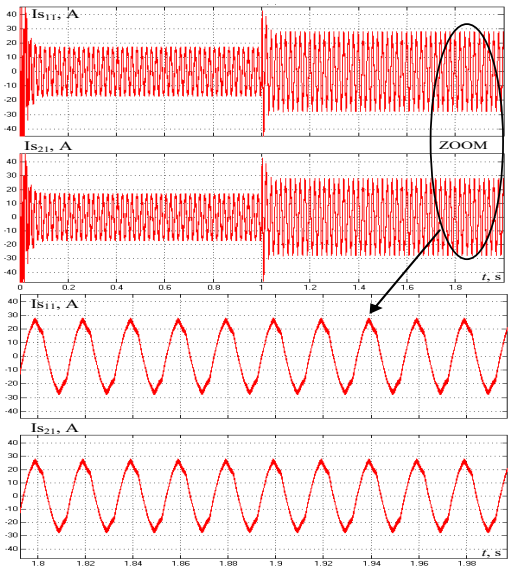


Fig. 7. The simulation results of the stator currents

The harmonic content of the stator current $Is_{11}$ of the winding A is shown in Fig. 8.

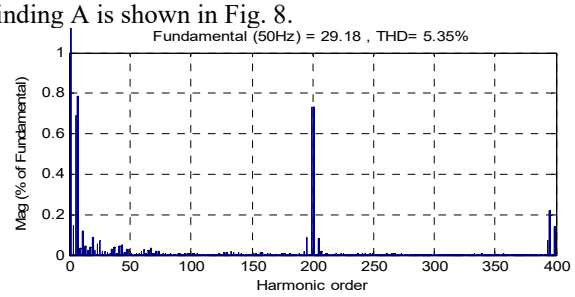


Fig. 8. The harmonic content of the stator current

**Case 2. Supply of the DOEWPMSM by two 2-levels inverters in cascading.** To enhance the performance of the DOEWPMSM in terms of voltage, current and torque quality, it's essential to supply it with a multi-level inverter. As shown in Fig. 9, this inverter is a cascaded configuration of two 2-level inverters [19].

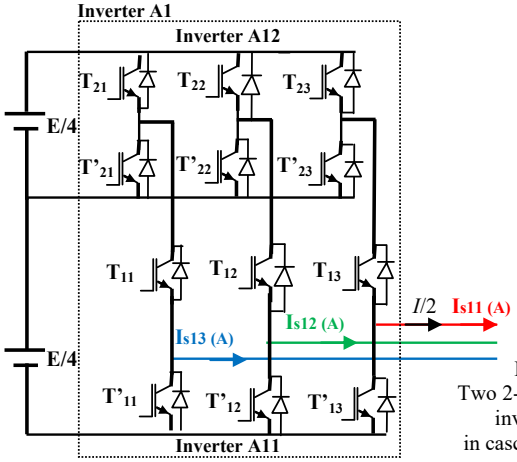


Fig. 9. Two 2-levels inverters in cascading

In order to control the two cascaded 2-level inverters, the phase disposition PWM technique was used, as shown in Fig. 10.

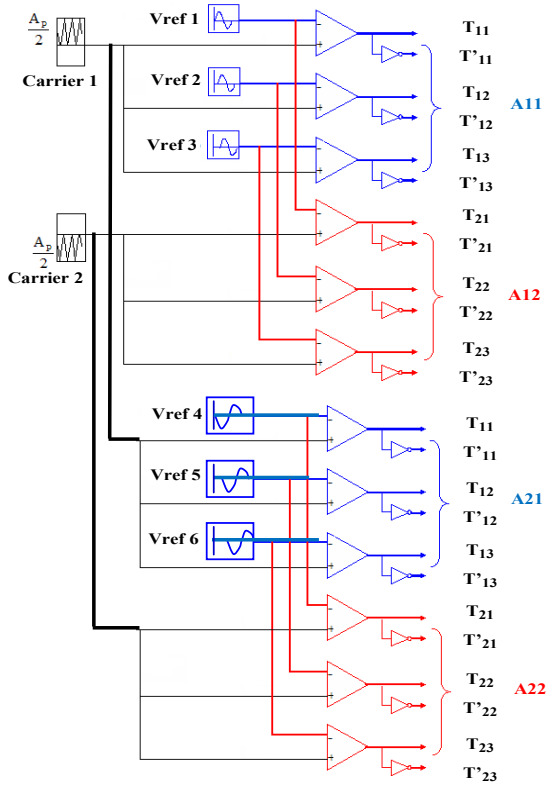


Fig. 10. Principle of the phase disposition PWM technique

Three reference voltages with a frequency of $f_s$ and a 120° phase shift between them are compared with two amplitude carriers. This method controls the two cascaded inverters at input A1 of stator winding A. Similarly, three other reference voltages, shifted by 180° relative to the first three, are compared with the same carriers to control the two cascaded inverters at input A2 of stator winding A. This same control principle is applied to the two cascaded inverters located at inputs B1 and B2 of stator winding B.

Figure 11 shows the pole voltages ($Vs_{A11}$–$Vs_{A12}$), ($Vs_{A21}$–$Vs_{A22}$) and the phase-to-phase voltage $U_A$ of the stator winding A, which have five voltage levels between phases of the machine. The same applies to the stator winding B.

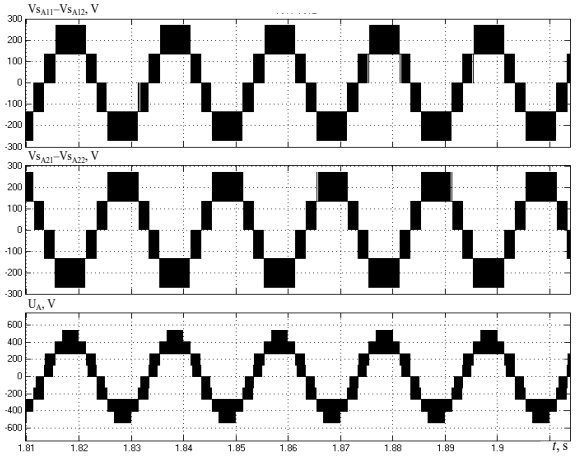


Fig. 11. The pole voltages and the phase-to-phase voltage of the stator winding A (case 2)

The harmonic content of the phase-to-phase machine voltage for the DOEWPMSM is shown in Fig. 12.

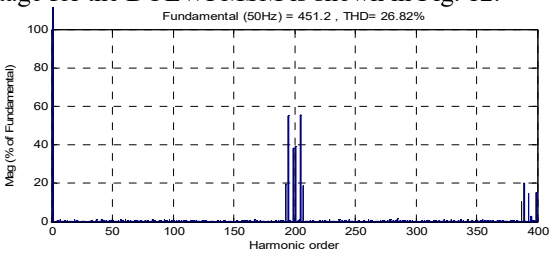


Fig. 12. The harmonic content of the machine voltage

Using multi-level voltage converters to feed the DOEWPMSM significantly improves the voltage level and reduces its THD from 44.27 % with a conventional inverter to 26.82 % with cascaded 2-level inverters. The enlarging effect of the torque is indicated in Fig. 13. Then, the torque undulation is:

$$\Delta T_{em} = \frac{193-180}{180}\cdot 100\% = 7.22\% .$$

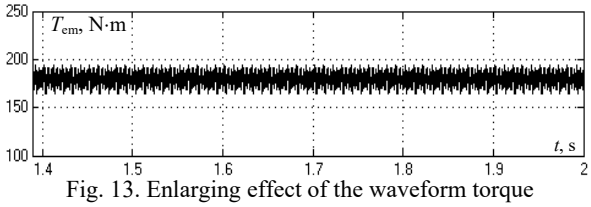


Fig. 13. Enlarging effect of the waveform torque

The harmonic content of stator current is shown in Fig. 14. Connecting the machine to two cascaded 2-level inverters, instead of a conventional inverter, improved the stator current's THD from 5.35 % to 3.86 %. It also reduced torque ripple from 17.5 % to 7.22 %.

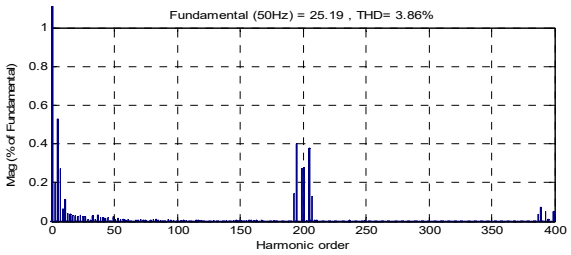


Fig. 14. The harmonic content of the stator current

**Case 3. Supply of the DOEWPMSM by three 2-levels inverters in cascading.** To demonstrate the performance improvement gained by using cascaded 2-level inverters, the proposed machine is also supplied by a second cascaded multi-level inverter structure at each input (A1, A2, B1 and B2). This structure is formed by three 2-level inverters connected in a cascade (Fig. 15).

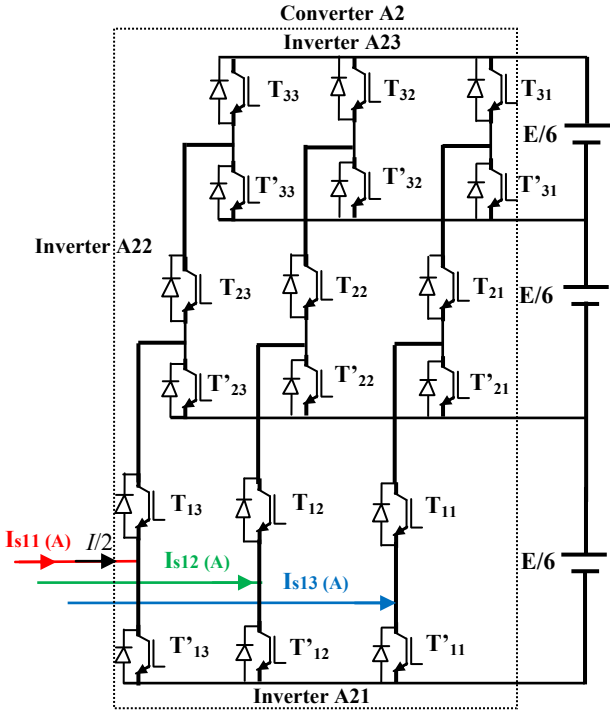


Fig. 15. Three 2-levels inverters in cascading

Figure 16 shows the pole voltages ($Vs_{A11}$–$Vs_{A12}$), ($Vs_{A21}$–$Vs_{A22}$) and phase-to-phase voltage $U_A$ of the stator winding A. The results indicate that an increase in the voltage level enhances the lifespan of this machine.

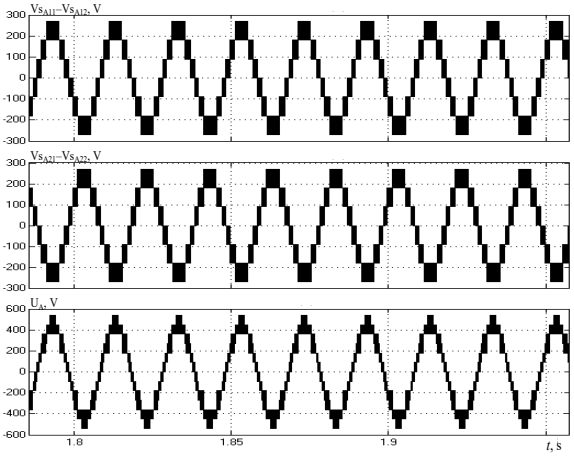


Fig. 16. The pole voltages and the phase-to-phase voltage of the stator winding A (case 3)

The enlarging effect of the waveform torque is shown in Fig. 17.

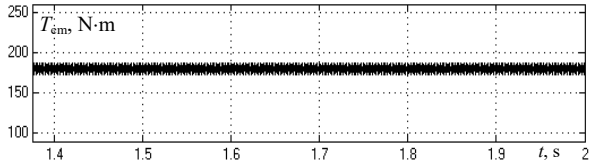


Fig. 17. Enlarging effect of the waveform torque

Then, the torque undulation is:

$$\Delta T_{em} = \frac{187.4 - 180}{180} \cdot 100\% = 4.11\% .$$

Table 1 presents the results obtained with three cascaded inverters, along with those from the two other types of power supply structures. This table clearly illustrates the advantages of the DOEWPMSM when combined with cascaded 2-level inverters. Indeed, the use of these cascaded structures improves stator current quality, voltage THD and reduces torque ripple.

Table 1

Different results for three structures

| Inverter A1 | 1 inverter | 2 cascaded inverters | 3 cascaded inverters |
|---|---|---|---|
| THD voltage, % | 44.27 | 26.82 | 16.42 |
| THD current, % | 5.35 | 3.86 | 1.63 |
| $\Delta T_{em}$, % | 17.5 | 7.22 | 4.11 |

Assuming the machine has a total power $P$. Table 2 summarizes the specifications for its power supply system. The table details the power ratings for the two cascaded inverters, as well as the required stator current and the voltage of the switches needed to supply the machine. This same process is applied to all inverter modules at each of the machine's inputs, ensuring consistent sizing across the entire system [19].

Table 2

Sizing of the two cascaded inverters

| Inverter A1 | Power inverter | Stator current, A | Switches voltage, V |
|---|---|---|---|
| Inverter A11 | $P/4$ | I/2 | $V_{T11} = E/2$ |
| Inverter A12 | $P/8$ | I/2 | $V_{T21} = E/4$ |

Table 2 demonstrates that using two cascaded inverters to supply the DOEWPMSM is not a constraint but rather a key component of power segmentation. The table shows that the cascaded inverter A12 has a significantly lower power rating $P/8$ than the principal inverter A11. This finding is crucial because it indicates that the system can be built with a smaller and more cost-effective secondary inverter while still achieving the benefits of a multilevel configuration.

The combination of a DOEWPMSM with cascaded inverters provides a reliable solution for degraded-mode operation. However, to ensure the drive system's continued performance, specific operational conditions must be met in the event of an inverter failure. This involves a precise reduction of the machine's speed to prevent a rise in current draw, which in turn avoids the overheating of both the motor windings and, most importantly, the semiconductor devices.

The characteristics of the machine are: nominal power $P$ = 40 kW, speed 1000 rpm, stator resistance $R_s$ = 65 mΩ, stator inductance $L_d = L_q$= 0.655 mH, mutual inductance of stator $d_{1,2}$ axis $M_d$ = 0.545 mH, mutual inductance of stator $q_{1,2}$ axis $M_q$ = 0.545 mH, magnet flux $\psi_f$ = 0.8 Wb, inertia moment $J$ = 0.02 kg·m$^2$, viscous force $F = 2\ 10^{-3}$ N·m·s/rad.

**Conclusions.** The novel smooth-pole dual open-end windings permanent magnet synchronous machine (DOEWPMSM) when associated with cascaded inverters structures offers a significant advantage over the conventional 2-levels inverters. The mathematical model of the DOEWPMSM is presented and simulated in MATLAB/Simulink. The machine is first fed by conventional 2-level inverter and then by cascaded 2-level inverter structures. The new machine offers such benefits:

- a good solution for power segmentation, reducing clutter, improving the availability of the drive system, and increasing redundancy in degraded mode compared to a classic synchronous machine.
- When the new machine is powered by cascaded 2-level inverter structures, it provides a better voltage level between the machine phases. With a conventional 2-level inverter, three levels are obtained. With two 2-level inverters in cascading, five levels are obtained, and with three 2-level inverters in cascading, seven levels are obtained.
- A better voltage THD. If the THD is 44.27 % with a conventional inverter, it drops to 16.42 % when powered by three 2-level inverters in cascading.
- A better quality of stator current. With a conventional inverter, the THD is 5.35 %. Using three cascaded 2-level inverters, the THD becomes 1.63 %.
- A better torque quality. The value decreases from 17.5 % to 4.11 % with three cascaded 2-level inverters.
- A reduced the DC bus voltage value of $E$ going from $E/2$ to $E/6$ with three cascaded 2-level inverters.
- An extended bandwidth.

In future work it is planned to experimentally confirm the advantages of the proposed new DOEWPMSM and powered using cascaded 2-level inverters.

**Conflict of interest.** The authors declare that they have no conflicts of interest.

REFERENCES


*1.* Nemouchi B., Rezgui S.E., Benalla H., Nebti K. Fractional-based iterative learning-optimal model predictive control of speed induction motor regulation for electric vehicles application. *Electrical Engineering & Electromechanics*, 2024, no. 5, pp. 14-19. doi: https://doi.org/10.20998/2074-272X.2024.5.02.

*2.* Chaib Ras A., Bouzerara R., Bouzeria H. An adaptive controller for power quality control in high speed railway with electric locomotives with asynchronous traction motors. *Electrical Engineering & Electromechanics*, 2024, no. 2, pp. 23-30. doi: https://doi.org/10.20998/2074-272X.2024.2.04.

*3.* Oshurbekov S.K., Kazakbaev V.M., Prakht V.A., Dmitrievskii V.A., Paramonov A.S. Analysis of electricity consumption of induction motors of IE1 and IE2 efficiency classes in a 11 kW pump installation. *Electrical Engineering & Electromechanics*, 2020, no. 5, pp. 18-24. doi: https://doi.org/10.20998/2074-272X.2020.5.03.

*4.* Ebrahimi F., Wndarko N.A., Gunawan A.I. Wild horse optimization algorithm implementation in 7-level packed U-cell multilevel inverter to mitigate total harmonic distortion. *Electrical Engineering & Electromechanics*, 2024, no. 5, pp. 34-40. doi: https://doi.org/10.20998/2074-272X.2024.5.05.

*5.* Parimalasundar E., Muthukaruppasamy S., Dharmaprakash R., Suresh K. Performance investigations of five-level reduced switches count H-bridge multilevel inverter. *Electrical Engineering & Electromechanics*, 2023, no. 6, pp. 58-62. doi: https://doi.org/10.20998/2074-272X.2023.6.10.

*6.* Benboukous M., Bahri H., Talea M., Bour M., Abdouni K. Comparative analysis of principal modulation techniques for modular multilevel converter and a modified reduced switching frequency algorithm for nearest level pulse width modulation. *Electrical Engineering & Electromechanics*, 2025, no. 4, pp. 26-34. doi: https://doi.org/10.20998/2074-272X.2025.4.04.

*7.* Sujatha M.S., Sreelakshmi S., Parimalasundar E., Suresh K. Mitigation of harmonics for five level multilevel inverter with fuzzy logic controller. *Electrical Engineering & Electromechanics*, 2023, no. 4, pp. 52-56. doi: https://doi.org/10.20998/2074-272X.2023.4.08.

*8.* Priyanka G., Surya Kumari J., Lenine D., Srinivasa Varma P., Sneha Madhuri S., Chandu V. MATLAB-Simulink environment based power quality improvement in photovoltaic system using multilevel inverter. *Electrical Engineering & Electromechanics*, 2023, no. 2, pp. 43-48. doi: https://doi.org/10.20998/2074-272X.2023.2.07.

*9.* De Gaetano D., Harikumaran J., Sala G., Degano M., Buticchi G., Gerada C. On Torque Improvement by Current Harmonic Injection in Isotropic and Anisotropic Multiphase Machines. *IEEE Journal of Emerging and Selected Topics in Industrial Electronics*, 2022, vol. 3, no. 3, pp. 845-853. doi: https://doi.org/10.1109/JESTIE.2021.3105337.

*10.* Sun J., Zheng Z., Li C., Wang K., Li Y. Optimal Fault-Tolerant Control of Multiphase Drives Under Open-Phase/Open-Switch Faults Based on DC Current Injection. *IEEE Transactions on Power Electronics*, 2022, vol. 37, no. 5, pp. 5928-5936. doi: https://doi.org/10.1109/TPEL.2021.3135280.

*11.* Chaabane H., Khodja D.E., Chakroune S., Hadji D. Model reference adaptive backstepping control of double star induction machine with extended Kalman sensorless control. *Electrical Engineering & Electromechanics*, 2022, no. 4, pp. 3-11. doi: https://doi.org/10.20998/2074-272X.2022.4.01.

*12.* Darsouni Z., Rezgui S.E., Benalla H., Rebahi F., Boumendjel M.A.M. Ensuring service continuity in electric vehicles with vector control and linear quadratic regulator for dual star induction motors. *Electrical Engineering & Electromechanics*, 2025, no. 2, pp. 24-30. doi: https://doi.org/10.20998/2074-272X.2025.2.04.

*13.* Chatterjee S., Kastha D. A New Multilevel Converter Configuration for Medium-Voltage Open-Winding PMSG-Based Wind Energy Conversion Systems. *IEEE Journal of Emerging and Selected Topics in Industrial Electronics*, 2024, vol. 5, no. 1, pp. 39-49. doi: https://doi.org/10.1109/JESTIE.2023.3293428.

*14.* Yu Z., Chen Y., Zhao J., Zhang X., Zhou X. Alternate Subhexagonal Center Dual-Inverter PWM Scheme for Open-End Winding DC-Biased-VRM Drive Using Adjustable Zero Voltage Vector With Dead-Time Effect Compensation. *IEEE Transactions on Transportation Electrification*, 2025, vol. 11, no. 3, pp. 7322-7333. doi: https://doi.org/10.1109/TTE.2025.3526609.

*15.* Jiang C., Liu H., Wheeler P., Wu F., Huo J. An Optimized Modulation for Five-Phase Open-End Winding PMSM With Sliding Clamped Strategy. *IEEE Transactions on Industrial Electronics*, 2023, vol. 70, no. 9, pp. 8819-8829. doi: https://doi.org/10.1109/TIE.2022.3212385.

*16.* Guizani S., Ben Ammar F. Dual open-end stator winding induction machine fed by redundant voltage source inverters. *Turkish Journal of Electrical Engineering & Computer Sciences*, 2015, vol. 23, pp. 2171-2181. doi: https://doi.org/10.3906/elk-1305-80.

*17.* Nayli A., Guizani S., Ben Ammar F. Modeling and analysis of a novel dual open-end stator windings wound rotor synchronous machine with dampers. *Turkish Journal of Electrical Engineering & Computer Sciences*, 2017, vol. 25, pp. 995-1009. doi: https://doi.org/10.3906/elk-1506-250.

*18.* Guizani S., Ben Ammar F. Torque and current enhancement based on dual open-end stator winding IM at 0° fed by two 2-level cascaded inverters. *Electrical Engineering*, 2018, vol. 100, no. 3, pp. 1869-1879. doi: https://doi.org/10.1007/s00202-017-0668-2.

*19.* Guizani S., Nayli A., Ben Ammar F. A generalized mathematical model of the two-level cascaded inverters feeding the open-end stator winding induction machine. *Journal of Electrical Engineering*, 2014, vol. 14, no. 4, 10 p.



*Received 26.07.2025*
*Accepted 14.09.2025*
*Published 02.01.2026*



*A. Nayli* [1,3], *Doctor of Electrical Engineering,*
*S. Guizani* [2,3], *Professor of Electrical Engineering,*
*F. Ben Ammar* [3], *Professor of Electrical Engineering,*
[1] University of Gafsa, IPEIG, Tunisia,
e-mail: abdelmonoem.nayli@gmail.com (Corresponding Author)
[2] University of El Manar, IPEIEM, Tunisia.
[3] MMA Laboratory, INSAT, University of Carthage, Tunisia.



*How to cite this article:*
Nayli A., Guizani S., Ben Ammar F. Association smooth-pole dual open-end windings permanent magnet synchronous machine with cascaded 2-level inverters for improved performances. *Electrical Engineering & Electromechanics*, 2026, no. 1, pp. 63-68. doi: https://doi.org/10.20998/2074-272X.2026.1.08

UDC 621.314 https://doi.org/10.20998/2074-272X.2026.1.09

N. Guettaf, S.E.I. Guettaf, T. Zeghloul, H. Nouri

# Numerical study of particles trajectories in a multifunctional electrostatic separator powered by photovoltaic system

***Introduction.*** *Electrostatic separation is a growing technology in the recycling industry. It is an effective technology for processing plastics and metallic materials in the form of granular mixtures or fine powders from waste electrical and electronic equipment.* ***Problem.*** *Understanding the various physical phenomena occurring in the separation zone is crucial for improving the efficiency of electrostatic separation devices. This has led to the adoption of efficient and reliable numerical models for simulating particle trajectories. The* ***goal*** *of the work is to represent graphically the trajectories of two insulating charged polypropylene particles of different sizes (2 mm and 4 mm) in the multifunctional electrostatic separator powered by photovoltaic (PV) system use a multipoint electrodes as charging device employing numerical simulation and demonstrate its effectiveness and reliability for the study of particles trajectories by integrating PV panels as a power source for electrostatic separators according to the recommendations of the new energy system.* ***Methodology.*** *Using the Euler-Cromer method as numerical model to solve the equation of motion of the particles. This method was based on the calculation of the electric field intensity, which is done by the COMSOL Multiphysics software, which uses the finite element method (FEM). The numerical simulation was carried out using MATLAB software by varying the voltage applied to the active electrodes of the multifunctional electrostatic separator suggested, and the distance between them, taking into account the influence of electrostatic and mechanical forces on the charged insulating particles as they pass through the separation zone. The* ***results*** *were showed that the numerical model used is an effective and reliable tool for the study of particles trajectories.* ***Scientific novelty*** *of this work is to integrate PV panels as the main low-voltage energy source at the input of the high-voltage generator supplying the electrostatic separator with an optimal voltage of 30 kV. In addition, this numerical study has used electrostatic forces, gravitational forces, and dynamic forces simultaneously.* ***Practical value.*** *The numerical simulation was contributed to a thorough understanding of various physical phenomena occurring in the separation zone and was considered a tool to validate experimental results.* References 31, tables 2, figures 14.

*Key words:* **electrostatic separation, electric field, photovoltaic system, numerical modeling, particle trajectories, waste electrical and electronic equipment.**

***Вступ***. *Електростатична сепарація є технологією, що розвивається в індустрії переробки. Це ефективна технологія для переробки пластику та металевих матеріалів у вигляді гранульованих сумішей або тонких порошків із відходів електричного та електронного обладнання.* ***Проблема***. *Розуміння різних фізичних явищ, що протікають у зоні поділу, має вирішальне значення для підвищення ефективності пристроїв електростатичної сепарації. Це призвело до прийняття ефективних та надійних чисельних моделей для моделювання траєкторій частинок.* ***Мета*** *статті полягає у графічному представленні траєкторії двох ізолюючих заряджених частинок поліпропілену різних розмірів (2 мм і 4 мм) в багатофункціональному електростатичному сепараторі, що працює від фотоелектричної (PV) системи, використовуючи багатоточкові електроди як зарядний пристрій, застосовуючи чисельне моделювання та демонструючи ефективність PV панелей як джерела живлення для електростатичних сепараторів відповідно до рекомендацій нової енергетичної системи.* ***Методика***. *Використання методу Ейлера-Кромера як чисельної моделі для вирішення рівняння руху частинок. Даний метод заснований на розрахунку напруженості електричного поля, яке виконується за допомогою програмного забезпечення COMSOL Multiphysics, що використовує метод скінченних елементів (FEM). Чисельне моделювання проводилося з використанням програмного забезпечення MATLAB шляхом зміни напруги, що подається на активні електроди пропонованого багатофункціонального електростатичного сепаратора, та відстані між ними з урахуванням впливу електростатичних та механічних сил на заряджені частинки ізолюючі при їх проходженні через зону поділу.* ***Результати*** *показали, що використана чисельна модель є ефективним і надійним інструментом для дослідження траєкторій частинок.* ***Наукова новизна*** *роботи полягає в інтеграції PV панелей як основного джерела енергії низької напруги на вході високовольтного генератора, що живить електростатичний сепаратор оптимальною напругою 30 кВ. Крім того, в даному чисельному дослідженні одночасно використовувалися електростатичні, гравітаційні та динамічні сили.* ***Практична значимість***. *Чисельне моделювання сприяло глибокому розумінню різних фізичних явищ, що відбуваються в зоні поділу, та розглядалося як інструмент для підтвердження експериментальних результатів.* Бібл. 31, табл. 2, рис. 14.

*Ключові слова:* **електростатична сепарація, електричне поле, фотоелектрична система, чисельне моделювання, траєкторії частинок, відходи електричного та електронного обладнання.**

**Introduction.** During recent years, the world has been experiencing a rapid pace of consumption of electrical and electronic devices for domestic and industrial use. This pace is due to two main factors: the remarkable technical advances that have affected most modern devices. The digital and electronic transformation has brought about a radical change in the lives, businesses, relationships, and affairs of individuals and society [1, 2]. At the end of 2022, waste electrical and electronic equipment (WEEE) was estimated at around 62 million tones, or an average of 7.8 kg per capita, of which 22.3 % (13.8 million tones) was destined for proper collection and recycling [3]. This category of waste has caused numerous economic, social, and environmental crises. It also occupies vast areas, which is a source of concern for human health and a major challenge for sustainable development [4].

Over the past 20 years, the recycling industry has emerged as a new resource for genuine environmental restructuring and has been embraced as a main solution in the WEEE recycling [4, 5]. Electrostatic separation is an efficient technique that is built into the new energy paradigm. In addition to the electrostatic separation, there are several other electrical separation methods used across industries like electrophoresis, electro pulse, dielectrophoresis, conductivity-based separation, and magneto-electrostatic hybrid separation. It stands out for its minimal energy consumption, low operating and maintenance costs, and environmental friendliness, but has drawbacks in the sensitivity of humidity and particle surface conditions [6–8]. It is also highly efficient compared to the other methods mentioned, and a feasible transformation technology for plastics, and metallic materials from WEEE, such as electric cables, and electronic cards [9], as well as in agricultural food [10], and mining products [11]. The WEEE recycling process

goes through 4 original stages, which are as follows. First, plastics and metals from WEEE are sorted according to their type. Second, they are cut into millimeter granular mixtures of sizes ranging from 1 to 6 mm or ground into fine powders of sizes less than 1 mm, having the same density and electrical conductivity [12–14]. Third, the granular mixtures or fine powders are charged by at least one or more electrical charging mechanisms such as corona discharge, electrostatic induction, and triboelectric effect. Finally, the granular or powdery mixtures are separated in an intense electric field generated by two electrodes coupled to a high-voltage DC power source of opposing polarity [4].

Currently, there are many efficient and reliable electrostatic separators that have been applied to sort the components of granular mixtures or fine powders. These include drum electrostatic separators [15], vertical electrode electrostatic separators [16], tribo-aero-electrostatic separators with conveyor belts [17], tribo-aero-electrostatic separators with two rotating disks [18], free-fall electrostatic separators [19], and multifunctional electrostatic separators of the metal belt conveyor type [20].

The multifunctional electrostatic separator and the free-fall electrostatic separator are two of the most favored and useful models for sorting the parts of electrical and electronic equipment, especially the insulating granular particles. This is because they work well and are reliable [19].

Utilizing numerical methods to model the separation process plays a vital role in minimizing the need for extensive experimental trials, as it offers deep insights into the associated physical phenomena. Consequently, researchers have employed particle trajectory simulations to investigate how different parameters impact the efficiency and result of the separation process [2].

The **goal** of the work is to represent graphically the trajectories of two insulating charged polypropylene particles of different sizes (2 mm and 4 mm) in the multifunctional electrostatic separator powered by photovoltaic (PV) system use a multipoint electrodes as charging device employing numerical simulation and demonstrate its effectiveness and reliability for the study of particles trajectories by integrating PV panels as a power source for electrostatic separators according to the recommendations of the new energy system.

The use of PV panels ensures the required voltage to power the suggested electrostatic separator. During the separation process, a 2 mm and 4 mm insulating particles are charged as they pass through the charge zone by coronal discharge generated by the multipoint configuration with the same charge as the electrode. They then reach the separation zone, where they are separated in the presence of an intense electric field. This work aims to represent graphically the charged particles trajectories using numerical simulation, demonstrate their effectiveness and reliability for the study of particles trajectories and improve the efficiency of electrostatic separators.

**Methods. Multifunctional electrostatic separator description.** Figure 1,*a* shows a design of a multifunctional electrostatic separator with two flexible verticals electrodes, powered by PV system. This system powered the separator.

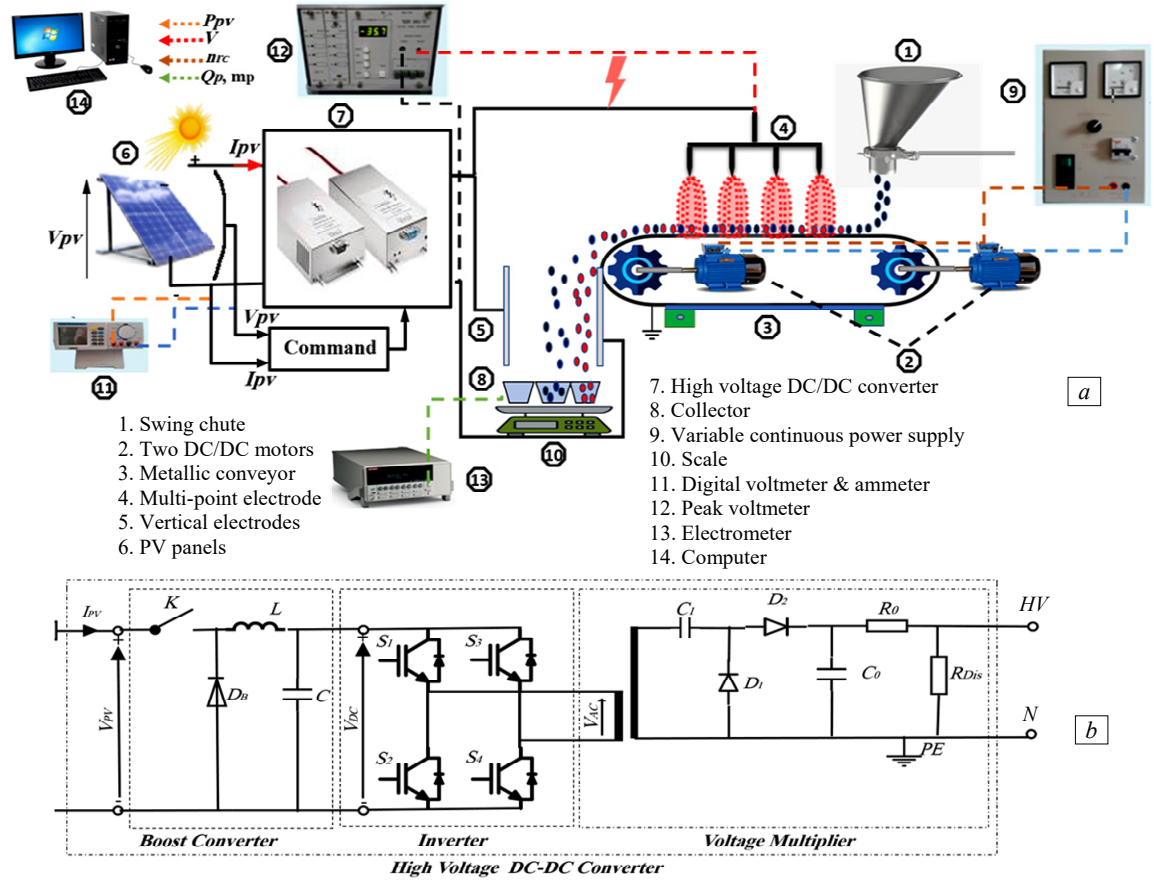


Fig. 1. *a* – multifunctional electrostatic separator with two flexible vertical electrodes powered by PV panels; *b* – basic electrical circuit that explains the conversion of the low-voltage primary source of direct voltage to high direct voltage for powered the separator

The design consists of a grounded metal belt conveyor, measuring 1000 mm in length and 100 mm in width. The conveyor belt is responsible for transporting the particles in the form of homogeneous spheres deposited on its surface to the electrical charging zone and the separation zone. This conveyor belt is driven by two DC or three-phase motors. These two motors are powered by an adjustable voltage source and rotated at an appropriate speed, where the charged particles fall into the electrostatic separation zone. A multi-point corona electrode in the form of needles perpendicular to the metal belt of the conveyor belt to generate corona discharges used to charge insulating particles. It consists of four points set 20 mm higher than the surface of the belt. Each point is 130 mm long and 2 mm in diameter, spaced 20 mm apart.

An electrostatic separation zone consists of two flexible vertical electrodes in the form of plates measuring 200 mm wide and 300 mm long, separated by a distance of 80 mm. The two electrodes can move back and forth between them.

The corona electrode and one of the vertical electrodes are connected to a 30 kV via a 500 V/30 kV high voltage DC/DC converter supplied by fourteen PV panels (Fig. 1,*b*). The voltages applied to the electrodes can vary from 20 kV to 30 kV for specific applications.

The multi-point electrode generates corona discharges that expose the insulating particles. They acquire electrical charges of the similar sign as the voltage applied to the corona electrode and fall into the electrostatic separation zone. When they freely fall into the separation zone, they are attracted to the electrode of opposite polarity and fall into the right part of the collector. However, the uncharged insulating particles, located in an intense electric field at the separation zone, fall into the middle part of the collector. The left part of the collector remains unchanged. Three collector boxes collect the separated insulating particles. The boxes are divided into two compartments and constituted in the form of a Faraday cage connected to an electrometer for measuring electrical charges, set on an electronic scale by measuring the mass of the separated particles.

You can record real-time information about how this electrostatic separator is working on a computer. The computer can record the power produced by the PV panels ($P_{pv}$), the voltages applied to the two active electrodes ($V$), the speed of the metal belt on the conveyor ($n_{rc}$), the number of charges on the particles ($Q_p$) and the masses of the particles ($m_p$).

**Numerical modeling.** This section involves the numerical modeling of the PV panels that power the electrostatic separator suggested, the electric field, the motion of the charged particles and their trajectories in the separation zone.

**PV panel modeling.** A PV panel, otherwise called a PV module, is generally made up of a set of elementary PV cells manufactured in the form of a thin layer of P-N junction semiconductor. These PV cells are connected in series and/or in parallel in order to obtain the required current, the required voltage, and the necessary power required to supply the load, due to the fact that each PV cell has a low nominal power. Figure 2 presents the model of the equivalent electrical circuit of a PV cell [21–23].

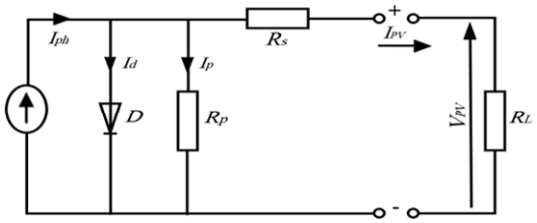

Fig. 2. The single-diode model represents the equivalent electrical circuit of a monocrystalline PV cell

The expression of the current generated by the single-diode PV cell is given as follows:

$$I_{ph} = I_d + I_p + I_{pv}; \quad (1)$$

$$I_{pv} = I_{ph} - I_d - I_p = \\ = I_{ph} - I_0 \cdot \left[ \exp\left(\frac{q \cdot (V_{pv} + R_s \cdot I_{pv})}{n \cdot k_B \cdot T}\right) - 1 \right] - \frac{V_{pv} + R_s \cdot I_{pv}}{R_p}, \quad (2)$$

where $I_{ph}$ is the photocurrent of the PV cell; $I_d$ is the current at the diode junction; $I_p$ is the current in the resistor $R_p$; $I_{pv}$ is the output current of the PV cell; $I_0$ is the saturation current of the diode or the dark current; $V_{pv}$ is the output voltage of the PV cell; $R_s$, $R_p$ are the series and parallel resistances of the PV cell; $n$ is the ideality coefficient of the cell; $k_B$ is the Boltzmann constant; $q$ is the electron charge; $T$ is the temperature of the PV cell.

The following equation provides the mathematical model for the PV panel, assuming that all the cells are identical:

$$I_{pv} = N_p \cdot I_{ph} - \\ - N_p \cdot I_0 \cdot \left[ \exp\left(\frac{q \cdot (N_s \cdot V_{pv} + (N_s/N_p) \cdot R_s \cdot I_{pv})}{n \cdot k_B \cdot T}\right) - 1 \right] - \quad (3) \\ - \frac{N_s \cdot V_{pv} + (N_s/N_p) \cdot R_s \cdot I_{pv}}{(N_s/N_p) \cdot R_p},$$

where $N_s$ is the number of cells in series; $N_p$ is the number of cells in parallel.

**Electrical field modeling.** This study uses a numerical model of the electric field to study the motion and trajectory of charged particles in electrostatic separators. The electric field is an important and essential factor for the electrostatic separation process. The electric field is responsible for the charge and the motion of the particles through the electrostatic force it generates. It is generated by applying a high voltage to the active electrode and the grounded electrode. To obtain the electric field strength $\boldsymbol{E}$, it must solve the Laplace equation or the Poisson equation, both of which are partial differential equations or use the COMSOL Multiphysics software, that uses the FEM [2, 24, 25] it can be expressed as follows:

$$\boldsymbol{E} = -\nabla V, \quad (4)$$

where $\boldsymbol{E}$ is the electric field intensity vector; $V$ is the electric scalar potential. The boundary conditions are [24]:

- The potential on the active electrode is equal to the high applied voltage.
- The potential on the grounded electrode is zero.
- The electric field on the active electrode is equal to the onset field strength.

**Modeling the motion of charged particles and their trajectories.** While moving, particles that have been

charged by the corona discharge used in this study are affected by electrostatic force, gravitational force, and aerodynamic force. When they fall freely at the middle of the electrostatic separation zone, where there is a strong electric field, they are subject to all of these forces [26–28].

**Gravitational force $F_g$.** Any charged particle with a mass $m_p$ experiences a gravitational force during free fall. The following relationship determines its value:

$$F_g = \begin{bmatrix} F_{g,x} \\ F_{g,y} \end{bmatrix} = \begin{bmatrix} 0 \\ -m_p \cdot g \end{bmatrix}, \quad (5)$$

where $m_p$ is the mass of the charged particle, and $g$ is the gravitational constant ($g$= 9.81 m/s).

**Electrostatic force $F_{el}$.** Any charged particle $Q_p$ located in a region of intense electric field is subject to an electric force of attraction or repulsion. Coulomb's law expresses it this way:

$$F_{el} = \begin{bmatrix} F_{el,x} \\ F_{el,y} \end{bmatrix} = Q_p \cdot \begin{bmatrix} E_x(x,y) \\ E_y(x,y) \end{bmatrix}, \quad (6)$$

where $Q_p$ is the charge of the charged particle, $E_x$, $E_y$ are the horizontal and vertical components of the electric field vector, respectively.

**Aerodynamic force $F_{aero}$.** Any charged particle in the form of a homogeneous sphere of radius $r_p$ experiences an aerodynamic force when it rubs against the air. The following formula gives the aerodynamic force:

$$F_{aero} = \begin{bmatrix} F_{aero,x} \\ F_{aero,y} \end{bmatrix} = \frac{1}{2} \cdot C_f \cdot \rho \cdot \pi \cdot r_p^{\,2} \cdot v \begin{bmatrix} v_x \\ v_y \end{bmatrix}, \quad (7)$$

where $C_f$ = 0.5 is the coefficient of friction; $\rho$ is the density of air; $r_p$ is the radius of the charged particle; $v_x$, $v_y$ are the components of the vector of the relative velocity of the particle.

Gravitational, electrostatic and aerodynamic forces act on the motion of charged particles, according to Newton's second law. It is defined by the following relationship [29–31]:

$$m_p \cdot a_n = \sum F = F_g + F_{el} + F_{aero}, \quad (8)$$

where $a_n$ is the particle acceleration.

For represent graphically the trajectory of charged particles, we based on the Euler-Cromer method to solve the equation of motion numerically. This method is given by the following relation [28]:

$$v_{n+1} = v_n + a_n \cdot \Delta t; \quad (9)$$

$$p_{n+1} = p_n + v_{n+1} \cdot \Delta t, \quad (10)$$

where $v$ is the velocity; $p$ is the position; $\Delta t$ is time step.

**Results and discussion.** In this paper we present the current-voltage ($I$–$V$) and power-voltage ($P$–$V$) characteristics of 14 PV panels by varying the solar irradiation using the PV module characteristics (Table 1), the evolution of the electric field in the electrical charging zone and the separation zone (Fig. 3) through the COMSOL Multiphysics program for two configurations (Table 2) and the graphical representation of the trajectories of two polypropylene insulating particles of 2 mm and 4 mm sizes in the separation zone through the Euler-Cromer method was programmed in MATLAB by varying the value of the voltage applied to the active electrodes and the inter-electrode distance and by injecting the intensity of the electric field previously obtained. The particle sizes for which the Euler-Cromer method is most effective range from 1 mm to 5 mm [2, 28].

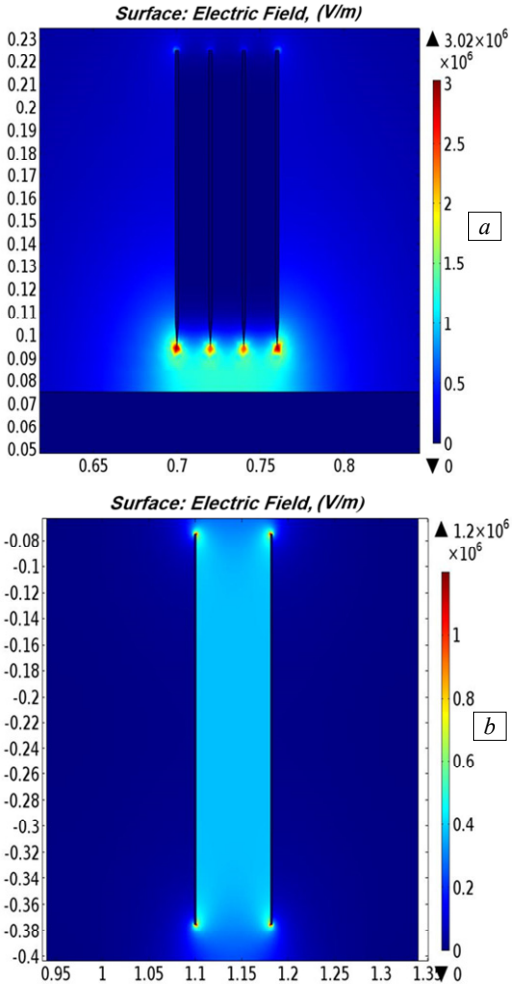


Fig. 3. The distribution of electric field:
*a* – the electric charging zone; *b* – the electrostatic separation zone

Table 1

PV characteristics of an ETSolar PV module

| Reference | ET-M572185 |
|---|---|
| Maximum power $P_{max}$, W | 185 |
| Open circuit voltage $V_{oc}$, V | 44.6 |
| Short circuit current $I_{sc}$, A | 5.8 |
| Rated voltage $V_{mpp}$, V | 36.3 |
| Rated current $I_{mpp}$, A | 5.09 |
| Cell per module | 72 |

Table 2

Two configurations of the inter-electrode distance

| Configurations | $D_1$, mm | $D_2$, mm | $D_3$, mm |
|---|---|---|---|
| Multipoint-conveyor | 60 | 40 | 20 |
| Verticals electrodes | 80 | 95 | 110 |

**PV characteristics of the ETSolar PV panels.** Figure 4 shows $I$–$V$ and $P$–$V$ characteristics of 14 ET-M572185 panels. These panels are linked in series to power the multifunctional electrostatic separator with two flexible verticals electrodes with a voltage of 30 kV via a high-voltage converter DC/DC of 500 V / 30 kV. The measurements were carried out at a temperature of 25 °C and 3 different solar radiation values (800 W/m$^2$, 900 W/m$^2$, 1000 W/m$^2$). Each of these solar radiation values corresponds to a maximum electrical power that the 14 panels could provide.

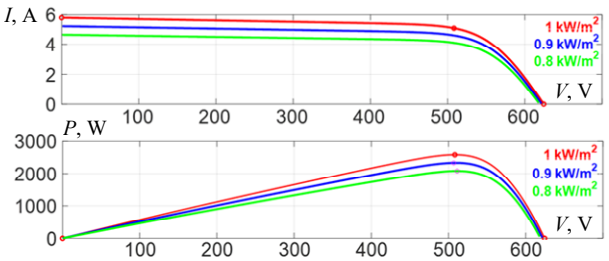

Fig. 4. *I–V* and *P–V* characteristics of 14 modules of type ET-M572185 at 25 °C

**Electric field variation. Electrical charging zone.** Figure 5 depicts the electric field variation at the conveyor generated by 4 points as a function of their positions *p*, which represents the electrical charging zone of insulating particles for an applied voltage of 30 kV and an inter-electrode distance of 20 mm. The multipoint-conveyor configuration allows the insulating particles to cross the region of the intense electric field produced by each point and acquire electric charges of the same sign as those of the corona electrode.

Figures 6, 7 show the electric field variation at the conveyor for 3 different applied voltages (20 kV, 25 kV, 30 kV) and 3 different inter-electrode distances for a multipoint-conveyor configuration shown in Table 2.

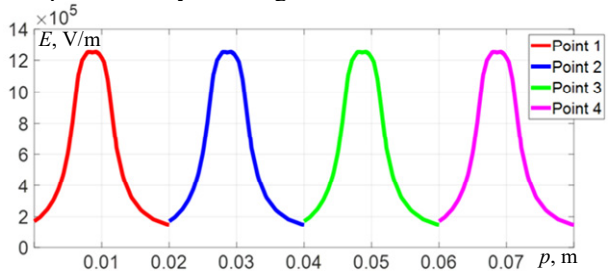

Fig. 5. Electric field variation at the conveyor

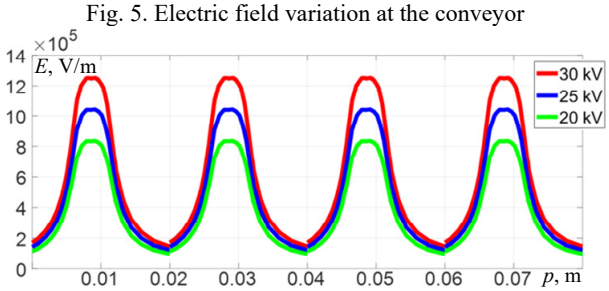

Fig. 6. Electric field variation at the conveyor for different applied voltages

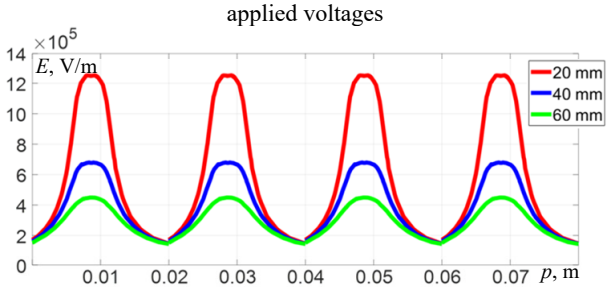

Fig. 7. Electric field variation at the conveyor for different distances

**Electrostatic separation zone.** Figures 8, 9 show the electric field variation generated in the separation zone. These results are for 3 values of the applied voltage of 20 kV, 25 kV and 30 kV and 3 values of the inter-electrode distance – 80 mm, 95 mm and 110 mm. The curves show that the electric field is uniform in this region. It is strong and intense, with a value of $3.75 \cdot 10^5$ V/m for a 30 kV voltage and an 80 mm distance between the electrodes. This investigation demonstrates the importance of the electric field process in electrostatic separators. That is electrostatic separation requires an intense electric field of the order of $10^6$ V/m.

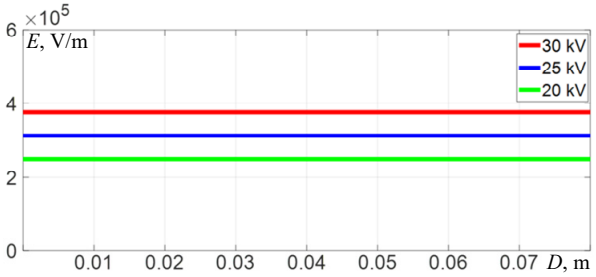

Fig. 8. Electric field variation at the ground for different applied voltages

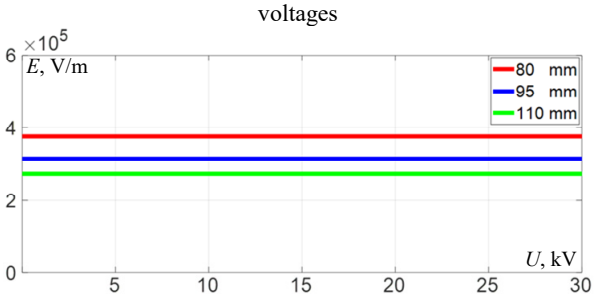

Fig. 9. Electric field variation at the ground for different distances

**Trajectories of the charged particles in the electrostatic separation zone.** We illustrate in Fig. 10–13 the trajectories of 2 mm and 4 mm polypropylene particle in the separation zone for three different values of the voltage applied to the active electrode (20 kV, 25 kV and 30 kV) and three different distances between the electrodes of 80 mm, 95 mm and 110 mm. These trajectories were obtained numerically.

For the case of a variation of the applied voltage and the distance, we can observe that the charged particle of size 2 mm is attracted with a strong acceleration by the opposite electrode without colliding with it. Moreover, the other electrode repels it when its sign matches. Indeed, the electrostatic force is dominant compared to the gravitational force due to the lightness and small diameter of the particle. Finally, the charged particle gathers in the left compartment of the collector box.

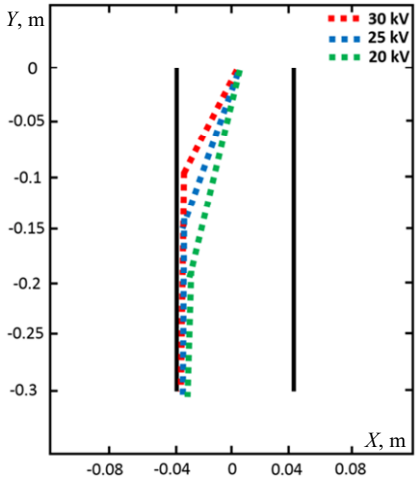

Fig. 10. 2 mm polypropylene particle trajectories for different voltages applied at an inter-electrode distance of 80 mm

In the case of a charged particle of size 4 mm, we can note that there is a ratio between the gravitational

force and the electrostatic force. As expected, the gravitational force is dominant compared to the electrostatic force. The large-diameter charged particle makes a slow acceleration due to the effect of gravitational force. The deflection of the charged particle increases proportionally to the increase in the applied voltage while keeping the same tangent, and it collects in the right compartment of the collector box.

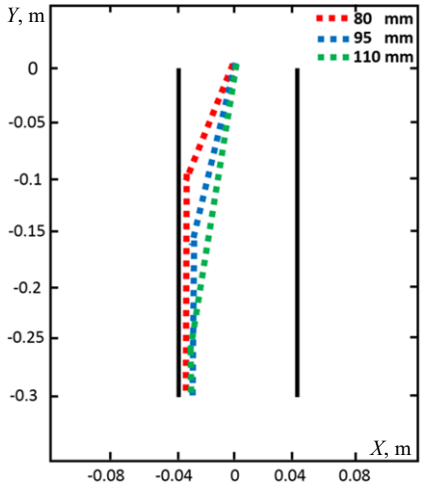


Fig. 11. 2 mm polypropylene particle trajectories for different distances at an applied voltage of 30 kV

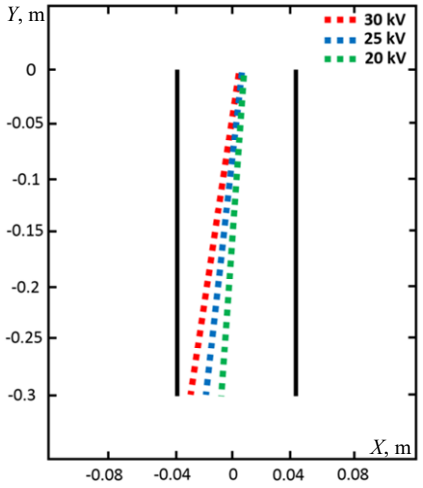


Fig. 12. 4 mm polypropylene particle trajectories for different voltages applied at a distance of 80 mm

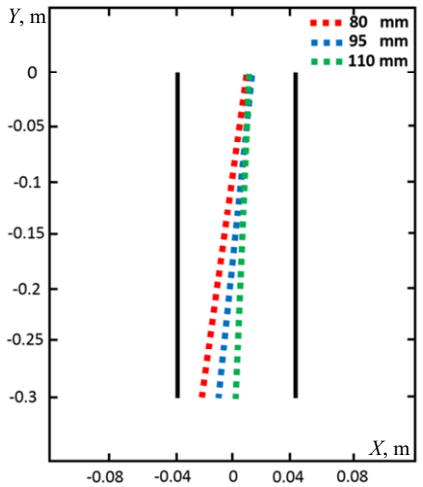


Fig. 13. 4 mm polypropylene particle trajectories for different distances at an applied voltage of 30 kV

Figure 14 shows the trajectories of two polypropylene particles of 2 mm and 4 mm sizes when a voltage of 30 kV is applied and there is an inter-electrode distance of 80 mm.

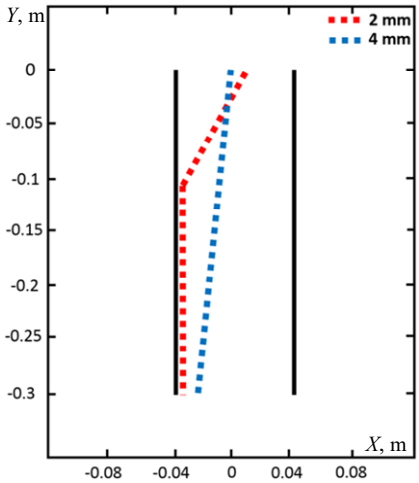


Fig. 14. 2 mm and 4 mm polypropylene particle trajectories at 30 kV and 80 mm

**Conclusions.** A design of the multifunctional electrostatic separator and the simulation results obtained in this article allow us to formulate the following conclusions.

The integration of PV system as a power source for electrostatic separators, and give it high priority according the recommendation of the new energy system due to its numerous advantages and effective contribution to sustainable development.

The multi-point configuration used in this work has a high efficiency for charging the insulating particles.

The numerical model based on the Euler-Cromer method that based on the calculation of the electric field intensity, which is done by the COMSOL Multiphysics software, and programmed in MATLAB software, is an effective and validated tool for the study of the particles trajectories. The numerical simulation has provided a profound comprehension of various phenomena that occur in the electrostatic separation zone. It is also considered a tool to validate experimental results.

Directions for further research may be the following: To conduct this work experimentally in the future and study the trajectories of conductive and nonconductive particles in the proposed electrostatic separator.

**Conflict of interest**. The authors declare that they have no conflicts of interest.

REFERENCES

***1.*** Senathirajah K., Attwood S., Bhagwat G., Carbery M., Wilson S., Palanisami T. Estimation of the mass of microplastics ingested – A pivotal first step towards human health risk assessment. *Journal of Hazardous Materials*, 2021, vol. 404, art. no. 124004. doi: https://doi.org/10.1016/j.jhazmat.2020.124004.

***2.*** Maammar M., Achouri I.-E., Zeghloul T., Medles K., Aksa W., Dascalescu L. Numerical Simulation and Experimental Observation of Charged Particles Trajectories in Roll-Type Electrostatic Separators. *IEEE Transactions on Industry Applications*, 2021, vol. 57, no. 6, pp. 6504-6511. doi: https://doi.org/10.1109/TIA.2021.3103485.

***3.*** Baldé C.P., Kuehr R., Yamamoto T. et al. Global Report on Waste Electrical and Electronic Equipment. *The Global E-waste Monitor*, 2024. 148 p. Available at: https://ewastemonitor.info/wp-content/uploads/2024/03/GEM_2024_18-03_web_page_per_page_web.pdf (Accessed 07 May 2025).

***4.*** Guettaf N., Anane Z., El Islem Guettaf S., Hassaine F., Nouri H. Study of the different parameter corona discharge in point-plane

Electrostatic Separator. *2022 19th International Multi-Conference on Systems, Signals & Devices (SSD)*, 2022, pp. 1831-1835. doi: https://doi.org/10.1109/SSD54932.2022.9955502.
**5.** Mekhalef Benhafssa A., Medles K., Boukhoulda M.F., Tilmatine A., Messal S., Dascalescu L. Study of a Tribo-Aero-Electrostatic Separator for Mixtures of Micronized Insulating Materials. *IEEE Transactions on Industry Applications*, 2015, vol. 51, no. 5, pp. 4166-4172. doi: https://doi.org/10.1109/TIA.2015.2434794.
**6.** He J., Tang H., Guo C., Zhu L., Huang S., Yang B. Synergist enhancement of effective desilication of graphite ore by rotary triboelectric separation and surface modification. *Powder Technology*, 2024, vol. 444, art. no. 119965. doi: https://doi.org/10.1016/j.powtec.2024.119965.
**7.** He J., Huang S., Chen H., Zhu L., Guo C., He X., Yang B. Recent advances in the intensification of triboelectric separation and its application in resource recovery: A review. *Chemical Engineering and Processing - Process Intensification*, 2023, vol. 185, art. no. 109308. doi: https://doi.org/10.1016/j.cep.2023.109308.
**8.** Pan X., Wong C.W.Y., Li C. Circular economy practices in the waste electrical and electronic equipment (WEEE) industry: A systematic review and future research agendas. *Journal of Cleaner Production*, 2022, vol. 365, art. no. 132671. doi: https://doi.org/10.1016/j.jclepro.2022.132671.
**9.** Bedeković G., Trbović R. Electrostatic separation of aluminium from residue of electric cables recycling process. *Waste Management*, 2020, vol. 108, pp. 21-27. doi: https://doi.org/10.1016/j.wasman.2020.04.033.
**10.** Perdana T., Kusnandar K., Perdana H.H., Hermiatin F.R. Circular supply chain governance for sustainable fresh agricultural products: Minimizing food loss and utilizing agricultural waste. *Sustainable Production and Consumption*, 2023, vol. 41, pp. 391-403. doi: https://doi.org/10.1016/j.spc.2023.09.001.
**11.** Radebe N., Chipangamate N. Mining industry risks, and future critical minerals and metals supply chain resilience in emerging markets. *Resources Policy*, 2024, vol. 91, art. no. 104887. doi: https://doi.org/10.1016/j.resourpol.2024.104887.
**12.** Sun B., Li B., Ma S., Zhu M., Dong C., Xiang M., Cheng H., Yu Y. The recycling potential of unregulated waste electrical and electronic equipment in China: Generation, economic value, and cost-benefit analysis. *Journal of Cleaner Production*, 2023, vol. 402, art. no. 136702. doi: https://doi.org/10.1016/j.jclepro.2023.136702.
**13.** Shahabuddin M., Uddin M.N., Chowdhury J.I., Ahmed S.F., Uddin M.N., Mofijur M., Uddin M.A. A review of the recent development, challenges, and opportunities of electronic waste (e-waste). *International Journal of Environmental Science and Technology*, 2023, vol. 20, no. 4, pp. 4513-4520. doi: https://doi.org/10.1007/s13762-022-04274-w.
**14.** Gao Y., Huang X., Xia D., Lyu C. Research on the recycling decision of WEEE in rural China under dual supervision. *Scientific Reports*, 2024, vol. 14, no. 1, art. no. 23875. doi: https://doi.org/10.1038/s41598-024-74158-1.
**15.** Catinean A., Dascalescu L., Lungu M., Dumitran L.M., Samuila A. Improving the recovery of copper from electric cable waste derived from automotive industry by corona-electrostatic separation. *Particulate Science and Technology*, 2021, vol. 39, no. 4, pp. 449-456. doi: https://doi.org/10.1080/02726351.2020.1756545.
**16.** Zeghloul T., Touhami S., Richard G., Miloudi M., Dahou O., Dascalescu L. Optimal Operation of a Plate-Type Corona-Electrostatic Separator for the Recovery of Metals and Plastics from Granular Wastes. *IEEE Transactions on Industry Applications*, 2016, vol. 52, no. 3, pp. 2506-2512. doi: https://doi.org/10.1109/TIA.2016.2533482.
**17.** Touhami S., Aksa W., Medles K., Tilmatine A., Dascalescu L. Numerical Simulation of the Trajectories of Insulating Particles in a Tribo-Aero-Electrostatic Separator. *IEEE Transactions on Industry Applications*, 2015, vol. 51, no. 5, pp. 4151-4158. doi: https://doi.org/10.1109/TIA.2015.2427276.
**18.** Tilmatine A., Benabboun A., Brahmi Y., Bendaoud A., Miloudi M., Dascalescu L. Experimental Investigation of a New Triboelectrostatic Separation Process for Mixed Fine Granular Plastics. *IEEE Transactions on Industry Applications*, 2014, vol. 50, no. 6, pp. 4245-4250. doi: https://doi.org/10.1109/TIA.2014.2319584.
**19.** Kimi I.E., Benhammou A., Touhami S., Rezoug M. Numerical modelling and experimental validation of an Enhanced multi-force model of free-fall electrostatic separators. *Particulate Science and Technology*, 2025, vol. 43, no. 1, pp. 52-64. doi: https://doi.org/10.1080/02726351.2024.2417363.
**20.** Székely L., Kiss I., Donghyeok G. Investigation of the separation of conductive and insulating objects on a laboratory made electrostatic separator. *Journal of Physics: Conference Series*, 2024, vol. 2702, no. 1, art. no. 012010. doi: https://doi.org/10.1088/1742-6596/2702/1/012010.
**21.** Latreche K., Taleb R., Bentaallah A., Toubal Maamar A.E., Helaimi M., Chabni F. Design and experimental implementation of voltage control scheme using the coefficient diagram method based PID controller for two-level boost converter with photovoltaic system. *Electrical Engineering & Electromechanics*, 2024, no. 1, pp. 3-9. doi: https://doi.org/10.20998/2074-272X.2024.1.01.
**22.** Bounechba H., Boussaid A., Bouzid A. Experimental validation of fuzzy logic controller based on voltage perturbation algorithm in battery storage photovoltaic system. *Electrical Engineering & Electromechanics*, 2024, no. 5, pp. 20-27. doi: https://doi.org/10.20998/2074-272X.2024.5.03.
**23.** Zorig A., Babes B., Hamouda N., Mouassa S. Improving the efficiency of a non-ideal grid coupled to a photovoltaic system with a shunt active power filter using a self-tuning filter and a predictive current controller. *Electrical Engineering & Electromechanics*, 2024, no. 6, pp. 33-43. doi: https://doi.org/10.20998/2074-272X.2024.6.05.
**24.** Guettaf N., Said H.A., Aissou M., Zegloul T., Nouri H. Modeling a Corona Discharge Separation of Fine Particles for Different Materials Used in Electrical Engineering. *Advanced Engineering Forum*, 2025, vol. 54, pp. 77-90. doi: https://doi.org/10.4028/p-U8GCnx.
**25.** Grechko O.M. Influence of the poles shape of DC electromagnetic actuator on its thrust characteristic. *Technical Electrodynamics*, 2024, no. 1, pp. 38-45. doi: https://doi.org/10.15407/techned2024.01.038.
**26.** Ireland P.M. Modelling dense particle streams during free-fall electrostatic separation. *Powder Technology*, 2024, vol. 434, art. no. 119290. doi: https://doi.org/10.1016/j.powtec.2023.119290.
**27.** Qin Y., Gao K., Li J., Xu Z. Particle trajectory model for tribo-electrostatic separating mixed granular plastics. *Cleaner Engineering and Technology*, 2021, vol. 4, art. no. 100219. doi: https://doi.org/10.1016/j.clet.2021.100219.
**28.** Maammar M., Touhami S., Rezoug M., Daioui K., Dascalescu L., Medles K. Experimental study and numerical simulation of particles trajectories in a flexible-electrode-type electrostatic separator. *Journal of Physics: Conference Series*, 2024, vol. 2702, no. 1, art. no. 012018. doi: https://doi.org/10.1088/1742-6596/2702/1/012018.
**29.** Xu Z., Li J., Lu H., Wu J. Dynamics of conductive and nonconductive particles under high-voltage electrostatic coupling fields. *Science in China Series E: Technological Sciences*, 2009, vol. 52, no. 8, pp. 2359-2366. doi: https://doi.org/10.1007/s11431-008-0198-2.
**30.** Labair H., Touhami S., Tilmatine A., Hadjeri S., Medles K., Dascalescu L. Study of charged particles trajectories in free-fall electrostatic separators. *Journal of Electrostatics*, 2017, vol. 88, pp. 10-14. doi: https://doi.org/10.1016/j.elstat.2017.01.010.
**31.** Touhami S., Aksa W., Maammar M., Zeghloul T., Medles K., Dascalescu L. Numerical simulation of the behavior of insulating particles in a free fall tribo-electrostatic separator with four vertical cylindrical electrodes. *Journal of Electrostatics*, 2019, vol. 97, pp. 8-14. doi: https://doi.org/10.1016/j.elstat.2018.11.004.

*Received 25.07.2025*
*Accepted 12.09.2025*
*Published 02.01.2026*

*N. Guettaf*[1]*, PhD,*
*S.E.I. Guettaf*[2]*, PhD,*
*T. Zeghloul*[3]*, Professor,*
*H. Nouri*[1]*, Professor,*
[1] Department of Electrical Engineering, LAS Laboratory, Setif 1 University - Ferhat Abbas, Setif, 19000, Algeria, e-mail: nacereddine.guettaf94@gmail.com (Corresponding Author)
[2] Department of Electrical Engineering, QUERE Laboratory, Setif 1 University - Ferhat Abbas, Setif, 19000, Algeria.
[3] IUT Angoulême, Pprime Institute-ENSMA, Poitiers University, Angoulême, 16000, France.

*How to cite this article:*
Guettaf N., Guettaf S.E.I., Zeghloul T., Nouri H. Numerical study of particles trajectories in a multifunctional electrostatic separator powered by photovoltaic system. *Electrical Engineering & Electromechanics*, 2026, no. 1, pp. 69-75. doi: https://doi.org/10.20998/2074-272X.2026.1.09

UDC 621.319 https://doi.org/10.20998/2074-272X.2026.1.10

G.V. Bezprozvannych, I.A. Pushkar

# Influence of gamma radiation on the electrical and mechanical properties of on-board systems cables

***Introduction.*** *Electrical and fiber-optic cables of on-board systems for transmitting monitoring, control and communication signals are increasingly used in nuclear power plants, aircraft systems and military applications. Such operating conditions are characterized by an increased level of ionizing radiation compared to the background: from 10 kGy in space applications to 1 GGy in the corium of a nuclear reactor.* ***Problem.*** *The resistance of polymer insulation to the action of ionizing radiation is determined on the basis of mechanical, thermophysical, physicochemical indicators that reflect the local characteristics of the polymer insulation of electrical cables. Modern special radiation-resistant optical fibers are capable of operating under the action of gamma radiation with a dose of 1 MGy. To ensure mechanical strength and protection of the optical fiber from moisture, high-strength structural elements and hydrophobic fillers are used in the optical cable. The* ***goal*** *of the work consists in establishing the effect of gamma radiation on unshielded cables with unshielded twisted pairs and optical cables with the determination of the dynamics of changes in the electrical properties of polyethylene insulation of conductors and mechanical properties of aramid yarns with a water-blocking coating, respectively.* ***Methodology*** *is based on the determination of the change in the electrical capacitance of each of the 8 polyethylene-insulated twisted pair conductors and the mechanical tensile strength of Kevlar yarns with a water-blocking compound, compared to the un-irradiated state, depending on the absorbed dose of gamma radiation of 100 kGy, 200 kGy and 300 kGy when processing samples of electrical and optical cables in the cobalt-60 ($Co^{60}$) installation.* ***Scientific novelty*** *consists in establishing the criterion for achieving the critical state of polymeric polyethylene insulation of insulated conductors and the effect of the influence of a water-blocking coating with ultra-high absorption capacity on the mechanical strength of aramid yarns under the action of gamma radiation on samples of an electric cable in a protective sheath of polyvinyl chloride plastic compound and an optical cable in a protective sheath based on a polymer fire-resistant composition, respectively.* ***Practical value*** *is qualified by the range of radiation resistance of structural elements to ensure the operational functionality and efficiency of cables of on-board systems under the action of gamma radiation.* References 50, tables 3, figures 6.

*Key words:* **on-board systems, unshielded cable with unshielded twisted pairs, optical cable, absorbed dose of gamma radiation, polyethylene insulation, electrical capacitance, aramid yarns, waterproof compound, mechanical tensile strength, radiation resistance.**

***Вступ.*** *Електричні та оптичні кабелі бортових систем для передачі сигналів моніторингу, керування та зв'язку все частіше використовуються на атомних електричних станціях, в системах літальних апаратів та військовому застосуванні. Такі умови експлуатації характеризуються підвищеним порівняно з фоновим рівнем іонізуючого випромінювання: від 10 кГр у космічних застосуваннях до 1 ГГр в активній зоні ядерного реактора.* ***Проблема****. Стійкість полімерної ізоляції до дії іонізуючого випромінювання визначається на підставі механічних, теплофізичних, фізико-хімічних показників, які відображають локальні характеристики полімерної ізоляції електричних кабелів. Сучасні спеціальні радіаційно-стійкі оптичні волокна здатні працювати при дії гамма-випромінення дози 1 МГр. Задля забезпечення механічної міцності та захисту від вологи оптичного волокна в оптичному кабелі застосовуються високоміцні конструктивні елементи та гідрофобні заповнювачі.* ***Мета*** *роботи полягає у встановленні впливу гамма-випромінення на неекрановані кабелі з неекранованими витими парами та оптичні кабелі з визначенням динаміки змінення електричних властивостей поліетиленової ізоляції провідників та механічних властивостей арамідних ниток з водозахисним покриттям відповідно.* ***Методика*** *ґрунтується на визначенні порівняно з неопроміненим станом змінення електричної ємності кожного з восьми ізольованих поліетиленом провідників витих пар та механічної міцності на розтяг кевларових ниток з водозахисним компаундом в залежності від поглиненої дози гамма-випромінення 100 кГр, 200 кГр та 300 кГр при обробці зразків електричного та оптичного кабелів в установці кобальт-60 ($Co^{60}$).* ***Наукова новизна*** *полягає у встановленні критерію досягнення критичного стану полімерної поліетиленової ізоляції ізольованих провідників та ефекту впливу водозахисного покриття з надвисокою поглинальною здатністю на механічну міцність арамідних ниток при дії гамма-випромінення на зразки електричного кабелю у захисній полімерній оболонці з поліхлорвінілового пластику та оптичного кабелю у захисній оболонці на основі полімерної вогнестійкої композиції відповідно.* ***Практична цінність*** *кваліфікується діапазоном радіаційної стійкості конструктивних елементів для забезпечення експлуатаційної функціональності та ефективності кабелів бортових систем в умовах дії гамма-випромінення.* Бібл. 50, табл. 3, рис. 6.

*Ключові слова:* **бортові системи, неекранований кабель з неекранованими витими парами, оптичний кабель, поглинена доза гамма-випромінення, поліетиленова ізоляція, електрична ємність, арамідні нитки, водозахисний компаунд, механічна міцність на розтяг, радіаційна стійкість.**

**Introduction.** As critical safety components, on-board cables play a crucial role in connecting various electronic and electrical systems, including radar systems, avionics, navigation equipment, and weapons systems [1–10]. The main purpose of on-board cables is to collect and manage data; distribute power with simultaneous data transmission; and provide reliable and secure communication with a high level of noise immunity. Twisted pair and optical cables are increasingly used for real-time transmission of monitoring, control, data, and communication signals in on-board systems and nuclear power plants (NPPs) [1–14].

The trend towards miniaturization continues to affect all aspects of on-board systems. Innovations in electrical insulation materials and cable designs make this possible without sacrificing system performance by creating hybrid cables by combining electrical and optical in a single design.

Cables must meet a list of requirements related to functional characteristics, dimensions, and weight. The operational functionality of cables in on-board systems is determined by their resistance to the influence of external and internal factors. The first ones include such operating conditions of cables as temperature, pressure, air humidity, the presence of external tensile mechanical loads [10], chemical aggressiveness of the external environment and the influence of radiation [12]. The operation of cables of on-board systems is characterized by an increased level of ionizing radiation compared to the background. Thus, at a NPP under normal operating conditions at elevated temperature, cables of the sealed zone are constantly exposed to gamma radiation [13–17]. Outside the radiation protection of the reactor, the radiation level approaches the background, and the temperature approaches the ambient temperature. Aerospace cables [12] are exposed to solar radiation, including intense solar flares. Military cables (aircraft, unmanned aerial vehicles) can also be exposed to natural and artificial radiation, including nuclear explosions [1, 7]. Radiation levels can range from 10 kGy when using cables in space applications to 1 GGy in the core of a nuclear reactor [17–19].

**Problem definition.** Ionizing energy sources (absorbed dose) fully determine the full effect of exposure to polymers used as electrical insulation of cables and optical quartz fibers [20–31].

The following main processes occur in polymers when exposed to ionizing radiation:

- creation of chemical bonds, both between and within macromolecules, destruction and decomposition of macromolecules with the release of gaseous and liquid components, change in the number and nature of double bonds (in the presence of oxygen) and other processes [23–27];
- long chains can connect into rigid three-dimensional networks (crosslinking process) or split into smaller molecules (destruction process). Both processes can occur simultaneously, so at a certain absorbed radiation dose, the final properties and structure of the polymer will be determined by the reaction that dominates [23–27].

For polyethylene, as the absorbed radiation dose increases, the degree of crosslinking increases and, at the same time, fragments of molecular decay accumulate, which in aggregate leads to a decrease in mechanical properties and material destruction [25, 26]. Radiation destruction of macromolecules leads to a decrease in mechanical strength, an increase (up to a certain limit) in relative elongation, and cracking. The polymer surface becomes sticky. The dose required for crosslinking polyethylene is (200–400) kGy [28, 29]. The radiation resistance of polyvinyl chloride plastic is determined by the permissible absorbed dose of gamma radiation at the level of 500 kGy [28] and is established, as for many other polymer materials, on the basis of mechanical, thermophysical, and physicochemical parameters [28–32]. These indicators reflect the indirect characteristics of polymer insulation, unlike electrical ones, which are basic and have an integral nature and reflect the state of cable insulation as a whole.

In optical cables, the effect of radiation separately on optical fibers is considered to the greatest extent [33–36]. Quartz optical fibers are characterized by higher values of the radiation dose at which structural damage occurs, compared to polymeric materials [37]. Under the action of gamma rays and neutrons, the ionization of quartz molecules occurs in the fiber, the migration of electrons and doping impurities, the change in the density of the distribution of valence electrons, hydroxyl ions $OH^-$ are formed from free hydrogen, and radiation absorption centers appear [36]. As a result, electromagnetic energy losses increase [35], i.e. the power of the optical signal propagating in the fiber decreases. Radiation-induced electromagnetic energy losses are determined both by the concentration of absorption centers in the matrix itself based on quartz oxide and by impurities (germanium oxide, phosphorus) [35, 36]. These losses depend on the type and energy of radiation, dose, exposure time, wavelength at which radiation-induced losses are measured, temperature, fiber type and manufacturing technology. After the end of the radiation exposure, optical fibers partially restore their original properties, in particular, an improvement in the indicators of induced electromagnetic energy losses in the optical fiber is observed, which is due to the relaxation of radiation defects [38].

It should be noted that the radiation effect is not always destructive, since it is known that special wires and cables with radiation-crosslinked polymer insulation are produced by the industry of many countries and are used in communication systems, military, aviation and space technology, electronic and computer equipment, nuclear installations, etc. [15]. At the same time, it is necessary to understand that the achievement of a positive radiation-stimulated effect occurs under a set of agreed technological conditions: dose rate, radiation temperature, cable tension force in the radiation field, etc., while under operating conditions these factors are quite random.

Special radiation-resistant optical fibers based on pure silicon oxide without impurities with a hermetic primary coating based on a highly saturated carbon varnish are being developed [39].

The operational functionality of optical fibers in onboard system cables is determined by two components: optical, which consists of the signal throughput at the appropriate distance, associated with the stability of the transmitting optical parameters, and mechanical, due to the preservation of fiber integrity. In practice, the mechanical tensile strength of an optical fiber with a diameter of 125 μm is approximately 5 GPa or 60 N for dynamic tensile strength and 3 GPa or 40 N for static tensile strength [40]. This is due to the loss of durability of optical fibers over time, which is explained by the growth of Griffiths cracks as a result of a chemical reaction under mechanical stress (stress corrosion) when the fiber breaks. Crack growth is also affected by environmental conditions, especially the humidity in which the fiber is located. In the presence of moisture, the fiber breaks even if the mechanical stress applied to it is less than the destructive one. It is static fatigue that limits the service life of the fiber [40, 41], which is a process of slow growth of micron cracks (defects) due to the

influence of moisture and tensile stresses. There is a possibility of fiber failure due to the growth of micron cracks. Moisture in the cable structure, together with the stimulated mechanical stress, causes a corrosion process at the crack tip located on the fiber surface. In this process, water molecules entering the crack from the environment activate the rupture of chemical bonds at the crack tip. This leads to an increase in the crack length under the action of the mechanical stress applied to the fiber. As the crack length increases, the stress concentration at its tip increases and the crack growth rate increases, which ultimately leads to fiber failure: the mechanical stress reaches a critical value. Therefore, the mechanical properties of optical fibers are the most important characteristics that determine the possibility of their practical use in on-board systems. To increase the mechanical strength and ensure the operational functionality of the optical fiber, special strength elements and hydrophobic materials are used in cable structures. These structural elements and materials for protecting the optical fiber from moisture are also exposed to significant influences, in particular radiation, with a change in properties, in particular mechanical. In any case, the issues of the influence of ionizing radiation not only on electrical insulating materials [27, 30, 42, 43] and optical fiber separately [34–36], but also on the cables of on-board systems in general remain unresolved. It is this approach that allows us to take into account the integral nature of the influence of complex physicochemical processes under the influence of gamma radiation on the electrical performance of electric cables and the mechanical strength of optical cables.

**The goal of the work** is to establish the effect of gamma radiation on unshielded cables with unshielded twisted pairs and optical cables with the determination of the dynamics of changes in the electrical properties of polyethylene insulation of conductors and the mechanical properties of aramid yarns with a waterproof coating, respectively.

**Test samples of on-board system cables.** Two types of cables were studied:

1. Electrical – unshielded cable with four unshielded twisted pairs of category 5e. Electrical insulation of copper conductors is made of polyethylene, protective polymer sheath – of polyvinyl chloride-based plastic. The outer diameter of the cable is 5.1 mm. The cable is designed to transmit signals in the frequency range up to 125 MHz.

2. Optical cable with single-mode optical fiber in a dense two-layer coating. The core and reflective sheath of the fiber with a diameter of 125 μm – based on quartz. Buffer primary polymer coating with a thickness of 62.5 μm – based on an ultraviolet-curing silicone varnish to ensure the mechanical integrity of the optical fiber. The second layer of the coating with a thickness of 325.5 μm is based on a thermoplastic organosilicon compound with a top layer of 15 μm of blue color. In the cable design, the power element is two strands of aramid tyarns based on Kevlar (organic fiber from the aromatic polyamide series) [44] to increase mechanical strength with a water-repellent compound applied to protect the optical fiber from moisture. The linear density of each strand of yarns is 805 tex [tex is the linear density: 1 tex = 1 g/km]. Each strand consists of 5 yarns with a linear density of 161 tex. The cable yarn is made on the basis of a polymer fire-resistant composition of orange color. The total diameter of the cable is 2.8 mm.

Table 1 shows the comparative properties of the mechanical characteristics of Kevlar® yarns manufactured by DuPont and other materials.

Table 1

Comparative analysis of mechanical and thermal properties of materials of power elements of optical cables [44]

| Power element material | Density, $kg/m^3$ | Tensile strength $\sigma$, $10^9$, Pa | Young modulus $E$, $10^9$, Pa | Relative elongation $\varepsilon$, % | Thermal expansion coefficient (in the longitudinal direction), $10^{-6}$, $K^{-1}$ |
|---|---|---|---|---|---|
| **Kevlar 49** | **1439.35** | **3.0** | **112.4** | **2.4** | **–2.2** |
| S-glass | 2491.19 | 3.45 | 85.5 | 5.4 | +1.7 |
| Steel rod | 7750.37 | 1.96 | 199.9 | 2.0 | +3.7 |
| High-strength carbon | 1799.19 | 3.1 | 220.6 | 1.4 | –0.1 |

The presented materials can be used as power elements of optical cables of on-board systems. Unique properties distinguish Kevlar® from other commercial artificial yarns due to the combination of high mechanical strength, high modulus of elasticity, impact strength, thermal stability with a high value of the negative coefficient of thermal expansion [44].

Thanks to the use of Kevlar yarns with a water-resistant compound, it is possible to ensure resistance to tensile forces, an optical cable of on-board systems 50 km long when the optical fiber operates at a working wavelength of 1.31 μm.

**Radiation irradiation procedure.** Samples in the amount of 15 segments of 5 m each from one coil of electrical and optical cables, respectively, were placed in a polyethylene container for processing in a cobalt-60 ($Co^{60}$) gamma radiation installation. The radiation exposure dose rate was 207 R/min. The processing time of the cable samples was determined by the absorbed dose. For each batch of 5 cable samples, the absorbed dose of gamma radiation was 100 kGy, 200 kGy and 300 kGy, respectively. The uniformity of the dose distribution when irradiating the material with gamma quanta energies of 1.17 MeV and 1.33 MeV, the radiation of which is accompanied by the decay of the $Co^{60}$ isotope, was ensured by choosing its equivalent thickness of no more than 20 mm [45]: the diameters of the electric and optical cables do not exceed the value of the equivalent thickness.

In the initial state and after the action of irradiation, a study was conducted on the influence of radiation dose on the electrical and mechanical properties of electrical and optical cables, respectively. At all stages of the study, the cables were in an unsealed state to reduce the influence of volatile substances on the analysis results. These substances, which accumulated in the free space of the cable core, diffused out of the cables.

**Numerical calculation of the electric field and capacitance of insulated conductors of an unshielded cable in a polymer protective sheath.** For electrical cables, the electrical capacitance is the most sensitive electrical parameter for assessing the influence of radiation on solid polymer insulation [46], taking into account the influence of complex physicochemical processes in structural elements, including the polymer protective sheath.

The justification of the inspection scheme for monitoring the electrical capacitance of solid polymer insulation of conductors of an unshielded cable with four twisted pairs in a polymer sheath was performed on the basis of numerical modelling of a plane-parallel electrostatic field by the secondary source method [46, 47]. The method is based on the superposition of electric fields of elementary electric charges located in a vacuum.

Figure 1,*a* shows a physical model of an unshielded cable with four unshielded twisted pairs. The numbers are: from 1 to 8 – conductors, 1' – 8' – polymer insulation.

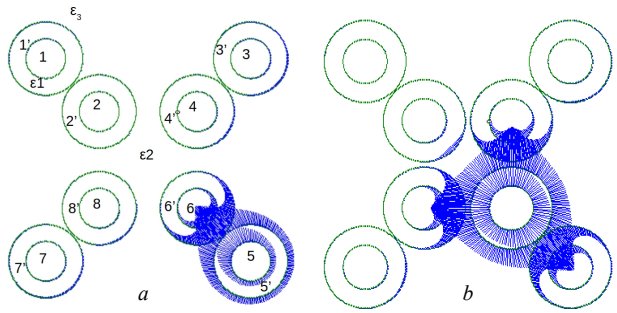


Fig. 1. Physical model of an unshielded cable with four unshielded twisted pairs (*a*) and the pattern of lines of the normal component of the intensity of the probing electric field (*b*), provided that one of the conductors is under potential and all others are at zero potential

The model neglects the helical surface of twisted pairs, which provides a plane-parallel electric field in the cable cross-section. The surfaces of conductors and conductor insulation are assumed to be circular cylindrical, which is consistent with the boundaries of the separation of media in the original problem. The difference in dielectric properties of the cable structural elements is taken into account: the dielectric permittivity of polyethylene insulation of conductors is $\varepsilon_1$=2.3; interphase air medium $\varepsilon_2$=1; protective polymer sheath $\varepsilon_2$=4.5. The cable is located in an air medium with dielectric permittivity ε=1.

To implement the secondary sources method, a transition is made from the calculation of the electric field in the original problem to the calculation of the electric field in a vacuum. To do this, instead of bound charges on the surfaces of the separation of the media of the original problem, free secondary electric charges are located in a vacuum (on an infinitely thin surface *S* of the same shape as the boundary of the separation of the media of the original problem).

The calculated surface density $\sigma$ (C/m$^2$) of these secondary charges must satisfy two conditions:

1) on surfaces reflecting conductors (electrodes), the specified potentials $U_i$ must be achieved;

2) on surfaces reflecting the boundaries of dielectric media, the condition of equality of the normal components of the electric displacement vector must be fulfilled:

$$\varepsilon_2 \cdot \left( E_n - \frac{\sigma_i}{2\varepsilon_0} \right) = \varepsilon_1 \cdot \left( E_n + \frac{\sigma_i}{2\varepsilon_0} \right), \qquad (1)$$

where $E_n$ is the normal component of the electric field strength at point *i*, created by all charges except the one located at this point on an infinitely small surface $\Delta S$; $\sigma_i/(2\varepsilon_0)$ is the normal component of the electric field strength at point *i*, created by the charge itself located at this point on an infinitely small surface $\Delta S$; $\varepsilon_0 = 8.85 \cdot 10^{-12}$ F/m is the electric constant.

The first and second conditions are written as Fredholm integral equations of the first (2) and second (3) kind, respectively:

$$\frac{1}{2\pi\varepsilon_0} \int_0^L \sigma_j \cdot \ln\left( \frac{r_{0j}}{r_{ij}} \right) \cdot \mathrm{d}l_j = U_i \, ; \qquad (2)$$

$$\frac{\sigma_i}{2\varepsilon_0} - \frac{\varepsilon_2 - \varepsilon_1}{\varepsilon_2 + \varepsilon_1} \cdot \frac{1}{2\pi\varepsilon_0} \int_{S-\Delta S} \sigma_j \cdot \frac{\cos\left(\overline{r_{ij}}, \overline{n_i}\right)}{r_{ij}} \cdot \mathrm{d}l_j = 0 \, , \qquad (3)$$

where *i* is the node number where the characteristics of the electric field are sought; *j* is the node number where the charge is located; $r_{ij}$ is the distance between points *i* and *j*; $r_{0j}$ is the distance from point *j* to point *O*, the potential of which can be taken as zero ($r_{0j}$ = 1 m for models whose transverse size lies in the centimeter range, which is true for the model of an unshielded cable with four twisted pairs); $\sigma_j$ is the secondary charge density at point *j*; $\mathrm{d}l_j$ is the length of an infinitely small section centered at point j; $\cos\left(\overline{r_{ij}}, \overline{n_i}\right)$ is the cosine of the angle between the vectors $\overline{r_{ij}}$ and $\overline{n_i}$ – the normal vector to the interface of the media at point *i*.

Only in this case will the electric field of the calculation model be identical to the field of the original problem. The calculation of the electric field is reduced to solving a component system of linear algebraic equations (SLAE), to which (2) and (3) are reduced. Based on the numerical solution of such a SLAE, the calculated surface density (in vacuum) of secondary charges and the electric field strength are determined:

$E_i = \frac{\sigma_i}{\varepsilon_0}$ – for the surfaces of conductors (electrodes),

$E_i = \frac{\sigma_i}{2\varepsilon_0}\left(1 + \frac{1}{\alpha}\right)$ – for the interface of dielectric media (the normal component of the electric field strength from the side of the positive direction of the normal), where is the parameter associated with the dielectric permittivities of adjacent media when the normal vector is oriented from a medium with a dielectric permittivity $\varepsilon_1$ (polyethylene insulation) to a medium with $\varepsilon_2$ (interphase air medium).

The actual density $\sigma'_i$ of surface charges on the surfaces of conductors insulated with a dielectric with a dielectric permittivity $\varepsilon_1$ is $\varepsilon_1$ times greater

$$\sigma' = \varepsilon_1 \cdot \sigma ,$$

which is taken into account when determining the total charge of each insulated core and electric capacitance under the condition of given potentials of the conductors.

Figures 1–4 present electric field patterns in the form of lines for the normal component of the electric field strength on the surface of conductors and the interface of dielectric media depending on the survey scheme under the condition of applying a potential of 1 V to:

- one conductor and the other seven being at zero potential (Fig. 1,*b*);
- two conductors and the other six being at zero potential (Fig. 2);
- three conductors and the other five being at zero potential (Fig. 3);
- four conductors and the other four being at zero potential (Fig. 4).

The points show the nodes on the surface of conductors (1–8) and insulation (1'–8') with the desired values of surface charge density and electric field strength in the calculation model of an unshielded cable with four unshielded twisted pairs.

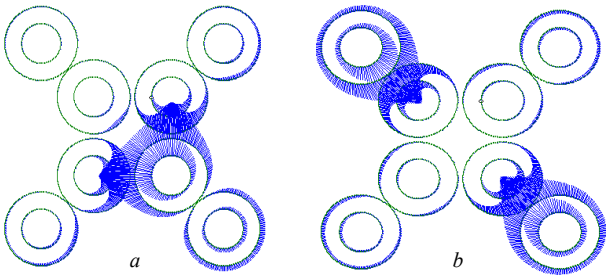

Fig. 2. Visualization of the normal component of the probing electric field strength under the condition of two insulated conductors 5 and 6 (*a*) and 1 and 6 (*b*) at a potential of 1 V

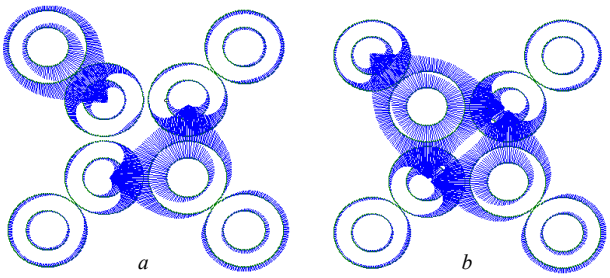

Fig. 3. Visualization of the normal component of the probing electric field strength under the condition of three insulated conductors 1, 5, and 6 (*a*) and 1 and 2, 5, and 6 (*b*) at a potential of 1 V

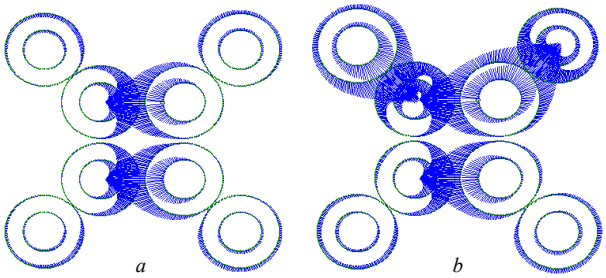

Fig. 4. Visualization of the normal component of the probing electric field strength under the condition of four insulated conductors 3, 4, 5, and 6 (*a*) and 1, 4, 6, and 7 (*b*) at a potential of 1 V

For the presented inspection schemes (Fig. 1–4), the probing electric field is concentrated both in the solid polyethylene insulation and in the interphase space of the insulated conductors, which allows determining the total $C_S$ and partial $C_{part}$ electric capacitances of the insulating gaps based on determining the actual density σ′ of surface charges and the total charge of each insulated conductor under the condition of a given potential.

For example, under the condition of applying a potential of 1 V to conductor 5 and zero potential to seven other conductors (Fig. 1,*a*), the partial capacitances $C_{5\text{-}1}$, $C_{5\text{-}2}$, $C_{5\text{-}3}$, $C_{5\text{-}4}$, $C_{5\text{-}6}$, $C_{5\text{-}7}$, $C_{5\text{-}8}$ of the insulating gaps between conductors 5-1, 5-2, 5-3, 5-4, 5-6, 5-7 and 5-8 are connected in parallel and determine the total capacitance $C_{5S}$ of conductor 5:

$$C_{5S} = C_{5\text{-}1} + C_{5\text{-}2} + C_{5\text{-}3} + C_{5\text{-}4} + C_{5\text{-}6} + C_{5\text{-}7} + C_{5\text{-}8}.$$

Given that two insulated conductors 5 and 6 (Fig. 2,*a*) are under a potential of 1 V and the other 6 are under zero potential, the partial capacitances of the insulating gaps between conductors 5,6-1, 5,6-2, 5,6-3, 5,6-4, 5,6-7 and 5,6-8 are connected in parallel and determine the total capacitance of conductors 5 and 6, respectively:

$$C_{5S} + C_{6S} = C_{5,6\text{-}1} + C_{5,6\text{-}2} + C_{5,6\text{-}3} + C_{5,6\text{-}4} + C_{5,6\text{-}7} + C_{5,6\text{-}8}.$$

The inspection scheme, provided that a potential of 1 V is applied to one of the conductors and zero to the other seven, can be written in binary. For example, when conductor 5 is under a potential of 1 V, the corresponding code looks like: 00001000 (Fig. 1, *a*). For conductor 6 – 00000100 (Fig. 1, *b*).

Table 2 shows individual results of determining the electrical capacitance of conductors depending on the survey code in accordance with Fig. 1–4.

Table 2

Electrical capacitance of insulated conductors of unshielded twisted pairs of unshielded cable

| Inspection code | Electrical capacitance of an insulated conductor *C*, pF/m | | | | | | | |
|---|---|---|---|---|---|---|---|---|
| | 1 | 2 | 3 | 4 | 5 | 6 | 7 | 8 |
| 00001000 | 1.041 | 0.263 | 1.972 | 3.712 | **43.13** | 29.06 | 3.706 | 1.974 |
| 00000100 | 0.223 | 2.494 | 2.061 | 20.58 | 28.10 | **76.31** | 2.059 | 20.58 |
| 00001100 | 1.363 | 2.717 | 6.285 | 22.64 | **15.26** | **48.20** | 6.281 | 22.63 |
| 10000100 | **42.21** | 28.32 | 8.445 | 4.120 | 28.30 | **42.17** | 8.439 | 4.119 |
| 10001100 | **41.95** | 30.79 | 10.51 | 24.70 | **47.98** | **14.11** | 10.49 | 24.69 |
| 01001100 | **29.44** | **73.55** | 8.345 | 43.21 | **15.03** | **45.71** | 8.339 | 43.20 |
| 00111100 | 7.644 | 25.35 | **8.966** | **25.56** | **8.966** | **25.56** | 7.644 | 25.35 |
| 10010110 | **39.89** | 51.13 | 38.60 | **51.16** | 12.05 | **27.19** | **10.72** | 27.39 |

The difference between the total and partial capacitance values according to the 00001000 inspection scheme is 2.9 %, according to the 00001100 inspection scheme – 2.5 %.

Even with the same survey scheme, the electrical capacitances of conductors in a cable with different orientation of twisted pairs are different due to the different configuration of the electric field and the distance between insulated conductors (compare Fig. 1,*a* and Fig. 1,*b*). For an ideal calculation model of a cable with four twisted pairs twisted with the same twist steps (Fig. 1), provided that one of the conductors is under potential, and all the other seven

are under zero, there are only two schemes in which the capacitances of insulated conductors, taking into account the influence of those located nearby, differ from each other (see Table 1). The value of the electric capacitance for the inspection codes 00000100 and 00001000 differs by 76.31/43.13=1.7693 times.

For the following inspection schemes, namely: two conductors - relative to six; three conductors – relative to five; four conductors - relative to four, there are four main survey schemes. All others are inverse. Comparison of the results of numerical calculations of the electric capacitance for the main and inverse differ by 0.4 %, which indicates the high accuracy of the numerical calculation of the electric field and the determination of the electric capacitance of the conductors based on it.

In practice, four pairs of the cable are twisted with different steps to increase noise immunity when transmitting digital signals. A polymer protective sheath based on polar plastic is tightly applied to the core of the twisted pairs. This causes a more complex field configuration for any scheme of applying potential to the conductors and performing a full set of inspection schemes. First of all, to determine the dynamics of the change in electrical capacitance, i.e. the properties of the solid insulation of each conductor according to the survey scheme, each of the 8 conductors is under an applied potential – relative to all the other seven under zero potential (see Fig. 1, Table 2). In this case, the probing electric field is concentrated mainly in the solid polymer insulation of each of the 8 conductors (see Fig. 1). Such a inspection scheme provides control of the individual electrical properties of the solid polymer insulation of the conductors and should be implemented in practice. In a real cable design, with such an inspection scheme, the electrical capacitances of the conductors in the initial unirradiated state differ by no more than 4 %, which requires high accuracy of control of electrical parameters.

**Dynamics of the change in electrical capacitance of insulated conductors depending on the absorbed dose of gamma radiation by cable samples.** The control of the electrical capacitance of electrical cable samples in the initial state and after the absorbed radiation dose of 100, 200 and 300 kGy was carried out for four frequency values of 0.1; 1; 10 and 1000 kHz using devices with two terminals, respectively. In the frequency range from 0.1 to 10 kHz, the measurement was performed in the mode of 10-fold accumulation of results with automatic averaging to increase the control accuracy. The total number of measurements for each sample was 241 measurements before and after exposure to radiation. The measurement results of each of the five samples in the initial state and after the corresponding radiation dose were averaged.

Figure 5 shows the dynamics of the change in the electrical capacitance of insulated conductors depending on the absorbed dose of gamma radiation at different frequency values. Curves 1 correspond to the values of the capacitance of the conductors in the initial state before the action of gamma radiation. Curves 2 – at an absorbed radiation dose of 100, 200 and 300 kGy, respectively.

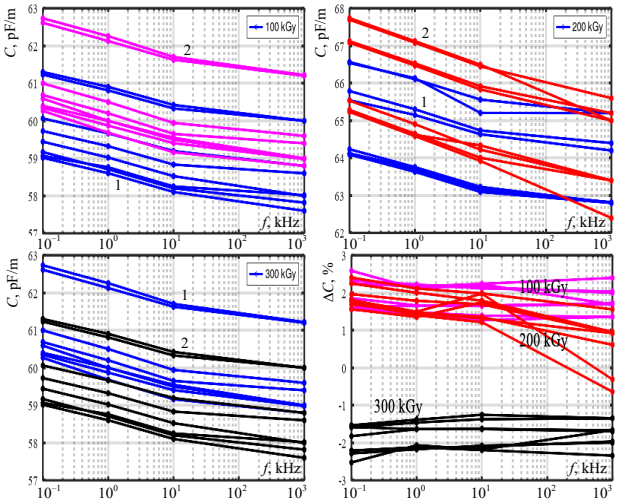


Fig. 5. Comparative analysis of the dynamics of changes in experimental frequency dependencies of electrical capacitance of polyethylene-insulated conductors before and after gamma radiation of twisted pair cable samples

Table 3 shows the determined pairwise linear correlation coefficients between the capacitance of insulated conductors of a twisted pair cable in the irradiated and non-irradiated states for different frequency values according to Fig. 5. Positive Pearson correlation coefficients indicate the presence of a significant direct relationship between the capacitance of conductors in the irradiated and non-irradiated states: the highest values at the level of 0.99 are observed in the frequency range from 0.1 kHz to 10 kHz at an irradiation dose of 200 kGy.

Table 3

Pearson pairwise correlation coefficients between the electrical capacitance of insulated conductors

| Frequency, kHz | | | |
|---|---|---|---|
| 0.1 | 1 | 100 | 1000 |
| Pairwise correlation coefficient between the values of the electrical capacitance of insulated conductors in the irradiated state relative to the unirradiated state | | | |
| 1-2 | 3-4 | 5-6 | 7-8 |
| When exposed to gamma radiation at a dose of 100 kGy | | | |
| 0.9725 | 0.9780 | 0.9705 | 0.9829 |
| 0.9777 | 0.9822 | 0.9755 | 0.9857 |
| 0.9762 | 0.9809 | 0.9740 | 0.9846 |
| 0.9721 | 0.9722 | 0.9653 | 0.9653 |
| When exposed to gamma radiation at a dose of 200 kGy | | | |
| **0.9866** | **0.9858** | **0.9870** | 0.9207 |
| **0.9875** | **0.9866** | **0.9864** | 0.9178 |
| **0.9866** | **0.9861** | **0.9864** | 0.9390 |
| **0.9887** | **0.9877** | **0.9846** | 0.9164 |
| When exposed to gamma radiation at a dose of 300 kGy | | | |
| 0.9725 | 0.9777 | 0.9762 | 0.9721 |
| 0.9780 | 0.9822 | 0.9809 | 0.9722 |
| 0.9705 | 0.9755 | 0.9740 | 0.9653 |
| 0.9829 | 0.9857 | 0.9846 | 0.9788 |

Figure 5 also shows the effect of radiation dose on the relative value of $\Delta C$ of the electrical capacitance in the irradiated state to the capacitance in the initial unirradiated state of cable samples (bottom figure, right). The relative value of the electrical capacitance is defined as: $(C_\gamma - C_0) / C_0 \cdot 100$, %, where $C_0$ is the electrical capacitance of the conductors in the initial state before the

action of gamma radiation; $C_\gamma$ is the electrical capacitance of the conductors under the action of gamma radiation.

At an absorbed radiation dose of 100 kGy and 200 kGy, the relative value of the capacitance is positive, which indicates the process of crosslinking of thermoplastic polyethylene insulation. At a radiation dose of up to 100 kGy, crosslinking of polyethylene insulation occurs with the formation of cross-linking intermolecular bonds. This process causes an increase in the density of the polymer and, as a consequence, an increase in the dielectric constant, i.e. the electrical capacitance of insulated conductors. At the same time, the dispersion of the electrical capacitance – the dependence of the electrical capacitance on the frequency, which is determined by the difference in the capacitance values for the frequency of 0.1 kHz and 1 MHz, is observed to a greater extent at an absorbed dose of 200 kGy (see Fig. 5). At this radiation dose, the process of intensive destruction of the polymer insulation begins with additional crosslinking of the structure, which increases the thermal stability of the insulation [48]. Destruction leads to the formation of polymer chains of shorter length in the structure of polyethylene insulation, which causes the manifestation of the process of their polarization in the low-frequency frequency range. This corresponds to the hypothesis of the slowed-down dipole-segmental polarization of polymers, which is detected precisely in the frequency range of the experimental studies conducted. In other words, at an absorbed radiation dose of more than 200 kGy, the destruction processes dominate over the crosslinking process of polymer insulation. For a radiation dose of 300 kGy, the relative value of the capacitance changes to the opposite and becomes negative (see Fig. 5). There is a decrease in the density of polyethylene insulation and, as a result, a decrease in the capacitance of insulated conductors (see Fig. 5).

**Determination of the mechanical strength of aramid yarns of an optical cable.** Mechanical indicators are most suitable for assessing the effect of radiation on the protective elements of cables and are widely used, for example, in diagnosing protective sheaths of electric cables. These include the following indicators [42, 43].

1) Relative elongation at break – the main indicator of the quality of polymer insulation of cables and optical fiber. The service life of polymer insulation of cables correlates well with the value of elongation at break. The values of elongation at break are (400 – 500) % for new polyethylene insulation and only 50 % for aged: at such elongation values, the service life of polyethylene insulation is considered exhausted [49].

2) The modulus of elasticity of insulation during torsion – an indicator alternative to elongation at break.

3) The modulus of elasticity during compression. This is the simplest way to assess the condition of cable sheaths.

These indicators are not suitable for assessing the condition of power elements of optical cables due to their design.

The evaluation of the effect of gamma radiation on a power element made of Kevlar yarns impregnated with a water-repellent compound was carried out based on the determination of the mechanical tensile strength. The test was carried out in accordance with ASTM D7269/D7269M-2 «Standard Test Methods for Tensile Strength of Aramid Yarns». ASTM D7269 is an international test Standard for determining the tensile strength of aramid yarns, cords twisted from such yarns, and fabrics woven from such cords. The ASTM D7269 standard covers several variants of testing procedures for aramid yarns and Kevlar-type fibers. This test was carried out using a tensile testing machine. The machine is a mechanical-electrical integration and consists of a force sensor, a transmitter, a microprocessor and a load drive mechanism. The high-precision electronic motor can be adjusted to five speeds, and the components are connected by plugs. The breaking load measurement was performed at a constant speed of a moving clamp with a pendulum. The clamp jaws are flat with a gasket to avoid slipping and catching of the threads during the tests. The test was performed on untwisted yarns. The nominal distance between the clamps (length of the yarn samples) is 200 mm. The clamping speed is 250 mm/min. The pretension of the yarns is (20 ± 2) mN/tex. The actual breaking load at thread breakage is taken as the arithmetic mean of five test results in the unirradiated state and after each absorbed dose of radiation of the optical cable samples, respectively.

**Influence of the absorbed dose of gamma radiation on the mechanical tensile strength of high-strength yarns with a waterproof compound of optical cables.** The Kevlar yarns themselves demonstrate high radiation resistance under the action of accelerated electron irradiation [44]. In Fig. 6, curve 1 confirms the high mechanical properties of Kevlar® 49 yarns [44]: a slight increase of 7 % in mechanical tensile strength relative to the initial, unirradiated state is observed at an absorbed dose of up to 2000 kGy [44].

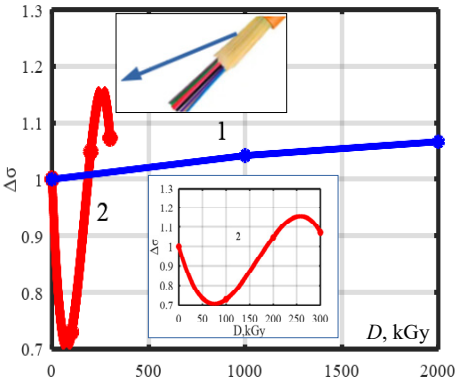


Fig. 6. Dynamics of change in mechanical tensile strength of Kevlar® 49 aramid yarns under irradiation with accelerated electrons (curve 1) [44] and of Kevlar-based aramid yarns impregnated with a water-repellent emulsion under the action of gamma radiation on optical cable samples

Irradiation of optical cable samples with Kevlar yarns impregnated with a water-repellent emulsion demonstrates a significant effect of the absorbed dose of gamma radiation on the mechanical strength of irradiated samples compared to the mechanical strength of unirradiated samples. Curve 2 in Fig. 6 corresponds to the experimental dependence of the mechanical tensile strength of high-strength Kevlar-based yarns with a

water-repellent compound, extracted from optical cable samples irradiated with a dose of 100, 200 and 300 kGy. The points on curve 2 are the result of averaging the mechanical strength values. The smooth curve 2 is a polynomial approximation of a 5th-order polynomial [50].

In the considered range of absorbed gamma radiation dose, a characteristic decrease in mechanical tensile strength by 30 % is observed at a dose of 75 kGy and an increase by 11.5 % at a dose of about 250 kGy relative to the initial unirradiated state. The decrease in mechanical strength of aramid yarns is observed due to the influence of a water-protective adsorbent. Under the influence of radiation, additional polymerization of the water-oil emulsion of polymers with ultra-high absorption capacity occurs. This leads to its shrinkage, which causes a strong effect of the influence on the mechanical strength of aramid yarns. At higher values of the absorbed radiation dose, the influence of the water-oil emulsion of polymers with ultra-high absorption capacity decreases. In this case, processes of direct influence of gamma radiation on aramid yarns with an increase in their mechanical strength are observed: the process of radiation crosslinking of organic fiber based on aromatic polyamides is traced.

**Conclusions.**

1. Based on numerical modeling of the electrostatic field in an unshielded electrical cable with different orientations of four unshielded twisted pairs, an inspection scheme was justified to control the individual electrical properties of solid polymer insulation of insulated conductors.

2. Experimental studies have proven the effect of an absorbed dose of 100 kGy, 200 kGy and 300 kGy of gamma radiation on the processes of crosslinking and destruction of polyethylene insulation of samples of an unshielded electrical cable. This is indirectly confirmed by the dynamics of changes in the electrical capacitance of insulated conductors of unshielded four twisted pairs according to the test scheme: each insulated conductor under potential – against all seven others under zero potential.

3. A criterion for achieving a critical state of polymer polyethylene insulation of insulated conductors under the action of gamma radiation of cables is proposed. The criterion is based on the change in the sign of the relative electrical capacitance of insulated conductors in the irradiated state to the unirradiated state of the cables of on-board systems. In the range of the absorbed dose of gamma radiation from 100 kGy to 200 kGy (in the frequency range from 0.1 kHz to 10 kHz), the relative electrical capacitance has a positive sign. At an absorbed dose of 300 kGy, it has a negative sign.

4. The synergistic effect of the influence of a water-repellent adsorbent on the mechanical strength of aramid yarns of the power element under the action of gamma radiation on samples of the optical cable of on-board systems has been experimentally proven. In the range of the absorbed dose of radiation up to 175 kGy, a decrease in the mechanical tensile strength of aramid yarns is observed, which is due to the influence of the adsorbent itself. At a gamma radiation dose of more than 175 kGy, the effect of the adsorbent decreases. The effect of radiation strengthening of the mechanical strength of aramid yarns by 11.5 % relative to the unirradiated state is observed at an absorbed dose of 250 kGy.

5. The conducted experimental studies provide grounds for increasing the radiation resistance of structural elements and the overall efficiency of the operation of electrical and optical cables of on-board systems under gamma radiation.

**Conflict of interest.** The authors declare no conflict of interest.

REFERENCES


***1.*** Sahoo S., Zhao X., Kyprianidis K. A Review of Concepts, Benefits, and Challenges for Future Electrical Propulsion-Based Aircraft. Aerospace, 2020, vol. 7, no. 4, art. no. 44. doi: https://doi.org/10.3390/aerospace7040044.

***2.*** Aretskin-Hariton E., Schnulo S.L., Hendricks E.S., Chapman J.W. Electrical Cable Design for Urban Air Mobility. *American Institute of Aeronautics and Astronautics. Aerospace Research Central.* January 2020. doi: https://doi.org/10.2514/6.2020-0014.

***3.*** Bode I. Emergent Normativity: Communities of Practice, Technology, and Lethal Autonomous Weapon Systems. *Global Studies Quarterly*, 2024, vol. 4, no. 1, pp. 1-11. doi: https://doi.org/10.1093/isagsq/ksad073.

***4.*** Dorczuk M. Modern weapon systems equipped with stabilization systems: division, development objectives, and research problems. *Scientific Journal of the Military University of Land Forces*, 2020, vol. 197, no. 3, pp. 651-659. doi: https://doi.org/10.5604/01.3001.0014.3959.

***5.*** Borghei M., Ghassemi M. Insulation Materials and Systems for More- and All-Electric Aircraft: A Review Identifying Challenges and Future Research Needs. *IEEE Transactions on Transportation Electrification*, 2021, vol. 7, no. 3, pp. 1930-1953. doi: https://doi.org/10.1109/TTE.2021.3050269.

***6.*** *Fiber Optic Cable In Military Application Market Analysis, Size, and Forecast 2025-2029: North America (US and Canada), Europe (France, Germany, Russia, UK), Middle East and Africa, APAC (China, India, Japan, South Korea), South America, and Rest of World (ROW)*. Report. 2025, 222 p. Available at: https://www.mordorintelligence.com/industry-reports/military-fibre-optic-cables-market (Accessed 27 May 2025).

***7.*** Brunelle R., Pegge C. A history of avionic fiber optic cable development and future requirements. *IEEE Conference Avionics Fiber-Optics and Photonics*, 2005, pp. 1-2. doi: https://doi.org/10.1109/AVFOP.2005.1514127.

***8.*** Patel H.K., Shah S.S. Detailed analysis of fiber optic networks and its benefits in defense applications. *International Journal of Advanced Research in Engineering and Technology*, 2015, vol. 6, no. 2, pp. 01-08. Available at: https://iaeme.com/Home/article_id/IJARET_06_02_001 (Accessed 27 May 2025).

***9.*** Ruffin P.B. A review of fiber optics technology for military applications. *Proceedings of SPIE - The International Society for Optical Engineering*, 2000, vol. 10299, pp. 1-24, art. no. 1029902. doi: https://doi.org/10.1117/12.419796.

***10.*** Kyselak M., Vavra J., Slavicek K., Grenar D., Hudcova L. Long Distance Military Fiber-Optic Polarization Sensor Improved by an Optical Amplifier. *Electronics*, 2023, vol. 12, no. 7, art. no. 1740. doi: https://doi.org/10.3390/electronics12071740.

***11.*** Marques C., Leal-Júnior A., Kumar S. Multifunctional Integration of Optical Fibers and Nanomaterials for Aircraft Systems. *Materials*, 2023, vol. 16, no. 4, art. no. 1433. doi: https://doi.org/10.3390/ma16041433.

***12.*** Rovera A., Tancau A., Boetti N., Dalla Vedova M.D.L., Maggiore P., Janner D. Fiber Optic Sensors for Harsh and High Radiation Environments in Aerospace Applications. *Sensors*, 2023, vol. 23, no. 5, art. no. 2512. doi: https://doi.org/10.3390/s23052512.
***13.*** Lee H.-K., Choo J., Shin G., Kim J. Long-Reach DWDM-Passive Optical Fiber Sensor Network for Water Level Monitoring of Spent Fuel Pool in Nuclear Power Plant. *Sensors*, 2020, vol. 20, no. 15, art. no. 4218. doi: https://doi.org/10.3390/s20154218.
***14.*** Esposito F., Stancalie A., Campopiano S., Iadicicco A. Editorial to the Special Issue Optical Fiber Sensors in Radiation Environments. *Sensors*, 2023, vol. 23, no. 22, art. no. 9117. doi: https://doi.org/10.3390/s23229117.
***15.*** *Nexans. Nuclear industry Cable Applications. A practical guide*. 2016, 24 p.
***16.*** Šaršounová Z., Plaček V., Prajzler V., Masopustová K., Havránek P. Influence of Optic Cable Construction Parts on Recovery Process after Gamma Irradiation. *Energies*, 2022, vol. 15, no. 2, art. no. 599. doi: https://doi.org/10.3390/en15020599.
***17.*** Cheymol G., Maurin L., Remy L., Arounassalame V., Maskrot H., Rougeault S., Dauvois V., Le Tutour P., Huot N., Ouerdane Y., Ferdinand P. Irradiation Tests of Optical Fibers and Cables Devoted to Corium Monitoring in Case of a Severe Accident in a Nuclear Power Plant. *IEEE Transactions on Nuclear Science*, 2020, vol. 67, no. 4, pp. 669-678. doi: https://doi.org/10.1109/TNS.2020.2978795.
***18.*** London Y., Sharma K., Diamandi H., Hen M., Bashan G., Zehavi E., Zilberman S., Berkovic G., Zentner A., Mayoni M., Stolov A., Kalina M., Kleinerman O., Shafir E., Zadok A. Opto-Mechanical Fiber Sensing of Gamma Radiation. *Journal of Lightwave Technology*, 2021, vol. 39, no. 20, pp. 6637-6645. doi: https://doi.org/10.1109/JLT.2021.3102698.
***19.*** Francesca D.Di, Brugger M., Vecchi G.L., Girard S., Morana A., Reghioua I., Alessi A., Hoehr C., Robin T., Kadi Y. Qualification and Calibration of Single-Mode Phosphosilicate Optical Fiber for Dosimetry at CERN. *Journal of Lightwave Technology*, 2019, vol. 37, no. 18, pp. 4643-4649. doi: https://doi.org/10.1109/JLT.2019.2915510.
***20.*** Naikwadi A.T., Sharma B.K., Bhatt K.D., Mahanwar P.A. Gamma Radiation Processed Polymeric Materials for High Performance Applications: A Review. *Frontiers in Chemistry*, 2022, vol. 10. art. no. 837111. doi: https://doi.org/10.3389/fchem.2022.837111.
***21.*** Drobny J.G. *Radiation Technology for Polymers.* Boca Raton, CRC Press, 2021, 338 p. doi: https://doi.org/10.1201/9780429201196.
***22.*** *Radiation Technologies and Applications in Materials Science.* Edited by Subhendu Ray Chowdhury. Boca Raton, CRC Press, 2022, 416 p. doi: https://doi.org/10.1201/9781003321910.
***23.*** Tamada M. Radiation Processing of Polymers and Its Applications. *Radiation Applications*, 2018, pp. 63-80. doi: https://doi.org/10.1007/978-981-10-7350-2_8.
***24.*** Ashfaq A., Clochard M.-C., Coqueret X., Dispenza C., Driscoll M.S., Ulański P., Al-Sheikhly M. Polymerization Reactions and Modifications of Polymers by Ionizing Radiation. *Polymers*, 2020, vol. 12, no. 12, art. no. 2877. doi: https://doi.org/10.3390/polym12122877.
***25.*** Azevedo A.M.de, da Silveira P.H.P.M., Lopes T.J., da Costa O.L.B., Monteiro S.N., Veiga-Júnior V.F., Silveira P.C.R., Cardoso D.D., Figueiredo A.B.-H. da S. Ionizing Radiation and Its Effects on Thermoplastic Polymers: An Overview. *Polymers*, 2025, vol. 17, no. 8, art. no. 1110. doi: https://doi.org/10.3390/polym17081110.
***26.*** Barlow A., Biggs J.W., Meeks L.A. Radiation processing of polyethylene. *Radiation Physics and Chemistry*, 1981, vol. 18, no. 1-2, pp. 267-280. doi: https://doi.org/10.1016/0146-5724(81)90080-7.
***27.*** Liu B., Gao Y., Li J., Guo C., Gao J., Chen Y., Du B. Aging Behavior of Polypropylene as Cable Insulation Under Gamma-Ray Irradiation. *IEEE Transactions on Dielectrics and Electrical Insulation*, 2024, vol. 31, no. 2, pp. 956-964. doi: https://doi.org/10.1109/TDEI.2023.3337753.
***28.*** Manas D., Ovsik M., Mizera A., Manas M., Hylova L., Bednarik M., Stanek M. The Effect of Irradiation on Mechanical and Thermal Properties of Selected Types of Polymers. *Polymers*, 2018, vol. 10, no. 2, art. no. 158. doi: https://doi.org/10.3390/polym10020158.
***29.*** Sirin M., Zeybek M.S., Sirin K., Abali Y. Effect of gamma irradiation on the thermal and mechanical behaviour of polypropylene and polyethylene blends. *Radiation Physics and Chemistry*, 2022, vol. 194, art. no. 110034. doi: https://doi.org/10.1016/j.radphyschem.2022.110034.
***30.*** Besprozvannykh G.V., Naboka B.G., Morozova E.V. Radiation resistance of internal cables for general industrial use. *Electrical Engineering & Electromechanics*, 2006, no. 3, pp. 82-86. (Rus).
***31.*** Liu Z., Miyazaki Y., Hirai N., Ohki Y. Comparison of the effects of heat and gamma irradiation on the degradation of cross-linked polyethylene. *IEEJ Transactions on Electrical and Electronic Engineering*, 2020, vol. 15, no. 1, pp. 24-29. doi: https://doi.org/10.1002/tee.23023.
***32.*** Maléchaux A., Colombani J., Amat S., Marque S.R.A., Dupuy N. Influence of Gamma Irradiation on Electric Cables Models: Study of Additive Effects by Mid-Infrared Spectroscopy. *Polymers*, 2021, vol. 13, no. 9, art. no. 1451. doi: https://doi.org/10.3390/polym13091451.
***33.*** Li D., Sriraman A., Ni Y., Ellis I., Spencer M.P., Zwoster A., Fifield L.S. Dose Rate Effects in the Aging of Nuclear Cable Insulation Subjected to Gamma Radiation. *2022 IEEE Conference on Electrical Insulation and Dielectric Phenomena (CEIDP)*, 2022, pp. 372-375. doi: https://doi.org/10.1109/CEIDP55452.2022.9985382.
***34.*** Girard S., Kuhnhenn J., Gusarov A., Brichard B., Van Uffelen M., Ouerdane Y., Boukenter A., Marcandella C. Radiation Effects on Silica-Based Optical Fibers: Recent Advances and Future Challenges. *IEEE Transactions on Nuclear Science*, 2013, vol. 60, no. 3, pp. 2015-2036. doi: https://doi.org/10.1109/TNS.2012.2235464.
***35.*** Prajzler V., Masopoustova K., Sarsounova Z. Gamma radiation effects on plastic optical fibers. *Optical Fiber Technology*, 2022, vol. 72, art. no. 102995. doi: https://doi.org/10.1016/j.yofte.2022.102995.
***36.*** Bezprozvannykh G.V., Naboka B. G., Morozova E.V. The influence of impurities on radiation-induced losses in optical fibers. *Bulletin of NTU «KhPI»*, *Series: Energy: Reliability and Energy Efficiency*, 2006, no. 7, pp. 53-58. (Rus).
***37.*** Campanella C., De Michele V., Morana A., Mélin G., Robin T., Marin E., Ouerdane Y., Boukenter A., Girard S. Radiation Effects on Pure-Silica Multimode Optical Fibers in the Visible and Near-Infrared Domains: Influence of OH Groups. *Applied Sciences*, 2021, vol. 11, no. 7, art. no. 2991. doi: https://doi.org/10.3390/app11072991.
***38.*** Von White II G., Tandon R., Serna L., Celina M., Bernstein R. *An Overview of Basic Radiation Effects on Polymers and Glasses*. U.S. Department of Energy, 2013, 35 p. Available at: https://www.osti.gov/servlets/purl/1671997 (Accessed 19 May 2025).
***39.*** Bezprozvannykh G.V., Naboka B.G., Morozova E.V. Relaxation of radiation-induced losses in quartz-based optical fibers after the end of irradiation. *Bulletin of NTU «KhPI»*, *Series: Energy: Reliability and Energy Efficiency*, 2005, no. 42, pp. 57-60. (Rus).
***40.*** Li J., Chen Q., Zhou J., Cao Z., Li T., Liu F., Yang Z., Chang S., Zhou K., Ming Y., Yan T., Zheng W. Radiation Damage Mechanisms and Research Status of Radiation-

Resistant Optical Fibers: A Review. *Sensors*, 2024, vol. 24, no. 10, art. no. 3235. doi: https://doi.org/10.3390/s24103235.
***41.*** Bickham S.R., Glaesemann G.S., Shu Y., Scannell G.W. Reliability and Bend Loss of Optical Fibers in Tight Bend Applications. *2021 IEEE CPMT Symposium Japan (ICSJ)*, 2021, pp. 146-149. doi: https://doi.org/10.1109/ICSJ52620.2021.9648876.
***42.*** Bezprozvannych G.V., Mirchuk I.A. Correlation between electrical and mechanical characteristics of cables with radiation-modified insulation on the basis of a halogen-free polymer composition. *Electrical Engineering & Electromechanics*, 2018, no. 4, pp. 54-57. doi: https://doi.org/10.20998/2074-272X.2018.4.09.
***43.*** Bezprozvannych G.V., Mirchuk I.A. Influence of technological dose of irradiation on mechanical and electrical characteristics of polymeric insulation of wires. *Problems of Atomic Science and Technology*, 2018, vol. 117, no. 5, pp. 40-44.
***44.*** *Kevlar Aramid Fiber Technical Guide. DuPont*. 2017, 24 p. Available at: https://www.dupont.com/content/dam/dupont/amer/us/en/safety/public/documents/en/Kevlar_Technical_Guide_0319.pdf (Accessed 17 May 2025).
***45.*** Klepikov V.F., Prokhorenko E.M., Lytvynenko V.V., Zakharchenko A.A., Hazhmuradov M.A. Control of macroscopic characteristics of composite materials for radiation protection. *Problems of Atomic Science and Technology*, 2015, vol. 96, no. 2, pp. 193-196.
***46.*** Bezprozvannych G.V., Moskvitin Y.S., Kostiukov I.O., Grechko O.M. Dielectric parameters of phase and belt paper impregnated insulation of power cables. *Electrical Engineering & Electromechanics*, 2025, no. 2, pp. 69-78. doi: https://doi.org/10.20998/2074-272X.2025.2.09.
***47.*** Bezprozvannych G.V., Gontar Y.G., Pushkar I.A. Electrostatic field in unshielded power cables with different configurations of core. *Technical Electrodynamics*, 2025, no. 4, pp. 29-41. (Ukr). doi: https://doi.org/10.15407/techned2025.04.029.
***48.*** Bezprozvannych G.V., Grynyshyna M.V., Kyessayev A.G., Grechko O.M. Providing technical parameters of resistive cables of the heating floor system with preservation of thermal resistance of insulation. *Electrical Engineering & Electromechanics*, 2020, no. 3, pp. 43-47. doi: https://doi.org/10.20998/2074-272X.2020.3.07.
***49.*** Gillen K.T., Assink R.A., Bernstein R. *Final Report on Aging and Condition Monitoring of Low-Voltage Cable Materials*. Scandia National Laboratories, Nuclear Energy Plant Optimization (NEPO). SAND2005–7331, 2005. 287 p.
***50.*** Bezprozvannykh G.V., Moskvitin Y.S. *Applied Programming in GNU Octave*. Kharkiv, NTU «KhPI» Publ., 2025. 202 p. (Ukr).

*Received 18.07.2025*
*Accepted 20.09.2025*
*Published 02.01.2026*

*G.V. Bezprozvannych*[1], *Doctor of Technical Science, Professor,*
*I.A. Pushkar*[2], *Deputy General Director for Production, Postgraduate Student*,
[1] National Technical University «Kharkiv Polytechnic Institute», 2, Kyrpychova Str., Kharkiv, 61002, Ukraine,
e-mail: Hanna.Bezprozvannukh@khpi.edu.ua (Corresponding Author)
[2] Scientific and Production Enterprise ALAY,
95 A2, Vidradny Ave., office 202, Kyiv, 03061, Ukraine,
e-mail: ihor.pushkar@ieee.khpi.edu.ua

*How to cite this article:*
Bezprozvannych G.V., Pushkar I.A. Influence of gamma radiation on the electrical and mechanical properties of on-board systems cables. *Electrical Engineering & Electromechanics*, 2026, no. 1, pp. 76-85. doi: https://doi.org/10.20998/2074-272X.2026.1.10

**Матеріали приймаються за адресою:**
**Кафедра "Електричні апарати", НТУ "ХПІ", вул. Кирпичева, 2, м. Харків, 61002, Україна**
**Електронні варіанти матеріалів по e-mail: a.m.grechko@gmail.com**

**Довідки за телефонами: +38 067 359 46 96 Гречко Олександр Михайлович**

**Передплатний індекс: 01216**